

09:45:18

OCA PAD AMENDMENT - PROJECT HEADER INFORMATION

06/24/94

Active

Project #: E-18-674 Cost share #: E-18-321 Rev #: 13  
Center #: 10/24-6-R6819-0A0 Center shr #: 10/22-1-F6819-0A0 OCA file #:  
Contract#: DE-FC05-89CE90052 Mod #: AMENDMENT M002 Work type : RES  
Prime #: Document : COOP AG  
Contract entity: GTRC  
Subprojects ? : N CFDA: 81.049  
Main project #: PE #:

Project unit: MSF Unit code: 02.010.112  
Project director(s):  
COCHRAN J K JR MSF (404)894-6104

Sponsor/division names: US DEPT OF ENERGY / DOE OAK RIDGE - TN  
Sponsor/division codes: 141 / 017

Award period: 890901 to 921031 (performance) 930130 (reports)

Sponsor amount	New this change	Total to date
Contract value	0.00	722,200.00
Funded	0.00	722,200.00
Cost sharing amount		72,284.00

Does subcontracting plan apply ? : N

Title: THIN-WALL HOLLOW CERAMIC SPHERES FROM SLURRIES - PHASE IV: THERMAL INSULATION

PROJECT ADMINISTRATION DATA

OCA contact: E. Faith Gleason	894-4820
Sponsor technical contact	Sponsor issuing office
CHARLES A. SORRELL, CE-232 (202)586-1514	MELISSA Y JOHNSON, CONTRACT MGT BRAN (615)576-7599
FORRESTAL66 FORRESTAL U. S. DEPARTMENT OF ENERGY WASHINGTON, D C 20585	PROCUREMENT & CONTRACT DIV, U.S. DOE P.O.BOX 2001 OAK RIDGE, TN 37831-8757

Security class (U,C,S,TS) : U ONR resident rep. is ACO (Y/N): N  
Defense priority rating : N/A DOE supplemental sheet  
Equipment title vests with: Sponsor GIT X  
PRIOR WRITTEN APPROVAL REQUIRED FOR ITEMS OVER \$500.

Administrative comments -

AMENDMENT M002 ESTABLISHES END DATE AS 10/31/92, IN ACCORDANCE WITH NOTIFICATION SENT TO DOE 5/26/92. (REF. LETTER DATED 3/24/94 RE: "DEVIATION".)

GEORGIA INSTITUTE OF TECHNOLOGY  
OFFICE OF CONTRACT ADMINISTRATION

NOTICE OF PROJECT CLOSEOUT

Closeout Notice Date 04/29/96

Project No. E-18-674\_\_\_\_\_

Center No. 10/24-6-R6819-0A0\_

Project Director COCHRAN J K JR\_\_\_\_\_

School/Lab MSE\_\_\_\_\_

Sponsor US DEPT OF ENERGY/DOE OAK RIDGE - TN\_\_\_\_\_

Contract/Grant No. DE-FC05-89CE90052\_\_\_\_\_ Contract Entity GTRC

Prime Contract No. \_\_\_\_\_

Title THIN-WALL HOLLOW CERAMIC SPHERES FROM SLURRIES - PHASE IV: THERMAL INSULA

Effective Completion Date 921031 (Performance) \_\_\_\_\_ (Reports)

Closeout Actions Required:	Y/N	Date Submitted
Final Invoice or Copy of Final Invoice	Y	930330
Final Report of Inventions and/or Subcontracts	Y	_____
Government Property Inventory & Related Certificate	Y	_____
Classified Material Certificate	N	_____
Release and Assignment	N	_____
Other _____	N	_____

Comments \_\_\_\_\_  
\*\*\*NOTE\*\*\* USE SPONSOR FORMS FOR PATENT, PROPERTY. \_\_\_\_\_

Subproject Under Main Project No. \_\_\_\_\_

Continues Project No. \_\_\_\_\_

Distribution Required:

Project Director	Y
Administrative Network Representative	Y
GTRI Accounting/Grants and Contracts	Y
Procurement/Supply Services	Y
Research Property Management	Y
Research Security Services	N
Reports Coordinator (OCA)	Y
GTRC	Y
Project File	Y
Other _____	N
_____	N

NOTE: Final Patent Questionnaire sent to PDPI.

January 11, 1990

Ms. M.Y. Johnson  
Contract Specialist  
Department of Energy  
Oak Ridge Operations  
P.O. Box 2001  
Oak Ridge, TN 37831-8758

Dear Ms. Johnson:

Enclosed is DOE Form 538, "Notice of Energy RD&D Project".  
Sorry for the delay in completing this requirement. Please call  
if additional information is needed.

Sincerely yours,

A.T. Chapman  
Co-PI Contract Number  
DE-FC05-89ER90052

/lmw

U. S. DEPARTMENT OF ENERGY  
NOTICE OF ENERGY RD&D PROJECTDescriptive TITLE of work  
(150 characters including spaces)Thin Wall Hollow-Ceramic Spheres From Slurries-Phase IV:  
Thermal Insulation, Water Processing Technology Transfer

CONTRACT or grant number <u>DE-FC05-89CE</u>		3. Performing organization CONTROL number (internal) <u>E-18-674</u>
1. MASTER contract number (GOCO's) _____		3A. Budget and Reporting code <u>10/24-6-R6819-0A0</u>
2. Responsible PATENT office <u>Oak Ridge</u>		3B. Funding YEAR for this award <u>1989</u>
Original contract start date <u>9/1/89</u>		4B. Current contract close date <u>8/31/92</u>
A. Current contract start date <u>9/1/89</u>		4C. Anticipated project termination date _____
Work STATUS <input type="checkbox"/> Proposed <input type="checkbox"/> Renewal <input checked="" type="checkbox"/> New <input type="checkbox"/> Terminated		5B. CONGRESSIONAL district <u>5th</u>
A. Manpower (FTE) _____		5C. STATE or Country where work is being performed <u>Georgia</u>
		5D. COUNTRY sponsoring research _____
Name of PERFORMING organization <u>Georgia Tech Research Corporation</u>		
A. DEPARTMENT or DIVISION School of Materials Engr. Georgia Institute of Technology	6B. Street Address Bunger-Henry Bldg. 778 Atlantic Drive	6C. City, State, Zip Code Atlanta, GA 30332-0245
7. Circle only one code for TYPE of Organization Performing R&D:  CU - College, university, or trade school FF - Federally funded RD&D centers or laboratory operated for an agency of the U. S. Government IN - Private industry NP - Foundation or laboratory not operated for profit ST - Regional, state or local government facility TA - Trade or professional organization US - Federal agency XX - Other EG - Electric or gas utility		
8A. Contractor's PRINCIPAL INVESTIGATOR/s or project manager Name/s (Last, First, MI) <u>Chapman, Alan T.; Cochran, Joe K.</u>		
8B. PHONE/s (in order of PI names with commercial followed by FTS) Comm. <u>(404) 894-6075</u> ; FTS _____ ; Comm. <u>(404) 894-6104</u> ; FTS _____		
8C. PI/s address (if different from that of Performing Organization) _____ _____		



DOE SUPPORTING Organization (DOE Assistant Secretary and office sponsoring the work; technical monitor; and administrative monitor).

PROGRAM division or office CE-12  
(full name) Energy Conversion and Utilization Technologies Program Office Code  
TECHNICAL monitor (Last, First, MI) Wolf, Stanley  
Address Materials Program Manager 9D. Phone Comm. (202) 586-5377  
Forrestal Bldg, Rm. 5E-066 FTS \_\_\_\_\_  
1000 Independence Ave., SW, Washington, DC 20585  
ADMINISTRATIVE monitor (Last, First, MI) Johnson, Melissa Y.

FUNDING in thousands of dollars (K\$). Funds represent budget obligations for operating and capital equipment (FY runs October 1 – September 30).

Funding organization(s)	Current FY <u>89</u>	Next FY _____
A. DOE	522.2	
B. Recipient	52.9	
C.		

D. Does the current FUNDING cover more than one year's work? Yes X No \_\_\_\_\_  
E. If yes, provide dates (from when to when). 9/1/89 - 6/30/91

Descriptive SUMMARY of work. Enter a Project Summary using complete sentences limited to 200 words covering the following: Objective(s), state project objectives quantifying where possible (e.g., "The project objective is to demonstrate 95% recovery of sulfur from raw gas with molten salt recycling at a rate of one gallon per minute."); approach, describe the technical approach used (how the work is to be done); expected product/results, describe the final products or results expected from the project and their importance and relevance.

The primary objective of this project is to perform the necessary Research and Development as associated technology transfer to develop a new generic materials and technology using spherical ceramic shells for thermal insulation. The programs is divided into three major tasks:

1. To demonstrate that by properly opacifying sphere walls with efficient infrared wavelength scattering phases the high temperature thermal conductivity for the hollow spheres will be significantly reduced compared to the same spheres without opacified walls. Power slurries containing the opacifying agent must be developed that possess a rheology suitable for use in the sphere formation process, and the thermal conductivity of prototype spheres documented.
2. To convert sphere formation to water-based slurries rather than the current acetone-based systems. Use of organic liquids limits the type powders used for sphere formation to expensive optimum rheology size distributions and requires considerable expense for both acetone recovery and polymer bonding. If spheres could be collected from a water-based system using a rapid chemical reaction or rheology control combined with evaporation, process control expense and raw material cost could be drastically reduced making hollow spheres economically viable for many applications.
3. To develop a product engineering and information dissemination plan (technology transfer) to demonstrate the potential advantages of this generic technology to end-use industries. Various mechanisms will be employed to disseminate this information and this task will be coordinated with the ECUT Materials Program Manager.

PUBLICATIONS available to the public. List the five most descriptive publications that have resulted from this project in the last year that are available to the public. (Include author, title, where published, year of publication, and any other information you have to complete full bibliographic citation.) Use the back of this form or additional sheets if necessary.

1. S.A. Rickles, J.K. Cochran, T.H. Sanders, "The Production and Compressive Characteristics of a Low Density Syntatic Metal/Ceramic/Foam," Proceedings of 13th Annual Conference on Composites and Advanced Materials, ed., R.E. Banks, Cocoa Beach, Florida, American Ceramic Society, Columbus, Ohio, January, 1989.
2. W.J. Drury, S.A. Rickles, T.H. Sanders, J.K. Cochran, "Deformation Energy Absorption Characteristics of a Metal/Ceramic Cellular Solid," Proceedings of TMS Conference on Light Weight Alloys, TMS Annual Meeting, Las Vegas, Nevada, February, 1989.
3. M.K. Adicks, "Strength Characterization of thin-Wall Hollow Ceramic Spheres From Slurries," M.S. Thesis, Georgia Institute of Technology, Atlanta, GA, May, 1989.
4. T.J. Hwang, "A Model for Viscosity of Organic Based Oxide Dispersions", Ph.D. Dissertation, Georgia Institute of Technology, June 1989.

5. KEYWORDS (Listed five terms describing the technical aspects of the project. List specific chemicals and CAS number, if applicable.)

Ceramic Spheres  
Thin-wall Shells  
High Temperature Insulation  
Slurry Processing  
Light-weight Insulation

6. RESPONDENT. Name and address of person filling out the Form 538. Give telephone number, including extension (if you have FTS number, please include it) at which person can be reached. Record the date this form was completed or updated. The information in Item 14 will not be published.

Respondent's Name: Dr. A.T. Chapman Phone No.: (404) 894-6075 Date: 1/11/90

GA Inst. of Technology  
Street: School of Materials Engineering

City: Atlanta, State: Georgia Zip: 30332-0245

Additional space for furnishing information in items 1 to 14. (Indicate item numbers to which answers apply.)

Item No.	

NOTICE: Return this form to the office indicated in the reporting requirements for your award agreement covering this project. If you have completed a similar programmatic office project description during the current Fiscal Year, complete only the new data elements on this form and send it and a copy of the description completed earlier to Department of Energy, Office of Scientific and Technical Information, P. O. Box 62, Oak Ridge, TN 37831.





Office of Grants and Contracts Accounting

Georgia Institute of Technology  
Hinman Building  
Atlanta, Georgia 30332-0259  
404-894-4624; 2629  
Fax: 404-894-5519

September 20, 1990

Ms. Melissa Y. Johnson, Contract Specialist  
U. S. Department of Energy-Oak Ridge Operations  
P. O. Box 2001  
Oak Ridge, TN 37831-8758


REFERENCE: Grant No. DE-FC05-89CE90052

Dear Ms. Johnson,

Enclosed in triplicate is the Financial Status Report (SF-269) for Grant No. DE-FC05-89CE90052 covering the period September 01, 1989 to August 31, 1990.

If you should have questions or need additional information, please contact Geraldine Reese of this office at (404) 894-2629.

Sincerely,

  
David V. Welch, Director  
Grants and Contracts Accounting

DVW/djt

Enclosures

cc: Dr. S. D. Antolovich, Mat Eng 0245  
Dr. A. T. Chapman, Mat Eng 0245  
Dr. J. K. Cochran, Jr., Mat Eng 0245  
Ms. Mary Wolfe, OCA/CSD 0420 ✓  
File: E-18-674/R6819-OA0

# FINANCIAL STATUS REPORT

(Short Form)

(Follow instructions on the back)

<b>1. Federal Agency and Organizational Element to Which Report is Submitted</b>  U. S. DEPARTMENT OF ENERGY	<b>2. Federal Grant or Other Identifying Number Assigned By Federal Agency</b>  DE-FC05-89CE90052	<b>OMB Approval No.</b> 0348-0039	<b>Page</b> 1	<b>of</b> 1	<b>pages</b>
--	---	--------------------------------------	------------------	----------------	--------------

<b>3. Recipient Organization (Name and complete address, including ZIP code)</b> GEORGIA TECH RESEARCH CORPORATION P. O. BOX 100117 ATLANTA, GEORGIA 30384
---

<b>4. Employer Identification Number</b> 58-0603146	<b>5. Recipient Account Number or Identifying Number</b> E-18-674/R6819-OA0	<b>6. Final Report</b> <input type="checkbox"/> Yes <input checked="" type="checkbox"/> No	<b>7. Basis</b> <input checked="" type="checkbox"/> Cash <input type="checkbox"/> Accrual
--	--	---	--

<b>8. Funding/Grant Period (See Instructions)</b> From: (Month, Day, Year) September 01, 1989	To: (Month, Day, Year) August 31, 1992	<b>9. Period Covered by this Report</b> From: (Month, Day, Year) September 01, 1989	To: (Month, Day, Year) August 31, 1990
---	---	---	---

10. Transactions:	I Previously Reported	II This Period	III Cumulative
a. Total outlays	-0-	314,159.52	314,159.52
b. Recipient share of outlays	-0-	64,605.00	64,605.00
c. Federal share of outlays	-0-	249,554.52	249,554.52
d. Total unliquidated obligations			225,328.19
e. Recipient share of unliquidated obligations			-0-
f. Federal share of unliquidated obligations			225,328.19
g. Total Federal share (Sum of lines c and f)			474,882.17
h. Total Federal funds authorized for this funding period			522,200.00
i. Unobligated balance of Federal funds (Line h minus line g)			47,317.29

<b>1. Indirect Expenses</b>	<b>a. Type of Rate (Place "X" in appropriate box)</b> <input checked="" type="checkbox"/> Provisional <input type="checkbox"/> Predetermined <input type="checkbox"/> Final <input checked="" type="checkbox"/> Fixed			
	<b>b. Rate</b> FY90 @ 62.5% FY91 @ 62.5%	<b>c. Base</b> MTDC	<b>d. Total Amount</b> \$95,832.65	<b>e. Federal Share</b> \$95,832.65

<b>2. Remarks: Attach any explanations deemed necessary or information required by Federal sponsoring agency in compliance with governing legislation.</b>  GEORGIA TECH FISCAL YEAR ENDS JUNE 30	Questions pertaining to this report should be directed to: Ms. Geraldine Reese (404) 894-2629
---	--

<b>3. Certification:</b> I certify to the best of my knowledge and belief that this report is correct and complete and that all outlays and unliquidated obligations are for the purposes set forth in the award documents.
---

<b>Typed or Printed Name and Title</b> David V. Welch, Director, Grants & Contracts Accounting	<b>Telephone (Area code, number and extension)</b> (404) 894-2629
<b>Signature of Authorized Certifying Official</b> 	<b>Date Report Submitted</b> September 20, 1990

ATTACHMENT

FINANCIAL STATUS REPORT 09/01/89 - 08/31/90  
U. S. DEPARTMENT OF ENERGY  
GRANT NO. DE-FC05-89CE90052

	<u>DIRECT COSTS</u>	<u>INDIRECT COSTS</u>
FY90 @ 62.5%	\$121,464.83 <sup>(1)</sup>	\$32,257.04
FY91 @ 62.5%	75,672.00	20,160.65

REPORT PERIOD

09/01/89 - 08/31/90	\$153,721.87	\$95,832.65
---------------------	--------------	-------------

(1) \$389.65 EXCLUDED FROM INDIRECT COSTS

GIT CONTRIBUTIONS

	<u>DIRECT COSTS</u>
FY90 EQUIPMENT	\$64,605.00

Georgia Institute of Technology  
Lyman Hall/Emerson Building  
Atlanta, Georgia 30332-0259  
404-894-4624; 2629

October 1, 1991

Ms. Melissa Y. Johnson, Contract Specialist  
U. S. Department of Energy-Oak Ridge Operations  
P. O. Box 2001  
Oak Ridge, TN 37831-8758


REFERENCE: Grant No. DE-FC05-89CE90052

Dear Ms. Johnson,

Enclosed in triplicate is the Financial Status Report (SF-269A) for Grant No. DE-FC05-89CE90052 covering the period September 1, 1990 thru August 31, 1991.

If you should have questions or need additional information, please contact Geraldine Reese of this office at (404) 894-2629.

Sincerely,

  
David V. Welch, Director  
Grants and Contracts Accounting

DVW/djt

Enclosures

c: Dr. S. D. Antolovich, Mat Eng 0245  
Dr. J. K. Cochran, Jr., Mat Eng 0245  
Ms. Mary Wolfe, OCA/CSD 0420 ✓  
File: E-18-674/R6819-OA0



# FINANCIAL STATUS REPORT

(Short Form)

(Follow instructions on the back)

<b>1. Federal Agency and Organizational Element to Which Report is Submitted</b>  U.S. Dept. of Energy		<b>2. Federal Grant or Other Identifying Number Assigned By Federal Agency</b>  DE-FC05-89CE90052		<b>OMB Approval No.</b> 0348-0038	<b>Page</b> 1	<b>of</b> 1 pages																																								
<b>3. Recipient Organization (Name and complete address, including ZIP code)</b> GEORGIA TECH RESEARCH CORPORATION P. O. BOX 100117 ATLANTA, GEORGIA 30384																																														
<b>4. Employer Identification Number</b>  58-0603146		<b>5. Recipient Account Number or Identifying Number</b>  E-18-674/R6819-OA0		<b>6. Final Report</b> <input type="checkbox"/> Yes <input checked="" type="checkbox"/> No		<b>7. Basis</b> <input checked="" type="checkbox"/> Cash <input type="checkbox"/> Accrual																																								
<b>8. Funding/Grant Period (See instructions) From: (Month, Day, Year)</b> September 01, 1989		<b>To: (Month, Day, Year)</b> August 31, 1992		<b>9. Period Covered by this Report From: (Month, Day, Year)</b> September 01, 1990		<b>To: (Month, Day, Year)</b> August 31, 1991																																								
<b>10. Transactions:</b> <table border="1" style="width: 100%; border-collapse: collapse;"> <thead> <tr> <th style="width: 50%;"></th> <th style="width: 15%; text-align: center;">I Previously Reported</th> <th style="width: 15%; text-align: center;">II This Period</th> <th style="width: 20%; text-align: center;">III Cumulative</th> </tr> </thead> <tbody> <tr> <td>a. Total outlays</td> <td style="text-align: right;">314,159.52</td> <td style="text-align: right;">320,311.60</td> <td style="text-align: right;">634,471.12</td> </tr> <tr> <td>b. Recipient share of outlays</td> <td style="text-align: right;">64,605.00</td> <td style="text-align: right;">47,666.12</td> <td style="text-align: right;">112,271.12</td> </tr> <tr> <td>c. Federal share of outlays</td> <td style="text-align: right;">249,554.52</td> <td style="text-align: right;">272,645.48</td> <td style="text-align: right;">522,200.00</td> </tr> <tr> <td>d. Total unliquidated obligations</td> <td></td> <td></td> <td style="text-align: center;">-0-</td> </tr> <tr> <td>e. Recipient share of unliquidated obligations</td> <td></td> <td></td> <td style="text-align: center;">-0-</td> </tr> <tr> <td>f. Federal share of unliquidated obligations</td> <td></td> <td></td> <td style="text-align: center;">-0-</td> </tr> <tr> <td>g. Total Federal share (Sum of lines e and f)</td> <td></td> <td></td> <td style="text-align: right;">522,200.00</td> </tr> <tr> <td>h. Total Federal funds authorized for the funding period</td> <td></td> <td></td> <td style="text-align: right;">522,200.00</td> </tr> <tr> <td>i. Unobligated balance of Federal funds (Line h minus line g)</td> <td></td> <td></td> <td style="text-align: center;">-0-</td> </tr> </tbody> </table>								I Previously Reported	II This Period	III Cumulative	a. Total outlays	314,159.52	320,311.60	634,471.12	b. Recipient share of outlays	64,605.00	47,666.12	112,271.12	c. Federal share of outlays	249,554.52	272,645.48	522,200.00	d. Total unliquidated obligations			-0-	e. Recipient share of unliquidated obligations			-0-	f. Federal share of unliquidated obligations			-0-	g. Total Federal share (Sum of lines e and f)			522,200.00	h. Total Federal funds authorized for the funding period			522,200.00	i. Unobligated balance of Federal funds (Line h minus line g)			-0-
	I Previously Reported	II This Period	III Cumulative																																											
a. Total outlays	314,159.52	320,311.60	634,471.12																																											
b. Recipient share of outlays	64,605.00	47,666.12	112,271.12																																											
c. Federal share of outlays	249,554.52	272,645.48	522,200.00																																											
d. Total unliquidated obligations			-0-																																											
e. Recipient share of unliquidated obligations			-0-																																											
f. Federal share of unliquidated obligations			-0-																																											
g. Total Federal share (Sum of lines e and f)			522,200.00																																											
h. Total Federal funds authorized for the funding period			522,200.00																																											
i. Unobligated balance of Federal funds (Line h minus line g)			-0-																																											
<table border="1" style="width: 100%; border-collapse: collapse;"> <tr> <td rowspan="2" style="width: 10%; vertical-align: top;"><b>1. Indirect Expense</b></td> <td colspan="6" style="vertical-align: top;"> <b>a. Type of Rate (Place "X" in appropriate box)</b>  <input checked="" type="checkbox"/> Provisional <input type="checkbox"/> Predetermined <input type="checkbox"/> Final <input checked="" type="checkbox"/> Fixed         </td> </tr> <tr> <td style="width: 25%; vertical-align: top;"> <b>b. Rate</b>          SEE ATTACHED       </td> <td style="width: 15%; vertical-align: top;"> <b>c. Base</b>          MTDC       </td> <td style="width: 20%; vertical-align: top;"> <b>d. Total Amount</b>          123,006.92       </td> <td colspan="3" style="width: 35%; vertical-align: top;"> <b>e. Federal Share</b>          104,685.80       </td> </tr> </table>							<b>1. Indirect Expense</b>	<b>a. Type of Rate (Place "X" in appropriate box)</b> <input checked="" type="checkbox"/> Provisional <input type="checkbox"/> Predetermined <input type="checkbox"/> Final <input checked="" type="checkbox"/> Fixed						<b>b. Rate</b> SEE ATTACHED	<b>c. Base</b> MTDC	<b>d. Total Amount</b> 123,006.92	<b>e. Federal Share</b> 104,685.80																													
<b>1. Indirect Expense</b>	<b>a. Type of Rate (Place "X" in appropriate box)</b> <input checked="" type="checkbox"/> Provisional <input type="checkbox"/> Predetermined <input type="checkbox"/> Final <input checked="" type="checkbox"/> Fixed																																													
	<b>b. Rate</b> SEE ATTACHED	<b>c. Base</b> MTDC	<b>d. Total Amount</b> 123,006.92	<b>e. Federal Share</b> 104,685.80																																										
<b>2. Remarks: Attach any explanations deemed necessary or information required by Federal sponsoring agency in compliance with governing legislation.</b>  <div style="text-align: right; padding-right: 50px;">         Questions pertaining to this report should be directed to: Ms. Geraldine Reese          (404) 894-2629       </div> GEORGIA TECH'S FISCAL YEAR ENDS JUNE 30.																																														
<b>3. Certification:</b> I certify to the best of my knowledge and belief that this report is correct and complete and that all outlays and unliquidated obligations are for the purposes set forth in the award documents.																																														
<b>Typed or Printed Name and Title</b>  David V. Welch, Director, Grants & Contracts Acctg.					<b>Telephone (Area code, number and extension)</b>  (404) 894-2629																																									
<b>Signature of Authorized Certifying Official</b> 					<b>Date Report Submitted</b>  October 1, 1991																																									

Attachment

U. S. Department of Energy  
 Financial Status Report  
 Grant No. DE-FC05-89CE90052  
 Period covered: 09/01/90 - 08/31/91

	<u>Direct Costs</u>	<u>Indirect Costs</u>
FY90 @ 62.5% Fixed	\$121,464.83 <sup>(1)</sup>	\$ 75,672.00
FY91 @ 62.5% Fixed	171,317.80	107,073.62
FY92 @ 61.5% Provisional	28,898.92	17,772.83
 <u>Report Period</u>		
09/01/90 - 06/30/91	139,060.76	86,912.97
07/01/91 - 08/31/91	28,898.92	17,772.83

(1) \$389.65 EXCLUDED FROM INDIRECT COSTS

GIT CONTRIBUTIONS

	<u>Direct Costs</u>	<u>Indirect Costs</u>	<u>Equipment</u>
FY90 @ 62.5%	\$ 64,605.00 <sup>(1)</sup>	\$ -0-	(1) \$64,605.00
FY91 @ 62.5%	27,395.00	17,121.87	
FY92 @ 61.5%	1,950.00	1,199.25	

Georgia Institute of Technology

Hinman Building

Atlanta, Georgia 30332-0259

USA

404•894•4624; 2629

Fax: 404•894•5519

March 30, 1993

Ms. Melissa Y. Johnson, Contract Specialist  
Special Acquisitions Branch  
U. S. Department of Energy  
Procurement and Contracts Division  
P. O. Box 2001  
Oak Ridge, TN 37831-8757

REFERENCE: Grant # DE-FC05-89CE90052

Dear Ms. Johnson,

Enclosed in triplicate is the Financial Status Report (SF-269A) for Grant No. DE-FC05-89CE90052 covering the period September 01, 1991 through October 31, 1992.

If you should have questions or need additional information, please contact Geraldine Reese of this office at (404) 894-2629.

Sincerely,

David V. Welch  
Director

DVW/GMR/djt

Enclosures

c: Dr. M. Marek, Mat Eng 0245  
Dr. J. K. Cochran, Jr., Mat Eng 0245  
Ms. Danielle Herrmann, OCA/CSD 0420✓  
File: E-18-674/R6819-0A0

RECEIVED

APR 01 1993

OFFICE OF CONTRACT  
ADMINISTRATION

# FINANCIAL STATUS REPORT

(Short Form)

(Follow instructions on the back)

1. Federal Agency and Organizational Element to Which Report is Submitted  U. S. Department of Energy		2. Federal Grant or Other Identifying Number Assigned By Federal Agency  DE-FC05-89CE90052		OMB Approval No. <b>0348-0039</b>	Page <b>1</b>	of <b>2 pages</b>
3. Recipient Organization (Name and complete address, including ZIP code) GEORGIA TECH RESEARCH CORPORATION P. O. BOX 100117 ATLANTA, GA 30384						
4. Employer Identification Number  58-0603146		5. Recipient Account Number or Identifying Number  E-18-674/R6819-OAO		6. Final Report <input type="checkbox"/> Yes <input checked="" type="checkbox"/> No		7. Basis <input checked="" type="checkbox"/> Cash <input type="checkbox"/> Accrual
8. Funding/Grant Period (See Instructions) From: (Month, Day, Year) September 01, 1989		To: (Month, Day, Year) October 31, 1992		9. Period Covered by this Report From: (Month, Day, Year) September 01, 1991		To: (Month, Day, Year) October 31, 1992
10. Transactions:				I Previously Reported	II This Period	III Cumulative
a. Total outlays				634,471.12	240,193.98	874,665.10
b. Recipient share of outlays				112,271.12	40,193.98	152,465.10
c. Federal share of outlays				522,200.00	200,000.00	722,200.00
d. Total unliquidated obligations						-0-
e. Recipient share of unliquidated obligations						-0-
f. Federal share of unliquidated obligations						-0-
g. Total Federal share (Sum of lines c and f)						722,200.00
h. Total Federal funds authorized for this funding period						722,200.00
i. Unobligated balance of Federal funds (Line h minus line g)						-0-
11. Indirect Expense	a. Type of Rate (Place "X" in appropriate box) <input type="checkbox"/> Provisional <input type="checkbox"/> Predetermined <input type="checkbox"/> Final <input checked="" type="checkbox"/> Fixed					
	b. Rate  SEE ATTACHED	c. Base  MTDC	d. Total Amount  84,886.85	e. Federal Share  75,292.85		
12. Remarks: Attach any explanations deemed necessary or information required by Federal sponsoring agency in compliance with governing legislation. <div style="text-align: right; margin-top: 10px;">Questions pertaining to this report should be directed to: Ms. Geraldine Reese (404) 894-2629</div>						
13. Certification: I certify to the best of my knowledge and belief that this report is correct and complete and that all outlays and unliquidated obligations are for the purposes set forth in the award documents.						
Typed or Printed Name and Title  David V. Welch, Director, Grants & Contracts Accounting					Telephone (Area code, number and extension)  (404) 894-2629	
Signature of Authorized Certifying Official  C					Date Report Submitted  March 30, 1993	

Attachment

Page 2

U. S. Department of Energy

Grant # DE-FC05-89CE90052

Financial Status Report 03/30/93

Period Covering: 09/01/91 - 10/31/92

	<u>Direct Costs</u>	<u>Indirect Costs</u>
FY90 @ 62.5% Fixed	\$121,464.83	\$ 75,672.00
FY91 @ 62.5% Fixed	171,317.80	107,073.62
FY92 @ 61.5% Fixed	131,351.41	80,781.11
FY93 @ 55.2%	22,254.66	12,284.57

	<u>REPORT PERIOD</u>	
09/01/91 - 06/30/92	102,452.49	63,008.28
07/01/92 - 10/31/92	22,254.66	12,284.57

GIT Contributions

	<u>Direct Costs</u>	<u>Indirect Costs</u>	<u>Equipment</u> *
FY90 @ 62.5%	\$64,605.00	\$ -0-	\$64,605.00
FY91 @ 62.5%	27,395.00	17,121.87	
FY92 @ 61.5%	32,541.70	10,793.25	14,999.98
FY93 @ 55.2%	8.28	-0-	

\*Excluded from Indirect Costs



E18-674  
3

Quarterly Project Status Report  
1 September through 31 December 1989

Thin-Wall Hollow Ceramic Spheres from Slurries

A.T. Chapman and J.K. Cochran

School of Materials Engineering  
Georgia Institute of Technology  
Atlanta, Georgia 30332-0245

Project De-FC05-89CE90052

This document is the first quarterly status report for the Phase IV effort (initiated 1 Sept 89) for the development of "Thin-Wall Hollow Spheres from Slurries." During this phase three major tasks are emphasized: 1) the use of opacifiers to reduce the high temperature thermal conductivity of the spheres, 2) convert the slurries used in sphere formation from the existing organic-based to aqueous - based systems and 3) product engineering and information dissemination (technology transfer) to end-use industries. In Section I Milestones are abbreviated as a more detailed presentation is included in the quarterly Federal Assistance Milestone Plan accompanying this report.

I. Milestones

The list of project milestones shown in Table 1 includes all the major tasks undertaken in the Phase IV effort. Major technical accomplishments are presented in the next section.

Table I. Milestones (Tasks) for Hollow Sphere Project

---

<u>TASKS</u>		<u>STATUS</u>
I.	Thermal Insulation	
1.	Develop Slurries Containing Opacifying Agents	Active
2.	Sphere Formation	
	a. Opacified Spheres	Active
	b. Modeling	Active
3.	Strength of Opacified Spheres	Inactive
4.	Thermal Conductivity Measurements	Active
5.	Bonded Sphere Monoliths	Active
II.	Aqueous Slurries	
1.	Rheology Measurements	Active
2.	Strength Development through	
	a. Gels	Active
	b. Polymer-crosslinking	Inactive
	c. Chemical Reactions	Inactive
III.	Technology Transfer	
1.	Advisory Meeting	Active
2.	Industrial Visits	Planning
3.	Trade Shows	Inactive



## II. Technical Highlights

### 1. Reduce Thermal Conductivity of the Spheres

The major objective of this area of research is to decrease the thermal conductivity (T/C) of loose sphere beds as well as bonded sphere structures to values that approach the high temperature insulating characteristics of ceramic fiber. As described in the Annual Progress Report FY-89, September 1989, the incorporation of voids or thermal pores in the sphere walls significantly decreased the T/C of the spheres. It is proposed the voids act as scattering centers to retard the flow of radiant energy through the sphere walls at elevated temperatures. During this reported period, an initial attempt to evaluate the roll of sphere size on T/C and to measure the T/C of a commercially available insulating firebrick was performed.

To evaluate the effect of sphere size and to some extent density on T/C, a mixture of various size aerospheres (3.75, 3.00, 2.25 mm diameter) were blended with about 50 W/o fines (-30 mesh fused  $\text{Al}_2\text{O}_3$  spheres). The mixture was tested in the ANTER T/C rig and the resultant T/C is shown as curve A in Figure 1. By comparison curve B shows the T/C of monosize aero-spheres 3 mm in diameter. These curves display the expected trends where the blend has the higher low temperature T/C since the density of the mixture ( $\sim 60 \text{ lbs/ft}^3$ ) is about twice that of the monosize spheres ( $\sim 30 \text{ lbs/ft}^3$ ) and conduction through sphere wall dominates. However, in the higher temperature regime, the increased number of surfaces resulting from the high packing efficiency of the mixed sizes acts to reflect and scatter more radiation than the monosize spheres. Most encouraging was the observed decrease in slope (rate of T/C increase with temperature) for the blended sphere sizes. Also note all the spheres used in the blend (curve

# THERMAL CONDUCTIVITY OF AEROSPHERES/IFB

17.APGM.THERMAL

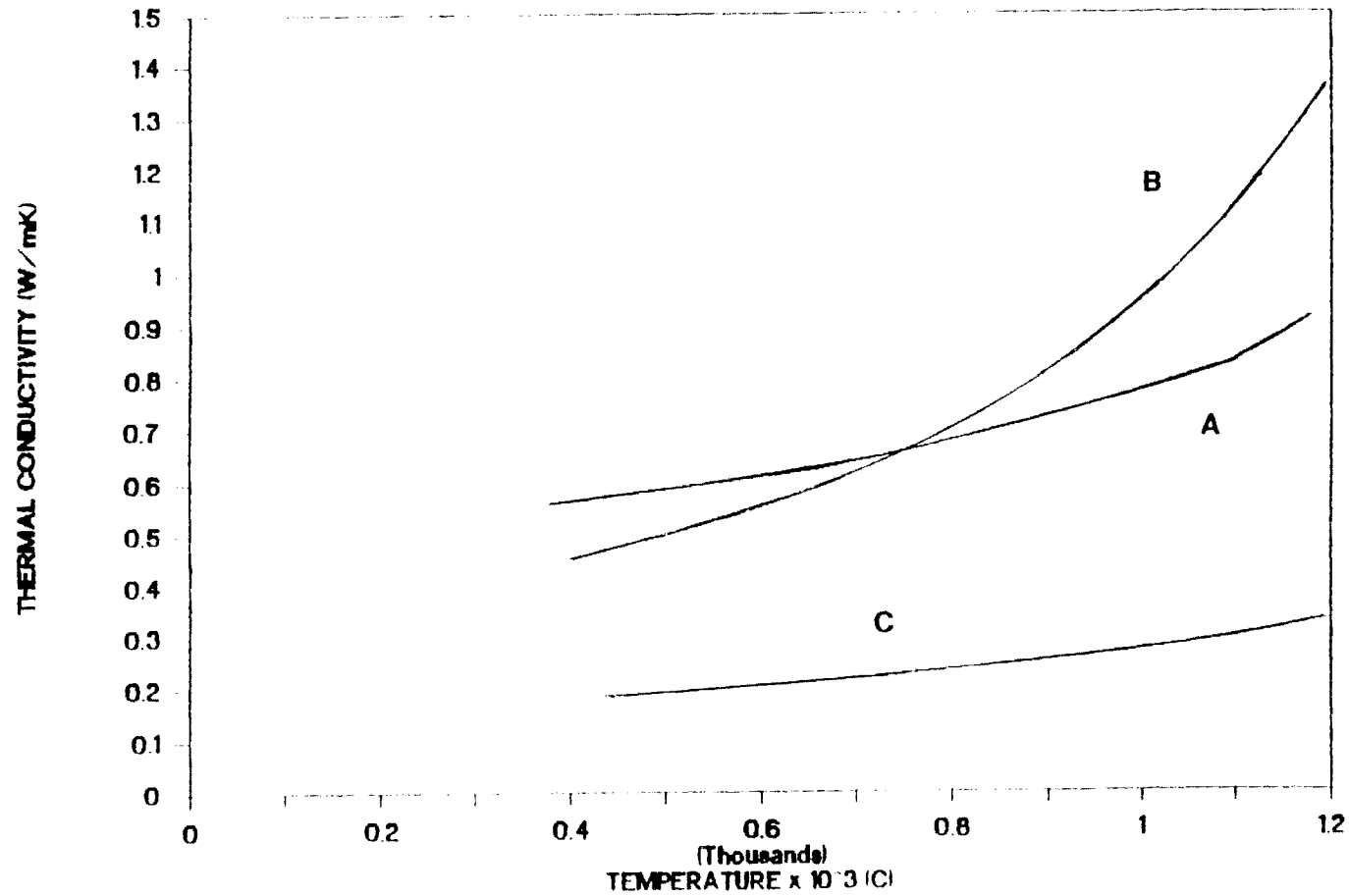


Figure 1. Thermalconductivity Versus Temperature of a Blend of Aerosphere Sizes (curve A), Monosize Aerospheres (curve B) and K-23 Insulating Firebrick (curve C).

A) possessed dense sphere walls. Without being too overly optimistic it certainly appears that by using a distribution of sphere sizes and an opacifier in the wall and selecting a sphere composition such as mullite (which has an inherent bulk conductivity lower than alumina) that the hollow spheres may well approach the T/C of ceramic fiber.

The final data shown in Figure 1 (curve C) was generated by testing a stack of K-23 insulating fire brick in the Anter T/C equipment. This material has probably the lowest T/C in the 1100-1200°C range of any material (including fiber) so this would be a demonstrated goal for the spheres. Published T/C data for the K-23 IFB is available from the manufacturer and the data shown in Curve C is about 15% higher than the T/C reported by Thermal Ceramics, the manufacturer of the K-23. This reasonable agreement provides confidence that the T/C values measured with the ANTER equipment are indeed realistic, considering the well known difficulty in reproducing T/C data in different test facilities.

## 2. Aqueous - Based Slurry Systems

An effort is underway to convert the sphere formation process from an acetone-based to a water-base ceramic powder slip system. There are many benefits to be gained from this conversion including; 1) elimination of an acetone disposal or recovery system, 2) exposure of personnel and the environment to an organic solvent, and 3) a significant reduction in the cost of producing the spheres.

The most promising avenue for a successful water-based slip system so far identified at Georgia Tech is the use of natural gums to gel the water in the sphere shortly after formation, and provide the strength necessary for a soft landing of the free falling sphere. These gums are commonly produced from selected species of seaweed and used in the food industry for such applications

as jelly and ice cream. Therefore, there are no health hazards associated with these naturally occurring gums.

In the sphere formation process utilizing water the dispersion consisting of the powder, dispersant, and jelling agent or gum is fed through the nozzle at temperatures averaging about 90°C where the gum is in solution and the viscosity of the slip is relatively low (~ 100 cp). Immediately after forming the sphere, the temperature is reduced by evaporation as well as entering cooler air at which point the liquid portion of the dispersion is thickened or gelled by the long entangled chains of the gums coming out of solution.

A search of the literature has identified three gels of potential use with the spheres: 1) a mixture of xanthan gum and vegetable gum, 2) agar, and 3) kappa-carrageenan. Work with these materials is underway to assess the gelling behavior as well as gel strength. Rheology of these systems is being studied as a function of solids content and with alkali additions which may be used to control gelling characteristics.

### 3. Technology Transfer

The major activity in this area occurred in Atlanta on Saturday, November 11, when personnel from industry, universities, and government met to review the hollow-sphere technology with the goal of commercializing this product. A formal report has been written by Dr. Carl VanderLinden, who is heading the technology transfer effort, describing the findings of this group. In general, this conference identified potential application areas and thought it appropriate to inform people about the spheres at trade shows and through individual visits rather than by trying to attract a large audience through a formal technology transfer conference. To support the effort by Dr. VanderLinden, a subcontract has been included in the existing contract to cover industrial visits by Dr.

VanderLinden. These visits are scheduled during the winter and spring of this year and Dr. Cochran will also attend most of these meetings.

#### 4. Matching Funds

Georgia Tech has provided \$65,000 in matching funds to purchase equipment needed to support contract work. The equipment has been purchased, was received in December and is being utilized in several tasks. The equipment includes (1) a laser particle size analyzer (0.1 to 700 $\mu$ m) (2) a multipoint surface area analyzer, (3) a mercury porosimeter for pore size distributions and (4) a helium picnometer.

## List of Investigators Participating in Project

Participation in days/week

Project: Thin-Wall Hollow Spheres from Slurries  
J.K. Cochran and A.T. Chapman

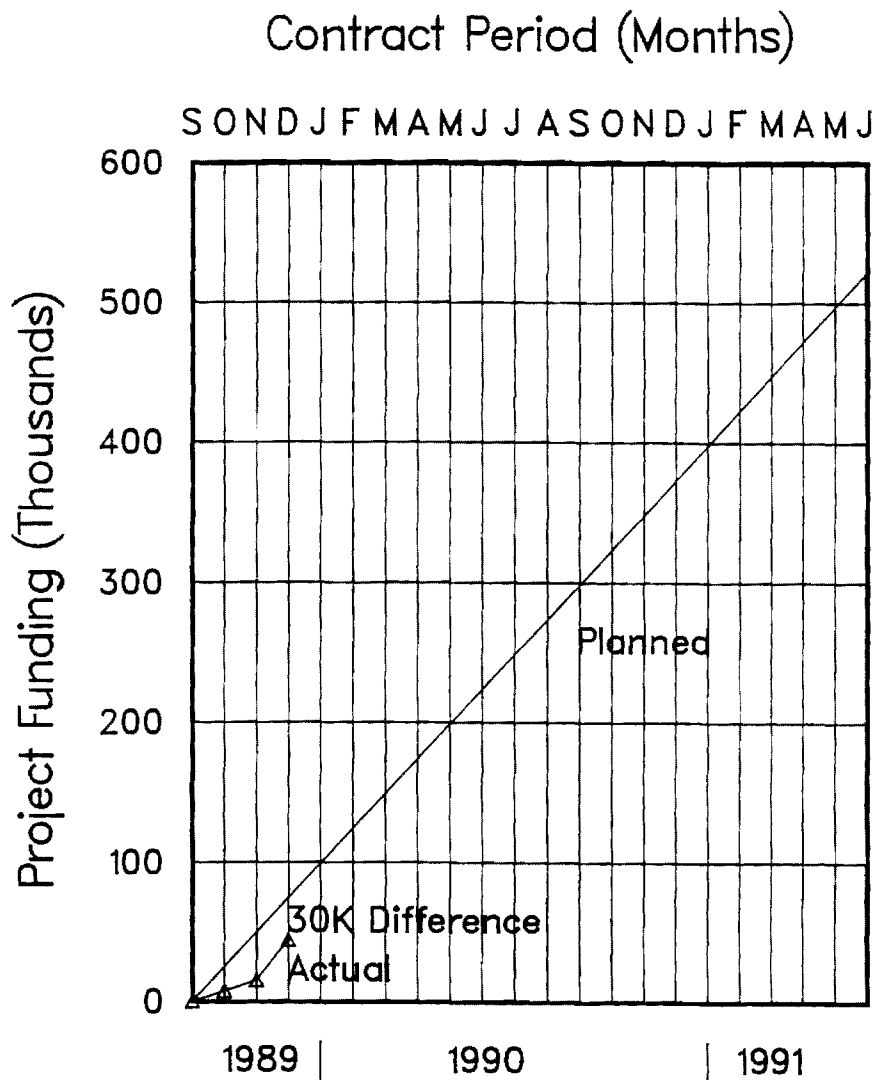
Reporting Period: 1 September - 31 December, 1989

	Name	Type of Position	Planned Project Time	Approximate Time
A.	J.K. Cochran	Project Dir.	2	2 (40%)
B.	A.T. Chapman	Project Dir.	2	2 (40%)
C.	T.J. Hwang	Post Doctoral	5	5
D.	J.H. Chung	Student	2-3	2.5
E.	P.R. Chu	Student	2-3	2.5
F.	S. Furlong	Student	2-3	2.5
G.	C. Moore	Student	2-3	2.5

## COST INFORMATION

Project: Thin-Wall Hollow Spheres -  
J.K. Cochran and A.T. Chapman

Reporting Period: Phase IV, 1 September - 31 December 1989



1. Program/Project Identification No.		DE-FCOS-89CE90052		2. Program/Project Title		Thin-Wall Holl						
3. Performer (Name, Address)				School of Materials Engineering J.K. Cochran and A.T. Chapman Georgia Tech, Atlanta, GA 30332								
6. Identification Number	7. Planning Category (Work Breakdown Structure Task)	8. Program/Project Duration										
		← 1990 →										
		S	O	N	D	J	F	M	A	M	J	J
TASK I	Slurries with opacifiers											
Thermal	Forming Spheres											
Insulations	Spheres Strength											
	T/C Measurements											
	Bonded Monoliths											
TASK II	Rheology											
Aqueous	Gels											
Slurries	Polymers											
	Reactions											
TASK III	Advisory Mtgs											
Technology	Industrial Visits											
Transfer	Trade Shows											
10. Remarks												
11. Signature of Recipient and Date												
12. Signature of DO												



A 12-1-4  
5

Quarterly Project Status Report  
1 January through 31 March 1990

Thin-Wall Hollow Ceramic Spheres from Slurries

A.T. Chapman and J.K. Cochran

School of Materials Engineering  
Georgia Institute of Technology  
Atlanta, Georgia 30332-0245

Project De-FC05-89CE90052

This document is the second quarterly status report for the Phase IV effort (initiated 1 Sept 89) for the development of "Thin-Wall Hollow Spheres from Slurries." During this phase three major tasks are emphasized: 1) the use of opacifiers to reduce the high temperature thermal conductivity of the spheres, 2) convert the slurries used in sphere formation from the existing organic-based to aqueous - based systems and 3) product engineering and information dissemination (technology transfer) to end-use industries. In Section I Milestones are abbreviated as a more detailed presentation is included in the quarterly Federal Assistance Milestone Plan accompanying this report.

I. Milestones

The list of project milestones shown in Table 1 includes all the major tasks undertaken in the Phase IV effort. Major technical accomplishments are presented in the next section.

Table I. Milestones (Tasks) for Hollow Sphere Project

---

	<u>TASKS</u>	<u>STATUS</u>
I.	Thermal Insulation	
1.	Develop Slurries Containing Opacifying Agents	Active
2.	Sphere Formation	
	a. Opacified Spheres	Active
	b. Modeling	Active
3.	Strength of Opacified Spheres	Inactive
4.	Thermal Conductivity Measurements	Active
5.	Bonded Sphere Monoliths	Active
II.	Aqueous Slurries	
1.	Rheology Measurements	Active
2.	Strength Development through	
	a. Gels	Active
	b. Polymer-crosslinking	Planning
	c. Chemical Reactions	Inactive
III.	Technology Transfer	
1.	Advisory Meeting	Completed
2.	Industrial Visits	Active
3.	Trade Shows	Inactive

## II. Technical Highlights

### 1. Reduce Thermal Conductivity of the Spheres

During this reporting period the concept of forming sphere walls consisting of two phases with significantly different refractive index (to promote radiation scattering) was evaluated as an approach to reduce the high temperature T/C of the spheres. Also the T/C of a basic sphere, spinel ( $\text{MgO} \cdot \text{Al}_2\text{O}_3$ ), was measured.

Spheres consisting of 50/50 v/o of alumina ( $\text{Al}_2\text{O}_3$ ) and mullite ( $3\text{Al}_2\text{O}_3 \cdot 2\text{SiO}_2$ ) grains in the walls were successfully fabricated. This sample had a bed density of 19 lbs/ft<sup>3</sup> with a sphere diameter of ~3.0 mm. The T/C of these mixed oxide spheres was measured with the ANTER equipment and is shown in Figure 1. The T/C of pure  $\text{Al}_2\text{O}_3$  and mullite spheres of the closest density and diameter are presented for comparison in Figure 1. Clearly the mixed oxide sphere has a 30 to 40% lower T/C than the pure oxides and the prospects of exploiting this concept to reduce T/C using phases with greater differences in refractive index (i.e.  $\text{Al}_2\text{O}_3$  -  $\text{ZrO}_2$ ) will be investigated in future tests.

During an industrial visit to a major refractory company there was interest expressed in a basic-type sphere ( $\text{MgO}$ ,  $\text{CaO}$ ,  $\text{MgO} \cdot \text{Al}_2\text{O}_3$  etc) since no light weight aggregate of this composition is commercially available. Based on this interest an effort to form  $\text{MgO}$  and  $\text{MgO} \cdot \text{Al}_2\text{O}_3$  spheres was undertaken. Spinel spheres were successfully made by dispersing  $\text{MgO}$  and  $\text{Al}_2\text{O}_3$  powders in acetone and forming spheres using the coaxial nozzle. Firing at 1550°C formed a product that was almost 100% spinel as measured by x-ray analysis. These basic spheres possessed a bed density of 28 lbs/ft<sup>3</sup> and a diameter of ~3.0mm. The T/C for this material is also shown in Figure 1 and is significantly below alumina and mullite at 1200°C. This is somewhat surprising considering the bulk T/C of spinel is

about equal to  $\text{Al}_2\text{O}_3$  and higher than mullite. The low T/C may reflect the presence of a porous microstructure formed during the reaction of the  $\text{Al}_2\text{O}_3$  and MgO grains initially present in the as-blown sphere walls. Efforts to fabricate a pure MgO sphere are in progress.

Recently ORNL has conducted T/C measurements on  $\text{Al}_2\text{O}_3$  spheres containing opacification (thermal pores). The ORNL data confirms the reduced T/C produced by the pores and the ORNL and GA TECH data, obtained on identical spheres, is shown in Figure 2. In the temperature range of overlap (400-550°C) the ORNL data is some 25% lower than the GA TECH data obtained from the ANTER T/C equipment. Since the T/C data for the IFB measured at GA TECH was also some 15% higher than the manufacture's specification (as reported in the last Quarterly Report), an effort will be made to determine the absolute accuracy of the T/C values obtained from the ANTER rig, especially at T/C values between 0.5 to 1.0 w/m°K.

## 2. Aqueous-Based Slurries Systems

The last report described the need for converting the slurry processing of the ceramic powders used to form spheres from an organic to an aqueous-based system. The initial work in this area has been performed using naturally occurring gums to gel the slurry systems and provide the necessary rigidity in the free falling spheres to survive a landing on a hard surface. Carrageenan was identified as the gum possessing the optimum properties for the sphere forming and collecting process. The typical gelling and melting characteristics of this class of material is shown in Figure 3 where the viscosity versus cycling temperature are plotted. After the initial solution process the dispersions containing the gelling agent are heated to high temperature (~80°C) to provide a low viscosity slurry for forming the sphere and subsequently rapidly cooled

to below 50°C to induce the gelling process. Most encouraging during this work was the demonstration that, indeed, the aqueous-based systems could be gelled during the 3 to 5 second free-fall residence time and the sphere wall developed adequate strength to maintain a "sphere-like" geometry during landing.

At present the sphere forming characteristics of the aqueous slurries have not quite matched the acetone-based systems. For example, the slurries containing carrageenan must employ 3 to 4 w/o of the gum to provide enough gel strength to maintain the shape during free-fall and survive the landing. Unfortunately these slurries, with a high volume loading of solids ( $\text{Al}_2\text{O}_3$  powder), are very viscous and do not possess the film-forming capacity of the organic systems. As a result the typical density of the aqueous processed spheres is 40-50  $\text{lbs/ft}^3$  compared to 20-30  $\text{lbs/ft}^3$  for the acetone derived spheres. Additionally, because of the softer wall and landing damage the sphericity of the aqueous spheres do not match that of the organic base spheres. Work is continuing on aqueous systems and the study of the gelling concept is ongoing because of the economic attractiveness of the water-based systems.

### 3. Technology Transfer

The dissemination of sphere technology and property information to industrial community was initiated in January 1990. Dr. Carl VanderLinden has arranged many of the visits and Cochran and VanderLinden has made presentations to some dozen companies this reporting period. Extensive trip reports have been provided by Dr. VanderLinden. This activity has been productive and as a result of these contacts, 1) small diameter spheres has been provided for fluidized bed trials and 2) basic spheres ( $\text{MgO} \cdot \text{Al}_2\text{O}_3$ ) have been fabricated for evaluation by a major refractory company. Additional visits are planned to the Chicago and Cleveland areas.

# THERMAL CONDUCTIVITY OF AEROSPHERES

SiO<sub>2</sub> 14,18,36,37,38

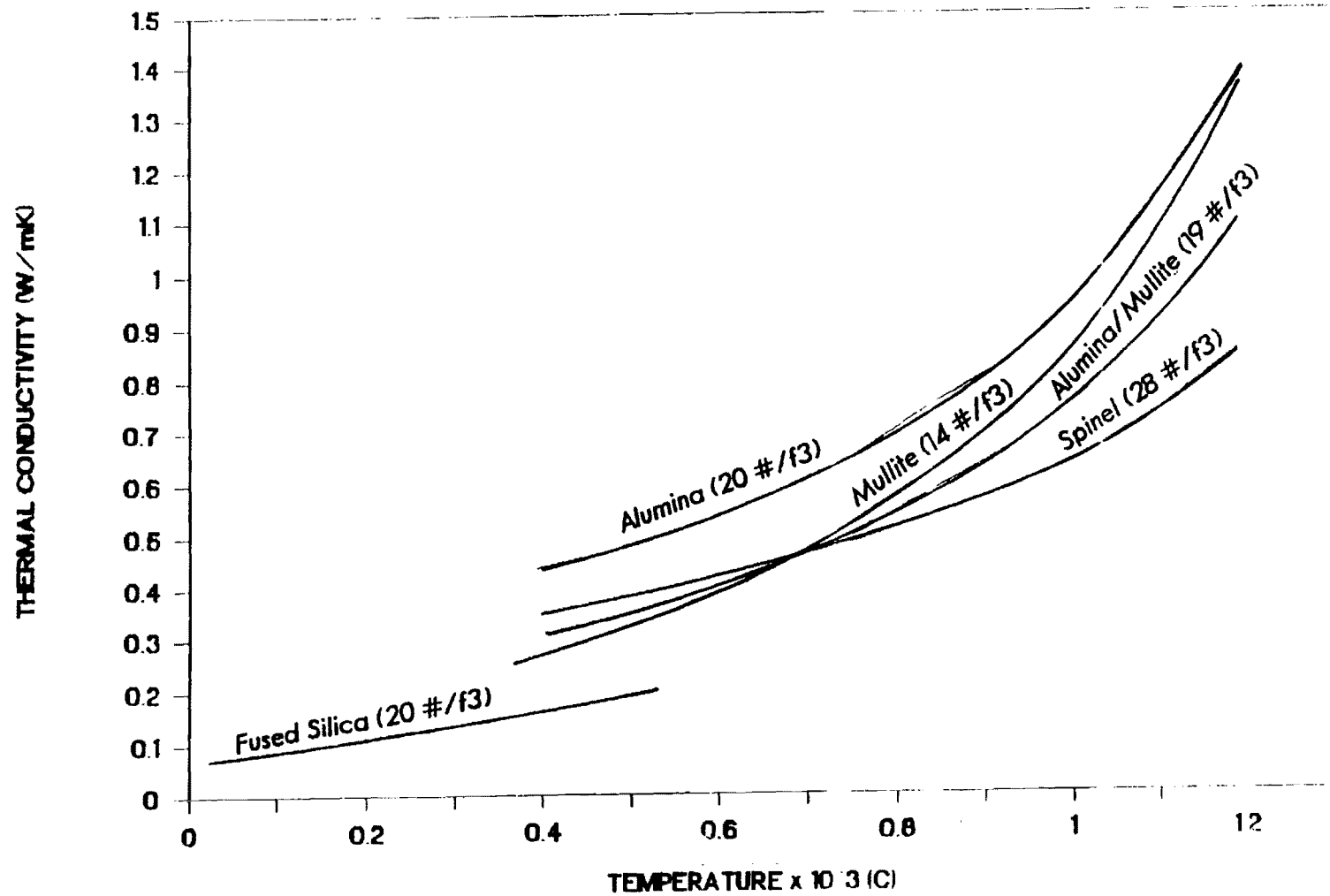


Figure 1. Thermal Conductivity Versus Temperature of Alumina, Mullite, an 50/50 v/o Alumin/Mullite Blend and Spinel Spheres.

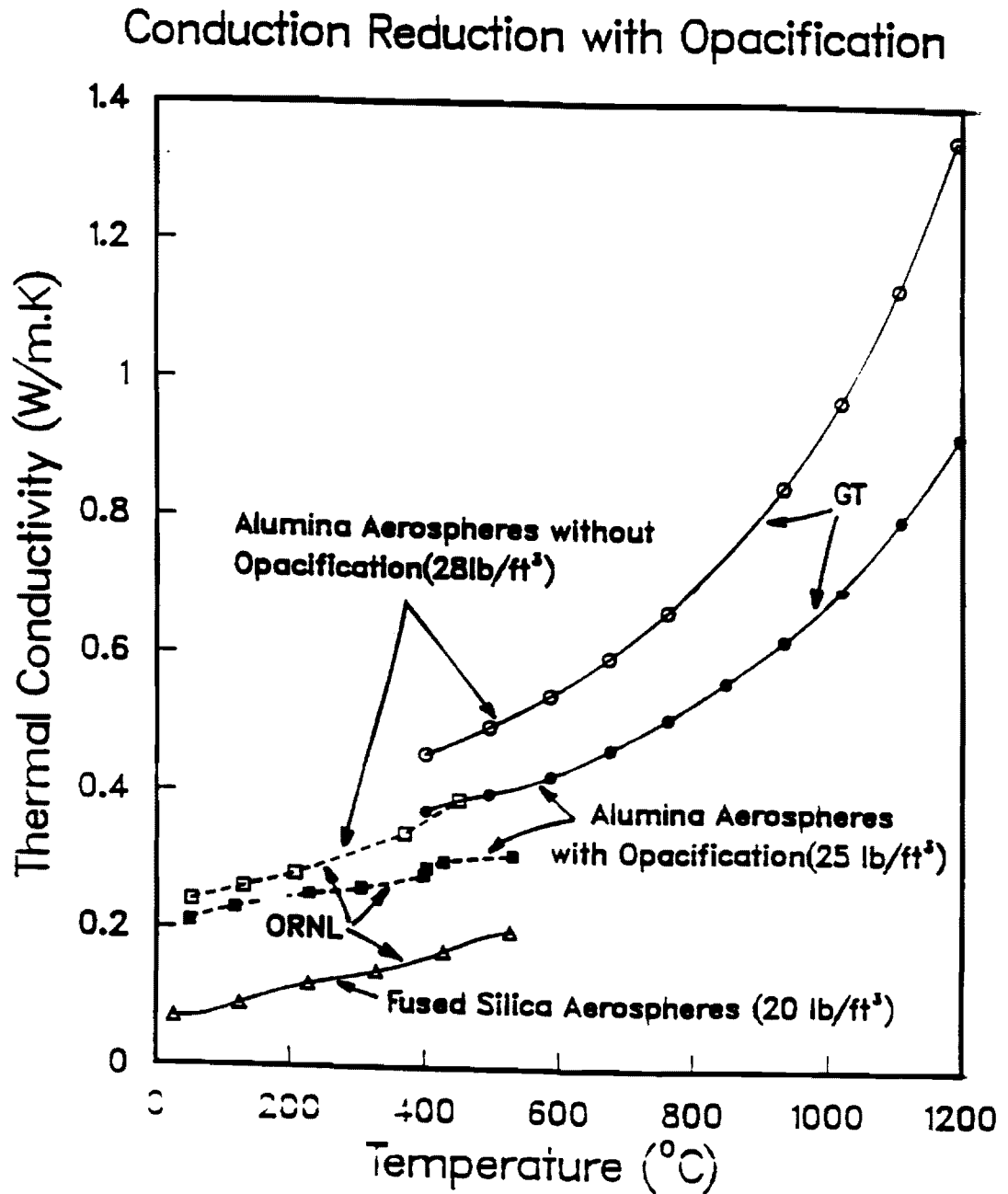


Figure 2. Comparison of Thermal Conductivity Values Measured at Georgia Tech and ORNL for Alumina Aerospheres With and Without Thermal Pores.

### Water Gels Are Thermo Reversible

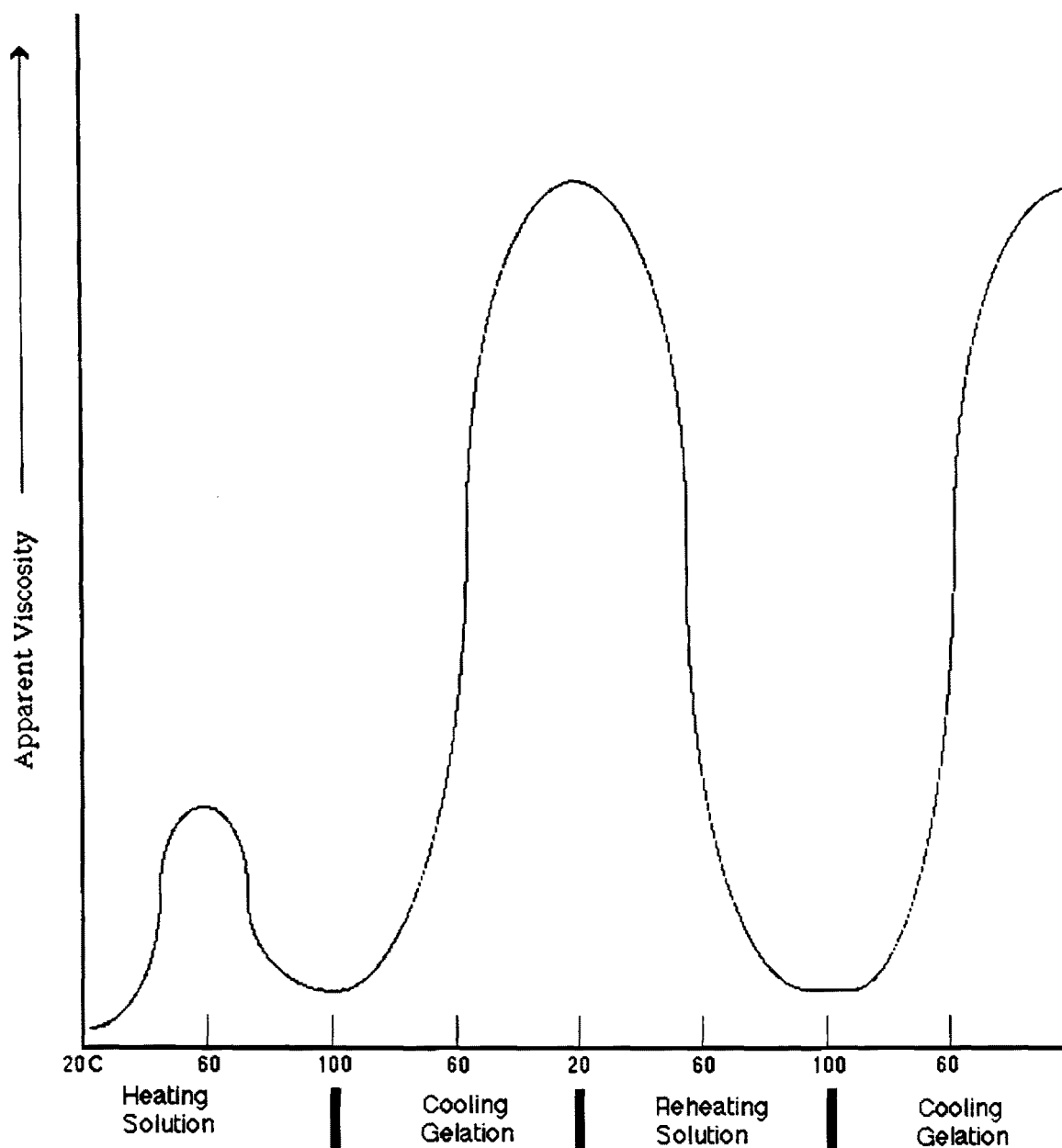


Figure 3. Schematic Design of the Reversible Change in Viscosity of Aqueous Solutions Containing Gelling Agents.



## List of Investigators Participating in Project

Participation in days/week

Project: Thin-Wall Hollow Spheres from Slurries  
J.K. Cochran and A.T. Chapman

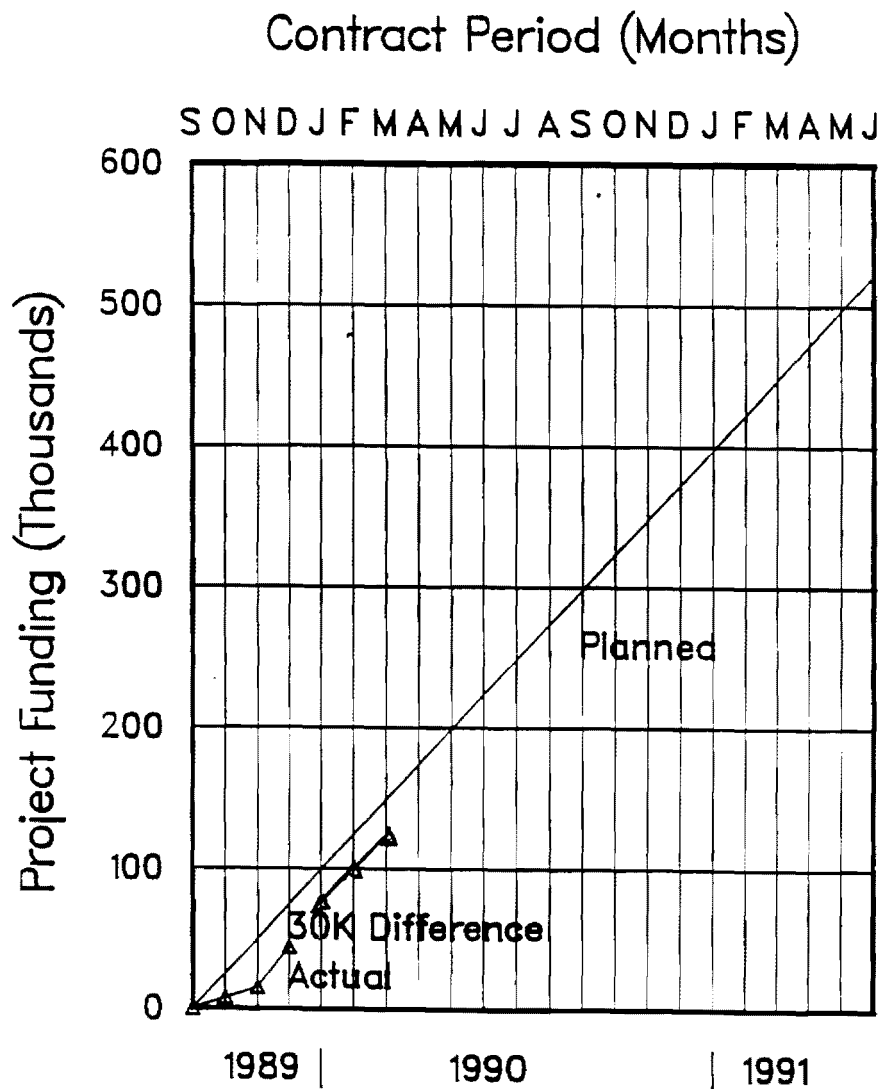
Reporting Period: 1 January - 31 March 1990

	Name	Type of Position	Planned Project Time	Approximate Time
A.	J.K. Cochran	Project Dir.	2	2 (40%)
B.	A.T. Chapman	Project Dir.	2	2 (40%)
C.	T.J. Hwang	Post Doctoral	5	5
D.	J.H. Chung	Student	2-3	2.5
E.	P.R. Chu	Student	2-3	2.5
F.	S. Furlong	Student	2-3	2.5
G.	C. Moore	Student	2-3	2.5
H.	T. Ford	Student	2-3	2.5

## COST INFORMATION

Project:Thin-Wall Hollow Spheres -  
J.K. Cochran and A.T. ChapmanReporting Period:

Phase IV, 1 January - 31 March 1990



Quarterly Project Status Report  
1 April through 30 June 1990

Thin-Wall Hollow Ceramic Spheres from Slurries

A.T. Chapman and J.K. Cochran

School of Materials Engineering  
Georgia Institute of Technology  
Atlanta, Georgia 30332-0245

Project De-FC05-89CE90052

This document is the third quarterly status report for the Phase IV effort (initiated 1 Sept 89) for the development of "Thin-Wall Hollow Spheres from Slurries." During this phase three major tasks are emphasized: 1) the use of opacifiers to reduce the high temperature thermal conductivity of the spheres, 2) convert the slurries used in sphere formation from the existing organic-based to aqueous - based systems and 3) product engineering and information dissemination (technology transfer) to end-use industries. In Section I Milestones are abbreviated as a more detailed presentation is included in the quarterly Federal Assistance Milestone Plan accompanying this report.

I. Milestones

The list of project milestones shown in Table 1 includes all the major tasks undertaken in the Phase IV effort. Major technical accomplishments are presented in the next section.

Table I. Milestones (Tasks) for Hollow Sphere Project

---

	<u>TASKS</u>	<u>STATUS</u>
I.	Thermal Insulation	
1.	Develop Slurries Containing Opacifying Agents	Active
2.	Sphere Formation	
a.	Opacified Spheres	Active
b.	Modeling	Active
3.	Strength of Opacified Spheres	Inactive
4.	Thermal Conductivity Measurements	Active
5.	Bonded Sphere Monoliths	Active
II.	Aqueous Slurries	
1.	Rheology Measurements	Active
2.	Strength Development through	
a.	Gels	Active
b.	Polymer-crosslinking	Planning
c.	Chemical Reactions	Inactive
III.	Technology Transfer	
1.	Advisory Meeting	Completed
2.	Industrial Visits	Active
3.	Trade Shows	Inactive

## II. Technical Highlights

### 1. Reduce Thermal Conductivity of the Spheres

During this reporting period the concept of forming sphere walls consisting of two phases with significantly different refractive index (to promote radiation scattering) was continued as an approach to reduce the high temperature T/C of the spheres. The high temperature T/C of spheres containing a 50/50 v/o of zirconia-alumina grains in the sphere walls reduced the T/C of loose spheres to the lowest value attained to date, with the possible exception of fused silica. Also this reporting period the first T/C measurement of a bonded sphere monolith is described.

Spheres consisting of  $\text{Al}_2\text{O}_3$  and  $\text{ZrO}_2$  without any stabilizer were successfully fabricated using the coaxial nozzle. This sample possessed a bed density of 35 lbs/ft<sup>3</sup> with a sphere diameter of ~3.0 mm. The T/C of these two-phase spheres was measured with the ANTER equipment to ~1200°C and the results are shown in Figure 1. The data for the other sphere compositions, presented in the previous quarterly report, are included in Figure 1 for comparison. Clearly the addition of zirconia to alumina produced a 50% decrease in the T/C, compared to pure alumina. The prospects of using mixed oxides along with thermal pores for scattering radiation by the spheres and utilizing efficient sphere packing for additional insulation may generate T/C values approaching ceramic fiber.

In previous work the spheres have been bonded together to form monolithic structures by using a slip of basically the same composition as the spheres to form small "fillets" at the contact points between the spheres. Many samples have been fabricated primarily for measuring strengths of bonded shapes. A

cylindrical monolithic structure, formed by bonding mullite spheres with mullite slip, was fabricated using longitudinal rods to leave channels in the cylinder for the central heater and radial thermocouples of the Anter T/C equipment. The T/C of this bonded structure, loose mullite spheres and mullite spheres with thermal pores are shown in Figure 2. As anticipated the T/C of the bonded shape was slightly higher at low temperature and slightly lower at 1200°C. Using mullite spheres with thermal pores to fabricate bonded mullite shapes should yield T/C values equivalent or lower than insulating fire brick. Work to evaluate and reduce the T/C of bonded shapes is continuing.

## 2. Aqueous-Based Slurry Systems

Previous reports described the advantages of converting the sphere forming process from an organic-based to an aqueous-based system. Water soluble organic systems that form rigid gels after processing (using temperature, pH, etc) are difficult to find. The "gelcast" system developed at ORNL was considered as a candidate process for developing strength in the free-falling sphere. The cost and, more importantly, the health risk associated with handling the pre-gel solution were major disadvantages of this system. During the sphere fabrication the exposure of personnel to the liquid would be much greater, for example, than an injection molding operation. In our opinion, this system would have a high probability of hardening spheres in free fall. However, because of health concerns, we have decided not to investigate this system any further.

Recent interest has shifted to colloidal  $\text{SiO}_2$  as a means to "freeze" the sphere shape in free fall. In addition, several food gels are being reinvestigated to determine the maximum limits to which they can be employed in sphere formation. Limitation in the past have been the inability to produce  $\text{Al}_2\text{O}_3$  spheres at densities less than 40 lb/ft<sup>3</sup> and the inability to work with

clay based slurries using these gels. Future reports will detail the initial efforts using Ludox to develop sphere strength in the "green" state and continuing efforts on food gels.

### 3. Technology Transfer

A dissemination of sphere technology and property information to the industrial community was initiated in January 1990. Carl VanderLinden has arranged most of the visits and Cochran and VanderLinden have made presentations to industrial firms in the Chicago and northern Ohio region this reporting period. Trip reports have been provided by Dr. VanderLinden describing the details of these visits. As a result of these meetings, many additional applications have been uncovered where a unique property of the spheres provides a refractory product not previously available. The interest in a magnesia or spinel sphere is continually expressed and efforts to make such a sphere are well underway at Georgia Tech. During the visit to the Amoco Research Center, north of Chicago, the need for a refractory to withstand the very corrosive atmospheres (containing fluorine and chlorine) present in incinerators used in most petrochemical plants was identified. Prospects of making a silica-free sphere-based refractory shape that has the insulating characteristics of IFB's is currently being explored with Amoco.

# THERMAL CONDUCTIVITY OF AEROSPHERES

SI0214.18.36.37.38

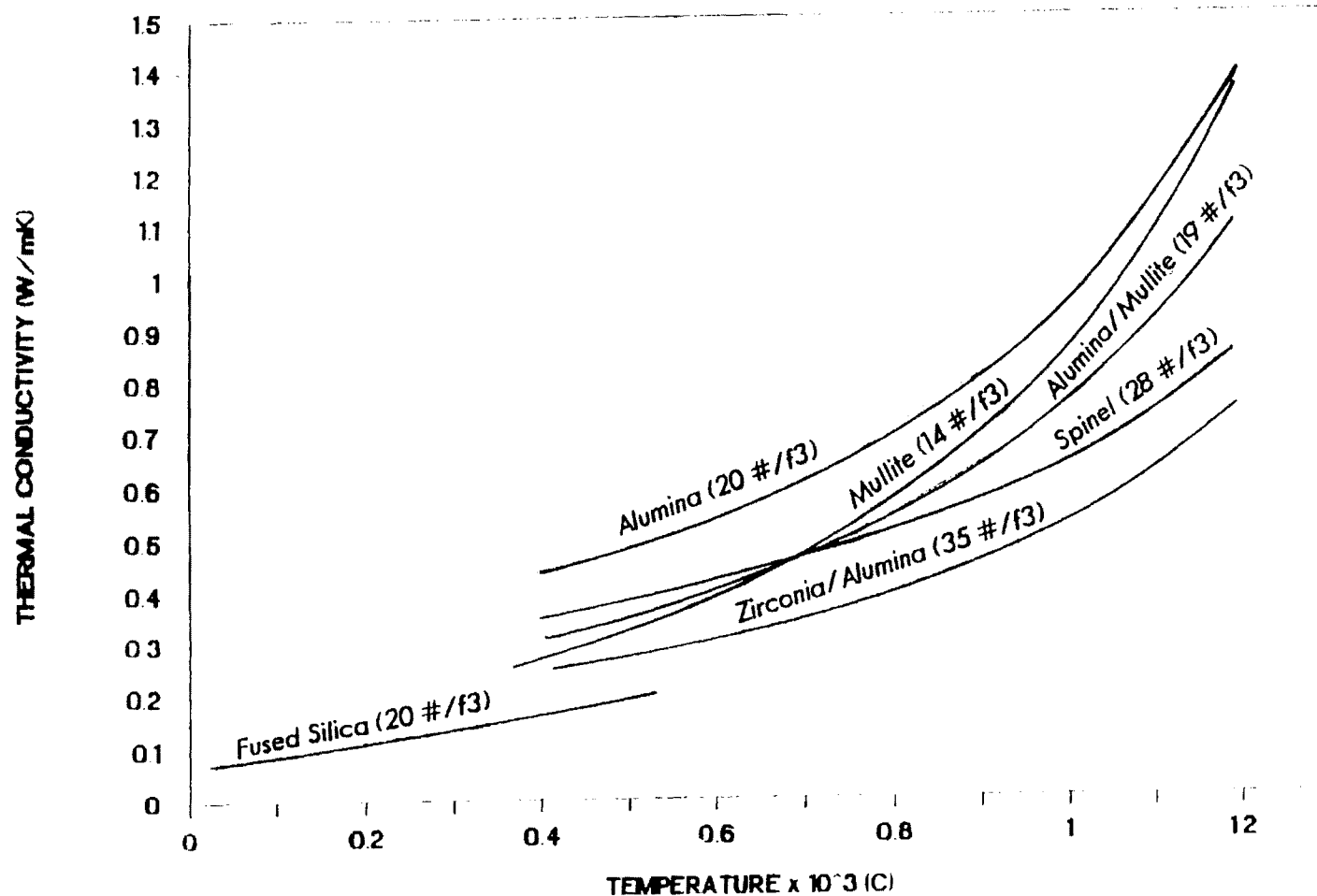


Figure 1. Thermal Conductivity Versus Temperature of Zirconia/Alumina Spheres and Other Compositions Reported in Previous Quarterly Report (for comparison).



## THERMAL CONDUCTIVITY OF MULLITE SPHERES

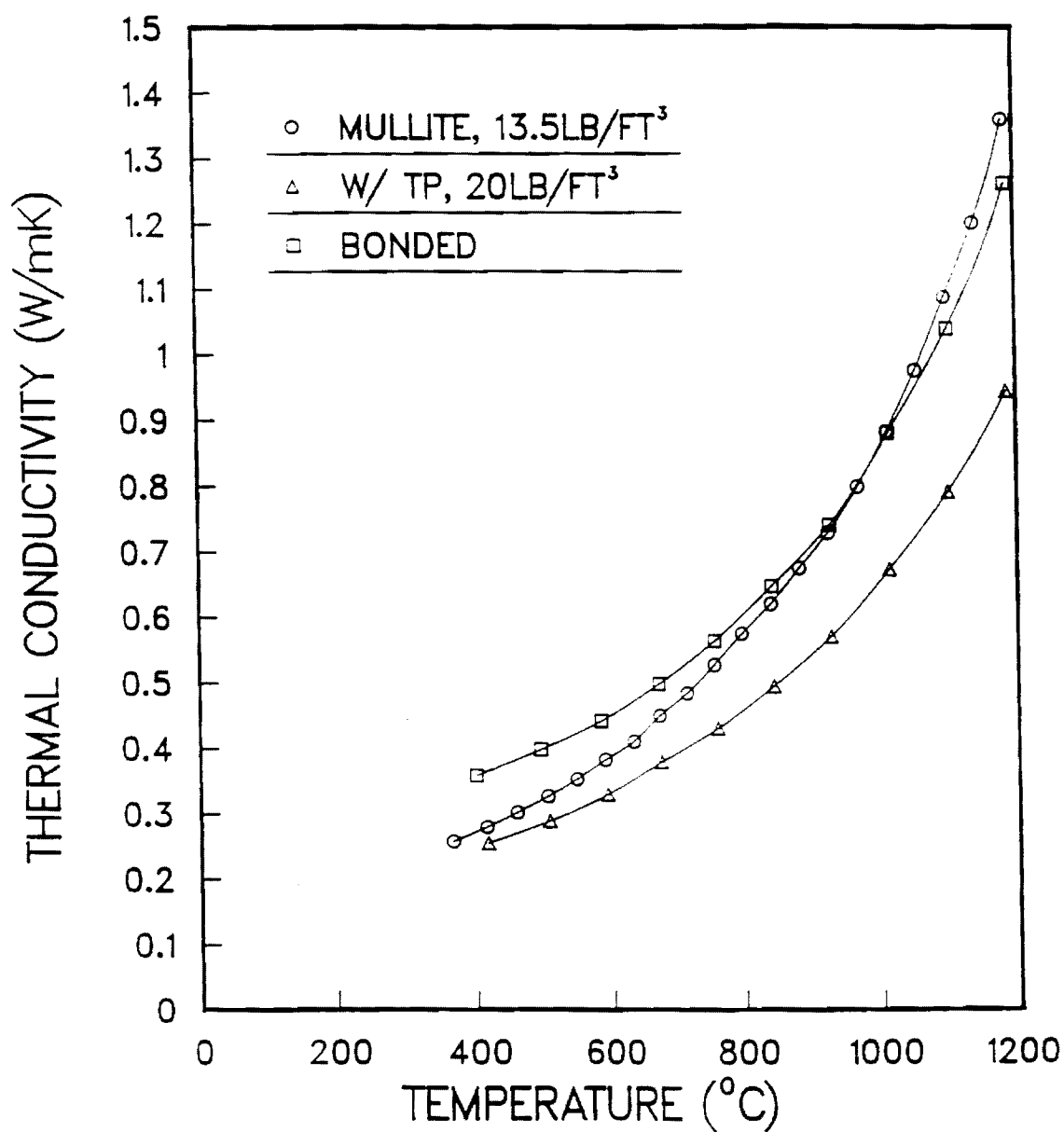


Figure 2. Thermal Conductivity of Bonded Mullite Spheres and Loose Mullite Spheres with and without Thermal Pores.

## List of Investigators Participating in Project

Participation in days/week

Project: Thin-Wall Hollow Spheres from Slurries  
J.K. Cochran and A.T. Chapman

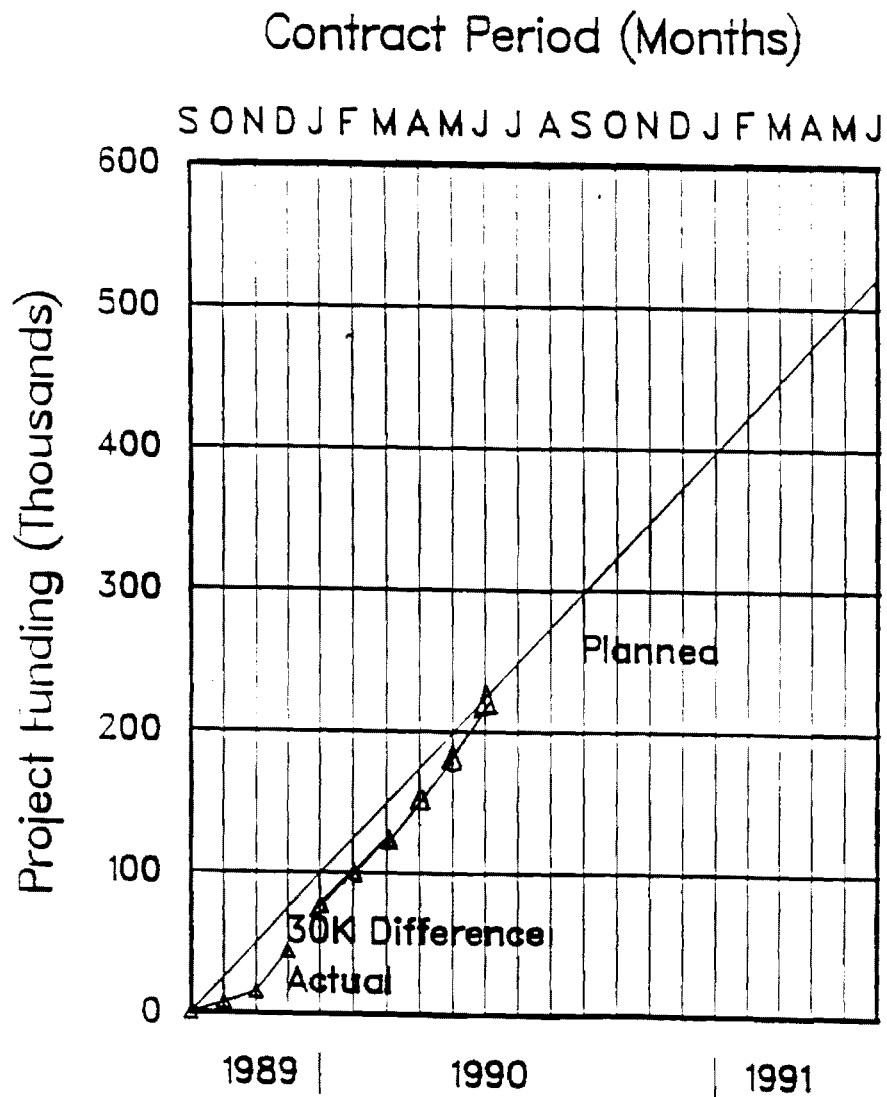
Reporting Period: 1 April - 30 June 1990

	Name	Type of Position	Planned Project Time	Approximate Time	
A.	J.K. Cochran	Project Dir.	2	2	(40%)
B.	A.T. Chapman	Project Dir.	2	2	(40%)
C.	T.J. Hwang	Post Doctoral	5	5	
D.	J.H. Chung	Student	2-3	2.5	
E.	P.R. Chu	Student	2-3	2.5	
F.	S. Furlong	Student	2-3	2.5	
G.	C. Moore	Student	2-3	2.5	
H.	T. Ford	Student	2-3	2.5	

## COST INFORMATION

Project:Thin-Wall Hollow Spheres -  
J.K. Cochran and A.T. ChapmanReporting Period:

Phase IV, 1 April - 30 June 1990



6. Identification Number	7. Planning Category (Work Breakdown Structure Task)	8. Program/Project Duration											
		<div style="text-align: center;"> <span>←</span> <span style="margin: 0 20px;">1990</span> <span>→</span> </div> <div style="display: flex; justify-content: space-around; font-weight: bold;"> <span>S</span><span>O</span><span>N</span><span>D</span><span>J</span><span>F</span><span>M</span><span>A</span><span>M</span> </div>											
TASK I	Slurries with opacifiers												
Thermal	Forming Spheres												
Insulations	Spheres Strength												
	T/C Measurements												
	Bonded Monoliths												
TASK II	Rheology												
Aqueous	Gels												
Slurries	Polymers												
	Reactions												
TASK III	Advisory Mtgs												
Technology	Industrial Visits												
Transfer	Trade Shows												
10. Remarks													
11. Signature of Recipient and Date													12.

2-12-1991  
13

Quarterly Project Status Report  
1 October through 31 December 1990

Thin-Wall Hollow Ceramic Spheres from Slurries

A.T. Chapman and J.K. Cochran

School of Materials Engineering  
Georgia Institute of Technology  
Atlanta, Georgia 30332-0245

Project DE-FCO5-89CE90052

This document is the fifth quarterly status report for the Phase IV effort (initiated 1 Sept 89) for the development of "Thin-Wall Hollow Spheres from Slurries." During this phase three major tasks are emphasized: 1) the use of opacifiers to reduce the high temperature thermal conductivity of the spheres, 2) convert the slurries used in sphere formation from the existing organic-based to aqueous - based systems and 3) product engineering and information dissemination (technology transfer) to end-use industries. In Section I Milestones are abbreviated as a more detailed presentation is included in the quarterly Federal Assistance Milestone Plan accompanying this report. During this reporting period, a paper titled "Reduction of High Temperature Thermal Conductivity of Thin-wall Ceramic Spheres" has been published in ASTM STP 1116. A copy of this paper is also enclosed.

I. Milestones

The list of project milestones shown in Table 1 includes all the major tasks undertaken in the Phase IV effort. Major technical accomplishments are presented in the next section.

Table I. Milestones (Tasks) for Hollow Sphere Project

---

	<u>TASKS</u>	<u>STATUS</u>
I.	Thermal Insulation	
1.	Develop Slurries Containing Opacifying Agents	Active
2.	Sphere Formation	
a.	Opacified Spheres	Active
b.	Modeling	Active
3.	Strength of Opacified Spheres	Inactive
4.	Thermal Conductivity Measurements	Active
5.	Bonded Sphere Monoliths	Active
II.	Aqueous Slurries	
1.	Rheology Measurements	Active
2.	Strength Development through	
a.	Gels	Active
b.	Polymer-crosslinking	Inactive
c.	Chemical Reactions	Active
III.	Technology Transfer	
1.	Advisory Meeting	Completed
2.	Industrial Visits	Active
3.	Trade Shows	Inactive

## II. Technical Highlights

### 1. Reduce Thermal Conductivity of the Spheres

In previous reports, the thermal conductivity of standard spheres were significantly reduced by incorporating thermal pores or by utilizing two crystalline phases with different refractive index in the sphere wall. These structures effectively increased radiation scattering, especially at the higher temperatures. The majority of this work was conducted using refractory oxides, such as alumina, mullite and zirconia which have use-temperatures well above 1600°C. Good quality clays, i.e kaolinite, are candidate raw materials for use in forming thin-wall spheres. However, to provide proper rheology for sphere formation, the solids content of the dispersions made from clays have to be much lower than that of the refractory oxides listed above. Therefore, forming monosize spheres which may be adequately dried using clay dispersions has been difficult. An alternate sphere forming process has been developed which uses clay and organic liquid slurries. The process forms spheres ~1 mm in diameter. The following outlines the sphere-forming process suitable for use with clay dispersions and some interesting thermal conductivity (T/C) measurements made on the resultant clay spheres.

As noted above, clay has been a candidate sphere forming material throughout this program, primarily because clay is inexpensive and clays form mullite which possesses attractive high temperature properties. Typical clay dispersions contain only 30 to 35 volume percent solids, compared to the 50 v/o for  $\text{Al}_2\text{O}_3$ . As a consequence, drying a standard clay sphere sufficiently to develop strength for free-fall landing without major damage has been difficult. In this alternate process, the clay dispersion is forced through a small diameter ( $\sim \frac{1}{2}$  mm) orifice without an inner jet. The liquid stream breaks up below

the nozzle and surface forces spherodize the droplets. A small evaporation cavity is formed in each sphere. The resulting wall thickness and bed density are much larger than that achieved with the "blown" sphere using the coaxial nozzle. After firing, the clay spheres typically possess diameters less than 1 mm and bed densities between 30 and 60 lbs/ft<sup>3</sup>, depending on degree of densification. The product derived from this process has been loosely termed a "Drip Sphere". This technique may be used with most compositions, i.e. Al<sub>2</sub>O<sub>3</sub>, mullite etc., and significantly widens the range of geometries available from the powder slurries.

The properties of three samples of clay spheres formed by the "drip" process designated Samples A, B and C are given below and the T/C data in Figure 1.

- (1) Sample A - Betacote, sintered at 1400°C resulting in a bed density of ~ 60 lbs per/ft<sup>3</sup>.
- (2) Sample B - Betacote, sintered at 1100°C resulting in a bed density of ~ 40 lbs per/ft<sup>3</sup>, and
- (3) Sample C - Alphatex, a porous structure calcined clay sintered at 1100°C with a bed density of about 28 lbs per cubic foot.

In the T/C measurements, samples were placed in the Anter radial heat flow apparatus and were measured to 1200°C. The resulting data are shown in Figure 1. Clearly, the use of the alphatex clay, Sample C, and the ability to maintain a relatively fine voids in the metakaolin structure produce a material with a thermal conductivity in the range of the K23 insulating firebrick as well as refractory fiber. In the T/C curve of Sample C, the very



rapid increase in conductivity above 1100°C is somewhat artificial and resulted because of the onset of shrinkage of the metakaolin leaving fissures and cracks in the structure. In contrast, the higher density betacote samples A and B displayed significantly higher thermal conductivity and the thermal conductivity increased as the density of the sintered samples increased. Therefore, it is anticipated that the alphetex after sintering through 1400 to 1500°C would exhibit a thermal conductivity approaching that of Sample A.

During the ongoing attempts to decrease the thermal conductivity of the thin wall hollow spheres, it has become increasingly evident that it will be necessary to engineer the structure of the sphere monolith through variations in the wall geometry in order to optimize the reduction of heat flow as a function of temperature. Clearly, according to the T/C results above, incorporating an alphetex matrix around the spheres would produce the lowest conductivity composite in the 800 to 1100°C range. In the next quarterly report, some structures formed by bonding spheres of various diameters and compositions together will be reported in the continuing effort to develop a sphere composite that approaches the low conductivity of today's refractory fiber.

## 2. Aqueous-Based Slurry Systems

As described in previous reports, the sphere forming characteristics of the aqueous slurries using food gums have not matched that of acetone-base slurries. Use of food gels has required high gum loading in the slurries to provide enough gel strength to maintain the hollow sphere shape during the free-fall landing. The high gel content slurries were too viscous to form low density and round spheres compared to the organic systems. To improve gel properties, detailed strength measurements of the food gum, carrageenan 911, with addition of a variety of cations were conducted during this reporting period.

The carrageenan gel strength is affected by the type and concentration of cations present in the water solutions. The manufacturer of carrageenan stated that potassium ions gave the optimum strength. However, since their customer are almost entirely in the food industry, we felt that it was necessary to try cations that might further promote the gel strength but were never investigated by the manufacturer due to cation toxicity if ingested. As a result, the strength of carrageenan 911 with various cations was measured and plotted in Figure 2. From these data, it is noted that cesium provides almost the same strength as potassium, but all other cations fail to meet our criteria.

Furthermore, we found that on cycling to high temperatures to redissolve the carrageenan, a lower viscosity resulted, Figure 3. The decrease in viscosity is substantial compared to only a marginal decrease in strength.

At present, we are trying to arrive at a mathematical model that will describe the gel strength as a function of carrageenan and cation concentration. Viscosities of the food gels are being characterized in order to optimize the slurry compositions which yield high gel strength and low viscosity.

### III Technology Transfer

Carl Vander Linder and Joe Cochran made two technology transfer visit to the Washington, D. C. and the Pennsylvania -- New Jersey area during this reporting period. Hollow sphere technology was presented to the Naval Research Laboratory and W. R. Grace, and a review of the transfer program being used to disseminate hollow sphere technology was made to seven people at DOE covering the offices of Industrial Technology and Building System. In the PA--NJ area, Carborundum, Quigley, Bethlehem Steel, Resco

Refractories, and Premier Refractories were all given a two hour presentation and all were well received. Dr. Vander Linden has provided trip reports to AIM headquarters covering these visits. New areas that are becoming important as a result of these visits are radiant burner tiles and low mass kiln furniture. These will be present in more detail in the next quarterly report.

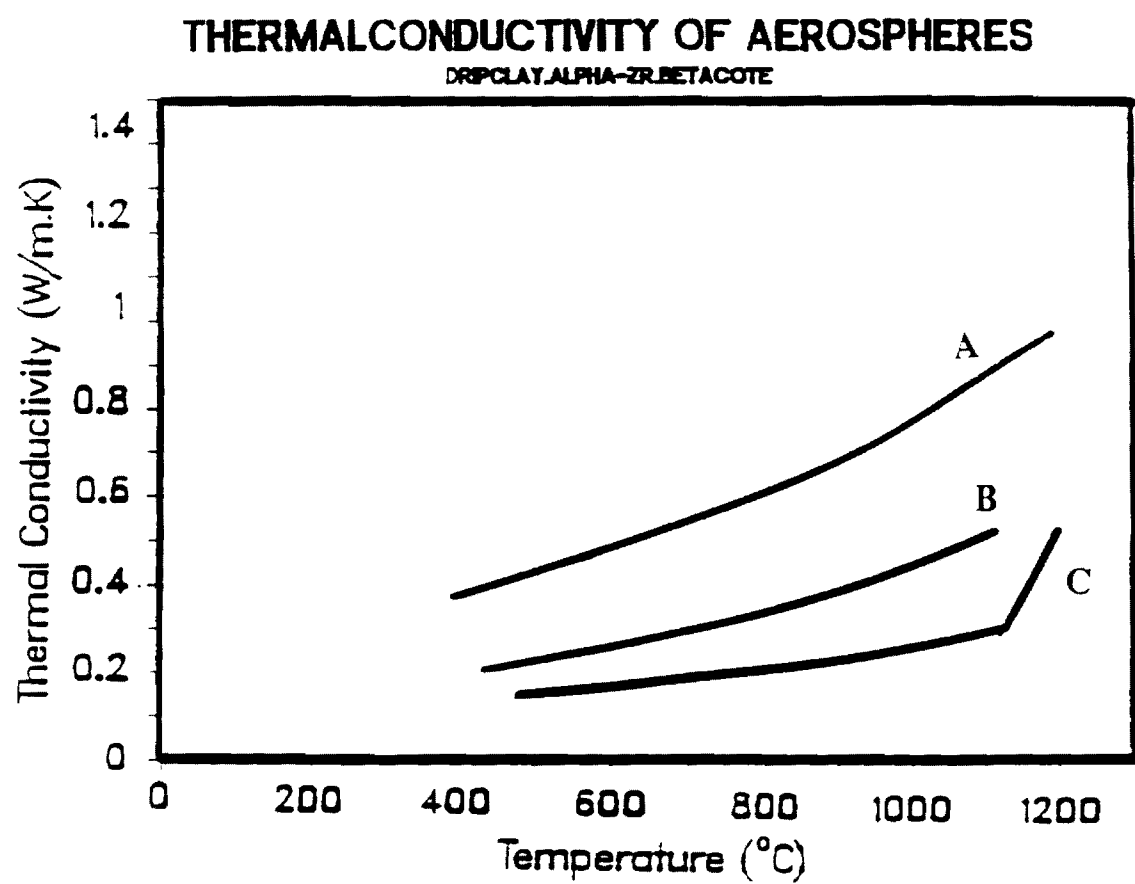


Figure 1. Thermal Conductivity of Betacote and Alphatex "Drip" Spheres.

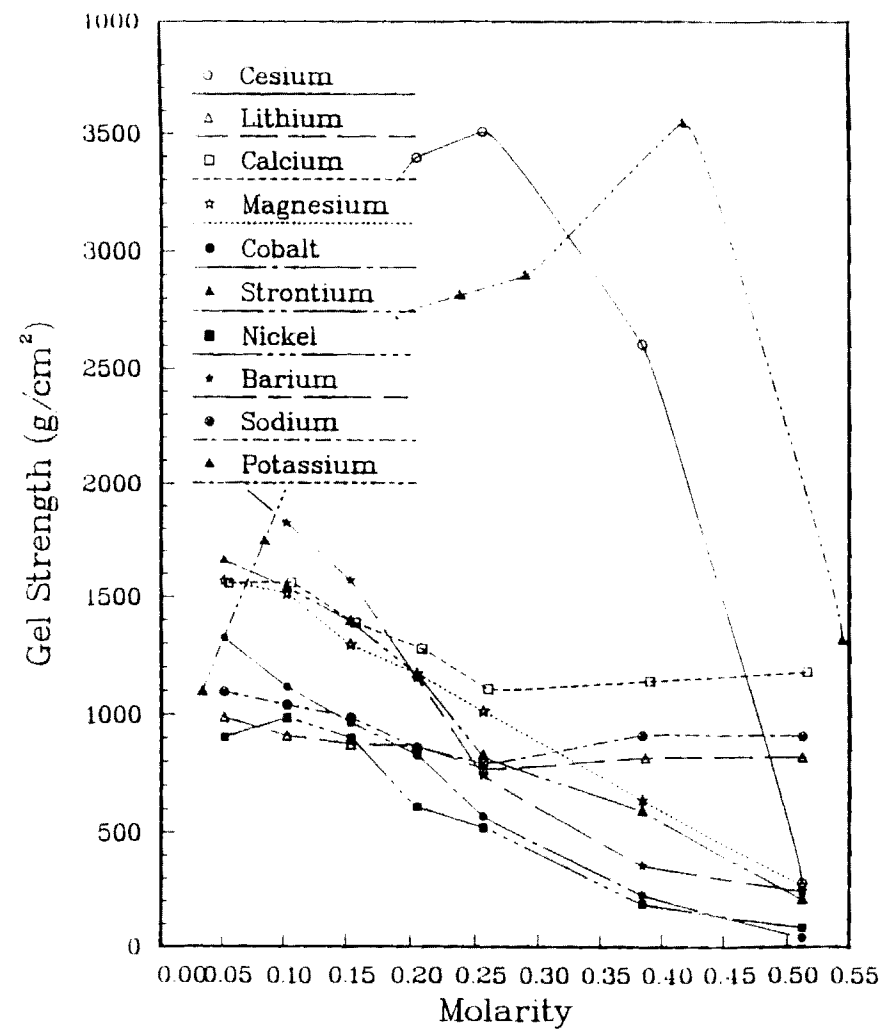


Figure 2. Effect of Cation Type and Concentration on Carrageenan Gel Strength.

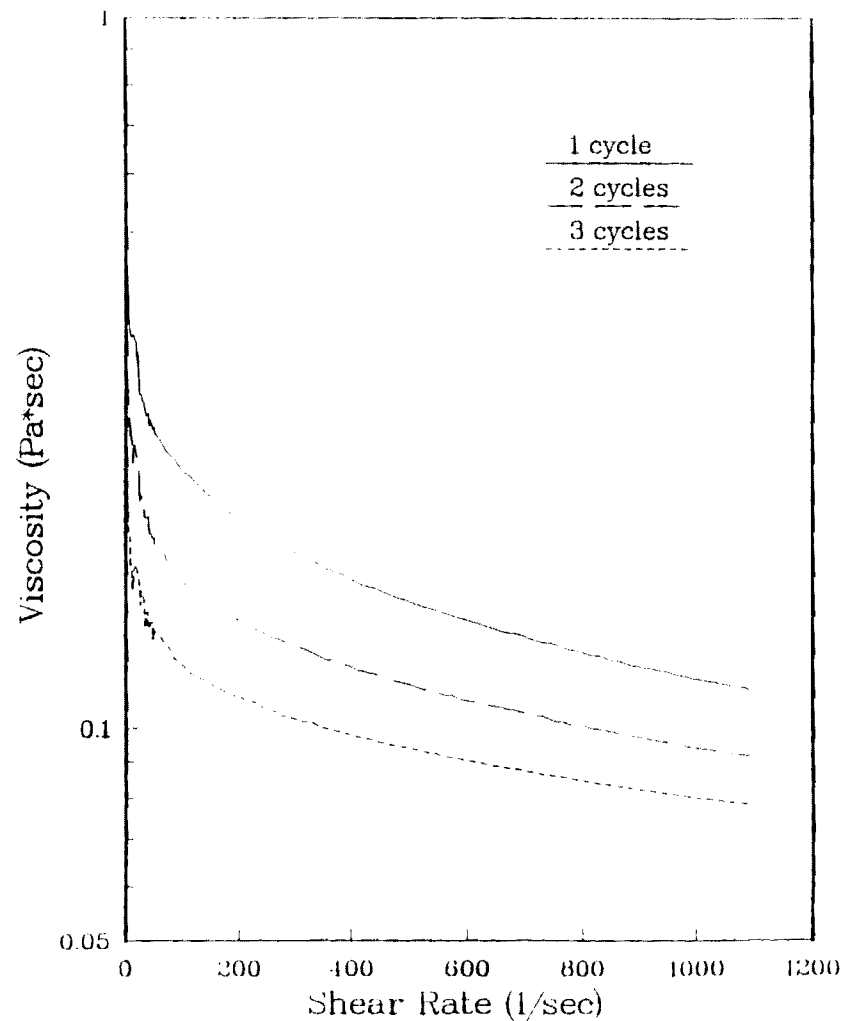


Figure 3. Viscosity of Carrageenan 911 with 0.6 w/o  $K^+$  at 90° C After Three Cycles to Redissolve the Gel.

# List of Investigators Participating in Project

Participation in days/week

Project: Thin-Wall Hollow Spheres from Slurries  
J.K. Cochran and A.T. Chapman

Reporting Period: 1 October - 31 December, 1990

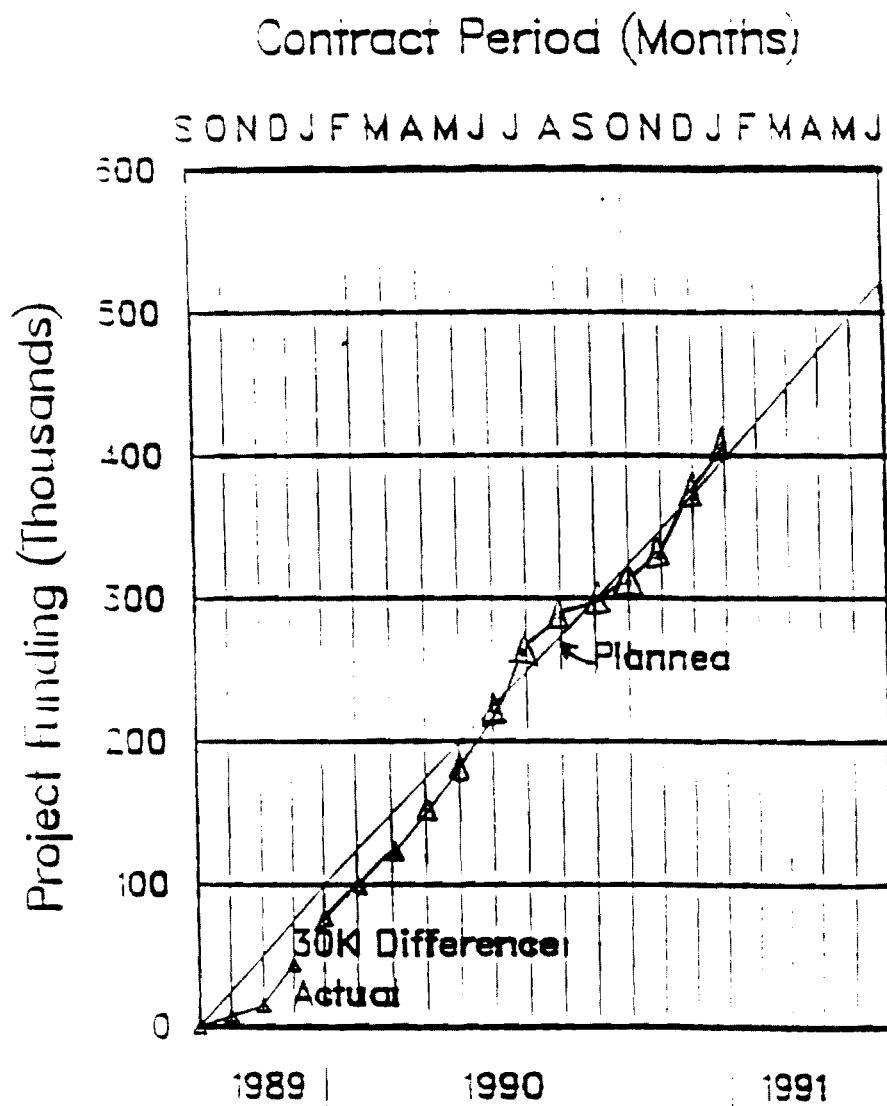
	Name	Type of Position	Planned Project Time		Approximate Time	
			Supported by			
A.	J.K. Cochran	Project Dir.	2	GT-DOE	2	(40%)
B.	A.T. Chapman	Project Dir.	2	GT-DOE	2	(40%)
C.	T.J. Hwang	Post Doctoral	5	DOE	5	
D.	J.H. Chung	Student (PhD)	2-3	DOE	2.5	
E.	P.R. Chu	Student (PhD)	2-3	DOE	2.5	
F.	S. Furlong*	Student (MS)	2-3	DOE	2.5	
G.	C. Moore	Student (MS)	2-3	DOE	2.5	
H.	T. Ford	Student (MS)	2-3	GT	2.5	
I.	R. Clancy	Student (MS)	2-3	GT	2.5	
J.	G. Carlson	Student (MS)	2-3	GT	2.5	
K.	T. Ozell	Student (MS Special Problem)		NA		

\* Completed MS Thesis June 90.

## COST INFORMATION

Project: Thin-Wall Hollow Spheres -  
J.K. Cochran and A.T. Chapman

Reporting Period: Phase V, 1 October - 31 December 1990



DE-FCOS-89CE90052

## 2. Program/Project Title

Thin-Wall Hollow Ceramic Spheres From Slurries

## Performer (Name, Address)

J.R. Cochran and A.T. Chapman School of Materials Engineering  
Georgia Tech, Atlanta, GA 30332

Identification Number	7. Planning Category (Work Breakdown Structure Tasks)	8. Program/Project Duration																	
		A 1990 → 1991 →																	
		S	O	N	D	J	F	M	A	M	J	J	A	S	O	N	D	J	F
TASK I	Slurries with opacifiers																		
hermal	Forming Spheres																		
sulations	Spheres Strength																		
	T/C Measurements																		
	Bonded Monoliths																		
TASK II	Rheology																		
queous	Gels																		
urries	Polymers																		
	Reactions																		
ASK III	Advisory Mtgs																		
chnology	Industrial Visits																		
ansfer	Trade Shows																		

Remarks

Signature of Recipient and Date

12. Signature of DOE Reviewing Representative and Date



U.S. DEPARTMENT OF  
FEDERAL ASSISTANCE

1. Program/Project Identification No. DE-FCOS-89CE90052	2. Program/Project Title Thir
---	----------------------------------

3. Performer (Name, Address)  
 School of Materials Engineering  
 J.K. Cochran and A.T. Chapman Georgia Tech, Atlanta, GA 30332

6. Identification Number	7. Planning Category (Work Breakdown Structure Tasks)	8. Program/Project Duration									
		A 1990									
		S	O	N	D	J	F	M	A	M	
TASK I	Slurries with opacifiers										
Thermal	Forming Spheres										
Insulations	Spheres Strength										
	T/C Measurements										
	Bonded Monoliths										
TASK II	Rheology										
Aqueous	Gels										
Slurries	Polymers										
	Reactions										
TASK III	Advisory Mtgs										
Technology	Industrial Visits										
Transfer	Trade Shows										

10. Remarks

E-8-174  
n/a

Quarterly Project Status Report  
1 January through 31 March, 1991

Thin-Wall Hollow Ceramic Spheres from Slurries

A.T. Chapman and J.K. Cochran

School of Materials Engineering  
Georgia Institute of Technology  
Atlanta, Georgia 30332-0245

Project DE-FCO5-89CE90052

This document is the sixth quarterly status report for the Phase IV effort (initiated 1 Sept 89) for the development of "Thin-Wall Hollow Spheres from Slurries." During this phase three major tasks are emphasized: 1) the use of opacifiers to reduce the high temperature thermal conductivity of the spheres, 2) convert the slurries used in sphere formation from the existing organic-based to aqueous - based systems and 3) product engineering and information dissemination (technology transfer) to end-use industries. In Section I Milestones are abbreviated as a more detailed presentation is included in the quarterly Federal Assistance Milestone Plan accompanying this report. During this reporting period, a paper titled "Fabrication of Thin-Wall Hollow Nickel Spheres and Low Density Synthesis Foams" was published in Proceedings of TMS Contrace on Light Weight Alloys, TMS Annual Meeting, New Orleans, LA, Feb. 1991. A copy of this paper is also enclosed.

I. Milestones

The list of project milestones shown in Table 1 includes all the major tasks undertaken in the Phase IV effort. Major technical accomplishments are presented in the next section.

Table I. Milestones (Tasks) for Hollow Sphere Project

	<u>TASKS</u>	<u>STATUS</u>
I.	Thermal Insulation	
1.	Develop Slurries Containing Opacifying Agents	Active
2.	Sphere Formation	
a.	Opacified Spheres	Active
b.	Modeling	Active
3.	Strength of Opacified Spheres	Inactive
4.	Thermal Conductivity Measurements	Active
5.	Bonded Sphere Monoliths	Active
II.	Aqueous Slurries	
1.	Rheology Measurements	Active
2.	Strength Development through	
a.	Gels	Active
b.	Polymer-Crosslinking	Inactive
c.	Chemical Reactions	Inactive
III.	Technology Transfer	
1.	Advisory Meeting	Completed
2.	Industrial Visits	Active
3.	Trade Shows	Active

## II. Technical Highlights

### 1. Thermal Conductivity of Bonded Shapes

Until recently, most thermal conductivities of aerospheres were measured in loose form. It has been suggested that a significant portion of the thermal resistance of these loose beds results from point contact between the spheres and that bonding of spheres with fillets at points of contacts would significantly increase thermal conductivity. To evaluate this possibility, mullite, alumina, and mullite-zirconia Aerospheres were bonded to form monolithic closed cells foams with low density and high strength. Thermal conductivity of these foams are compared to loose spheres of like composition in Figures 1, 2 and 3. The high volume of trapped gas within the spheres and between the interstices disrupts conduction heat transfer and reduces low-temperature (below 800°C) conductivity. However, at elevated temperatures the radiation transparency of the sphere walls significantly increases the thermal conductivity. Zirconia particles acted as an opacifying or scattering phase and reduced the high-temperature thermal conductivity in the two-phase, mullite-zirconia, spheres.

The conductivity of hollow spheres bonded at the points of contact should mimic parallel plate conduction at low temperatures (350°C) and can be modelled from the standard parallel plate equation:

$$k_m = k_p V_p + k_s V_s + k_b V_b \quad (1)$$

where  $k_m$  is the thermal conductivity of the sample,  $V_n$  is the volume fraction and  $k_n$  is the thermal conductivity of the pore phase (p), sphere phase (s) and bonding phase (b). The phase exhibiting the highest conductivity has the greatest influence on the thermal conductivity of the mixture.

To apply equation (1), the conductivity of beds of loose spheres can be used to estimate the Aerosphere contribution,  $k_s$ , to the bonded samples. A bed of monosized spheres packs to a density of 63% and interconnects at several points of contact with neighboring spheres. The remaining 37% interstitial pore space is also continuous through the interstices in the packed bed. Therefore, equation (1) can be modified to calculate the thermal conductivity of the spheres,  $k_s$ ,

$$k_s = \frac{k_{LB} - k_p V_p}{V_s} \quad (2)$$

where  $k_{LB}$  is conductivity of the loose sphere bed as shown in (Figures 1, 2 & 3),  $k_p$  is conductivity of air (.0495 W/m·K at 350°C), and  $V_p$  and  $V_s$  are 37% and 63%, respectively. Estimates of  $k_s$  are presented in Table 1.

Figures 1 and 2 show small increases in the low temperature conductivity of bonded mullite and mullite-zirconia spheres compared to the respective loose spheres. The bonding phase increased density and conduction heat flow which raised the conductivity of the bonded samples. The increased density also provided additional radiation scattering which reduced high-temperature conductivity of bonded mullite spheres. However, refiring mullite-zirconia spheres in the bonding process must have increased the sphere wall transparency because no reduction in high temperature conductivity was observed as would be expected due to increase density.

To estimate the effect of the bonding phase on low temperature conductivity, the sphere conductivity,  $k_s$ , was calculated from the measured conductivity of the loose bed,  $k_{LB}$ , Table 1. Using equation 1, the conductivity of the bonded foam,  $k_m$ , was predicted based

on a published value of 5.02 w·m/k for the mullite bond phase. The bond phase was predicted to increase the conductivity of mullite foams approximately 0.25 w/m·k. This is reasonable agreement with the measured increases of 0.10 to 0.12 w/mk if one considers that tortuosity would increase the conduction path and reduce the conductivity below that predicted by equation 1. Thus, rather than dramatically increasing conductivity, bonding spheres did not result in as large an increase as would be predicted.

Bonded alumina spheres had a significantly higher conductivity than loose spheres, Figure 3. As predicted in Table 1, the high conductivity of the alumina bonding phase, would be expected to dramatically increase the thermal conductivity of the bonded sample. An increase of 1.1 w/m·k was predicted and an increase of 0.6 was observed. This is reasonable agreement again considering totuosity. Obviously, a low conductivity bond phase is desirable for a bonded sphere refractory.

Figure 3 compares the thermal conductivity of bonded mullite and mullite-zirconia spheres with insulating firebrick. The bonded-spheres are competitive up to a mid-temperature range of 1000°C where conduction heat transfer is the dominant mode. Above this temperature, lack of radiation scattering allowed thermal conductivity to increase significantly. The bonded-spheres showed a reduction in density of 40% - 45% compared to firebrick.

## 2. Aqueous-Based Slurry Systems

Work continued well into this quarter to form low density hollow spheres using the polysacceride gel, carrageenan as the bonding mechanism for the spheres. Carrageenan is a thermally reversible gel which forms a liquid solution above 80°C and gels rapidly when cooled below 70°C to form a strong gel. It has been demonstrated that the rate of gelling

is fast enough on cooling to harden the hollow spheres in free flight. An extensive study has been completed to determine the effect of cation ( $K^+$  and  $Cs^+$ ) concentration and carrageenan content on the gel strength which has resulted in an empirical mathematical model expressing gel strength to within 15-20% over a  $K^+$  concentration of 0 to 1.5 w/o and carrageenan contents from 0-5 w/o. The object of this study was to determine if usable gel strengths could be reached at a low enough carrageenan content to produce a viscosity sufficiently low to form low density spheres. Unfortunately, we have concluded that at low alumina-carrageenan slurry viscosities compatible with sphere formation, gel strengths are insufficient for collecting hollow spheres. Furthermore, even a low concentration of clay (kaolin) in carrageenan based slurries produce very high viscosities and one object of transforming to water based slurries is to produce low cost clay based spheres. Thus, we have abandoned food gels as the harden mechanism and have begun investigating colloidal silica dispersions as a potential gelling mechanism.

Colloidal silica dispersions (Ludox) are marketed at relatively high solid contents (up to 50 v/o) with viscosities which are sufficiently low to add large quantities of good rheological powders (up to 50 v/o) and still maintain viscosities compatible with hollow sphere formation. These colloidal silica based dispersions can be gelled with good gel strengths by additions of salts of various types. By sensitizing these dispersions with salts, changing pH, and increasing temperature, we have demonstrated that gel times can be reduced to under 10 seconds. Studies are underway to determine if gel times can be reduced to less than 1 sec. which is required for hardening hollow spheres in free fall. Studies are being initiated to see if gas phase reactions can be used to initiate this gelling process in the sphere walls during free fall.

### III. Technology Transfer

Two areas of potential products receiving continued interest are radiant burner tiles through the Gas Research Institute and low mass kiln insulation at the Y-12 Plant. In the last quarter, a radiant burner system manufacturer has tested six mullite bonded mullite aerosphere monoliths 2x14x14 cm as radiant burner tiles. In these tests, gas-air mixtures are passed through the tile and burned on the front surface. On ignition of the flame, the tile surface heats rapidly to 2300°F while the back surface remains below the gas-air ignition temperature. This is a severe thermal shock condition and the mullite aerospace monoliths have yet to have a failure. In another application requiring good thermal shock resistance, a mullite aerosphere monolith 10 cm thick and 100 cm in diameter has been fabricated and delivered to the Y-12 plant to serve as an insulation cover for a vacuum induction furnace where the temperature will be 1450°C on the hot face and the cold face will be facing a water cooled metal lid. Both of these applications are in progress and will be reported later.

A technology transfer trip is planned with Dr. Carl Vander Linden in April to California. Eight companies will be visited in five days including Rohr Industries, NASA, Hi Temp Corp., and National Refractories. In addition, Ceramic Fillers Inc., will have a booth at the American Ceramic Society Exposition in Cincinnati in May demonstrating aerosphere technology.

Table 1. Thermal Conductivity of Bonded and Loose Spheres at 350°C.

Spheres Material	Bond Material	$k_{LB}$ (w/mk)	$k_s$ (Eq.2) (w/mk)	$k_b$ (w/mk)	$k_p$ (w/mk)	$k_m$ (Eq.1) (w/mk)	$k_m$ (measured) (w/mk)
Alumina	Alumina	.40	0.733	20.92	0.0495	1.52	1.02
Mullite	Mullite	.25	0.368	5.02	0.0495	0.499	0.37
Mull-Zr	Mullite	.25	0.368	5.02	0.0495	0.499	0.35



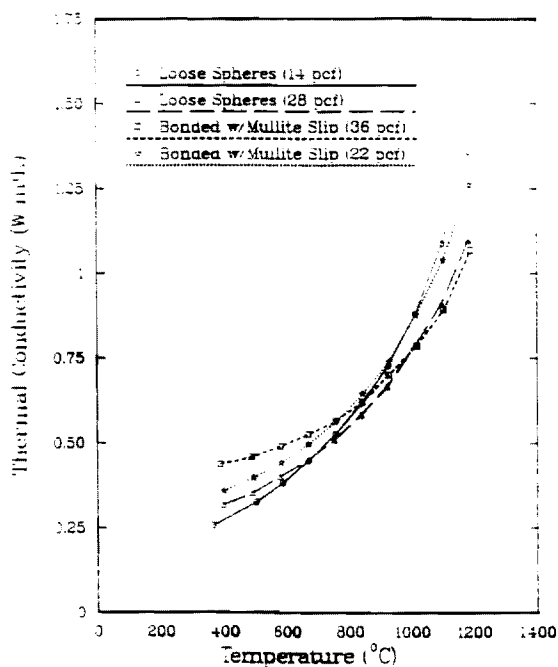


**Figure 1.** Thermal Conductivities of Loose Bed and Bonded Mullite Spheres.

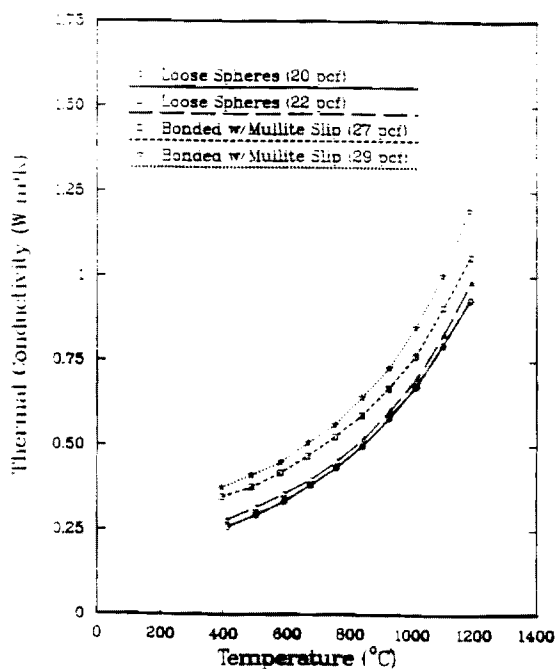


**Figure 2.** Thermal Conductivities of Loose Bed and Bonded Mullite-Zirconia Spheres.

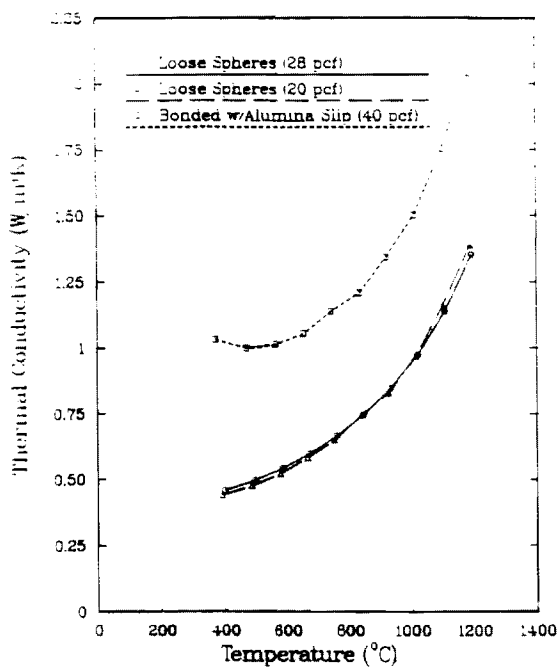


**Figure 3.** Thermal Conductivities of Loose Bed and Bonded Alumina Spheres.

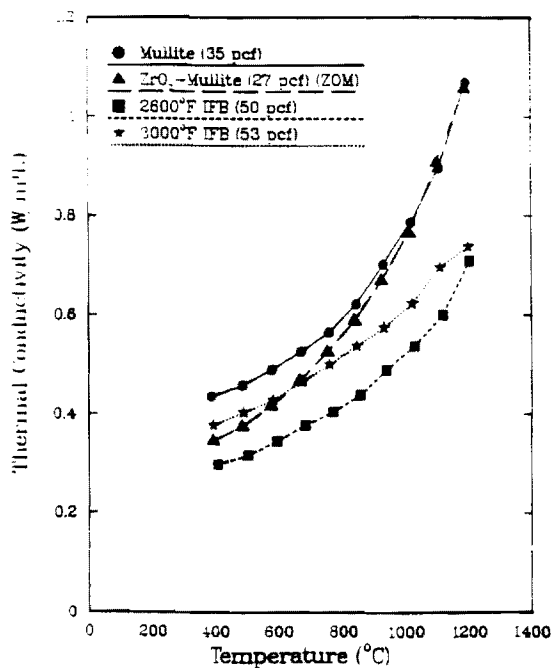


**Figure 4.** Thermal Conductivities of Bonded Aerospheres and Insulating Firebrick.

# List of Investigators Participating in Project

Participation in days/week

Project: Thin-Wall Hollow Spheres from Slurries  
J.K. Cochran and A.T. Chapman

Reporting Period: 1 January through 31 March, 1991

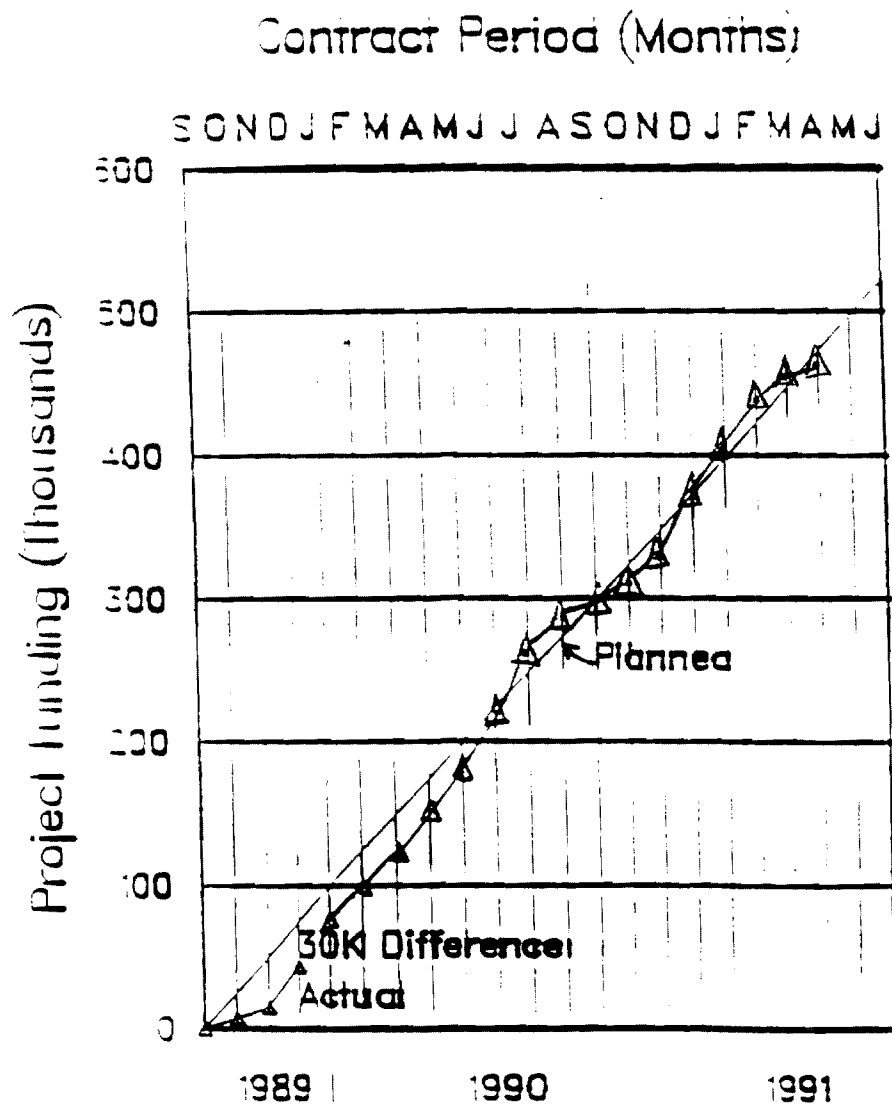
Name	Type of Position	Planned Project Time		Approximate Time	
		Supported by			
A. J.K. Cochran	Project Dir.	2	GT-DOE	2	(40%)
B. A.T. Chapman	Project Dir.	2	GT-DOE	2	(40%)
C. T.J. Hwang	Post Doctoral	5	DOE	5	
D. J.H. Chung	Student (PhD)	2-3	DOE	2.5	
E. P.R. Chu	Student (PhD)	2-3	DOE	2.5	
F. S. Furlong*	Student (MS)	2-3	DOE	2.5	
G. D. Moore	Student (MS)	2-3	DOE	2.5	
H. T. Ford	Student (MS)	2-3	GT	2.5	
I. R. Clancy	Student (MS)	2-3	GT	2.5	
J. G. Carlson	Student (MS)	2-3	GT	2.5	
K. T. Ozell	Student (MS Special Problem)		NA		

\* Completed MS Thesis June 90.

## COST INFORMATION

Project: Thin-Wall Hollow Spheres -  
J.K. Cochran and A.T. Chapman

Reporting Period: 1 January through 31 March, 1991



FABRICATION OF THIN-WALL HOLLOW NICKEL SPHERES

AND LOW DENSITY SYNTACTIC FOAMS

R.B. Clancy, T.H. Sanders Jr., and J.K. Cochran  
Georgia Institute of Technology  
Atlanta, GA. 30332-0245

Abstract

A process has been developed at Georgia Tech to fabricate thin-wall hollow spheres from conventional oxide powders at room temperature. The polymer-bonded powder shells are fired in air to sinter the walls, leaving the shells either impervious or porous. Alternatively, the oxide shells can be preferentially reduced to produce thin-wall hollow metal spheres which can be bonded together to produce an ultra light weight closed-cell foam. The processing and properties of this unique class of low density structures will be discussed.

## Introduction

In recent years, metal foams have come into prominence as a promising engineering material, combining useful properties such as high impact energy absorption capacity and low thermal conductivity with an intrinsic ultra-light weight. Recent research in this area includes incorporating hollow ceramic spheres in an aluminum matrix, producing a light weight syntactic foam having a relative density of 60% of a conventional aluminum alloy<sup>1</sup>. One of the most versatile metal foams is nickel. Its applications include electrodes for alkaline storage batteries and fuel cells<sup>2</sup>, infrared radiant gas burners, improved filtration in fluid control systems<sup>3</sup>, efficient solar collector cells<sup>4</sup>, heater-filter material for circulating air heaters, wall and floor heating tiles<sup>5</sup>, abradable seals in turbine engines<sup>6</sup>, and thermal and electrical insulating materials<sup>7</sup>. However, some have noted that significant progress in the development and applications of metal foams may be stymied by less-expensive conventional competition. Improvement in the manufacturing processes could alleviate this hurdle by reducing the cost, thus increasing potential uses of metal foams<sup>3</sup>.

One novel production technique involves reduction of hollow oxide spheres to the metal and the bonding of these metal spheres into a syntactic foam. The low cost and simplicity of ceramic powder production methods, combined with the inherent control over many variables involved with the sphere fabrication, positions this unique approach as one due further consideration.

## Processing of NiO Foam

A slurry containing 1-10 micron particle size NiO powder and a polymer additive was blown through a coaxial nozzle to produce hollow spheres at high rates. The process allows for rapid hardening of the shell, and the polymer provides adequate green strength for handling. The spheres were conventionally sintered in air at 1550 C for 3 hours in order to eliminate the polymer and densify the walls to provide strength and stability to the ceramic shells. The resultant spheres were approximately 2 mm in diameter with a wall thickness of 50-100 microns. The sintered NiO spheres are then wet with a slurry of the constituent NiO powder and polymer, then packed tightly into polyethylene vials. During drying, a bridge of NiO and polymer forms on the point contact between spheres. After drying sufficiently, the loaded vials are sintered in air at 1550 C for 3 hours. The polyethylene and polymer evaporate and the NiO grains in the bridges between spheres densify, providing strength and binding to the oxide monolith. This metal foam precursor consists of bonded hollow NiO spheres with an average sintered density of 1.10 g/cc, which corresponds to a relative density of 16.5% compared to dense NiO.

R. B. Clancy

2

1

## Reduction of NiO Spheres

The sintered NiO monoliths were reduced in a freely flowing hydrogen atmosphere in an induction furnace using a graphite cylinder susceptor, which was in a quartz tube for atmosphere control. Hydrogen was purged through the tube at 500 cc/min. and the tube was evacuated initially to remove all gases and water vapor. The NiO monolith was reduced at 900-1000 C for approximately 40 minutes. During reduction, water vapor condensed on the inside of the quartz tube and the disappearance of this condensate signaled the completion of reduction. Final densification of the Ni sphere monolith was at 1200 C, and the hydrogen flow was lowered to 50 cc/min. in order to reduce temperature gradients in the metal foam. Sintering for 45 minutes was sufficient to produce good bonding between spheres (Figure 1).

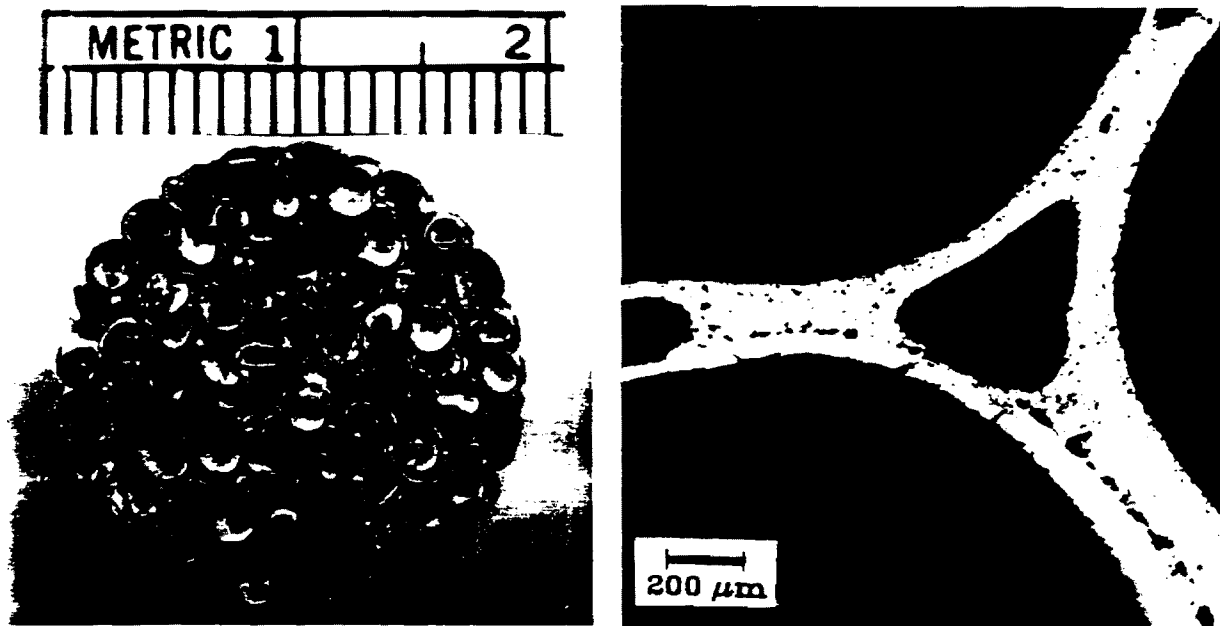


Figure 1. Macroscopic (a) and Microscopic (b) Views of Cross Section of Nickel Hollow Sphere Syntactic Foam Showing Point of Contact Bonding. Note the good bonding in neck region.

The bonded hollow nickel spheres approximate a metal foam (Fig. 2), and the structure had an average density of 1.10 g/cc, with relative densities ranging from 10.3% to 15.1%. Complete reduction of the oxide monolith to metal was confirmed by X-ray diffraction.

The flexible fabrication parameters allow for control over many variables which ultimately effect the properties of the metal foam. The diameter of the spheres, density and thickness of the walls, thickness of the metal bridge bonding

R. R. (Lancet)

5

5

spheres, ultimate grain size in the metal, as well as possible alloy compositions are all subject to manipulation. A previous study<sup>7</sup> found that optimization of the formation process allows sphere diameter and density variations of less than 5% within a given batch (Fig. 3). This uniformity permits dense packing of spheres, in either FCC, HCP, or a random array. The combination of a constructed closed-cell structure with uniformity of cell size and spatial distribution is termed a "syntactic foam." Drury, et.al. (ref.9) also found that increasing cell uniformity enhanced energy absorption capacity and energy absorption efficiency, terms which will be explained in the following section.

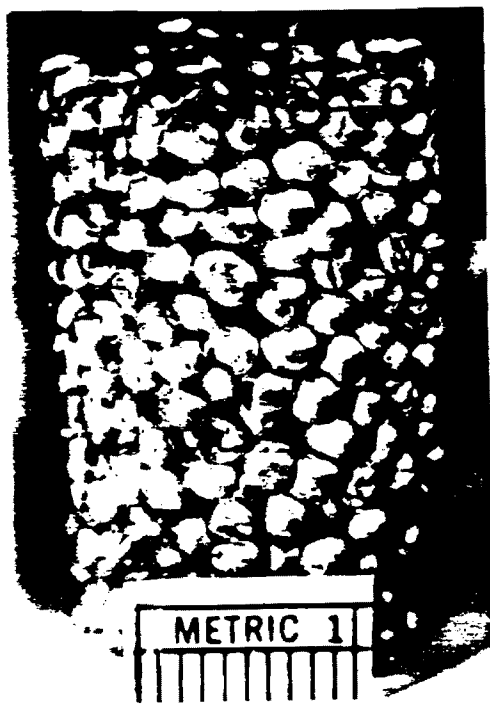


Figure 2. Bonded Nickel Foam Cylinder Used for Compressive Strength Measurements.

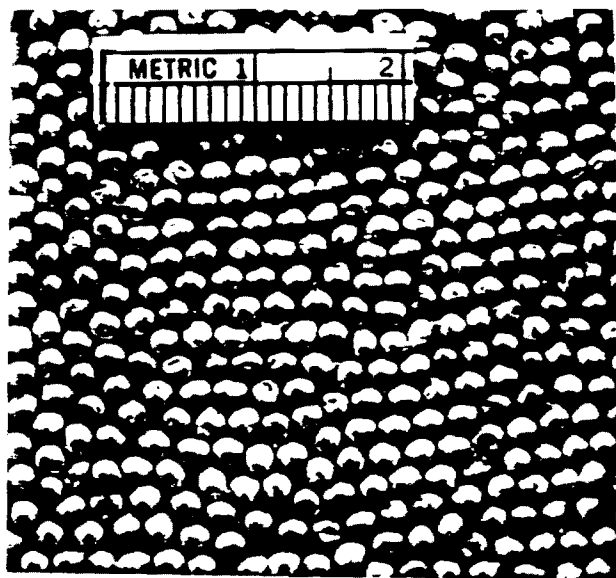


Figure 3. Unbonded Hollow Nickel Spheres Showing Narrow Range of Sphere Diameter.

## Properties of Ni Foam

### Microstructure

A Scanning Electron Microscope micrograph of the Ni spheres (Fig. 4) reveals nickel grain size ranging from 1-8 microns on the surface, illustrating little, if any, grain growth during reduction and sintering. The small metal grain size would be expected to translate into high strength walls and is a direct result of the flexible parameters provided in using a fine grain oxide powder precursor.



Figure 4. Microstructure of Nickel Sphere Wall Showing 1-8 Micron Grain Size.

### Mechanical Properties

The compressive strength of the nickel foam was measured by uniaxial loading at a crushing speed of 0.1 inch/min., Fig. 5. M.F. Ashby<sup>10</sup> suggests that the curve exhibits three separate sections of behavior (Fig. 6): linear elasticity, plastic collapse, and finally densification. The linear-elastic region for this Ni foam ends in the vicinity of 350 psi. During linear elasticity, the cell walls bend, eventually yielding and buckling in the region of collapse. Densification begins when the cell walls are forced together, compressing the void space out of the material and effectively transforming the foam into a solid.

The modulus of elasticity,  $E$ , was calculated as 14.3 ksi for the initial linear elastic region; though this value is far less than 1% of the modulus of nickel, a more accurate estimate of the relative strength of the Ni foam might be found in the specific stiffness, which is modulus divided by density. The specific stiffness of the nickel foam was 95.6 MPa cc/g, which is 0.59% of that of solid nickel.

Further estimation of the relative strength of the foam may be found by comparing with known values; one source measured tensile strength as a function of density and found a yield strength of 700 psi for Ni foam with 20% relative density (ref.3). Under the assumption that the behavior of foams in tension is similar to that in compression, as noted by Ashby (ref.10), we may compare this value with that of the



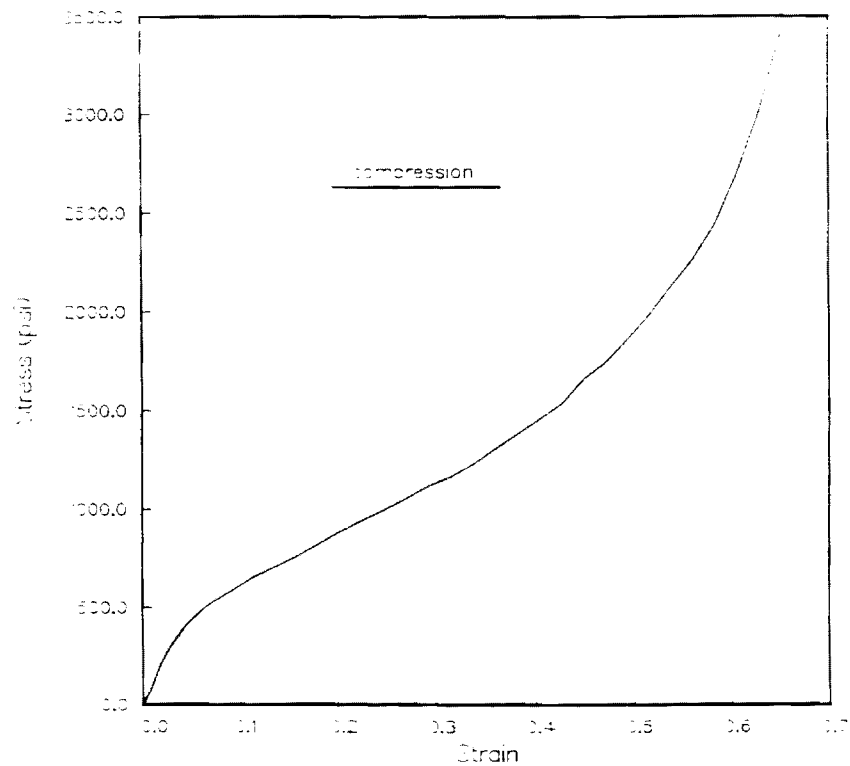


Figure 5. Compression Stress-Strain Behavior for Ni Hollow Sphere Syntactic Foam at 12% Relative Density.

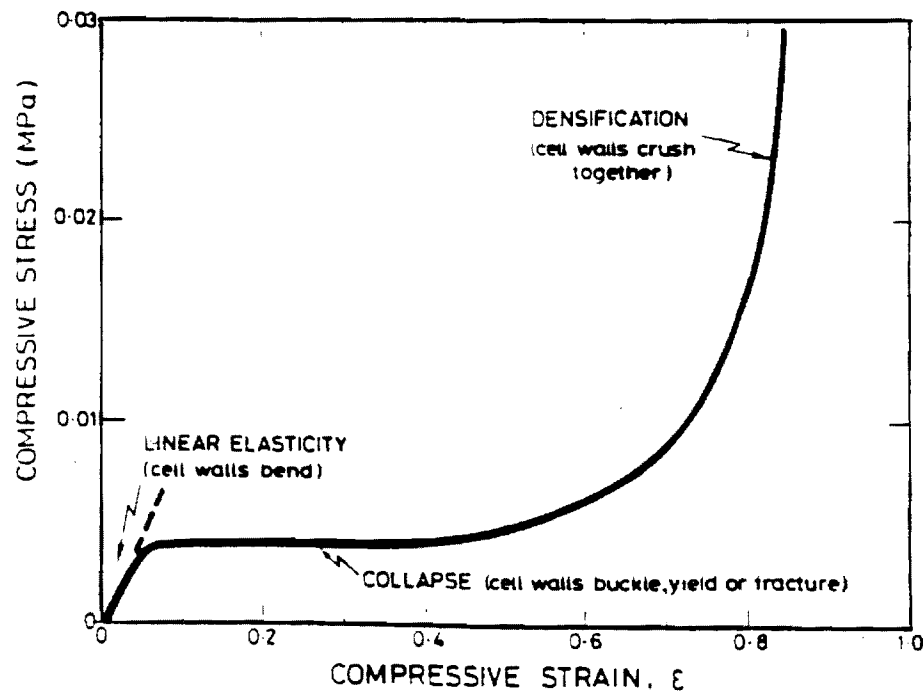


Figure 6. Idealized Compression Stress-Strain Curve for a Foam after Ashby (ref. 10).

K.B. Clancy

5

7

bonded nickel syntactic foam. Ashby, in establishing mathematical models for the behavior of foams, relates the change in relative yield strength with relative density as

$$\frac{\sigma^*}{\sigma_y} = C \left( \frac{\rho}{\rho_s} \right)^2 \quad (1)$$

where  $\sigma^*$  and  $\rho$  are the plastic collapse stress and density of the foam,  $\sigma_y$  and  $\rho_s$  are the yield strength and density of the cell-wall material, and  $C$  is a dimensionless constant. The yield strength of the 11.6% relative density bonded Ni foam was 350 psi (Fig. 5); following the relationship in equation 1, this value translates to 1040 psi for an increase to 20% relative density, which is nearly a 50% increase in yield strength over the previously tested foam.

Ashby further establishes that the linear elasticity of closed-cell foams should follow a relation given by

$$\frac{E}{E_s} = B \left( \frac{\rho}{\rho_s} \right)^3 \quad (2)$$

where  $E$  and  $\rho$  are the respective modulus and density of the foam,  $E_s$  and  $\rho_s$  are the modulus and density of the solid parent material, and  $B$  is a dimensionless constant (ref.10). The bonded hollow nickel sphere closed-cell foam follows this relation with a value of 0.43 for  $B$ ; assuming this initial data is predictive, an eightfold increase in modulus may be expected with a doubling of the foam's density.

In order to determine the usefulness of a foam for cushioning and impact energy absorption, two characteristics of the material are determined from the stress-strain curve<sup>11</sup>. The energy absorption capacity (energy per unit volume) is the area under the stress-strain curve and is most useful as a comparative value. The energy absorption efficiency compares the absorption behavior of the tested material with an ideal (perfectly plastic) model, which would exhibit a flat (constant stress) plastic region during collapse. These terms will be further examined after additional samples have been tested.

#### Processing of Ni-Cu Monel Foam

In addition to the novel processing methods presented by forming a pure metal foam from oxide powder origins, the techniques covered above are being adapted to produce an alloy foam, predictably of equally fine microstructure and properties. Monel, a series of nickel-copper alloys ranging in composition, was chosen for this experiment due to the ease

K. B. Clancy

1

7

of reduction of both NiO and Cu<sub>2</sub>O to their metallic component as well as the continuous series of solid solutions presented by the Ni-Cu alloys, with each having the FCC lattice of the components. The copper addition theoretically provides good corrosion resistance at elevated temperatures, expanding the applicability of the previously constructed syntactic nickel foam.

NiO and Cu<sub>2</sub>O powders were combined in the proper proportion to lead ultimately to 80Ni-20Cu monel. The blown NiO-Cu<sub>2</sub>O spheres were air-sintered at 1350 for 3 hours, and reduced under identical procedures as those noted for nickel sphere formation. This effort is in the initial stages and no attempt has been made to bond the ceramic spheres together and reduce the monolith to a metal foam. The reduced spheres were examined by X-ray diffraction and found to be a solid solution FCC structure with the lattice parameter between Cu and Ni with a value in accordance with Vegard's law. The density of the spheres measured 1.35 g/cc, corresponding to a 15.2% relative density. Further characterization will be performed to confirm the presence of an alloy and to examine the microstructure in order to determine the grain size. Strength of bonded monel foams will be measured and compared with reference data to determine the effect the minute grain size expected.

### Conclusion

The unique fabrication process involved in bonded hollow spheres as metal foam may provide the ease and reduced cost necessary to further spur research in this infant field of engineering materials. The only limiting factors relate to optimizing the rheology of the oxide slip and the ease of reducing the oxide to the metal state. The initial successes of creating a nickel foam of 11.6% relative density and an alloy of 15.2% relative density on first attempts leaves considerable promise for optimizing properties of the closed-cell foams through manipulation of the processing variables.

### Acknowledgements

This work was funded by the Advanced Industrial Materials Program of the Office of Industrial Technologies, Department of Energy, under Project DE-FC05-89CE90052, and is indebted to the seminal advice and encouragement of the late Prof. Ted Chapman of Georgia Tech.

R. B. Chinn

2

7

## References

1. S.A. Rickles, "Microstructural and Compressive Properties of a Metal/Ceramic Syntactic Foam", M.S. Thesis, Georgia Institute of Technology; May, 1989.
2. I.M.Fedorchenko, Sov. Powder Metall. Met. Ceram. 18 625 (1979).
3. D.C.Dilley, Mach. Prod. Eng. 125 (1974) 24.
4. G.A.Weimer, Iron Age 218 (1976) 33.
5. L.A.Cohen, W.A.Power, and D.A.Fabel, Mater. Eng. 67 (1968)44.
6. I.Amato, P.G.Cappelli and P.C.Martinenco, Wear 34 (1975) 65.
7. H.Bray, Eng. Mater. Des. 16 (1972) 19.
8. G.J.Davies and S.Zhen, J. Mater. Sci. 18 (1983) 1911.
9. W.J. Drury, S.A. Rickles, T.H. Sanders Jr., J.K. Cochran, "Deformation Energy Absorption Characteristics of a Metal/Ceramic Cellular Solid"; Conf. Proc. 1989 TMS Annual Mtg.; E.W. Lee, E.H. Chia, N.J. Kim, editors.
10. M.F. Ashby, Met. Trans. A 14A (Sept.1983) 1763-1766.
11. P.H. Thorton and C.L. Magee, Met. Trans. A 6A (1975) 1253-1263.

R.B. Clancy

U.S. DEPARTMENT OF ENERGY  
FEDERAL ASSISTANCE MILESTO

Program/Project Identification No. DE-FCOS-89CE90052 2 Program/Project Title Thin-Wal.

Performer (Name, Address)

J.K. Cochran and A.T. Cnapman School of Materials Engineering  
Georgia Tech, Atlanta, GA 30332

Identification Number	7 Planning Category (Work Breakdown Structure Task)	8. Program/Project Duration										
		S	O	N	D	J	F	M	A	M	J	J
Task I	Slurries with opacifiers											
Thermal	Forming Spheres											
Insulations	Spheres Strength											
	T/C Measurements											
	Bonded Monoliths											
Task II	Rheology											
Aqueous	Gels											
Slurries	Polymers											
	Reactions											
Task III	Advisory Meetings											
Technology	Industrial Visits											
Transfer	Trade Shows											

Remarks

Signature of Recipient and Date

12 Signature of D



Georgia Tech

E-18-674  
8, 11  
School of Materials Engineering

Georgia Institute of Technology  
Atlanta, Georgia 30332-0245  
(404) 894-  
FAX: (404) 853-9140

~~December 20, 1990~~

Jan 18, 1991

Dr. Peter Angelini  
AIM Program  
Department of Energy, CE-232  
1000 Independence Avenue, SW  
Washington, DC 20585

Dear Pete,

The enclosed Annual Progress Report is in the final stage of preparation. More information on presentations, matching funds, industrial support and testing, etc. ~~was~~ added to the final version. Joe and I thought this info may be useful in preparing justification for the future funding, starting in June of 91. A copy of Furlong's MS thesis on T/C of the spheres, and a small vial of bonded nickel spheres are also enclosed for your use. Lastly, the latest one page highlight on the mechanical properties of bonded spheres is also included. version.

Please call if we can be of any additional assistance in your temporary replacement role at AIM.

Sincerely,

A.T. Chapman  
Professor of Ceramic  
Engineering

ATC/gb

P.S. Happy Holidays !!!  
Sorry, it is so late  
Joe

## **THIN-WALL HOLLOW CERAMIC SPHERES FROM SLURRIES**

J.K. Cochran and A.T. Chapman  
School of Materials Engineering  
Georgia Institute of Technology  
Atlanta, GA 30332-0245  
Contract DE-FC05-89CE90052

### **INTRODUCTION**

The ongoing DOE supported program on "Thin-Wall Hollow Ceramic Spheres from Slurries" was initiated in January 1986. During Phase I the objective was to develop a process for fabricating the spheres. This was successfully done by dispersing ceramic powders in an organic liquid, blowing the individual spheres using a coaxial nozzle and drying the free-falling spheres in an updraft heated air column. Based on the success on Phase I the Phase II activity emphasized the assessment of the structural and insulation capability for the spheres, and modeling the sphere formation process. The Phase II program ended April 30, 1989 and was followed by a short four month effort, Phase III, to assess the potential of using an opacifier in the sphere walls to scatter radiation and decrease the high temperature thermal conductivity of sphere beds. In September 1, 1989, a two year follow on, Phase IV, program was initiated consisting of three major tasks:

- 1.) the use of opacifiers to reduce the high temperature thermal conductivity of the spheres,
- 2.) convert the slurries used in sphere formation from the existing organic-based to aqueous - based systems and
- 3.) product engineering and information dissemination (technology transfer) to end-use industries.



This Annual Report briefly reviews the very encouraging Phase IV results. Publications, presentations, personnel participating in the project, and allied budgetary information are also included.

## **TECHNICAL PROGRESS FY 1990**

### **Summary**

Through the use of scattering centers in the walls of the hollow ceramic spheres, the thermal conductivity (T/C) of sphere beds has been reduced 50-60% at elevated temperatures. The spheres have been successfully bonded into monolithic shapes and efforts to incorporate low T/C spheres along with decreasing the T/C of the bonding phase are ongoing. The goal is to engineer a sphere-based shape that approaches the T/C of refractory ceramic fiber.

Presently the sphere forming process utilizes ceramic powder dispersed in an organic liquid. There are many benefits to be derived if aqueous-based slurries can be employed to fabricate the spheres. Spheres have been formed, dried and fired using  $\text{Al}_2\text{O}_3$  powder dispersed in water, containing water soluble gels; however, the resulting product does not possess the low density and spherodicity achievable from the organic-based slurry. Additional methods to "gel" free falling water-based spheres are being examined.

The dissemination of sphere technology and property information was initiated this year, primarily through individual visits to many industrial firms. As a consequence of this activity, new and novel

applications have been identified and a variety of samples have been fabricated for industrial evaluation.

### **Milestones**

1. Reduce Thermal Conductivity of the Spheres, start 9/89, end 6/91. The major objective of this area of research is to decrease the thermal conductivity (T/C) of loose sphere beds, as well as bonded sphere structures, to values that approach the high temperature insulating characteristics of ceramic fiber. This has been approached by incorporating voids or thermal pores in the sphere walls and forming sphere walls consisting of two phases with significantly different refractive index. These microstructures act as scattering centers to retard the flow of radiant energy through the sphere walls, especially at evaluated temperatures. The T/C of mullite spheres with and without thermal pores and spheres containing a 50/50 v/o of zirconia-alumina grains in the sphere walls is shown in Figure 1. For comparison, the final curve in this Figure was generated by testing a stack of K-23 insulating fire brick in the Anter T/C equipment. This IFB probably possesses the lowest T/C in the 1100-1200°C range of any material (including fiber) so this is a demonstrated goal for the spheres. Clearly, using mixed oxides along with thermal pores for scattering radiation by the sphere walls and utilizing efficient sphere packing for additional insulation may generate insulating systems with T/C values approaching ceramic fiber.

In previous work the spheres have been bonded together to form monolithic structures by using a slip of basically the same composition as the spheres to form small "fillets" at the contact points between the spheres. Many samples have been fabricated primarily for measuring strengths of bonded shapes. A cylindrical monolithic structure, formed by bonding mullite spheres with mullite slip, was fabricated using longitudinal rods to leave channels in the cylinder for the central heater and radial thermocouples of the Anter T/C equipment. The T/C of this bonded structure and loose mullite spheres are shown in Figure 2. As anticipated the added bonding material between the spheres slightly increases the T/C at low temperatures and decreases the T/C at 1000°C and above. Most importantly, any T/C reduction in the basic unbonded sphere can be utilized in the bonded shape, as the bonding media does not significantly effect the overall T/C of the bonded structure. Work to evaluate and reduce the T/C of bonded shapes is continuing. It is important to note that as opacifiers have been added to the walls of these spheres, first as pores, then as mixed phases, the progressive reduction in high temperature thermal conductivity suggests that the goal of producing a T/C as low as ceramic fiber is achievable, Figure 3.

2. Aqueous - Based Slurry Systems, Start 9/89, End 6/91

An effort is underway to convert the sphere formation process from an acetone-based to a water-based ceramic powder slip system. There are many benefits to be gained from this

conversion including; 1) elimination of an acetone disposal or recovery system, 2) exposure of personnel and the environment to an organic solvent, and 3) a significant reduction in the cost of producing the spheres.

The most promising avenue for a successful water-based slip system so far identified at Georgia Tech is the use of natural gums to gel the water in the sphere shortly after formation, and provide the strength necessary for a soft landing of the free falling sphere. These gums are commonly produced from selected species of seaweed and used in the food industry for such applications as jelly and ice cream. Therefore, there are no health hazards associated with these naturally occurring gums.

At present the sphere forming characteristics of the aqueous slurries have not quite matched the acetone-based systems. For example, the slurries containing gels must employ 3 to 4 w/o of the gum to provide enough gel strength to maintain the shape during free-fall and survive the landing. Unfortunately these slurries, with a high volume loading of solids ( $\text{Al}_2\text{O}_3$  powder), are very viscous and do not possess the film-forming capacity of the organic systems. As a result the typical density of the aqueous processed spheres is 40-50 lbs/ft<sup>3</sup> compared to 20-30 lbs/ft<sup>3</sup> for the acetone derived spheres. Additionally, because of the softer wall and landing damage, the sphericity of the aqueous spheres do not match that of

the organic-based spheres. Work is continuing on aqueous-based slurries because of the economic attractiveness of these systems.

3. Technology Transfer, Start 9/89, End 6/91

In the fall of 1989 personnel from industry, universities, and government met to review the hollow-sphere technology with the goal of commercializing this technology. In general, this group identified potential application areas and thought it appropriate to inform industry about the spheres at trade shows and through individual visits, rather than by trying to attract a large audience through a formal technology transfer conference.

The dissemination of sphere technology and property information to the industrial community was initiated in January 1990. Dr. Carl Vander Linden has arranged most of the visits and Cochran and VanderLinden have made presentations to some 50 companies between January and September 1990. Extensive trip reports have been prepared by Dr. Vander Linden.

As a result of these visits, many new applications have been uncovered where a unique property of the spheres provides a refractory product not previously available. Three examples follow: a) The interest in a basic magnesia or spinel sphere is continually expressed and spheres of these compositions have been prepared at Georgia Tech, b) During a visit to a

major oil company, the need for a refractory to withstand the very corrosive atmospheres (containing fluorine and chlorine gases) present in hazardous waste incinerators used in most petrochemical plants was identified, and samples have been provided for testing by the interested company, and c) The industry sponsored, Gas Research Institute, stated the need for a flat burner plate to spread heat uniformly over wide areas for drying. The capability to produce low expansion refractory ceramic spheres along with the uniform channels between the monosized spheres suggested bonded-sphere plates may provide a superior product for this application, and samples have been fabricated for testing. These samples have been provided to a GRI sponsored company and they have performed well to date as radiant gas burner plates. This is an extreme thermal shock condition and suggests that bonded aerosphere monoliths have excellent thermal shock resistance.

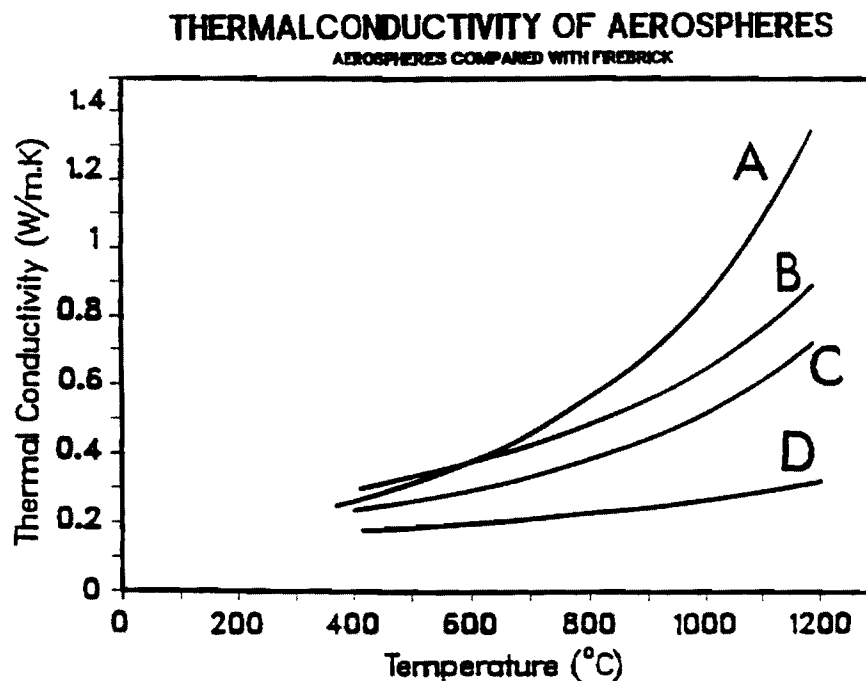


FIGURE 1. Thermal Conductivity of Mullite Spheres (Curve A), Mullite Spheres with Thermal Pores (B), Alumina-Zirconia Spheres - 50/50 v/o (C) and K-23 Insulating Firebrick (D).

# THERMAL CONDUCTIVITY OF MULLITE SPHERES

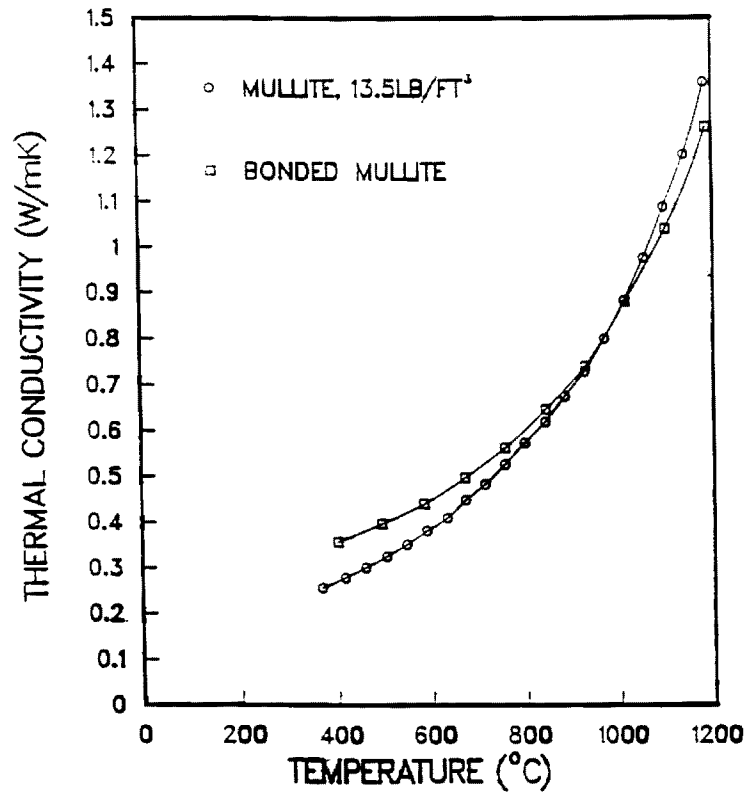


FIGURE 2. Thermal Conductivity of Bonded Mullite Spheres and Loose Mullite Spheres without Thermal Pores.

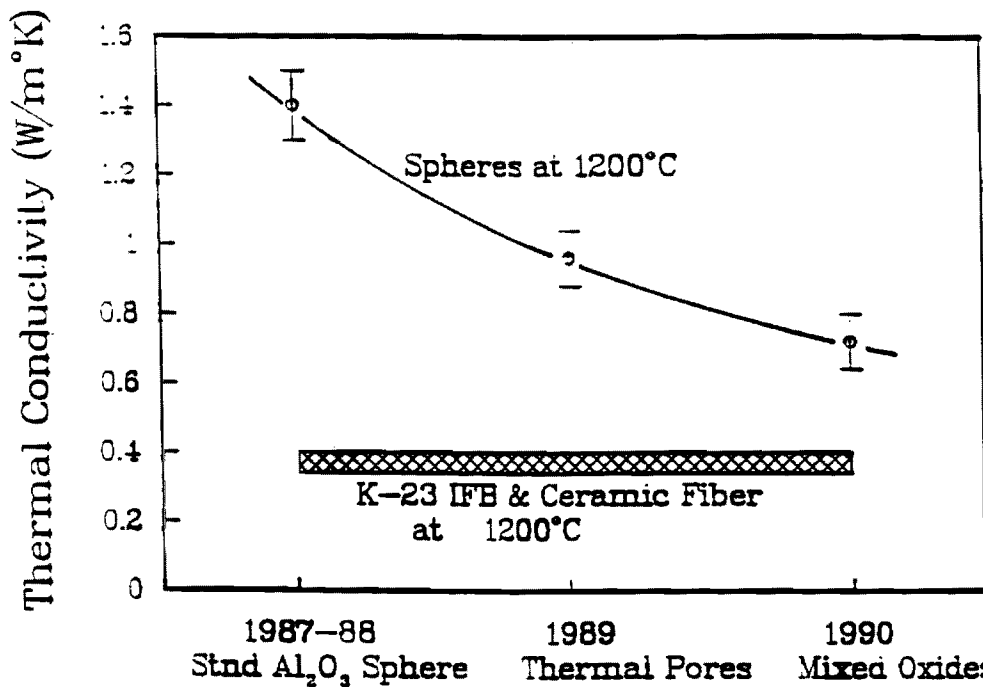


FIGURE 3. Reduction in Thermal Conductivity of Hollow Ceramic Spheres between 1987 through 1990.

## **PUBLICATIONS**

1. S.D. Furlong, "Reduction of Radiative Thermal Conductivity in Thin-Wall Hollow Ceramic Spheres Using Scattering Phases, M.S. Thesis, School of Materials Engineering, Georgia Institute of Technology, Atlanta, GA
2. A.T. Chapman, J.K. Cochran, T.R. Ford, S.D. Furlong, and D.L. McElroy, "Reduction of High Temperature Thermal Conductivity of Thin-Wall Ceramic Spheres", Insulation Materials: Testing and Applications, Volume 2, ASTM STP 1116, R.S. Graves and D.C. Wysocki, Eds., American Society for Testing and Materials, Philadelphia, 1991. (in preparation)
3. R. B. Clancy, J. K. Cochran, and T.H. Sanders, "Thin-Wall Hollow Metal Spheres and Monolithic Foams", Proceedings of Second International Conference on Light Weight Alloys, TMS Annual Meeting, New Orleans, LA, Feb. 1991. (in preparation)

## **PRESENTATIONS**

1. J.K. Cochran, S.D. Furlong, M.J. Shapiro, A.T. Chapman, and D.L. McElroy, "High Temperature Thermal Conductivity of Thin-Wall Hollow Spheres", XXI International Conference on Thermal Conductivity, Lexington, KY, Oct.16, 1989.
2. S.D. Furlong, J.K. Cochran, and A.T. Chapman, "High Temperature Insulation Capability of Thin-Wall Ceramic Spheres", Annual Meeting American Ceramic Society, Dallas, TX, April 25, 1990, Paper 101-C-90.
3. J.H. Chung, J.K. Cochran, and A.T. Chapman, "Compressive Strength of Thin-Wall Hollow Ceramic Spheres", Annual Meeting of American Ceramic Society, Dallas, TX, April 23, 1990, Paper 11-JVII-90.

## **LICENSES**

The base patents for coaxial nozzle formed hollow powder spheres is owned by Microcel Technology, Inc. Georgia Tech is allowed to develop this technology under a license from Microcel. Transfer of this technology to industry is proceeding through Ceramic Fillers, Inc. which holds an exclusive, worldwide license from Microcel for applications above 400C. Personnel from Georgia Tech and Ceramic Fillers work cooperatively in providing technology transfer.

## **INDUSTRIAL INPUT AND TECHNOLOGY TRANSFER**

During the past year a technology transfer planning conference was held in Atlanta in Nov. 1990 with representatives of six companies, DOE, and Georgia Tech. The committee recommended making visits to individual companies by a technology transfer team which consisted of Drs. Carl Vander Linden and Joe Cochran. As a result over 50 companies were visited and provided on average a two hour presentation of hollow sphere technology. The response has been excellent and active interaction is in progress with ten companies and Georgia Tech and/or Ceramic Fillers, Inc. Another fifteen companies have expressed interest in meaningful interaction but this is limited by Georgia Tech and CFI funding.



## **COST SHARING**

To assist in development of hollow sphere technology, Georgia Tech has provided funds for equipment and personnel. In addition, testing of spheres in a variety of applications is occurring at six companies as a result of technology transfer visits. Funding level for these efforts has been estimated and added as part of cost sharing. Total cost sharing summed to 213K.

1. From Georgia Tech (a) 65K for powder characterization equipment and (b) 36K for additional graduate student support.

2. From Industry (estimated) (a) AMOCO, 10K, Conductivity and Strength Testing, (b) IGT, 5K, Fluidized Bed Testing, (c) Plibrico, 2K, Permeability Testing, (d) GRI, 5K, Radiant Burner Testing, (e) Martin Marietta Refractories, 10K, Castable Testing, (f) Thermal Ceramics, 20K, Castable Testing, and (g) Ceramic Fillers, 60K, Sample Preparation for Above Testing.

## **ESTIMATED ENERGY SAVINGS**

The major application for hollow sphere technology is for insulation in the 2300 to 3200F range. If ceramic fibers are excluded, aerosphere insulation appears to be the best alternative for most applications at these temperatures. It has been estimated the ceramic fiber insulation in use above 2300F in the United States saves 0.1 quads. Energy savings by aerospheres in this application would be proportional to market share times the 0.1 quad value.

## **HIGHLIGHT - Aerosphere Insulating Concrete**

A project is in progress to measure the effects of mullite aerospheres as the aggregate in concrete. To date concretes have been produced with dry bulk densities in the 55-60 lb/ft<sup>3</sup> range and compressive strengths of 2000 psi. By comparison, typical residential grade concretes have bulk densities near 145 lb/ft<sup>3</sup> and compressive strengths of approximately 3000 psi. Based on data from A. Short and W. Kinniburgh, *Lightweight Concrete*, 3rd ed., Applied Science Publishers, Ltd., London, 1978, dry concrete at 55 lb/ft<sup>3</sup> should have a thermal conductivity 0.2 W/mK compared to 1.4 W/mK at 145 lb/ft<sup>3</sup>. Obviously, aerospheres are currently too expensive to be considered for such an application. However, with a difference of a factor of seven in thermal conductivity coupled with a significant cost reduction in aerospheres (assuming success in water based processing in the Georgia Tech program you are now funding), the energy savings would justify use of aerosphere insulating concrete as the slab in home construction. To see if these projected conductivities are valid, samples are being prepared for thermal conductivity measurement at ORNL some time in Jan. 1991.

# List of Investigators Participating in Project

Participation in days/week

Project: Thin-Wall Hollow Spheres from Slurries  
J.K. Cochran and A.T. Chapman

Reporting Period: FY 90

Name	Type of Position	Planned Project Time	Approximate Time
		Supported by	
A. J.K. Cochran	Project Dir.	2 GT-DOE	2 (40%)
B. A.T. Chapman	Project Dir.	2 GT-DOE	2 (40%)
C. T.J. Hwang	Post Doctoral	5 DOE	5
D. J.H. Chung	Student (PhD)	2-3 DOE	2.5
E. P.R. Chu	Student (PhD)	2-3 DOE	2.5
F. S. Furlong*	Student (MS)	2-3 DOE	2.5
G. C. Moore	Student (MS)	2-3 DOE	2.5
H. T. Ford	Student (MS)	2-3 GT	2.5
I. R. Clancy	Student (MS)	2-3 GT	2.5
J. G. Carlson	Student (MS)	2-3 GT	2.5
K. T. Ozell	Student (MS Special Problem)	NA	

\* Completed MS Thesis June 90.

## REFRACTORY INSULATING CERAMIC SHELLS

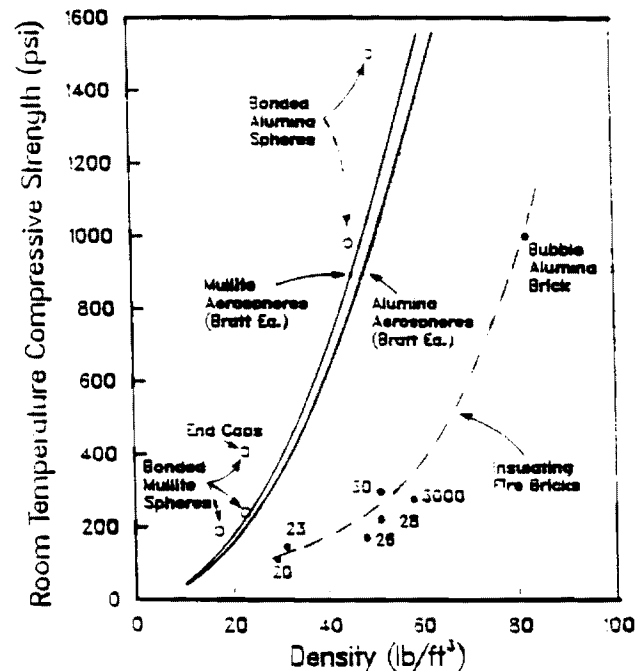
### *Structural Capability in a Thermal Insulation*

**PROBLEM** - Most thermal insulation serves little structural function because of low density, poor geometry which produces critical flaws, or lack of stiffness due to a fibrous morphology which does not support substantial compressive loads.

**RESULT** - A new class of safe thermal insulation useable over wide temperature ranges has been engineered from hollow, thin-wall spheres (Aerospheres) made of low conductivity ceramic or glass for ambient to high temperature use. Because of the perfection of the hollow spheres, structures made by bonding the spheres into monoliths have high compressive strength. For example, when compared to a common form of high temperature insulation, insulating fire bricks, aerosphere monoliths are five to eight times stronger at equivalent densities (see below).



Bonded Aerospheres and Insulating Fire Bricks



**SIGNIFICANCE** - for *energy conservation* - Potential ceramic insulation with improved performance and strength, cost effectiveness, and avoidance of health or environment hazards as compared to existing products.

**SIGNIFICANCE** - for *industrial competitiveness* - A high strength to thermal conductivity ratio allows improved insulation for structural members and a broader range of applications in the chemical, metals, and ceramic processing industries.

(Research at Georgia Institute of Technology under DOE-AIM support)

## **PROJECT SUMMARY**

### **ADVANCED INDUSTRIAL MATERIALS (AIM) PROGRAM**

**WORK ELEMENT:** Thermally Insulating Materials

**PROJECT TITLE:** Thin-Wall Hollow Spheres From Slurries

**PHASE:** Technology Proof-of-Concept **PHASE COMPLETION DATE:** 6-91 (IV)

**PERFORMING ORGANIZATION(S):** Materials Engineering, Georgia Tech

**PRINCIPAL INVESTIGATORS:** Joe Cochran and Ted Chapman, (404) 894-6104

**PHASE OBJECTIVES:** Phase IV

1. Reduce Thermal Conductivity of Spheres Using Opacifiers
2. Convert Sphere Processing to Water Based Slurries
3. Provide Meaningful Technology Transfer to Industry

**ULTIMATE OBJECTIVE:** Develop insulation material that is economical to manufacture, ecologically safe, free of health risks, usable to high temperatures, and competitive with existing insulations.

**TECHNICAL APPROACH:** Form hollow spheres from dispersions of inexpensive ceramic powders, engineer the sphere wall to minimize heat conduction, and bond spheres into structural monoliths.

**PROGRESS:** A commercially viable sphere formation process has been demonstrated yielding low density spheres and monoliths with properties approaching existing high temperature insulation materials.

**Patents:** 0 **Publications:** 1 **Proceedings** 2 **Presentations** 53

### **ACCOMPLISHMENTS:**

**Licenses:** 1 (To Georgia Tech from Microcel Technology for use of proprietary-patented process.)

**Known Follow-on Product(s):** 1. Insulating Furnace Cover (1600C, 40 inch dia.) Being Tested at Y-12 Plant, ORNL. 2. Radiant Gas Burner Plates Being Tested at GRI Sponsored Eclipse Corp.

**Industry Workshop:** Aerosphere Planning Conference Held Nov. '89

**Other Successful Technology Transfer Activities as Evidence of Industry Interest:** 1. Commercial Company, Ceramic Fillers, Inc. (CFI) operating aerosphere pilot plant in Atlanta, GA at ATDC and production facility (capability 800 tons/yr) in Laurens, SC. 2. Technology Transfer Visits to Fifty (50) Companies with Dr. Carl Vander Linden in which an average of a two hour presentation was made resulting in numerous follow-on activities.

**PROJECT TITLE:** Thin-Wall Hollow Spheres From Slurries

**CRITICAL ISSUES:** Reduce thermal conductivity to values competitive with fibrous insulation, develop lower cost water-based sphere forming system, continue introducing aerosphere technology to industry.

**FUTURE PLANS:** Continue Phase IV program as proposed. That is to reduce conductivity further, reduce cost to expand applications into larger markets, and explore specific product applications with the technology transfer procedure that has been so successful to date.

**POTENTIAL PAYOFF:** Insulating materials without the ecological and health dangers of existing technologies.

**FUNDING HISTORY:**

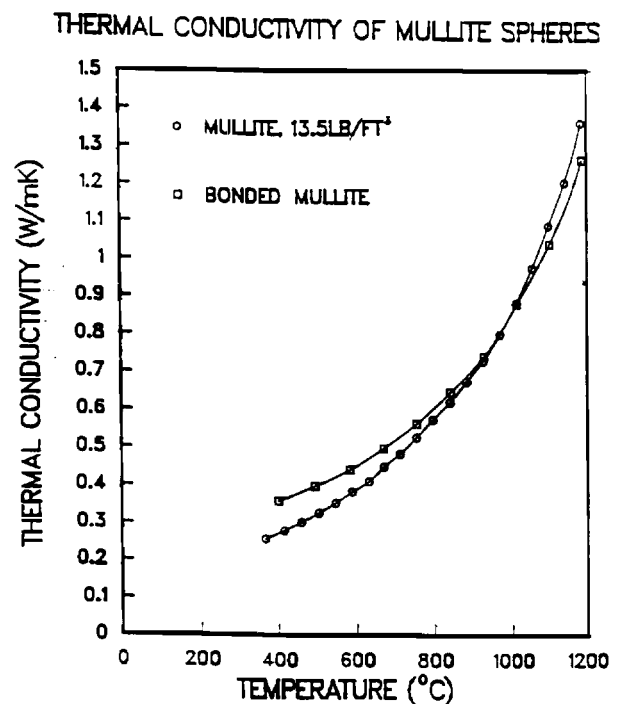
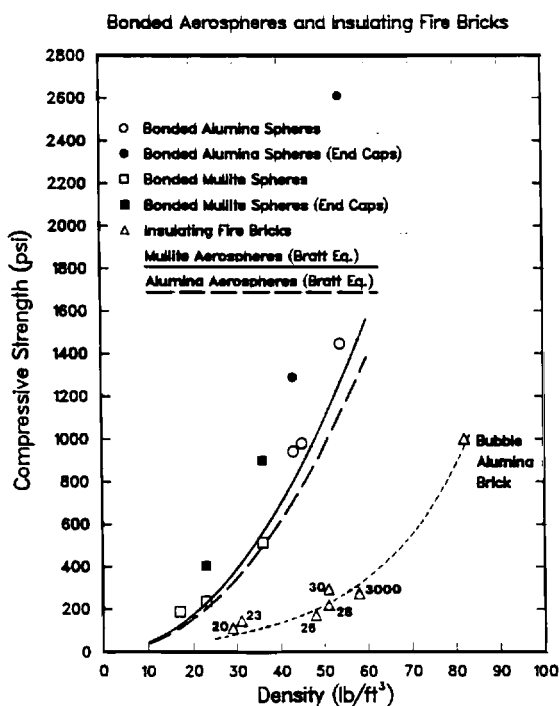
	FY 88	FY 89	FY 90
Amt	<u>\$219K</u>	<u>\$266K</u>	<u>\$285K</u>

Cum. Total to Date \$1264K (Includes Phases I-IV)

**OTHER SOURCES:** FY90 \$213K (Includes Ga Tech and Industry)

**ESTIMATED ENERGY SAVINGS:** Insulation now used in markets available to potential aerosphere products for applications above 2300F are estimated to save approximately 0.1 quads.

### HIGH SPECIFIC STRENGTH COUPLED WITH LOW THERMAL CONDUCTIVITY PROVIDES UNIQUE PROPERTIES FOR AEROSPHERE INSULATION



# Georgia Tech

E 18-694  
#19

School of Materials Engineering

**Georgia Institute of Technology**

Atlanta, Georgia 30332-0245

(404) 894-

FAX: (404) 853-9140

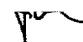
December 30, 1991

Dr. Peter Angelini, Manager  
Advanced Industrial Concepts (AIC) Materials Program  
Oak Ridge National Laboratory  
Building 4515, Mail Stop 6065  
One Bethel Road  
Oak Ridge, TN 37831-6065

Dear Pete:

Enclosed is the FY 1991 Annual Progress Report, Significant Accomplishment, and Project Summary for Contract DE-FCOS-89CE90052, "Thin Wall Hollow Ceramic Spheres From Slurries." If there are any changes you would like made, please give me a call.

Cordially,

  
Joe K. Cochran, Jr.  
Professor

JKC/gb

## **THIN-WALL HOLLOW CERAMIC SPHERES FROM SLURRIES**

J.K. Cochran  
School of Materials Engineering  
Georgia Institute of Technology  
Atlanta, GA 30332-0245  
Contract DE-FC05-89CE90052

### **INTRODUCTION**

The ongoing DOE supported program on "Thin-Wall Hollow Ceramic Spheres from Slurries" was initiated on January 1986. During Phase I, the objective was to develop a process for fabricating the spheres. This was successful by dispersing ceramic powders in an organic liquid, blowing the individual spheres using a coaxial nozzle, and drying the free-falling spheres in an updraft heated air column. Based on Phase I success, Phase II activity emphasized documenting the structural and insulation capability for the spheres, and modeling the sphere formation process. Phase II ended April, 1989 and was followed by four month effort, Phase III, to assess the potential of incorporating an opacifier in the sphere walls to scatter radiation and decrease the high temperature thermal conductivity of sphere beds. In September, 1989, a three year follow on, Phase IV, program was initiated consisting of three major tasks:

- 1) reduce thermal conductivity by incorporating opacifiers in the sphere wall,
- 2) convert the slurries from organic-based to aqueous-based systems, and
- 3) provide product engineering and information dissemination (technology transfer) to end-use industries.

This Annual Report briefly reviews the very encouraging Phase IV results. Publications, presentations, personnel participating in the project, and allied budgetary information are also included.

## TECHNICAL PROGRESS FY 1991

### Summary

In FY 1990, it was demonstrated that by incorporating micron sized, IR-opacifying, pores into the sphere walls, thermal conductivities (T/C) of the sphere beds could be decreased 50-60% at 1200°C. This year (FY 1991), opacification efforts shifted to incorporating a high index particulate phase ( $\text{ZrO}_2$ ) in a lower index sphere wall matrix (mullite) using an insitu reaction between zircon and alumina to provide an economical raw material base. It has also been demonstrated that spheres can be bonded into monoliths without significantly increasing T/C if a low conductivity bonding phase is used.

Efforts have continued to convert the sphere formation process from a organic liquid to water-based slurry system. After an extensive effort to use water soluble food gels as the hardening mechanism, this approach, which was promising, has been abandoned because it could not produce hollow spheres of low enough density. Another system, colloidal silica dispersions, has also been investigated and abandoned because a high strength gel could not be produced in a short enough time period ( $< 1$  sec) for spheres to survive collection. A new collection system is under intensive development which appears very promising.

Technology transfer continued under the direction of Dr. Carl Vander Linden resulting in 25 onsite presentations and development of new applications areas, radiant burner tiles, furnace linings, and hollow metal sphere foams. Bonded structures are being tested by the Gas Research Institute, the Y-12 Plant, Lawrence Livermore Laboratory, and Hi Temp Corporation. In addition, aerosphere technology was presented at a trade show, the American Ceramic Society Exposition, through sponsorship of Ceramic Fillers, Inc.

Two major modeling efforts which have been ongoing for three years have



culminated in FY 91 with successful models for hollow sphere formation based on fluid mechanical forces and a finite element parametric model for predicting strengths of hollow-spheres under two point and multipoint loading. The multipoint loading model allows prediction of strength of hollow sphere monolithic foams bonded at points of contact as a function of sphere wall material strength, foam density, and quantity of bonding phase.

### **Milestones**

#### **1. Reduce Thermal Conductivity of Hollow Spheres and Bonded Monoliths**

After the success demonstrated by using pores for reducing high temperature T/C, an extensive study has been made to opacify mullite spheres by adding zirconia to the sphere walls. One method of adding ZrO<sub>2</sub> to mullite was through the insitu reaction of zircon and alumina which reacts to zirconia and mullite at 1550 to 1600°C;



Using this insitu reaction, zirconia opacified spheres were produced, quantity of zirconia and mullite was measured by XRD, and zirconia particle size was measured. Thermal conductivities of loose sphere beds were as low as pore opacified mullite but lower conductivities did not result because it appears that reaction(1) contributes to densification which eliminates radiation scattering pores. Essentially, introducing zirconia as an opacifier is offset by reducing the quantity of opacifying pores, resulting in similar T/C.

Zirconia has also been introduced into mullite spheres by adding yttria partially-stabilized-zirconia to mullite forming powders. The size distribution of the zirconia has been varied in an attempt to optimize radiation scattering but no observable reductions in T/C were produced by varying zirconia particle size. In mullite based spheres, the lowest conductivities at 1200°C have been produced by pore opacification at sphere bed densities

of 0.5 g/cc. The larger index of refraction difference between pores and the mullite provides more efficient infrared scattering than between zirconia and mullite.

In addition to opacifying sphere walls, the effect of the bonding phase on T/C of sphere monoliths has been modeled and measured. This was documented in the last two quarterly reports. In summary, bonding spheres together at points of contact with low conductivity phases has little effect on thermal conductivity and use of high conductivity bonding phases produces large increases in T/C.

## 2. Aqueous-Based Slurry Systems

Work continued to form low density hollow spheres using the polysaccharide gel, carrageenan, as the bonding mechanism. Carrageenan is a thermally reversible gel which forms a liquid solution above 80°C and gels rapidly when cooled below 70°C to form a strong gel. The rate of gelling was shown to be fast enough on cooling to harden the hollow spheres in free flight. A study on the effect of cation ( $K^+$  and  $Cs^+$ ) concentration and carrageenan content on gel strength resulted in an empirical mathematical model expressing gel strength to within 15-20%. The object was to determine if usable gel strengths could be reached at a low enough carrageenan content to produce a viscosity sufficiently low to form low density spheres. Unfortunately, at low alumina-carrageenan slurry viscosities compatible with sphere formation, gel strengths were insufficient for collecting hollow spheres. Furthermore, clay (kaolin) in carrageenan based slurries have high viscosities and this system can not produce low cost clay based spheres. Thus food gels were abandoned and colloidal silica dispersions were investigated as a potential gelling mechanism.

Colloidal silica dispersions (Ludox) are marketed at relatively high solid contents (up to 50 w/o) with viscosities which are compatible with hollow sphere formation. These

colloidal silica based dispersions can be gelled with good strengths by additions of salts of various types. By sensitizing with salts, changing pH, and increasing temperature, we have demonstrated that gel times can be reduced to under 10 seconds. Gas phase reactions with ammonia were conducted to change pH of the sphere wall in free flight after sphere formation. Surface gelling could be produced but the reactions were too slow for the spheres to survive landing. A third (polymerization reactions) system is under investigation.

### 3. Technology Transfer

Technology transfer trips continued this year under the direction of Dr. Carl Vander Linden resulting in 25 presentations and many subsequent interactions particularly with Rohr Industries and Hi Temp Corporation. In addition, a trade show booth at the American Ceramic Society Exposition in Cincinnati in May, sponsored by Ceramic Fillers Inc. demonstrated aerosphere technology and generated considerable industrial interest.

As a result of these technology transfer contacts and the success that mullite radiant burner tiles have demonstrated under severe thermal shock conditions, the Gas Research Institute has funded a project to develop high emissivity radiant burner tiles based on the mullite aerosphere monoliths. Other aerosphere monolithic insulations currently being tested include three different types of induction furnace insulation at the Y-12 plant, insulation plates at High Temp Corporation, and alumina aerosphere boards at Lawrence Livermore Laboratory. The continued, growing interest in this technology by American industry is the best measure available for the success of the overall program.

### 4. Sphere Formation Model

The object of this model was to understand the aerosphere formation mechanism which would allow prediction and control of aerosphere formation frequency, sphere size,

and sphere density. Aerospheres produced from a coaxial nozzle at high liquid flow rates are formed as shown in Figure 1. Liquid exits the nozzle in a nearly cylindrical form and closes at a distance below the nozzle. The inner jet gas flow provides inflation pressure to form a sphere at the closed end. In modelling the process, only the hollow sphere stresses were considered since the cylinder remains approximately unchanged. The stresses on the aerosphere surfaces, Figure 2, are hydrostatic pressures, viscous stresses, and surface tension. An equation balancing these stresses was developed and solved which related the pressure ( $\Delta P$ ) inside the sphere to sphere radius ( $R$ ), shell thickness, gas flow rate, liquid flow rate, density, surface tension, and viscosity. The breakthrough for the model was recognizing that as the sphere radius increased with time, the pressure inside the sphere decreased until  $\Delta P$  was less than the pressure in the hollow cylinder cavity ( $\Delta P_{cav}$ ) from which the sphere was growing, Figure 3. Once the pressure in the sphere was less than the pressure in the hollow cylinder, the sphere would pinch off and a new sphere was initiated. This "critical pressure" allowed calculation of the time ( $t_b$ ) required for the sphere formation cycle. The sphere formation period was the inverse of the formation frequency. This frequency was accurately predicted for a variety of conditions, Figure 4. Knowing the frequency, sphere size, weight, and density could be calculated from gas and liquid flow rates. The success of this model allows prediction of conditions necessary to extend the process to sphere sizes and densities not yet achieved.

##### 5. Hollow Sphere Foam Strength From Finite Element Modeling.

Sphere strength under uniaxial two point loading for a hollow ceramic sphere was modeled. Parametric relationship of sphere strength was obtained from the finite element analysis. For a practical range of thin walled spheres produced to date, it can be safely

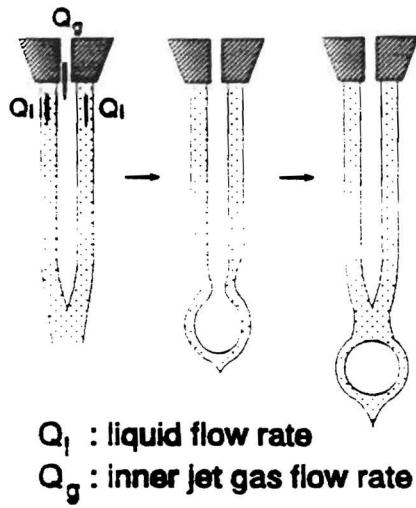


Figure 1. Aerosphere Formation at High Liquid Flow Rates.

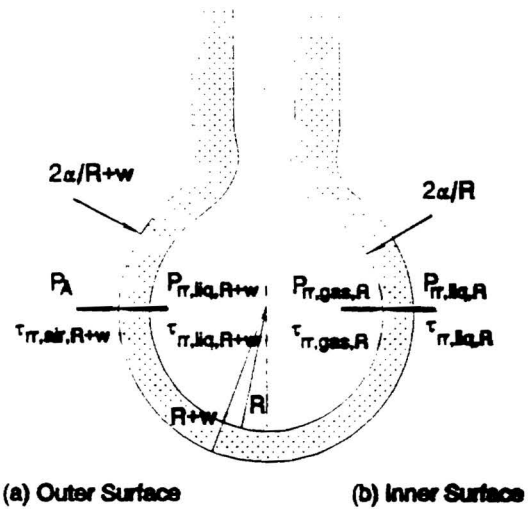


Figure 2. Stress Balance on the Hollow Sphere.

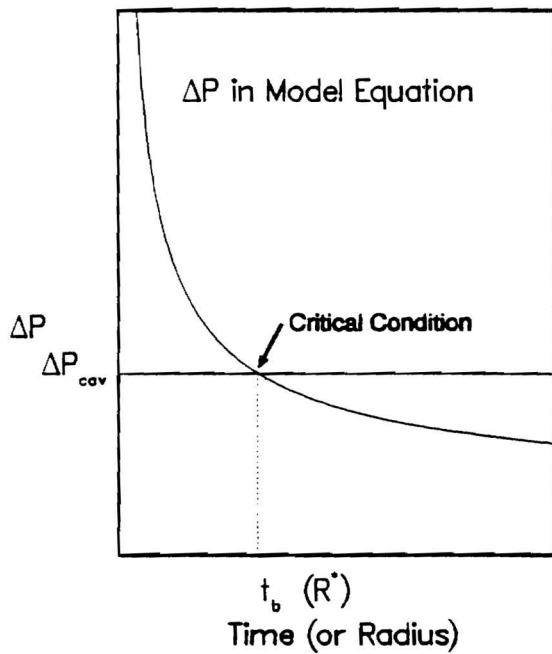


Figure 3. Critical Pressure Controlling Sphere Formation Frequency.

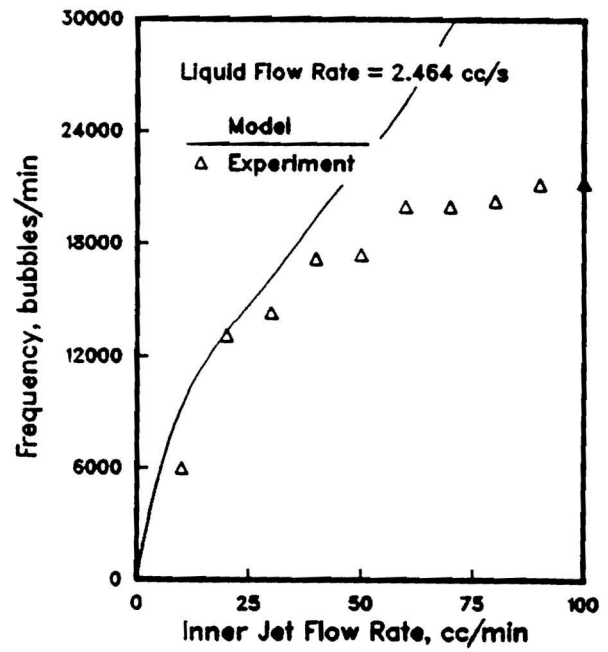


Figure 4. Comparison of Predicted and Experimental Frequencies.

stated that the sphere strength is a square function of relative density of a sphere,  $(\rho_s/\rho_o)$ ,

$$\sigma_s = C \sigma_o \left( \frac{\rho_s}{\rho_o} \right)^2 \quad (2)$$

where  $\sigma_s$  is sphere strength,  $\sigma_o$  is wall material strength,  $\rho_s$  is sphere density,  $\rho_o$  is wall material density, and  $C$  is a constant. This result is in agreement with the empirical results except that the coefficient,  $C$ , is approximately 2.5 times greater than measured experimentally using two point loading. One critical result from finite element stress analysis using Griffith criterion, was the prediction that failure take place near a loading point. This is in contradiction to the equatorial failure model previously suggested by Bratt et al. Failure near the loading point has been observed experimentally.

A closed cell foam can be fabricated by bonding the hollow spheres together. Bonding material fills the space between spheres at a contact point forming a neck as shown in Figure 5. The contact angle,  $\phi$ , varies with the amount of the bonding material used. Thus a hollow sphere in a bonded sphere foam experiences a distributed load rather than a point load. To better understand a sphere foam, compressive strength of a hollow sphere under uniaxial distribution loading was investigated first.

Finite element models were developed for various contact angles, i.e., for  $\phi = 10, 20$ , and  $30^\circ$ . Stresses, membrane forces, and bending moments showed similar patterns as in the two point loading analysis except that as the contact angle increased, the stress concentration effects at and near a loading area become less significant. For a given contact angle, the failure region moved from outside of the bonded area toward the point of contact as the density increased. For a given density, the strength increased dramatically as the contact angle increased, Figure 6. The strength vs. density squared relationship was no

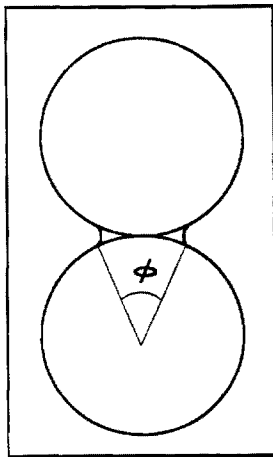


Figure 5. Contact Angle of Bond Between Spheres.

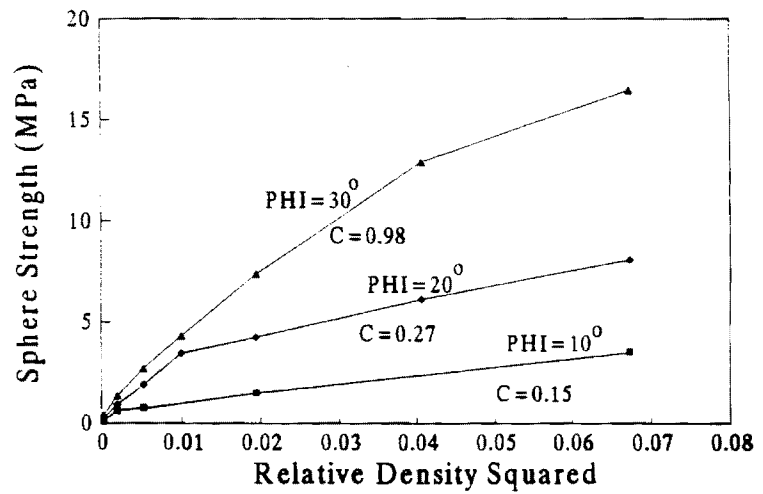


Figure 6. Effect of Contact Angle On Strength of Uniaxially Loaded Spheres.

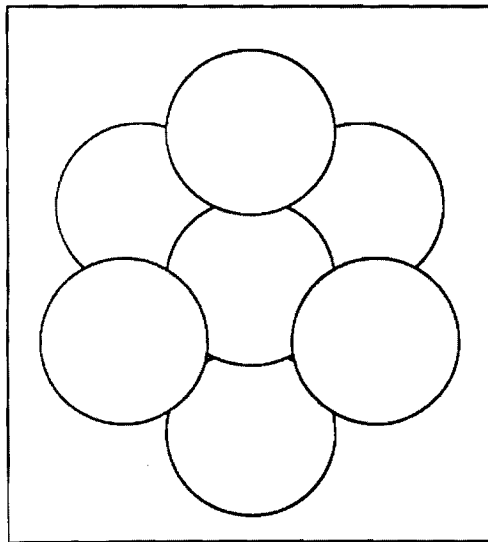


Figure 7. Foam Model Based On Central Octahedral Sphere in a Cubic Structure.

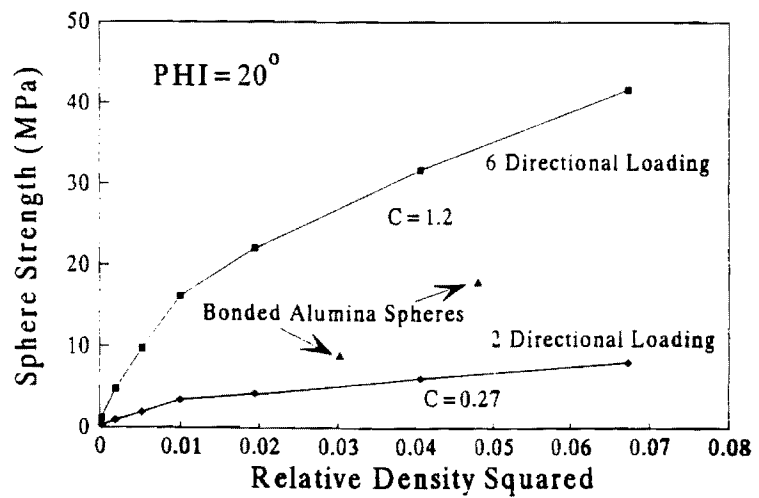


Figure 8. Comparison of 2 Directional and 6 Directional (Octahedral) Loading on Hollow Sphere Strength.

longer linear but the slope of the upper portion of the curve was used as an estimate of C.

Spheres in a bonded foam are randomly packed and in contact with six to eight surrounding spheres. To calculate the foam compressive strength, a basic unit structure was modeled as shown in Figure 7. The unit structure was idealized as a simple cubic where the octahedral site contacts six surrounding spheres at right angles. The sphere foam is assumed to be random packing of the unit structure. The packing factor for simple cubic is 0.52 and that of random packing is approximately 0.6. Thus, the proposed model must have a slightly higher packing factor than the simple cubic packing.

Under these assumptions, a finite element model was developed for sphere strength under six directional distributed loading. As in the uniaxial distributed compressive sphere strength analysis, analyses were performed for  $\phi = 10, 20, \text{ and } 30^\circ$ . Strengths showed a similar tendency to the uniaxial distributed load case except that coefficients were three to four times larger for the foam, Figure 8. Thus, bonded forms are predicted to have strengths three to four times larger than uniaxially loaded spheres. This has been observed experimentally and predicts hollow sphere foam strengths larger than other geometrical structures. Validity for the model is provided by the experimental data points on Figure 8 which have strength approximately half of the predicted value. Considering defects and uncertainty of bond contact angle, this is reasonable agreement.

## **PUBLICATIONS**

1. C.M. Moore, "Organic Gels for Injection Molding of Powders", MS Thesis, Materials Engineering, Georgia Institute of Technology, June, 1991.
2. T. R. Ford, "Thermal Conductivity of Bonded Hollow-Sphere Monoliths", MS Thesis, Materials Engineering, Georgia Institute of Technology, June, 1991.



3. P.R. Chu, "A Model for Coaxial Formation of Hollow spheres from Liquids", PhD Thesis, Materials Engineering, Georgia Institute of Technology, June, 1991.
4. R.B. Clancy, "Nickel and Nickel Alloy Hollow Spheres and Foams", MS Thesis, Materials Engineering, Georgia Institute of Technology, December, 1991.
5. T.A. Ozell, "Effect of Aerosphere Light Weight Aggregate on the Properties of Portland Cement Concrete, Special Problem, Civil Engineering, Georgia Institute of Technology, June, 1991.
6. A.T. Chapman, J.K. Cochran, T.R. Ford, S.D. Furlong, and D.L. McElroy, "Reduction of High Temperature Thermal Conductivity of Thin-Wall Ceramic Spheres", Insulation Materials: Testing and Applications, Volume 2, ASTM STP 1116, R.S. Graves and D.C. Wysocki, Eds., p.464-475, American Society for Testing and Materials, Philadelphia, 1991.
7. R. B. Clancy, J. K. Cochran, and T.H. Sanders, "Thin-Wall Hollow Metal Spheres and Monolithic Foams", Proceedings of Second International Conference on Light Weight Alloys, TMS Annual Meeting, New Orleans, LA, Feb. 1991. (in press)

## **PRESENTATIONS**

1. C.M. Moore, T.J. Hwang, and J.K. Cochran, "Gel Properties for Aqueous Ceramic Processing", Annual Meeting American Ceramic Society, Cincinnati, Ohio, April 30, 1991, Paper 54-C-91.
2. P.R. Chu and J.K. Cochran, "A Fluid Mechanic Model of Coaxial Nozzle Formation of Hollow Spheres From Newtonian Fluids", Annual Meeting American Ceramic Society, April 30, 1991, Paper 55-C-91.
3. R.B. Clancy, J.K. Cochran, and T.H. Sanders, "Bonded Hollow Nickel Spheres", Annual Meeting American Ceramic Society, Cincinnati, Ohio, April 30, 1991, Paper 56-C-91.
4. T.R. Ford, J.K. Cochran, and A.T. Chapman, "Refractory Applications of Ceramic Thin-Wall Hollow Spheres", Annual Meeting American Ceramic Society, Cincinnati, Ohio, May 1, 1991, Paper 50-R-91.
5. J.H. Chung, J.K. Cochran, and A.T. Chapman, "Compressive Strength-Density Model for Bonded Hollow Ceramic Sphere Foams", Annual Meeting of American Ceramic Society, Cincinnati, Ohio, April 29, 1991, Paper 18-C-91.

## **LICENSES**

The base patents for coaxial nozzle formed hollow powder spheres is owned by Microcel

Technology, Inc. Georgia Tech is allowed to develop this technology under a license from Microcel. Transfer of this technology to industry is proceeding through Ceramic Fillers, Inc. which holds an exclusive, worldwide license from Microcel for applications above 400C. Personnel from Georgia Tech and Ceramic Fillers work cooperatively in providing technology transfer.

## **INDUSTRIAL INPUT AND TECHNOLOGY TRANSFER**

During the past year, technology transfer continued under the direction of Dr. Carl Vander Linden resulting in 25 on-site presentations and development of new application areas; radiant burner tiles and several types of specialty insulation. The response has been excellent and active interaction is in progress with fifteen companies and Georgia Tech and/or Ceramic Fillers, Inc. In addition aerosphere technology was presented at a trade show, the American Ceramic Society Exposition, through sponsorship of Ceramic Fillers, Inc.

## **COST SHARING**

To assist in development of hollow sphere technology, Georgia Tech has provided funds for equipment and personnel. In addition, testing of spheres in a variety of applications is occurring at four companies as a result of technology transfer visits. Funding level for these efforts has been estimated and added as part of cost sharing. Total cost sharing summed to 194K for FY91 time period only.

1. From Georgia Tech (a) 15K for sphere formation equipment and (b) 36K for additional graduate student support.
2. From Industry (estimated) (a) GRI, 42K, Radiant Burner Development, (b) Y-12 Plant, 16K, Furnace Insulation Development, (c) Hi-Temp Corp., 15k, Specialty Insulation Testing, (d) Lawrence Livermore Laboratory, 10K, Specialty Insulation Testing, (e) Ceramic Fillers, 60K, Sample Preparation for Above Testing.

## **HIGHLIGHT - Sphere Formation and Foam Strength Models Completed**

Two major modeling efforts which have been ongoing for three years have culminated in FY 91 with successful models for hollow sphere formation based on fluid mechanical forces and a finite element parametric model for predicting strengths of hollow spheres under two point and multipoint loading. The sphere formation model allows prediction and control of aerosphere formation frequency, sphere size, and sphere density. The multipoint loading model allows prediction of strength of hollow sphere monolithic foams bonded at points of contact as a function of sphere wall material strength, foam density, and quantity of bonding phase.

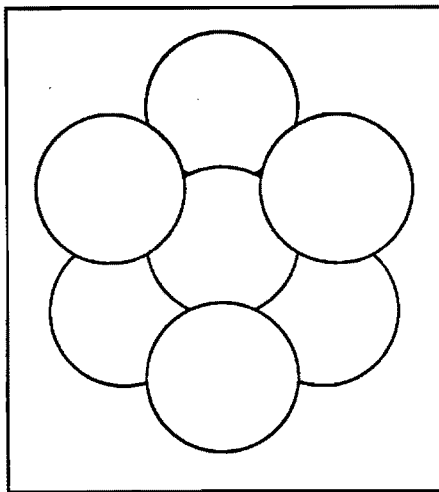
## REFRACTORY INSULATING CERAMIC SHELLS

### Finite Element Modeling Predicts Structural Capability

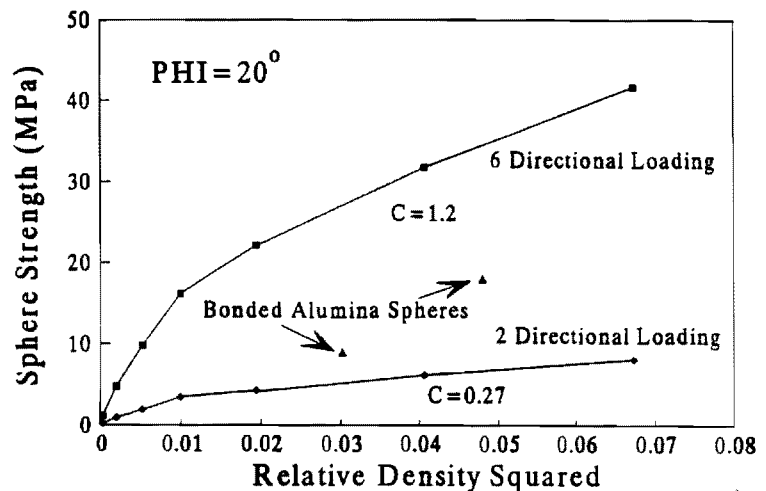
**PROBLEM** - Most thermal insulation serves little structural function because of low density, poor geometry which produces critical flaws, or lack of stiffness due to a fibrous morphology which does not support substantial compressive loads.

**RESULT** - A new class of safe thermal insulation useable over wide temperature ranges has been engineered from hollow, thin-wall spheres (Aerospheres) made of low conductivity ceramic or glass for ambient to high temperature use. Because of the perfection of the hollow spheres, structures made by bonding the spheres into monoliths have high compressive strength. Finite element analysis was used to successfully model the strength of hollow spheres under two point loading. By developing a foam model based on a central octahedrally loaded sphere in a cubic structure, sphere strength was predicted to increase a factor of four when bonded at points of contact into a foam. This model should demonstrate that bonded hollow sphere monoliths have exceptional specific strengths compared to other foam geometries such as open cell and honeycomb.

#### Foam Model Based on Octahedral Sphere in Cubic Structure



#### Four Fold Strength Increase for Hollow Spheres in Bonded Foam



**SIGNIFICANCE** - for energy conservation - Potential ceramic insulation with improved performance and strength, cost effectiveness, and avoidance of health or environment hazards as compared to existing products.

**SIGNIFICANCE** - for industrial competitiveness - A high strength to thermal conductivity ratio allows improved insulation for structural members and a broader range of applications in the chemical, metals, and ceramic processing industries.

(Research at Georgia Institute of Technology under DOE-AIC support)

## **PROJECT SUMMARY**

### **ADVANCED INDUSTRIAL CONCEPTS (AIC) MATERIALS PROGRAM**

**PROJECT TITLE:** Thin-Wall Hollow Spheres From Slurries

**PHASE:** FY92

**COMPLETION DATE:** 6-92 (IV)

**PERFORMING ORGANIZATION(S):** Materials Engineering, Georgia Tech

**PRINCIPAL INVESTIGATOR:** Joe Cochran, (404) 894-6104

**PHASE OBJECTIVES:** Phase IV

1. Reduce Thermal Conductivity of Spheres Using Opacifiers
2. Convert Sphere Processing to Water Based Slurries
3. Provide Meaningful Technology Transfer to Industry

**ULTIMATE OBJECTIVE:** Develop an economical insulation that is ecologically safe, health risk free, usable to high temperatures, and competitive with existing insulations.

**TECHNICAL APPROACH:** Form hollow spheres from dispersions of inexpensive ceramic powders, engineer the sphere wall to minimize heat conduction, and bond spheres into structural monoliths.

**PROGRESS:** A commercially viable sphere formation process has been demonstrated yielding low density spheres and monoliths with properties approaching existing high temperature insulation materials.

**Patents:** 0 **Publications:** 5 **Proceedings** 2 **Presentations** 32

### **ACCOMPLISHMENTS:**

**Licenses:** 1 (To Georgia Tech from Microcel Technology for use of proprietary-patented process.)

**Known Follow-on Product(s):** 1. Insulating Furnace Cover (1600C, 40 inch dia.) Being Tested at Y-12 Plant, ORNL. 2. Radiant Gas Burner Plates Being Tested by GRI.

**Industry Workshop:** Trade Show Booth at American Ceramic Society, April, 1991.

**Technology Transfer and Industry Interest:** 1. Commercial Companies, Ceramic Fillers, Inc. (CFI) operating aerosphere pilot plant in Atlanta, GA at ATDC and Microcel Technology, Inc. operating production facility (capability 800 tons/yr) in Laurens, SC. 2. Technology Transfer Visits to Companies with Dr. Carl Vander Linden in which twenty-five two hour presentations were made resulting in numerous follow-on activities.

**PROJECT TITLE:** Thin-Wall Hollow Spheres From Slurries

**CRITICAL ISSUES:** Reduce thermal conductivity to values competitive with fibrous insulation, develop lower cost water-based sphere forming system, continue introducing aerosphere technology to industry.

**FUTURE PLANS:** Continue Phase IV program as proposed. That is to reduce conductivity further, reduce cost to expand applications into larger markets, and explore specific product applications with the technology transfer procedure that has been so successful to date.

**POTENTIAL PAYOFF:** Insulating materials without the ecological and health concerns of existing technologies.

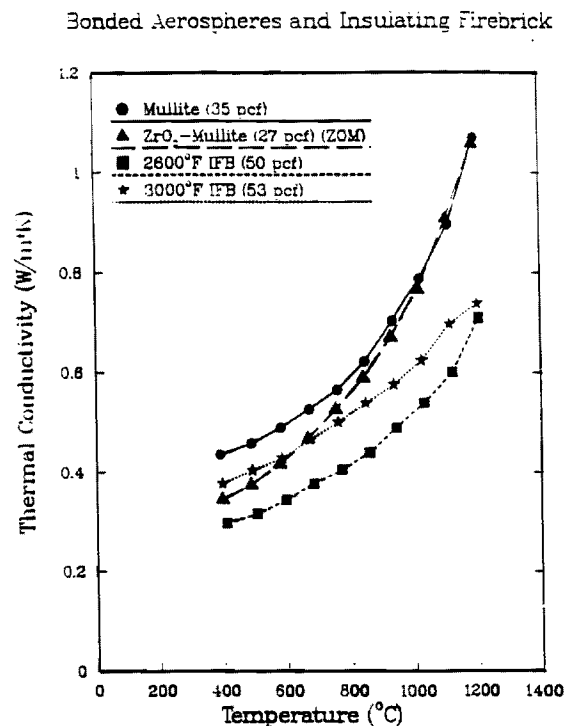
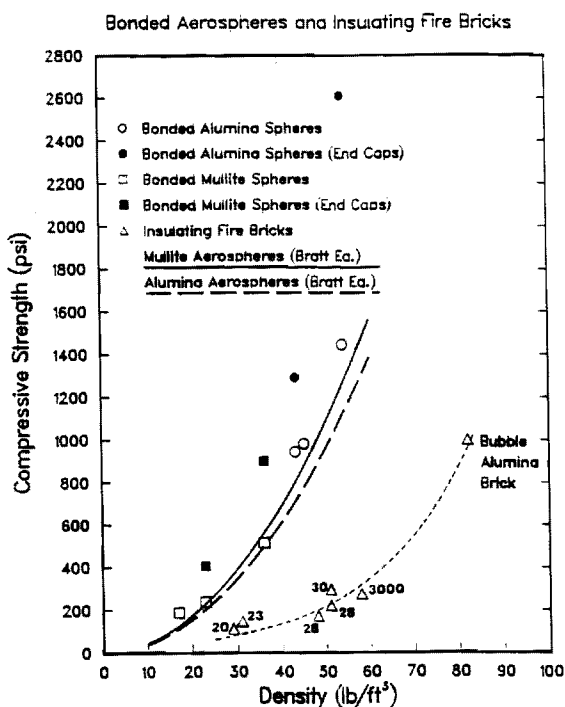
**FUNDING HISTORY:** FY 89                      FY 90                      FY 91  
Amt \$266K                      Amt \$285K                      Amt \$264K

Cum. Total to Date \$1464K (Includes Phases I-IV)

**OTHER SOURCES:** FY90 \$194K (Includes Ga Tech and Industry)

**ESTIMATED ENERGY SAVINGS:** Insulation now used in markets available to potential aerosphere products for applications above 2300F are estimated to save approximately 0.1 quads.

**HIGH SPECIFIC STRENGTH COUPLED WITH LOW THERMAL CONDUCTIVITY**  
**PROVIDES UNIQUE PROPERTIES FOR AEROSPHERE INSULATION**



# List of Investigators Participating in Project

Project: Thin-Wall Hollow Spheres from Slurries  
J.K. Cochran

Reporting Period: 1 October, 1990 through 30 September, 1991

Name	Type of Position	Planned Project Time (days/week)	Support	Approximate Time (days/week)
J.K. Cochran	Project Dir.	2	GT-DOE	(40%)
T.J. Hwang	Post Doctoral	5	DOE	5
J.H. Chung	Student (PhD)	2-3	DOE	2.5
P.R. Chu*	Student (PhD)	2-3	DOE	2.5
C. Moore*	Student (MS)	2-3	DOE	2.5 (9 mo.)
T. Ford*	Student (MS)		DOE	2.5 (9 mo.)
R. Clancy*	Student (MS)	2-3	DOE	2.5
G. Carlson	Student (MS)	2-3	GT	2.5
T. Ozell*	Student (MS)		NA	(Special Problem)
A. Jensen	Student (MS)	2-3	DOE	2.5 (6 mo.)
L. Touryan	Student (MS)	2-3	GT	2.5

\* Completed Thesis and Graduated.

E 177  
#17

## **THIN-WALL HOLLOW SPHERES FROM SLURRIES**

*A.T. Chapman, J.K. Cochran  
M.K. Adicks, G.E. Carlson, P.R. Chu, J.H. Chung,  
R.B. Clancy, T.R. Ford, S.D. Furlong, T.J. Hwang,  
C.M. Moore, M.J. Shapiro*

**Materials Engineering, Georgia Institute of Technology**

Poster Presentation for

The Annual Review Meeting  
Advanced Industrial Concepts Materials Program  
Department of Energy  
Albuquerque, NM  
June 10 and 11, 1991

**Quarterly Project Status Report  
for Period Ending  
June 30, 1991**

## **ABSTRACT**

**An ongoing program at Georgia Tech has successfully demonstrated the feasibility of producing monosize hollow spheres of many ceramic compositions on a production basis. The properties of the spheres, i.e. mechanical strength and thermal conductivity, have been documented and mathematical modeling of the sphere forming process has been successful. The present research effort has three main thrusts: 1) reduce the thermal conductivity of the spheres, especially at elevated temperatures, by incorporating opacifiers (for enhanced radiation scattering) in the sphere walls, 2) convert the liquid slurries used to form spheres from the present organic-based to an aqueous-based system and 3) disseminate information about sphere technology and properties to U.S. industry and support development of commercial products.**

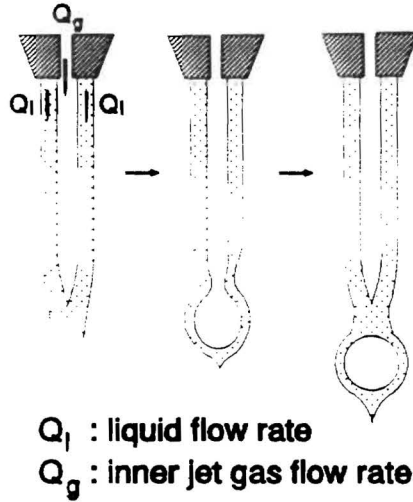
- As part of this effort, an original, more comprehensive sphere formation model based on fluid mechanical forces has been derived and validated as shown below.**
- Major redirection of property characterization toward understanding bonded hollow sphere closed cell foams has shown closed cell foams to be stronger than would have been predicted from individual spheres. This increased strength for foams caused reinvestigation of finite element analysis of hollow sphere geometries under different loading conditions to model the transition from single sphere compressive loading to the multiple point loading experienced in bonded foams.**
- Thermal conductivities of bonded sphere foams have demonstrated similar values to those of loose spheres for mullite foams but resulted in large increases in bonded alumina foams. Opacification efforts to reduce conductivities are continuing in the bonded foams but effects are not as clearly documented as for loose spheres.**
- Technology transfer in the form of industrial visits under the direction of Dr. Carl Vander Linden resulted in 27 onsite visits and development of new application areas; furnace linings, radiant burner tiles, and hollow metal sphere foam core structures.**



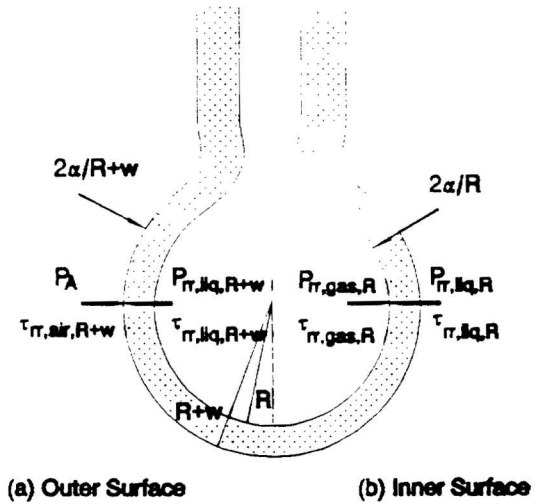
## MODEL FOR HOLLOW SPHERE FORMATION

**Objective:** To understand the aerosphere formation mechanism and therefore predict and control aerosphere formation frequency, aerosphere size, and density.

**Observation:** Aerospheres produced from a coaxial nozzle at high liquid flow rates are formed as shown below. Liquid exits the nozzle in a nearly cylindrical form and closes at a distance below nozzle. The inner jet gas flow provides inflation pressure to form a sphere at the closed end.



**Aerosphere Formation at High Liquid Flow Rates**



**Stress Balance on the Hollow Sphere**

**Considerations:** Only the hollow sphere stresses were considered since the cylinder remains approximately unchanged during the process. The stresses on the aerosphere surfaces are hydrostatic pressures, viscous stresses, and stresses caused by surface tension. The stress balance for the system is:

$$\Delta P + (P_{liq,R+w} - P_{liq,R}) + (\tau_{rr}|_{liq,R} - \tau_{rr}|_{liq,R+w}) = 2\alpha \left( \frac{1}{R} + \frac{1}{R+w} \right)$$

$\alpha$  : liquid surface tension  
 $\Delta P$  : pressure difference across the spherical shell  
 $P_A$  :  $= P_{air,R+w}$   
 $P_{air,R+w}$  : hydrostatic pressure of atmospherical air  
 $P_{liq,R+w}$  : hydrostatic pressure of liquid at outer surface of sphere  
 $P_{liq,R}$  : hydrostatic pressure of liquid at inner surface of sphere

$P_{gas,R}$  : hydrostatic pressure of gas inside the sphere  
 $\tau_{rr}|_{air,R+w}$  : viscous stress due to atmospherical air  
 $\tau_{rr}|_{liq,R+w}$  : viscous stress due to liquid at outer surface of sphere  
 $\tau_{rr}|_{liq,R}$  : viscous stress due to liquid at inner surface of sphere  
 $\tau_{rr}|_{gas,R}$  : viscous stress due to gas inside the sphere

**Model:** By solving the stress balance equation, a model equation is obtained:

$$\Delta P + \frac{\rho Q_g^2}{32\pi^2 R^4} \left[ 1 - \left( \frac{R}{R+w} \right)^4 \right] - \frac{4K(2\sqrt{3})^{n-1}}{n} \left( \frac{Q_g}{4\pi R^3} \right)^n \left[ 1 - \left( \frac{R}{R+w} \right)^{3n} \right] = \frac{2\alpha}{R} \left( 1 + \frac{R}{R+w} \right)$$

R : instantaneous inner radius of the hollow sphere

w : spherical shell thickness

$Q_g$  : inner jet gas flow rate

$Q_l$  : liquid flow rate

$\rho$  : liquid density

$\alpha$  : liquid surface tension

$K, n$  : characteristic constants for a power law fluid

for newtonian fluids

$K = \mu$ , viscosity constant

$n = 1$

The model equation describes the relation between the pressure inside the sphere ( $\Delta P$ ) and sphere size (R).

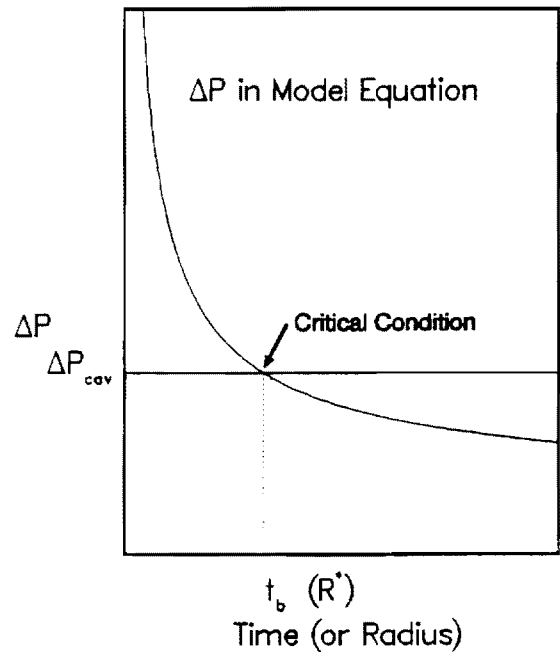
**Critical Pressure:** Frequency of sphere formation can be calculated from the time required to reach critical pressure. When pressure inside sphere becomes equal to the pressure inside the cylinder,  $\Delta P_{cav}$  (critical pressure), the sphere stops growing, closes, and the cycle begins again.

$$\Delta P_{cav} = \alpha \left( \frac{1}{R_o} + \frac{1}{R_o + \delta} \right)$$

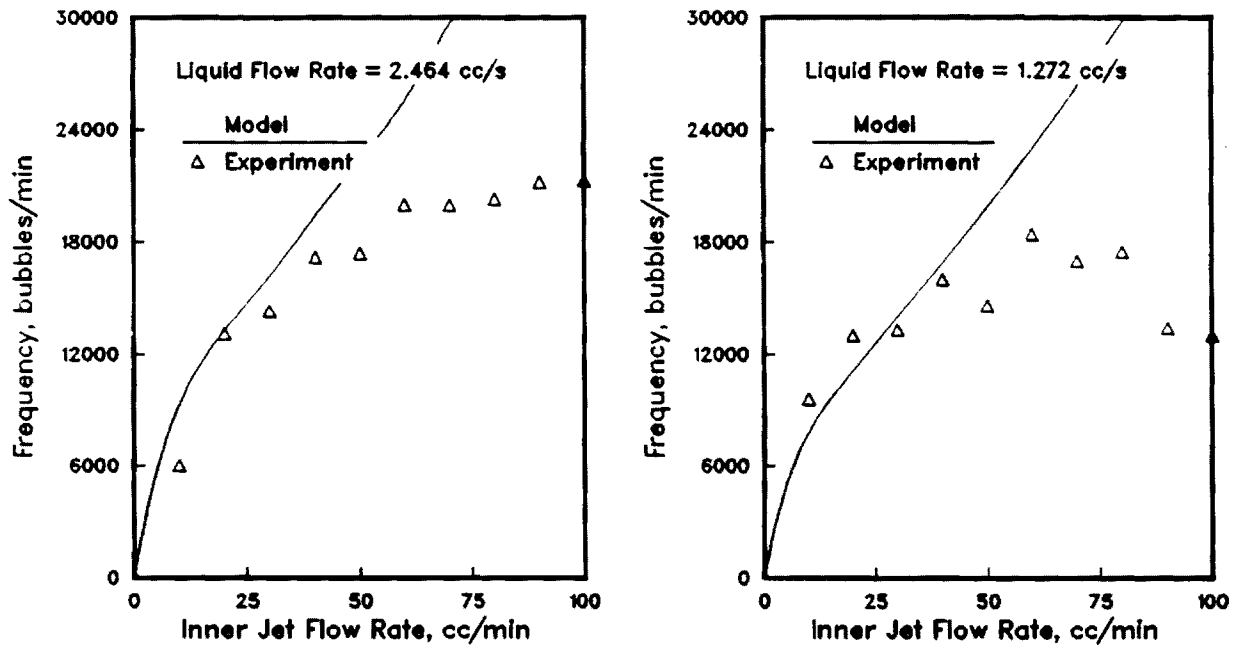
The corresponding inner radius of the sphere at the critical condition,  $R^*$ , can be used to calculate the sphere formation time period and frequency:

$$t_b = \frac{\frac{4}{3}\pi R^{*3}}{Q_g}$$

$$f = \frac{1}{t_b} = \frac{Q_g}{\frac{4}{3}\pi R^{*3}}$$



**Comparison between Model Predictions and Experimental Results:** The model predictions agree with experimental results very well at low inner jet gas flow rate,  $Q_g$ .



**Comparisons between Model Calculations and Experimental Frequencies**

**Deviations at High Inner Jet Flow Rates:** Deviations between model prediction and experimental data may be due to,

1. Possible deviation of sphere formation mechanism from proposed sphere formation mechanism.
2. Improper rheological constitutive relation which should be incorporated in the model.

\* S.Middleman, Fundamentals of Polymer Processing, McGraw-Hill, Inc. New York 1977.

## HOLLOW SPHERE STRENGTH - FINITE ELEMENT ANALYSIS

Sphere strength under uniaxial two point loading for a hollow ceramic sphere being modeled. Finite element analysis has reached the stage where a parameter relationship has been obtained. The relationship predicts that sphere strength is a square function of aspect ratio, (t/r).

$$\sigma_s = C \sigma_o \cdot (t/r)^2$$

$\sigma_s$  :  $\frac{F_c}{\pi r^2}$  (sphere strength)

$\sigma_o$  : Tensile Strength of Wall Material

$F_c$  : Compressive Force at Failure

t : Wall Thickness

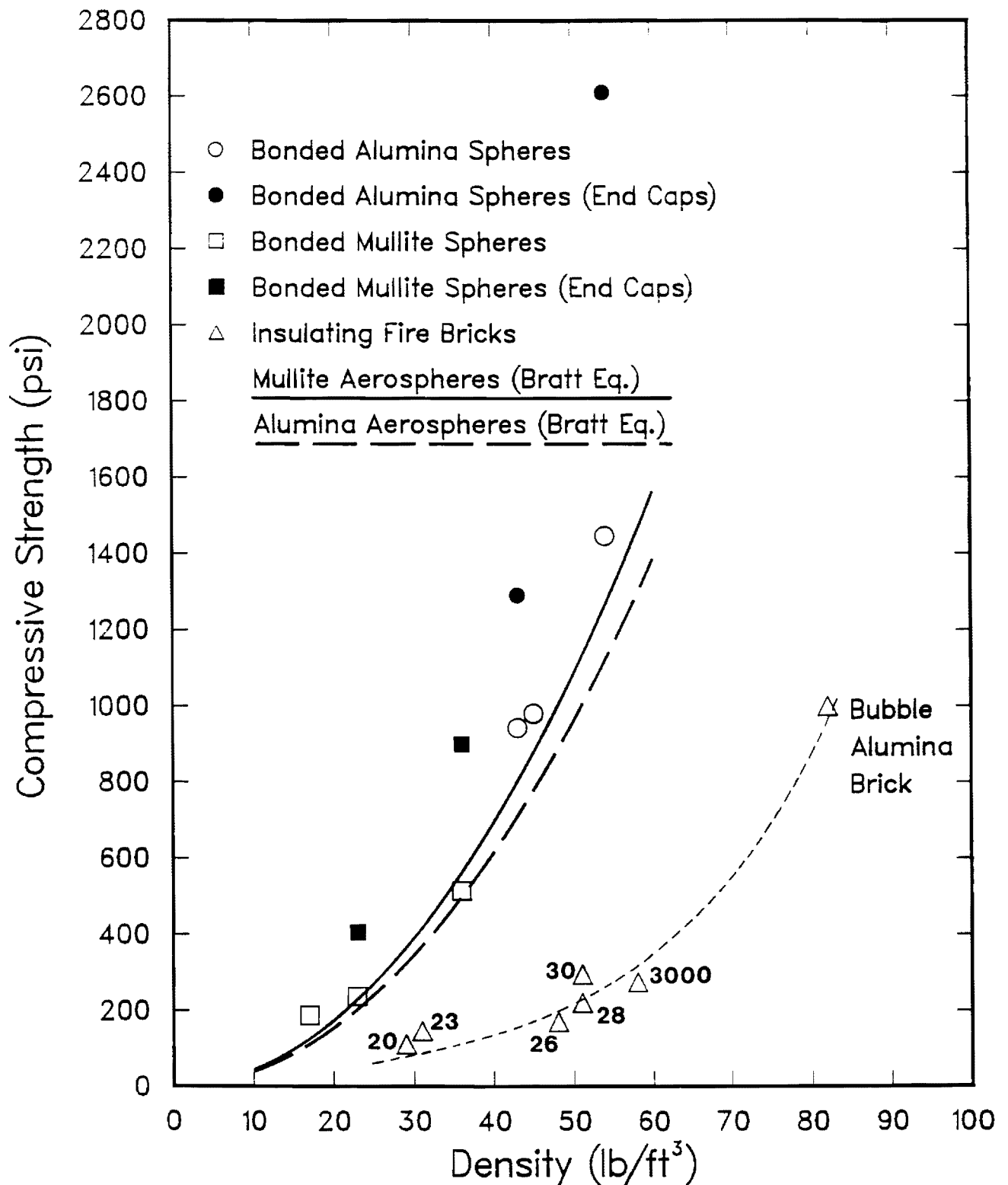
C : Constant

r : Radius

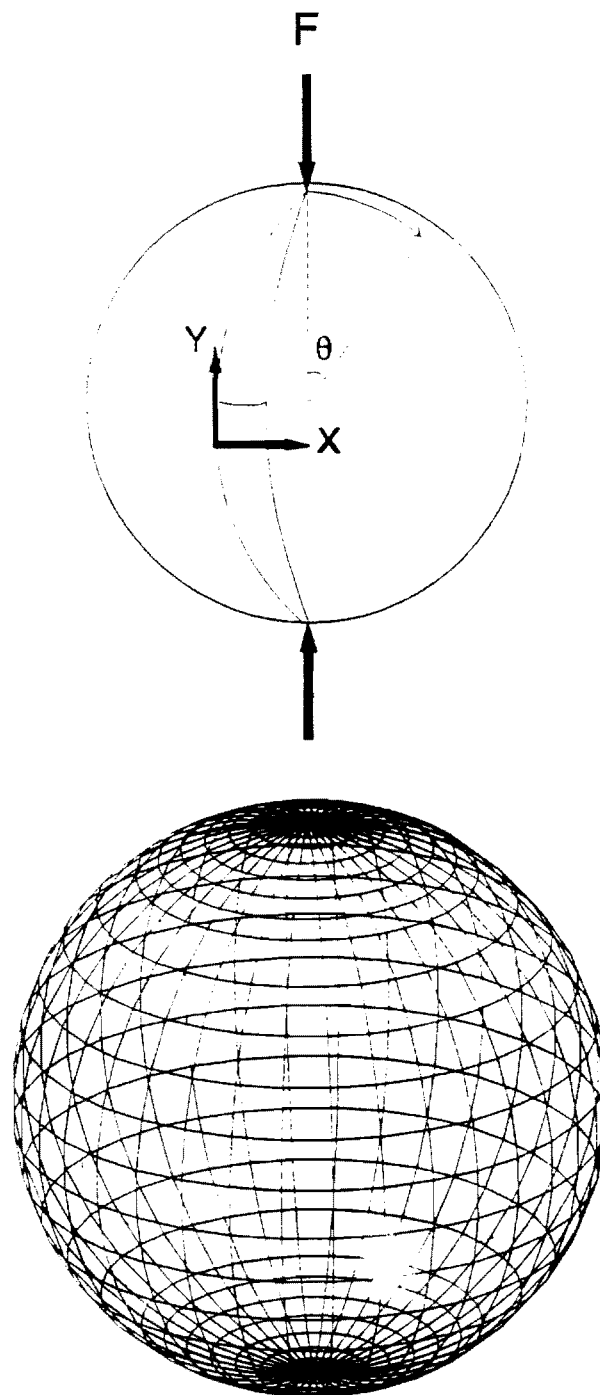
This result is in good agreement with the empirical result except the constant, C approximately 2.6 times higher than for the empirical relationship. Highlights of modelling include:

- (1) A finite element spherical shell mesh was generated for stress analysis.
- (2) Forces, bending moments, displacements, and stresses on a sphere were analyzed various aspect ratios (from 1/200 to 3/20).
- (3) From the finite element analysis, failure takes place near the loading point due to a tensile stress. Note that this is in contradiction to equatorial failure mode previously suggested by Bratt et al. Failure near the loading point has been observed experimentally.
- (4) Finite element modeling of compressive strengths of hollow ceramic spheres and extrapolating the results to predict the compressive behavior of a bonded sphere foam is in the final stage. Note that because failure is near the point of load distributing the load over 6-8 points, as is the case for hollow sphere foams bonded at points of contact, should increase the strength of spheres in the foam compared to the strength of uniaxially loaded spheres. Strengths of hollow sphere foams have been measured to be three to four times greater than for individual spheres which agrees with this hypothesis.

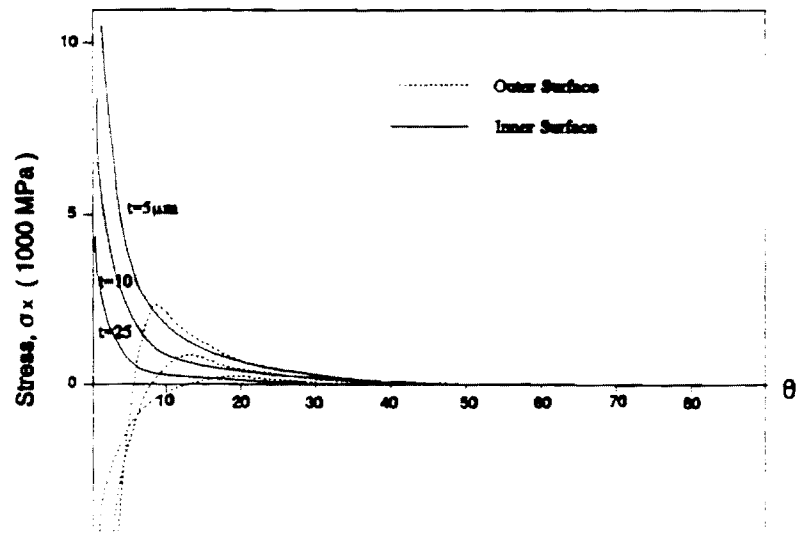
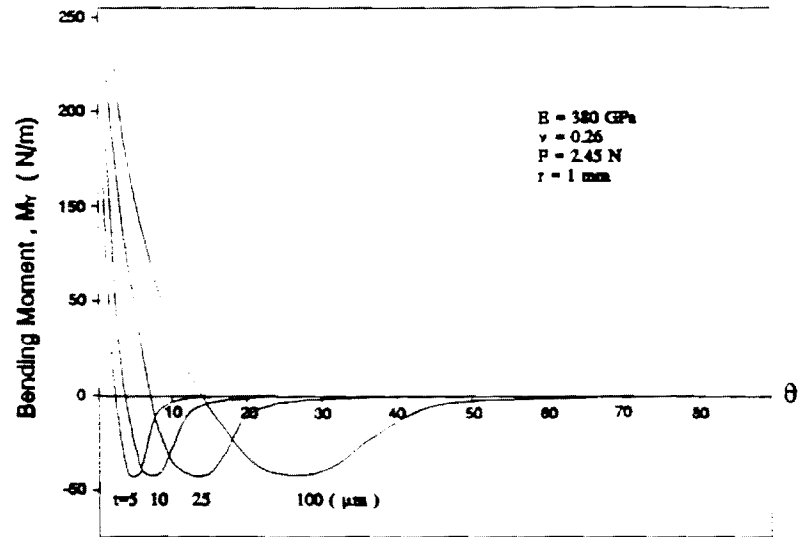
## Bonded Aerospheres and Insulating Fire Bricks



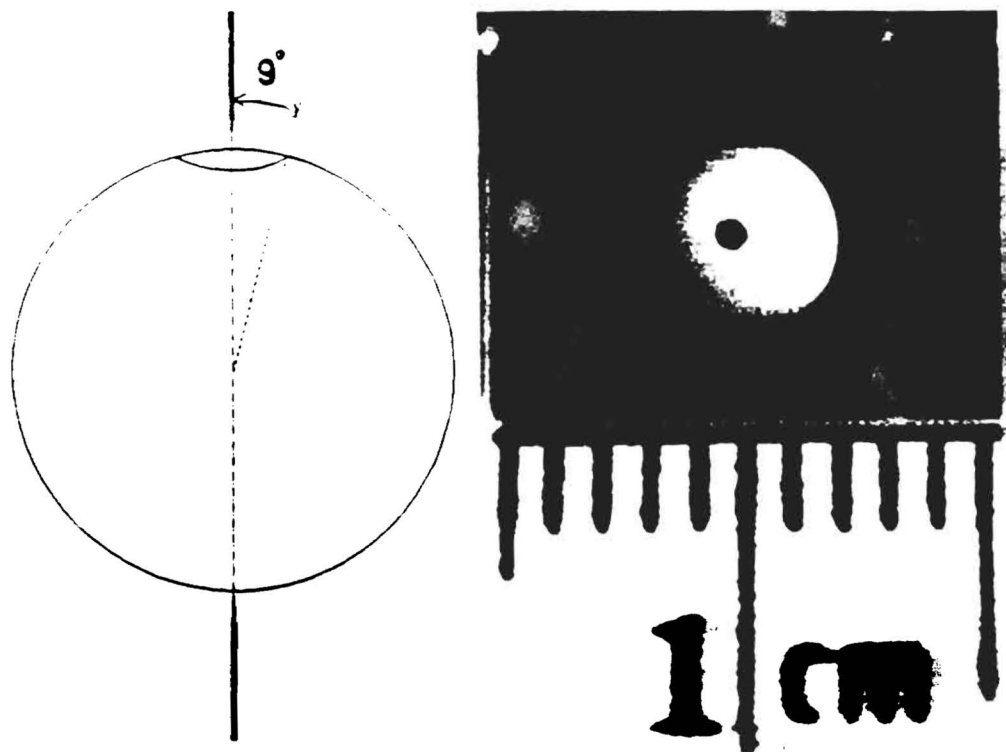
## Finite Element Coordinate System and Mesh



## Bending Moment and Stress vs $\theta$

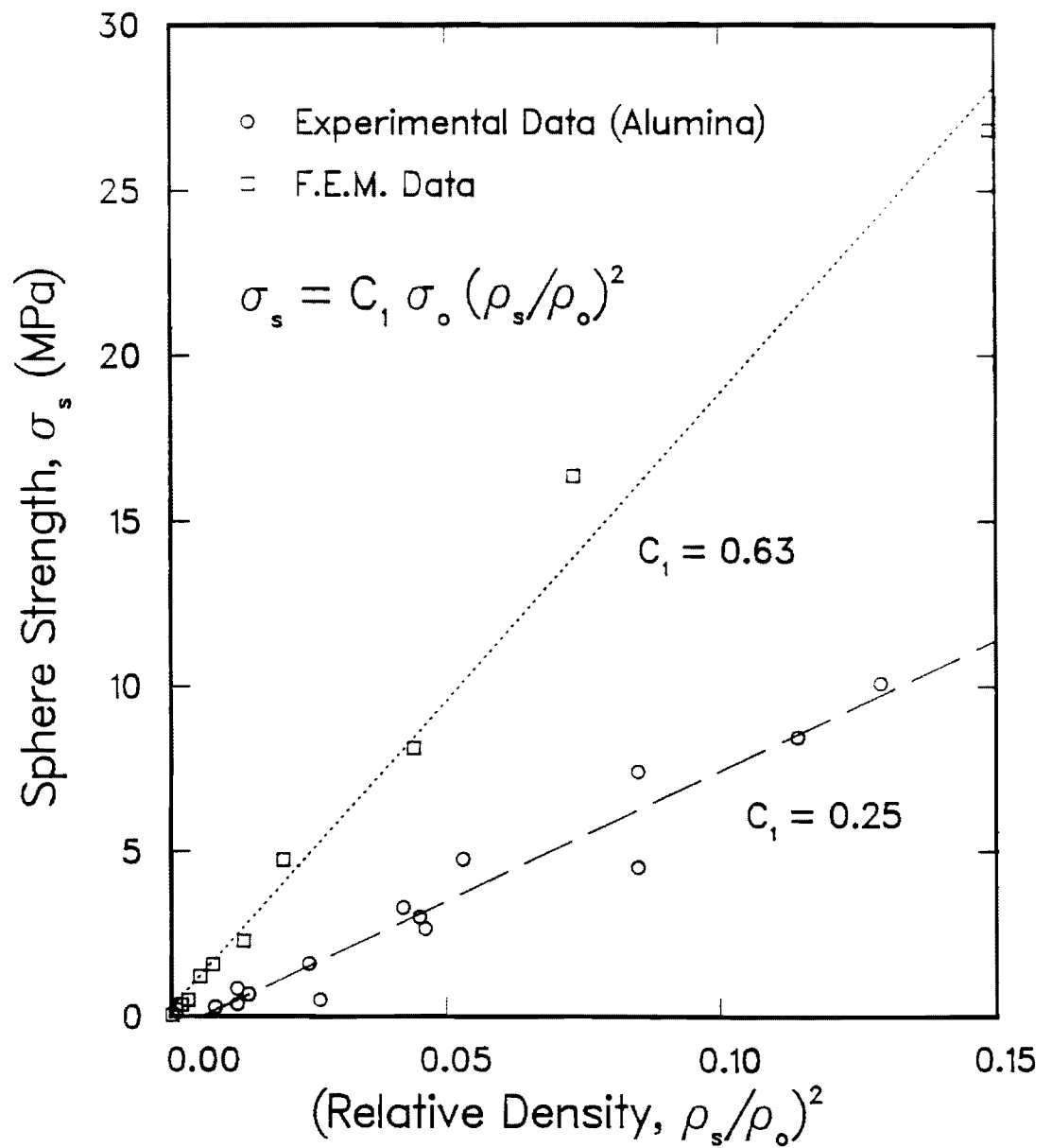


## Fracture 9° From Load Point





## FEM Failure at Maximum Bending Moment



## THERMAL CONDUCTIVITY OF BONDED SHAPES

Mullite, alumina, and mullite-zirconia Aerospheres were bonded to form monolithic closed cell foams with low density and high strength. Thermal conductivity of these foams are compared to loose spheres of like composition in Figures A, B and C. The high volume of trapped gas within the spheres disrupts conduction heat transfer and reduces low temperature (below 800°C) conductivity. However, at elevated temperatures the radiative transparency of the sphere walls significantly increases the thermal conductivity. Zirconia particles acted as an opacifying or scattering phase and reduced the high-temperature thermal conductivity in the two-phase, mullite-zirconia, spheres.

The conductivity of hollow spheres bonded at the points of contact should mimic parallel plate conduction at low temperatures (350°C) and can be modelled from the standard parallel plate equation:

$$k_m = k_p V_p + k_s V_s + k_b V_b$$

where  $k_m$  is the thermal conductivity of the sample,  $V_n$  is the volume fraction and  $k_n$  is the thermal conductivity of the pore phase (p), sphere phase (s) and bonding phase (b). The phase exhibiting the highest conductivity has the greatest influence on the thermal conductivity of the mixture.

To apply equation(1), the conductivity of loose spheres can be used to estimate the Aerosphere contribution,  $k_s$ , to the bonded samples. A bed of monosized spheres packs at a density of 63% and interconnects at several points of contact with neighboring spheres. The remaining 37% interstitial pore space is also continuous through the interstices in the packed bed. Therefore, equation (1) can be modified to calculate the thermal conductivity of the spheres,  $k_s$ ,

$$k_s = \frac{k_m - k_p V_p}{V_s} \quad (2)$$

where  $k_m$  is conductivity of the loose sphere bed (Figures A, B & C),  $k_p$  is for air (.041 W/m•K at 350°C), and  $V_p$  and  $V_s$  are 37% and 63%, respectively.

Figures A and B show small increases in the low temperature conductivity of bonded mullite and mullite-zirconia spheres compared to the respective loose spheres. The bonding phase increased density and conduction heat flow which raised the conductivity of the bonded samples. The increased density also provided additional radiation scattering which reduced high-temperature conductivity. The agreement between bonded and loose spheres at 350°C was predicted in the calculations shown in Table 1. The relatively low quantity of the mullite bonding phase was not predicted to increase the conductivity of the bonded sample significantly.

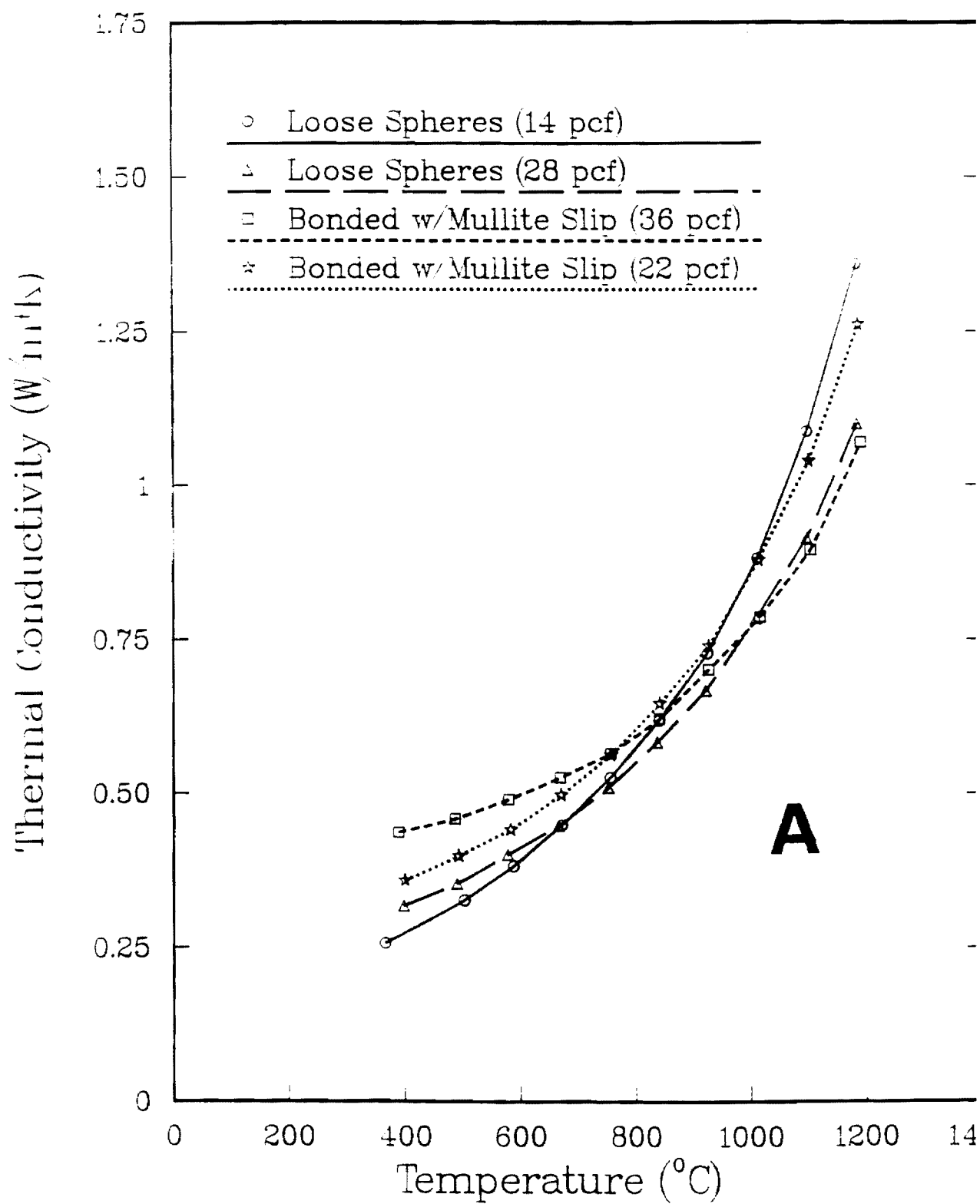
Bonded alumina spheres had a significantly higher conductivity than loose spheres, Figure C. As predicted, in Table 1, the high conductivity of the alumina bonding phase, dramatically, increased the thermal conductivity of the bonded sample. Obviously, a low conductivity bond phase is desirable for a bonded sphere refractory.

Figure D compares the thermal conductivity of bonded mullite and mullite-zirconia spheres with insulating firebrick. The bonded-spheres are competitive up to a mid-temperature range of 1000°C where conduction heat transfer is the dominant mode. Above this temperature, lack of radiation scattering allowed thermal conductivity to increase significantly. The bonded-spheres showed a reduction in density of 40% - 45% compared to firebrick.

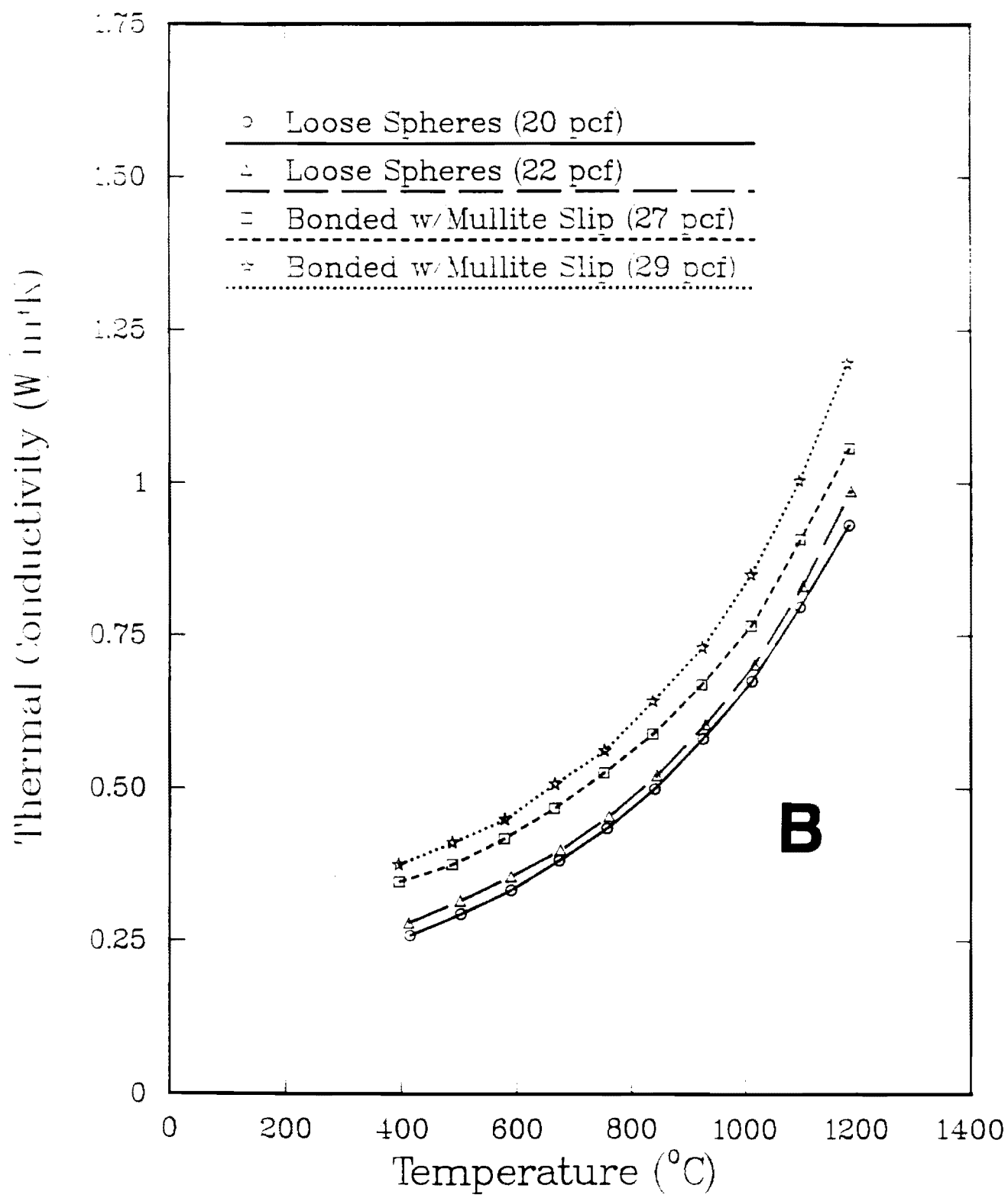
Table 1: Thermal Conductivity of Bonded and Loose Spheres at 350°C.

Sphere Material	Bond Material	$k_{sm}$ (Eq. 2)	$k_b$	$k_p$	$k_m$ (Eq. 1)	Data
Alumina	Alumina	0.733	20.92	0.0495	1.52	1.02
Mullite	Mullite	0.368	5.02	0.0495	0.499	0.37
Mull-Zr	Mullite	0.368	5.02	0.0495	0.499	0.35

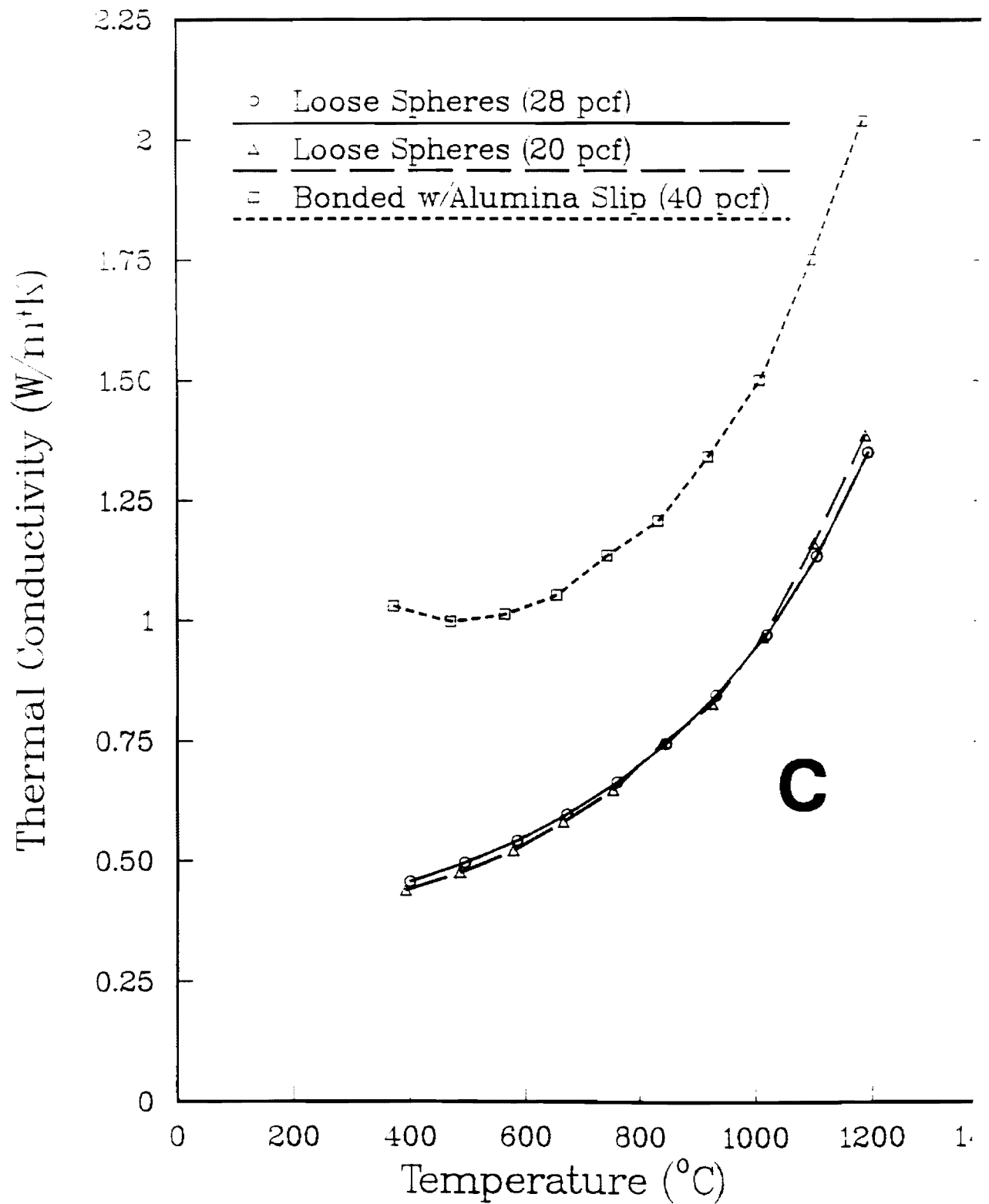
## Bonded vs Loose Mullite Spheres



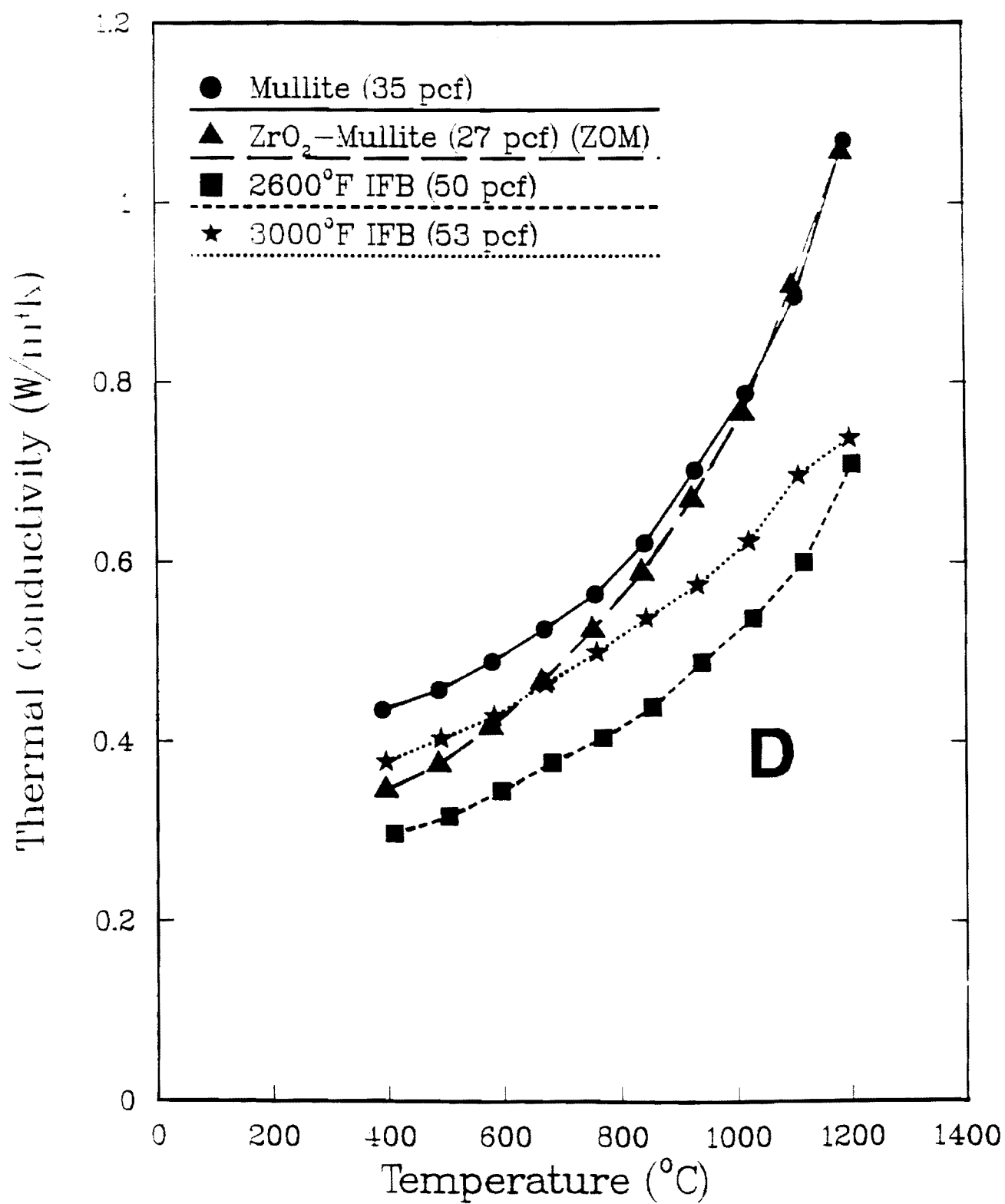
## Bonded vs Loose Mullite-Zirconia Spheres



## Bonded vs Loose Alumina Spheres



## Bonded Aerospheres and Insulating Firebrick



# **TECHNOLOGY TRANSFER**

## **ON SITE VISITS**

**8/1/90 - 6/1/91**

1. Alcoa (Three Visits)
2. Harbison-Walker Refractories
3. Refractories Institute
4. North American Refractories
5. Pittsburg-Corning Corporation
6. DOE-OIT
7. Naval Research Laboratories
8. Carborundum-Performance Refractories Div.
9. Quigley Company, Inc.
10. Bethlehem Steel Corporation
11. Resco Products, Inc.
12. Premier Refractories and Chemicals
13. Boeing Aircraft Corporation
14. Thermal Ceramics
15. Rohr Industries
16. Hi-Temp Insulation, Inc.
17. Naval Civil Engineering Laboratory
18. Allied Signal-Garrett Processing Div.
19. Pryor-Giggey Refractories
20. National Refractories
21. Suppression Engineering
22. NASA-Ames Research Center
23. DARPA-Materials Division



**INTERACTION - Y-12 PLANT**

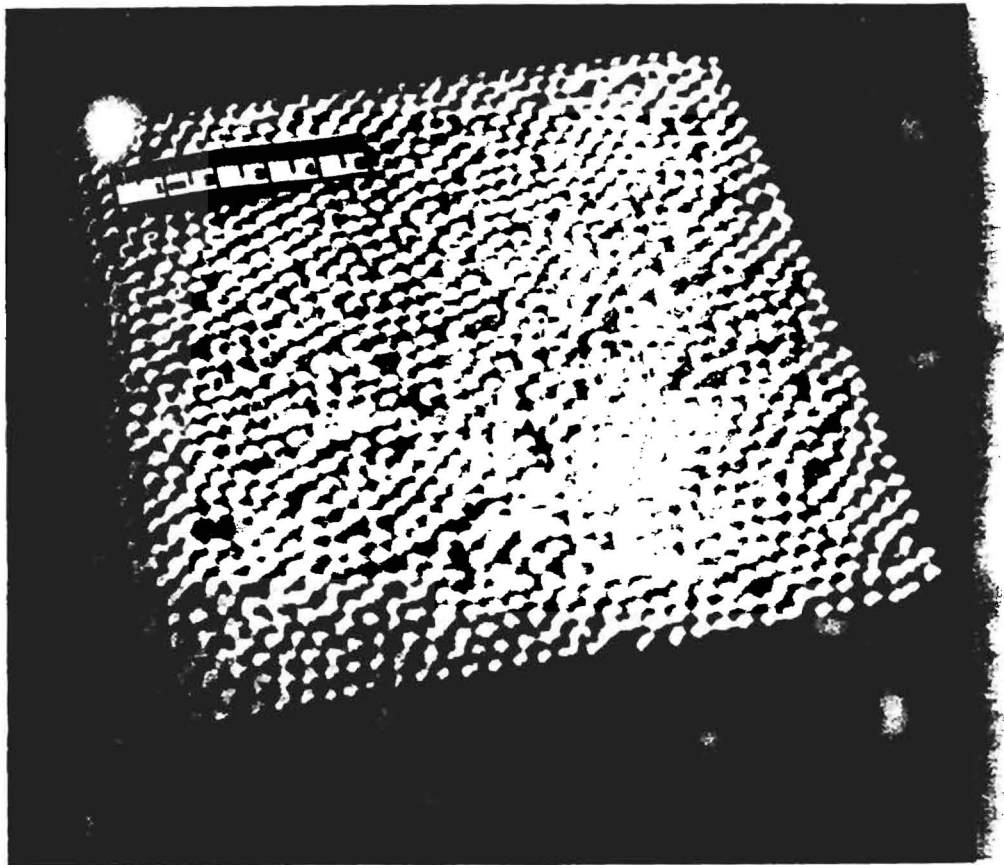
**Induction Furnace Insulation**

**Mullite Bonded Mullite - 30 pcf - 40 "dia x 4" thick**

**INTERACTION - GAS RESEARCH INSTITUTE**

**Radiant Gas Burner Tile**

**Mullite Bonded Mullite - 25 pcf**



## INTERACTION - ROHR INDUSTRIES

Hollow Sphere Metal Foam Cores

Nickel Spheres -  $\text{NiO} + \text{H}_2 \rightarrow \text{Ni} + \text{H}_2\text{O}$



## GRADUATE DEGREES FROM HOLLOW SPHERE PROJECT

### Ph.D. Degrees

1. T.J. Hwang, June 1989, "A Model for Viscosity of Organic Based Oxide Dispersions"
2. P.R. Chu, June 1991, "A Model for Coaxial Nozzle Formation of Hollow Spheres from Liquids"
3. J.H. Chung (Sept. 1991), "Compressive Mechanical Behavior of Thin Wall Ceramic Spheres and Sphere Cellular Monoliths"

### M.S. Degrees

1. M.J. Shapiro, March 1988, "Thermal Conductivity of Thin Wall Hollow Ceramic Spheres"
2. V. Munne, Sept. 1988, "Monolithic Structures Foamed from Phosphate Bonded Hollow Microspheres"
3. S.A. Rickles, March 1989, "Microstructural and Compressive Properties of Metal/Ceramic Syntactic Foam"
4. M.K. Adicks, March 1989, "Strength Characterization of Thin-Wall Hollow Ceramic Spheres From Slurries"
5. S.D. Furlong, Dec. 1990, "Reduction of Radiative Thermal Conductivity in Thin-Wall Hollow Ceramic Spheres Using Scattering Phases"
6. C.M. Moore, June 1991, "Organic Gels For Injection Molding of Powders"
7. T.R. Ford, June 1991, "Thermal Conductivity of Bonded Hollow Sphere Monoliths"
8. R. Clancy, (Sept. 1991), "Nickel and Nickel Alloy Hollow Spheres"
9. G.E. Carlson, (June 1992), "Thermal Conductivity of Zirconia-Mullite Hollow Spheres"

14

Continuation Preproposal for  
Advancing Hollow Sphere Technology

J. K. Cochran and A. T. Chapman  
School of Materials Engineering  
Georgia Tech  
Atlanta, Georgia 30332

1. Introduction

During the last four years, under DOE-ECUT and AIM support, a production process to form thin-wall, millimeter diameter, monosize spheres from virtually any powder, suitably dispersed in a liquid, has been developed. Many types of ceramic spheres have been fabricated using this process, and the thermal and mechanical properties of loose spheres and bonded monoliths have been measured. Commercialization of this unique low density material has been undertaken through visits and presentations to many segments of U.S. industry, and a pilot and production plant capable of producing prototype or large quantities of specific types of spheres and bonded shapes is in place. In the following sections of this document, the results and accomplishments of the ongoing development program are briefly reviewed. The continuing health risk associated with ceramic fiber and the prospects of this material facing severe regulation, as well as industry concerns with ceramic fiber, are documented. Lastly, a general plan for continuation of sphere development and commercialization programs for an additional year is outlined.

2. On-going Research Program.

During the last fifteen months, the major research effort has centered on reducing the thermal conductivity (T/C) of the spheres, especially at elevated temperatures, and reducing the cost and complexity of sphere formation by converting the powder dispersion from an organic to an aqueous-based system. Concurrently the dissemination of engineering and property information to U.S. industry has increased through visits and presentations to over 30 end-use companies with expressed interest in this technology. This activity has been very successful, and numerous samples are being evaluated and trials are underway at a number of industries.

Since the beginning of this program, the T/C of the spheres has been dramatically reduced through a variety of compositional and microstructural changes in the sphere wall. This has been possible because of the flexibility and versatility of the fabrication process. This decrease in T/C is graphically outlined in Figure 1. The conversion to a water-based system has not been as successful as the reduction in T/C. Spherical shaped particles have been produced using water soluble gels, although not with the same density or monosized characteristics as the organic-based spheres. A major effort in this area is ongoing.

### 3. Health Dangers of Ceramic Fiber

Ceramic fiber provides the best choice for high temperature insulation for furnace applications where minimizing heat loss is the dominant requirement for the insulation. However, the micron diameter fibers have been a suspect health risk in recent years, and presently the EPA is considering placing these materials in the same category as asbestos (See Occupation Safety and Health Reporter, Volume 20, Number 11, attached). In addition, many industries are looking for replacement insulating materials (see letter from Alcoa, dated July 30, 1990, also attached). In view of the current energy crisis brought on by the Middle East situation, as well as the probability some regulatory action restricting ceramic fiber is eminent, alternative high temperature insulating materials is a major need for U.S. Industry. This problem must be resolved if the U.S. is to remain competitive worldwide, and the thin-wall spheres are perhaps the most viable candidate to meet this need.

### 4. Proposed Future Work

The program at Georgia Tech is addressing the two major deterrents to the commercialization of this unique product, T/C and cost. While bonded sphere shapes match the T/C values available with conventional insulating fire brick (IFB), and interestingly are several times stronger than IFB's, the T/C of the spheres is still about twice that of ceramic fiber. We believe through the use of mixed compositions and microstructural control, we have a realistic chance to approach the T/C of ceramic fibers, without any of the accompanying health risks. We propose continuing the development of spheres with enhanced radiation scattering at high temperatures. The cost of the bonded sphere shape is significantly above that of intermediate temperature rated IFBs (1000-1400°C) but is very competitive with the bubble alumina brick that has a use temperature > 1600°C. We propose the continuing examination of process changes that will significantly reduce the cost of manufacturing spheres and bonded shapes.

Since the spheres provide some properties and/or compositions unavailable in existing products, we propose to select "niche" applications to exploit these benefits. This effort would be coordinated by Dr. Carl Vander Linden and include product development at Georgia Tech, production of prototype spheres at Ceramic Fillers, Inc. and actual performance testing by an end use industry. Examples of this activity might include the initial testing of basic MgO spheres or the use of high strength inert alumina spheres in the severe environment present in industrial incinerators.

During the course of this program some unique nonrefractory or insulation applications for the spheres, as well as alternate processing methods to produce light weight insulating materials, have surfaced. Three such cases are listed below where the feasibility of each has been experimentally demonstrated.

- A. Neon-filled spheres for displays
- B. Metal spheres for density reduction in closed cell metal foams
- C. Aqueous-based gel dispersions expanded by dissolution of CO<sub>2</sub> gas to form closed cell foams.

We propose a very limited effort in these areas (dependent on DOE interest) to assess the feasibility and justification for support of future development of these materials through DOE or other agencies.

Lastly, the present T/C equipment has an upper temperature limit of about 1200°C. In view of the emerging technologies requiring ever increasing processing temperatures, it is proposed to construct a T/C device which will measure T/C values to temperatures approaching 2000°C. This equipment will require no capital equipment funds as an existing RF generator at Georgia Tech will be employed to heat the central core of the test sample. The temperature will be monitored radially to provide comparative insulating behavior of the various sphere compositions and geometries.

## 5. Proposed Budget

A detailed budget breakdown will be provided as needed. The estimated cost for this program for the period of 1 July 91 through 30 June 1992 is \$250,000 plus an additional \$50,000 for the technology transfer activity.

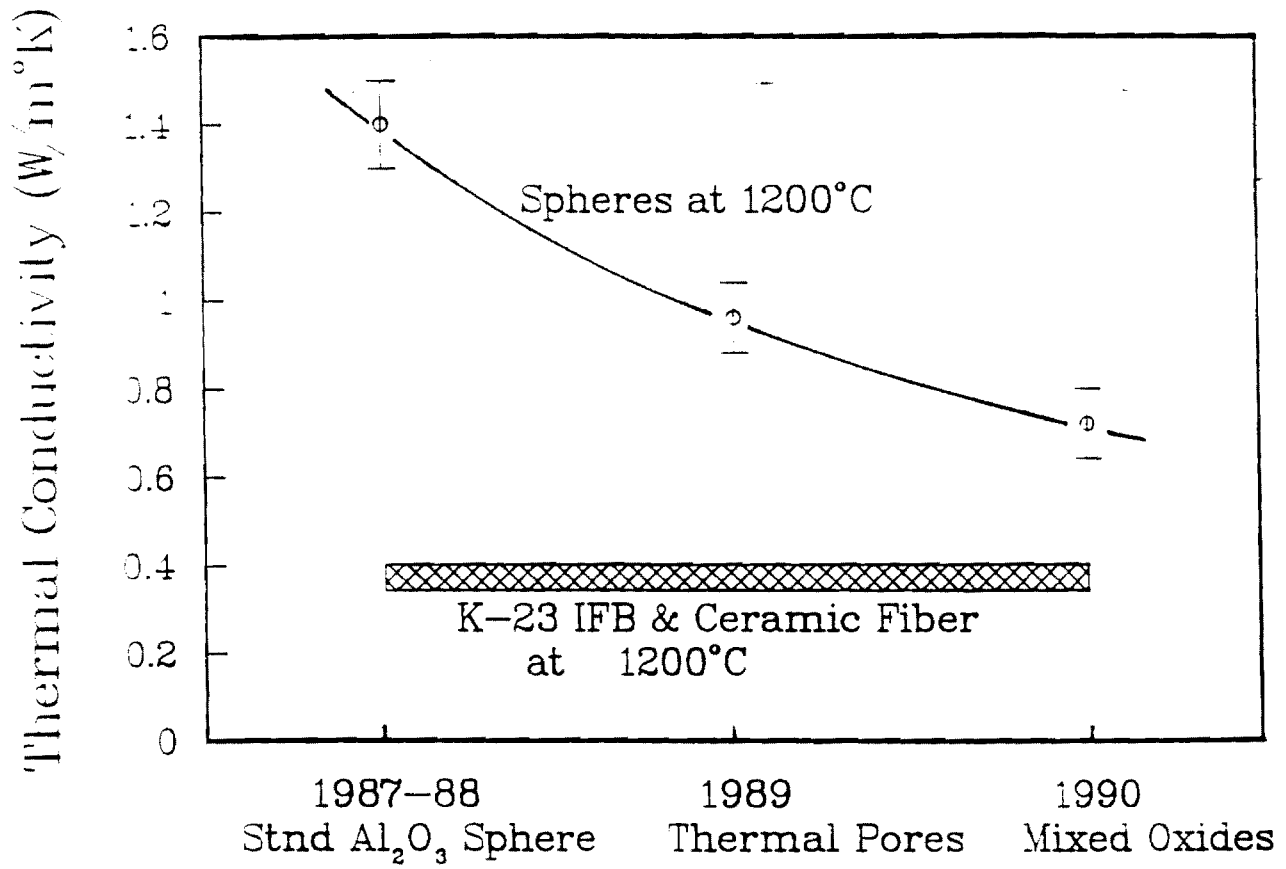


Figure 1. Reduction in Thermal Conductivity of Hollow Ceramic Spheres between 1987 through 1990.





# OCCUPATIONAL SAFETY & HEALTH REPORTER

*A weekly review of occupational safety and health developments*

Volume 20, Number 11

THE BUREAU OF NATIONAL AFFAIRS, INC.

August 15, 1990

## **Manmade Fibers**

### **REFRACTORY CERAMIC FIBERS ON TRACK TO RM3; EXPOSURE LEVELS SEEN AS GREATER THAN ASBESTOS**

After the Environmental Protection Agency's third risk management level one meeting on refractory ceramic fibers, agency officials July 30 reiterated an earlier decision to expedite their review and forward regulatory decisions on the substances to the highest level of risk management—an RM3 meeting.

Interim results from single and multiple dose inhalation oncongenicity studies with various refractory ceramic fibers have produced dose-related changes, EPA said. Three ongoing, industry-sponsored cancer studies were discussed at the June 21 RM1 meeting.

A "definitive assessment" from these studies is not yet available, according to the agency. But based on other studies and these early findings, agency officials concluded that RCFs are "at least as hazardous as asbestos, and may be more so," according to the public version of the June 21 RM1 meeting summary. The level of exposure to RCFs is greater than asbestos, according to agency documents.

EPA said it has one exposure survey from a processing plant that indicates "safe levels" of RCFs may not be found at most manufacturing sites. Currently, there is no permissible exposure limit under standards set by the Occupational Safety and Health Administration, the agency noted.

"[I]t can be qualitatively concluded that RCFs may pose a health risk to workers who install, repair, and replace RCF products," EPA said.

An OSHA spokesman said the agency has had informal discussions with EPA on RCFs but has not yet taken any formal action with respect to modifying MSDSs.

#### **RM3 Review**

RM3 meetings are chaired by Office of Toxic Substances Director Charles Elkins. Decisions to control substances under Section 6 of the Toxic Substances Control Act are made at the meetings. EPA can take a range of actions, including a ban, if the agency finds a substance poses an unreasonable risk. To date, there has been only one RM3 meeting; the topic was lead solder, agency officials said (see related news story in this issue).

The RM3 review would be independent of any TSCA Section 4(f) activities, EPA said. That section of the chemical control law authorizes EPA to take action, if the agency receives data that show a substance may cause cancer. EPA also must conclude there is a significant risk of serious harm to human beings.

"There is enough evidence to support bringing the case to Assistant Administrator [Linda Fisher] for a 4(f) decision," according to the May 10 meeting summary.

Refractory ceramic fibers (RCFs) may pose a significant risk to human health via inhalation, EPA said. The concern is primarily for "non-continuous fibers" because they are

more respirable than continuous RCFs, the agency said. Non-continuous fibers account for 86 percent of the RCF market, according to the agency.

EPA said there are three chemical forms of non-continuous fibers: ceramic aluminum silicate, also known as kaolin; alumina oxide; and zirconia oxide.

A second RM1 meeting was held July 5 to review materials on RCFs for a briefing for the office director. The RM1 panel also discussed an outline of factors to consider when making a TSCA Section 4(f) decision on RCFs, according to the meeting summary.

#### **Similar Effects**

Findings from health effects tests indicated that RCFs may have caused tumors in test animals exposed to the substance through inhalation, EPA said. These effects are similar to those caused by chrysotile asbestos, according to the May 10 RM1 meeting summary.

In addition to possible action under sections 6 and 4(f) of the chemical control law, EPA initiated several other actions, according to the meeting summaries. EPA will:

- ▶ Work with OSHA and industry to modify manufacturers' material safety data sheets to stipulate RCFs be handled in a manner similar to asbestos;
- ▶ Analyze the availability of alternatives;
- ▶ Contact the six known makers of RCFs to explain EPA's concern, followed by formal letters requesting exposure data; and
- ▶ List non-continuous RCFs on the Risk Reduction Candidate List.

ALUMINUM COMPANY OF AMERICA  
ALCOA BUILDING  
PITTSBURGH, PENNSYLVANIA 15219



1990 July 30

The Refractories Institute  
Suite 1517  
301 5th Avenue Building  
Pittsburgh, PA 15222

Attention: Mr. C. G. Marvin, Vice President

RE: REFRACTORY CERAMIC FIBER (RCF)

Dear Mr. Marvin:

Along with other companies, we at Alcoa are concerned about the potential problems associated with RCF. One of our objectives is to find out about safe, alternative products.

To that end, we have come to you for some help.

Specifically, please tell us:

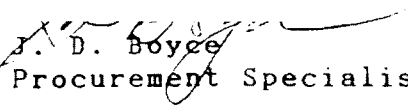
- what, if any, replacement products are now available (to us, mineral wool is not an acceptable replacement)
- what replacement products are close to commercialization with their timing
- what products are feasible as replacement for RCF.

If you have any detailed information and/or literature, please send it along with your reply. We know you share our concern and hope you will be prompt in your answer.

We hope to hear from you by August 31.

Thanks for your assistance.

Sincerely,

  
J. D. Boyce  
Procurement Specialist - Refractories

JDB/ck

cc: R. M. James - 6

## THIN-WALL HOLLOW CERAMIC SPHERES FROM SLURRIES

Statement of Work  
(7-1-91 to 6-30-92)

Phase IV (b) Thermal Insulation, Water Processing, Technology Transfer

### Task 1.0 - Thermal Insulation - Bonded Shapes

The objective of this effort is to reduce thermal conductivity to values competitive with ceramic fibers. However, rather than concentrating only on loose beds of spheres, a major portion of this task will be to optimize insulative capability of bonded shapes. This means that the bonding phase may be engineered for thermal resistance in addition to engineering the sphere wall. By having a two phase structure composed of spheres and the bonding phase, either the parallel plate or the Maxwell-Rayleigh model will apply for conductivity of this composite structure. Thus Task 1.0 will be subdivided into three areas-

Task 1.1 - Modeling - By applying the parallel plate and Maxwell-Rayleigh models, predictions of low temperature conductivities will be made to help make initial selection of bonding phase materials.

Task 1.2 - Improve Sphere Thermal Resistance - Several approaches will be used to improve individual hollow sphere resistance. Initially thermal pores will be combined with zirconia-opacified-mullite sphere walls to try to increase radiation scattering to even higher levels than now present. In addition, a search will be continued for new opacifying phases to be added to either mullite or alumina as the base sphere composition.

Task 1.3 - Bonded Monolith Thermal Resistance - Utilizing the improved spheres from Task 1.2 and the selected bonding phases from Task 1.1, the hollow spheres will be bonded with hopefully bonding phases of lower thermal conductivity to provide monoliths of increased thermal resistance.

### Task 2.0 - Mechanical Property Modeling and Measurement

Bonded hollow sphere foams have been shown to be considerably stronger than open cell foams of the same density and material. This has resulted because the spheres appear to be four to five times stronger in a bonded shape compared to loose spheres. Therefore, finite element modeling has recently been instituted and will be continued to calculate stresses on hollow spheres under two point uniaxial load and six point multiaxial load. This is a simulation of individual sphere loading compared to the multipoint loading in bonded foam structures. Hopefully, a parametric study will allow a simple predictive model for monoliths based on sphere wall strength and relative density.

### Task 3.0 - Water Based Processing

In the last year, the major effort to harden water based hollow spheres centered on use of thermally reversible polysaccharide food gels. These gels were successful in producing hollow sphere with bulk densities of 45-50lb/ft<sup>3</sup>. Unfortunately, it appears that producing hollow spheres of lower densities will not be achievable with this system. Therefore, two other approaches will be instituted.

Task 3.1 - Reactive Gas Gelling of Sols Combined with Thixotropic Additives - Original water based slurries were formulated with thixotropic additives producing high viscosities at low shear stress. This had sufficient strength to survive short free falls but did not allow spheroidization of the hollow shells. Longer falls required for well formed

spheres would collapse the shells. Recently, gelling of silica sols with ammonia gas has been partially successful in gelling water based systems. Although it sounds complex, neither process interferes with the other, so the two will be combined in an attempt to provide sufficient strength for sphere collection.

Task 3.2 - UV Curable Polymerization - Ultraviolet curable organic slurry systems are in common use today in a variety of industries to rapidly harden films and coating. The curing times are fast enough to be used for hardening hollow spheres in free flight. A search is underway for a water soluble UV curable polymer with rapid curing times and low viscosity. If this system can be located, much of the water based effort will be in this area and Georgia Tech will purchase the necessary UV radiation source if required.

#### Task 4.0 - Technology Transfer

Technology transfer will be continued during the next year but in a reduced manner compared to the last two years. With a reduced budget, funds are insufficient for an outside consultant and travel as required for onsite industrial presentations. However, many industrial interactions have been established by the highly successful industrial visits of the last two years. Continuing interaction will take the form of supplying spheres and bonded shapes for applications testing plus development of new compositions where required.

# BUDGET

Phase IV(b) July 1, 1991 - June 31, 1992

	<u>EFT</u>	<u>DOE</u>	<u>GA Tech</u>
1. Direct Salaries and Wages			
A. Program Director, J.K. Cochran Water Based Systems, Technology, Transfer	0.40	31,996	
B. Post Doctoral Associate, T.J. Huang, Slurry Rheology, Slurry Disposition	0.80	24,000	
C. Post Doctoral Associate, P.R. Chu Rapid Setting Water Systems	1.00	24,000	
D. M.S. Students, G. Carlson Rapid Setting Water Systems	0.50	12,000	
E. M.S. Student - Thermal Conductivity			12,000
-----			
Subtotal		91,996	12,000
2. Fringe Benefits - 26.3% of A,B, &C		21,039	
3. Supplies -		4,000	
4. Reports & Publications -		2,000	
5. Travel		4,000	
-----			
Total Direct Cost		123,035	12,000
Overhead 62.5%		76,897	7,500
Equipment			15,000
-----			
TOTAL ESTIMATED COSTS		199,932	34,500



U. S. DEPARTMENT OF ENERGY  
ANNOUNCEMENT AND DISTRIBUTION OF DEPARTMENT OF ENERGY (DOE)  
SCIENTIFIC AND TECHNICAL INFORMATION (STI)

(When submitting form, input should be typed, not handwritten.)

E-18-674 G

**PART I Information Product Identification**

**A. Identifiers**

**1. Product/Report Nos.**

E-18-674

**2. Award/Contract Nos.**

DE-FC05-89CE90052

**3. Title**

THIN-WALL HOLLOW CERAMIC SPHERES FROM SLURRIES - PHASE IV: THERMAL INSULATION

(Grantees and Awardees skip to Part 1.B.)

**4. Funding Office(s)**

**5. B&R Code(s)**

**6. Project ID(s)**

**7. CRADA Nos.**

**8. UC/C Category(ies)**

**9. Information Product Filename**

**B. Information Product Description**

☒ **1. Report**

a. Type ☐ Quarterly ☐ Semiannual ☐ Annual ☒ Final ☐ Topical

☐ Other (Specify) \_\_\_\_\_

b. Dates covered (mm/dd/yyyy) 09 / 01 / 89 thru 10 / 31 / 92

☐ **2. Conference**

a. Type ☐ Conference paper ☐ Published proceedings ☐ Other (Specify) \_\_\_\_\_

b. Conference title (No abbreviations) \_\_\_\_\_

c. Conference location (city/state/country) \_\_\_\_\_

d. Conference dates (mm/dd/yyyy) \_\_\_\_ / \_\_\_\_ / \_\_\_\_ thru \_\_\_\_ / \_\_\_\_ / \_\_\_\_

e. Conference sponsor(s) \_\_\_\_\_

☐ **3. Software** (Note: Additional forms are required. Follow instructions provided with this form.)

☐ **4. Other** (Provide complete description.) \_\_\_\_\_

(DOE/DOE Contractors complete; Grantees and Awardees complete as instructed by contracting officer)

**A. Recommendations** (Mark at least one)☒ 1. Unlimited Announcement (Available to U.S. and non-U.S. public)☐ 2. Unlimited Announcement/U.S. Dissemination Only☐ 3. Classified (Standard announcement)☐ 4. OpenNet

a. Non-NTIS Availability (Required if not available from NTIS)

(1) Accession Number \_\_\_\_\_ (2) Document Location \_\_\_\_\_

b. Field Office Acronym \_\_\_\_\_

c. Declassification date (mm/dd/yyyy) \_\_\_\_/\_\_\_\_/\_\_\_\_ Sanitized \_\_\_\_ Never classified

☐ 5. Special Handling (Legal basis must be noted below.)☐ a. Copyrighted material ☐ All ☐ Part (Specify) \_\_\_\_\_☐ b. Unclassified Controlled Nuclear Information (UCNI)☐ c. Export Control/ITAR/EAR☐ d. Temporary hold pending patent review☐ e. Translation of copyrighted material☐ f. Small Business Innovation Research (SBIR) Release date (mm/dd/yyyy) \_\_\_\_/\_\_\_\_/\_\_\_\_☐ g. Small Business Technology Transfer (STTR) Release date (mm/dd/yyyy) \_\_\_\_/\_\_\_\_/\_\_\_\_☐ h. Proprietary☐ i. Protected CRADA information Release date (mm/dd/yyyy) \_\_\_\_/\_\_\_\_/\_\_\_\_☐ j. Official Use Only (OUO)☐ k. Program-Directed Special Handling (Specify) \_\_\_\_\_☐ l. Other (Specify) \_\_\_\_\_**B. Releasing Official**☐ 1. Patent Clearance (Mark one)☐ a. Submitted for DOE patent clearance Date submitted (mm/dd/yyyy) \_\_\_\_/\_\_\_\_/\_\_\_\_☐ b. DOE patent clearance has been granted☒ c. DOE patent clearance not required☐ 2. Released by Name \_\_\_\_\_ Date (mm/dd/yyyy) \_\_\_\_/\_\_\_\_

Phone \_\_\_\_\_ E-mail \_\_\_\_\_



**THIN-WALL HOLLOW CERAMIC SPHERES  
FROM SLURRIES**

**ORNL/DOE-FCO5-89CE90052**

**Final Report**

**(ROUGH DRAFT)**

**Alan T. Chapman and Joe K. Cochran**

**Prepared by**

**School of Materials Science and Engineering  
Georgia Institute of Technology  
Atlanta, GA 30332**

**Funded by**

**Advanced Industrial Materials Program  
Office of Industrial Technologies  
Energy Efficiency and Renewable Energy  
U.S. Department of Energy**

## Table of Contents

Table of Contents

List of Figures

List of Tables

Abstract

1.0 Introduction

2.0 Coaxial Nozzle Formation of Hollow Spheres

2.1 Hollow Sphere Formation with Acetone Slurries

2.1.1 Background

2.1.2 Rheology of Acetone-Based Dispersions

2.1.3 Sphere Recovery System

2.2. Viscosity-Solids Relationship for Acetone Slurries

2.2.1 Slurry Preparation and Adsorption/Viscosity Procedures

2.2.2 Adsorption Isotherms and Viscosity-Solids Model

2.2.3 Conclusions

2.2.4 Bibliography

2.3 Model for Formation of Hollow Spheres

2.3.1 Experimental Sphere Formation

2.3.2 Model of Hollow Sphere Formation

2.3.3. Prediction of Sphere Dimensions and Verification

2.3.4 Conclusions

2.3.5 Glossary

2.3.6 References

2.4 Geometrical Characteristics of Thin Wall Hollow Spheres

2.5 Forming Spheres from Aqueous Slurries

2.5.1 Properties of Polysaccharides

2.5.2 Measurement of Gel Strength and Viscosity

2.5.3 Gel Strength and Viscosity of Carrageenan Slurries

2.5.4 Conclusions and Recommendations

2.5.5 Footnotes and Bibliography

- 3.0 Mechanical Behavior of Hollow Spheres and Foams
  - 3.1 Uniaxial Compressive Behavior of Brittle Hollow Spheres
    - 3.1.1 Previous Models
    - 3.1.2 Finite Element Procedures and Load Conditions
    - 3.1.3 Experimental Results and Discussions
    - 3.1.4 Conclusions
  - 3.2 Compressive Strength of Hollow Sphere Foams
    - 3.2.1 Compressive Strength of Cellular Solids
    - 3.2.2 Finite Element of Foam Compressive Strength
    - 3.2.3 Experimental Verification of Finite Element Model
  - 3.3 Isostatic Compressive Strength
    - 3.3.1 Background
    - 3.3.2 Isostatic Testing
    - 3.3.3 Theoretical Strength
- 4.0 Thermal Conductivity of Hollow Spheres
  - 4.1 Radiation Transfer in Ceramics
  - 4.2 Zirconia Opacification of Hollow Glass Sphere Walls
  - 4.3 Thermal Conductivity and Infrared Reflectance
- 5.0 Technology Transfer
  - 5.1 Advisory Meeting and Industrial Visits
  - 5.2 Technology Transfer Trip Report
  - 5.3 Technology Transfer Presentations

## **List of Figures**

- Figure 1.1.1      Thin-Walled Spheres Formed by the Coaxial Nozzle Process Showing Monosized Distribution and Uniform Wall Thickness.
- Figure 2.1.1      Viscosity of Alumina/Acetone Slips vs. Rotational Speed for Various PMMA Concentrations of 2008 Polymer.
- Figure 2.1.2      Viscosity of Alumina/Acetone Slips vs. Rotational Speed for Various PMMA Concentrations for 2008 Polymer.
- Figure 2.1.3      Viscosity of Alumina/Acetone Slops vs. Rotational Speed for Various PMMA 2008 Concentrations at a 2041 Concentration of 0.67 v/o.
- Figure 2.1.4      Viscosity of Alumina/Acetone Slips vs. Rotational Speed for Various PMMA 2008 Concentrations at 2041 Concentrations of 1.33 & 1.67 w/o.
- Figure 2.1.5      Plot of Viscosity at 30 RPM vs Elvacite 2008 Concentration Based on Solids Content.
- Figure 2.1.6      Effect of 2041 Content on Viscosity (304PM) of Alumina/Acetone Dispersions with 2008 Concentration Fixed at 2.3 w/o.
- Figure 2.1.7      Photograph of Components at the Top of the Sphere Recovery Tower.
- Figure 2.1.8      Schematic Process Diagram, Incorporating the 3.2 m Tall Sphere Recovery Tower, for the Manufacture of Low Density Ceramic Spheres.
- Figure 2.2.1      Particle Size Distribution of XA3000 and XA1000.
- Figure 2.2.2      Particle Size Distribution of HSY3.
- Figure 2.2.3      The Calibration Curve of the Refractive Index Versus Solution Concentration for PMMA/Acetone Solution - Used for Adsorption Analysis from HSY3, Temperature =  $18.1^{\circ} \pm 0.2^{\circ}\text{C}$ .

- Figure 2.2.4 The Calibration Curve of the Viscosity of PMMA Solution Versus PMMA Concentration.
- Figure 2.2.5 Adsorption Isotherms of PMMA onto XA1000 and XA3000 Alumina from Acetone.
- Figure 2.2.6 Adsorption Isotherm of PMMA onto HSY3 Zirconia from Acetone.
- Figure 2.2.7 BET Plot for the Adsorption of PMMA onto XA1000, XA3000 and HSY3.
- Figure 2.2.8 Comparison of the experimental results with the Eilers equation for  $[\eta]_f = 2.5$ ,  $\phi_{\max} = 0.7$  (curve 1)  $\phi_{\max} = 0.65$  (curve 2), and  $\phi_{\max} = 0.6$  (curve 3); the volume fraction of XA3000 slurry was corrected for the thickness of the adsorbed layer for  $\Delta = 28\text{\AA}$  and  $\Delta = 208.13\text{\AA}$ , using Eq. 2.2.8.
- Figure 2.2.9 Thickness of Adsorbed Polymer Layer Versus Solids Volume Fraction.
- Figure 2.2.10 Relative Viscosity Versus Apparent Viscosity Calculated from Eq. 2.2.16 and the Eilers Equation.
- Figure 2.2.11 Relative Viscosity Versus Apparent Viscosity Calculated from Eq. 2.2.16 and the Krieger-Dougherty Equation.
- Figure 2.3.1 (a) Cross Section of a Coaxial Nozzle. (b) Hollow Alumina Spheres Formation with Coaxial Nozzle from Alumina Slurry.
- Figure 2.3.2 (a) Hollow Ceramic Spheres with Narrow size Distribution. (b) Sphere Wall Thickness Variation.
- Figure 2.3.3 The Geometry and Stresses on (a) the Outer Surface and (b) the Inner surface of Hollow Sphere Formation.
- Figure 2.3.4. Schematic Description of Sphere Formation for (a) Higher and (b) Lower Liquid Flow Rates.
- Figure 2.3.5. Frequency vs. Inner Jet Gas Flow Rate for Silicone Fluid ( $\mu = 0.993$  poise,  $\alpha = 23$  dyne/cm,  $\rho = 0.97$  g/cm<sup>3</sup>) at a Variety of Liquid Flow Rates.

- Figure 2.3.6. The Pressure in the Transition Zone of the Cavity Affect the Magnitude of the Negative Curvature.
- Figure 2.3.7. The Pressure Inside the Cavities as a Function of Time and the Critical Condition.
- Figure 2.3.8. Iterative Method Used to Calculate Correct Frequency.
- Figure 2.3.9. Comparison of Experimental Results and Model Calculations of Frequency vs. Inner Jet Flow Rate for Silicone Fluid ( $\mu = 0.993$  poise,  $\alpha = 23$  dyne/cm,  $\rho = 0.97$  g/cm<sup>3</sup>) for High Liquid Flow Rates.
- Figure 2.4.1 Photographs of Fired, Thin-Wall, Alumina, Spheres Formed at Blowing Conditions (a) 40-20 and (b) 20-40.
- Figure 2.4.2 Crossection of Sphere Walls for Polycrystalline Alumina Spheres Fired at 1650°C, (a) 40-20 and (b) 20-40.
- Figure 2.4.3 Diameter Distributions for 64 Randomly Selected Thin Wall Hollow Alumina Spheres.
- Figure 2.4.4 Aspect Ratio Distributions for 64 Randomly Selected Thin Wall Hollow Alumina Spheres.
- Figure 2.5.1 Gel Thermoreversibility, Describes Repeated Low Viscosity Solutions at High Temperatures and Solid Gels at Low Temperatures
- Figure 2.5.2 Comparison of Hollow Spheres From (A) Acetone Based Slurries and (B) Aqueous Based Slurries Using Carrageenan as the Gelling Agent
- Figure 2.5.3 Idealized Molecular Structure of (A) Agarose and (B) Kappa Carrageenan
- Figure 2.5.4 Monovalent Cations Dissolved at Specific Molarities in Water with 3 wt% Kappa Carrageenan
- Figure 2.5.5 Gel Strength at Varying Concentrations of Potassium Ions in Aqueous Kappa Carrageenan Gels

- Figure 2.5.6      Curve-Fitting of Kappa Carrageenan Gel-Strengths in Figure (3.5.5), According to the Equation 2.5.2.
- Figure 2.5.7      Viscosity of (A) 3 Weight % and (B) 5 Weight % Kappa Carrageenan in Water, with Specific Concentrations of  $K^+$  Measured at 90 Degrees C.
- Figure 2.5.8      Viscosity of Alumina/Carrageenan Slurries at 90° C.
- Figure 3.1.1      Sphere Strength  $\sigma_s$ , vs. Relative Density Squared,  $(\rho_s/\rho_o)^2$ , Under Uniaxial Concentrated Loading.
- Figure 3.1.2      Deformation Mode of a Hollow Sphere under Contact Loading.
- Figure 3.1.3      Sphere Strength  $\sigma_s$ , vs. Relative Density Squared,  $(\rho_s/\rho_o)^2$ , Under Contact Loading by Rigid Platens.
- Figure 3.1.4      Sphere Strength vs. Relative Density Squared for Alumina Spheres.
- Figure 3.2.1      Two-Dimensional Model of Hexagonal Cells.
- Figure 3.2.2      Neck Area Between Spheres and Contact Angle of a Distributed Load Produced by Point Contact Bonding.
- Figure 3.2.3      Sphere Strength,  $\sigma_s$ , vs. Relative Density Squared,  $(\rho_s/\rho_o)^2$ , under Uniaxial Distributed Loading.
- Figure 3.2.4      Basic Unit Structure of Random-Packed Bonded Sphere Foam.
- Figure 3.2.5      Sphere Strength  $\sigma_s$ , vs. Relative Density Squared,  $(\rho_s/\rho_o)^2$ , under Six-Directional Distributed Loading.
- Figure 3.2.6      A Bonded Alumina Sphere Foam to be Tested under Compressive Load.
- Figure 3.2.7      Cross Section of Bonded Mullite Sphere Foam Showing Random Packing and Point Contact Bonding.
- Figure 3.2.8      Bonded Sphere Foam Compressive Strength (psi) vs. Foam Density (lb/ft<sup>3</sup>).

Figure 3.2.9	Foam Strength vs. Relative Sphere Density Squared.
Figure 3.3.1	Isostatic Compressive Strength Distributions for Alumina Hollow Spheres from Hg Porosimetry
Figure 3.3.2	Isostatic Compressive Strength Distributions for Alumina Hollow Spheres from Hg Porosimetry
Figure 3.3.3	Isostatic Failure of Alumina Hollow Spheres as a Function of Density for Buckling and Crushing Compared to Experimental Values
Figure 4.1.1	Scattering Factor, $K$ , as a Function of Wavelength, Radius of Scattering Center, and Relative Refractive Index.
Figure 4.1.2	Effect of Particle Size on the Scattering Cross Section of a Fixed Volume of Particles (1.0 vol%) for a Relative Refractive Index of 1.8 ( $\text{TiO}_2$ in Glass).
Figure 4.1.3	Independent and Dependent Scattering Regimes: $x$ vs. $F_v$
Figure 4.1.4	Thermal Conductivity of Alumina Hollow Spheres
Figure 4.2.1	Combined Particle Size Distributions of RDF 371, DK1, and DK3CL Zirconia Powders.
Figure 4.2.2	Comparison Between Georgia Tech Thermal Conductivity Measurements and Manufacturer's Specifications for K-23 and K-30 Firebrick.
Figure 4.2.3	Thermal Conductivity of Alumina Hollow Spheres Measured at Georgia Tech and the University of Kentucky.
Figure 4.2.4	Combined Reflectance of DK1, DK3CL, and RDF371 Opacified Glass Spectrometer Samples Vs. Zirconia Volume Percent.
Figure 4.2.5	Thermal Conductivity of Unopacified Glass Spheres Vs. Temperature.
Figure 4.2.6	Thermal Conductivity of DK1 Opacified Glass Spheres Vs. Temperature.



- Figure 4.2.7 Thermal Conductivity of DK3CL Opacified Glass Spheres Vs. Temperature.
- Figure 4.2.8 Thermal Conductivity of RDF 371 Opacified Glass Spheres Vs. Temperature.
- Figure 4.2.9 Thermal Conductivity of DK1 Opacified Glass Spheres Vs. Zirconia Volume Percent, at 1000°C.
- Figure 4.2.10 Combined Thermal Conductivity of DK1, DK3CL, and RDF 371 Opacified Glass Spheres VS. Zirconia Volume Percent, at 1000°C.
- Figure 4.3.1 Thermal Conductivity at 1000°C Vs. Reflectance for DK1 Opacified Glass.
- Figure 4.3.2 Thermal Conductivity at 1000°C Vs. Reflectance for DK1, DK3CL, and RDF 371 Opacified Glass.
- Figure 5.1.1 Point-Contact-Bonded, Hollow-Sphere, Mullite, Structural Insulation for Induction Furnace at Y-12 Plant.

## List of Tables

Table 2.2.2	Analysis of Adsorption Isotherms by BET Theory.
(a)	Fitting of Experimental Data to the BET Equation.
(b)	Adsorption Analysis Using the BET Equation.
(c)	Heat of Adsorption and $N_{m,area}$ .
(d)	Area Occupied by One PMMA Molecule Adsorbed on Oxide Surface.
Table 2.2.3	Viscosity of XA1000 Dispersion and Calculation of the Relative Viscosity.
Table 2.2.4	Viscosity of XA3000 Dispersion and Calculation of the Relative Viscosity.
Table 2.2.5	Viscosity of HSY3 Dispersion and Calculation of the Relative Viscosity.
Table 2.2.6	Mean and Standard Deviation of the Relative Viscosity of XA1000, XA3000 and HSY3 Dispersions.
Table 2.2.7	The values of $[\eta]_i$ , $\phi_{max}$ and $\sigma$ for XA1000, XA3000 and HSY3 for the Eilers and the Krieger-Dougherty Equations.
Table 3.2.1	Failure Locations on Hollow Spheres under Uniaxial Distributed Loading.
Table 3.2.2	Failure Locations on Hollow Alumina Spheres under Uniaxial Distributed Loading when Failure is Determined Outside the Loading Area.
Table 3.3.1	Isostatic Strength (psi) of Alumina Hollow Spheres at 20, 50, and 80 Percent Volume Loss and Relative Density.
Table 3.3.2	Predicted Isostatic Failures Loads.
Table 4.2.1	Diameters and Bulk Densities of Hollow Spheres.

## 1.0 INTRODUCTION

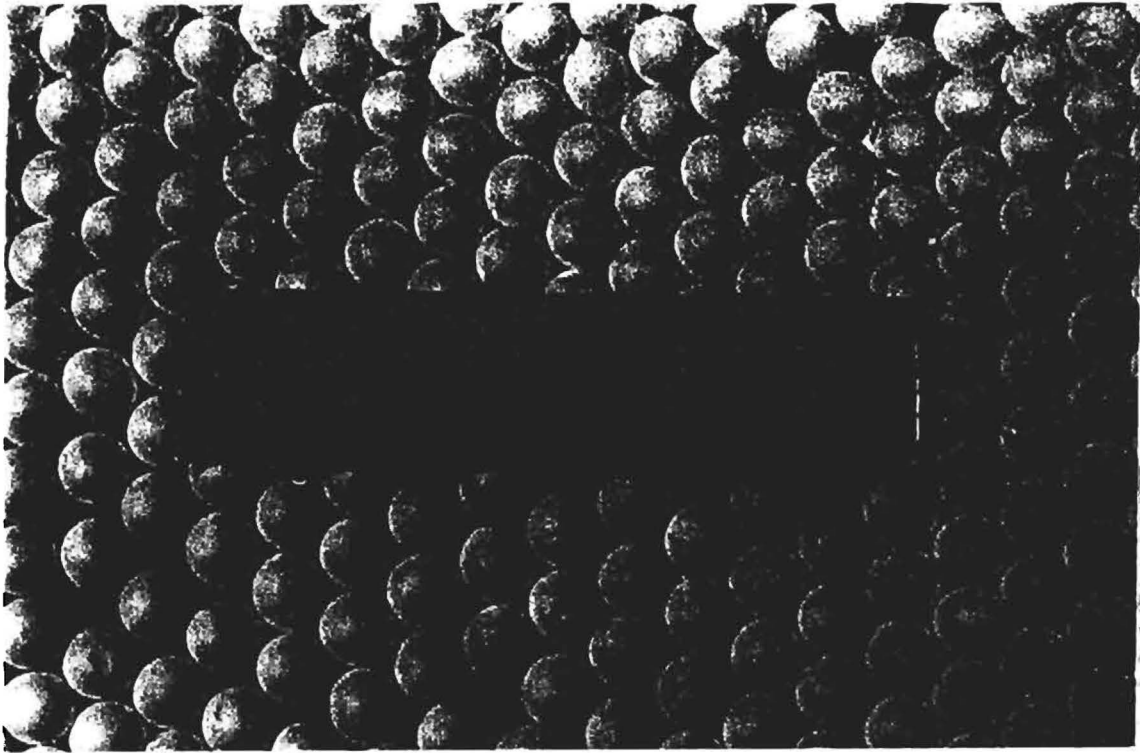
The overall objective of this effort was to develop a process for economically fabricating thin-wall hollow ceramic spheres from conventional ceramic powders using dispersions. This process resulted in successful production of monosized spheres in the mm size range which were point contact bonded into foams. Thin-wall hollow ceramic spheres of small (one to five millimeter) diameter have novel applications as high-temperature insulation and light structural materials when bonded into monolithic foams.

Other laboratories have fabricated small solid spheres, and in a few cases, even thin-wall hollow spheres of ceramics have been made either from the melt or from sol-gel processes. These approaches have limited the production to either the lower temperature melting ceramics, such as glass, or those that can be made from sol-gel solutions, such as alumina and are expensive. Small diameter spheres of SiC or Si<sub>3</sub>N<sub>4</sub> have not been made by other processes but could be made by the process presented here if applications emerge. The basic approach in the present work was to use a patented coaxial nozzle process for formation of hollow spheres from powder dispersions or slurries, permitting the use of virtually any ceramic composition.

This program ran continuously under several contracts from January, 1986 to December 1992. During Phase I of this program the objective was to develop a process for fabricating thin-wall hollow spheres from powder slurries using the coaxial nozzle fabrication method. This objective was successfully met by utilizing alumina powders dispersed in organic liquids, where the individual spheres could be blown at rates between 30 to 100 spheres/second, and dropped into a heated updraft air column to provide time sufficient for drying. The dried spheres had the strength necessary to survive landing and collection on a hard surface. These polymer bonded powder shells were then fired and sintered to dense walls and high strength hollow spheres. The resulting spheres were monosized to +/- 5% in diameter for fixed process parameters, could be varied in diameter from 1 to 5 mm, and wall thickness could be varied from 50 to 200 microns and could be made uniform in thickness, Figure 1.1.1. By varying diameter and wall thickness, bulk density of sphere beds could be varied from 5 to 50 % of theoretical density (10-100 lb/ft<sup>3</sup>).

Based on the success during Phase I, Phase II was revised to emphasize the assessment of the potential structural and insulation applications for the spheres and modeling of the sphere formation process was initiated. As more understanding developed, it was clear that to achieve successful structural application, the spheres had to be bonded into monolithic foams and the effort was further expanded to include both bonding into structures and finite element mechanical modeling which

NARROW SIZE RANGE



THIN UNIFORM THICKNESS WALLS

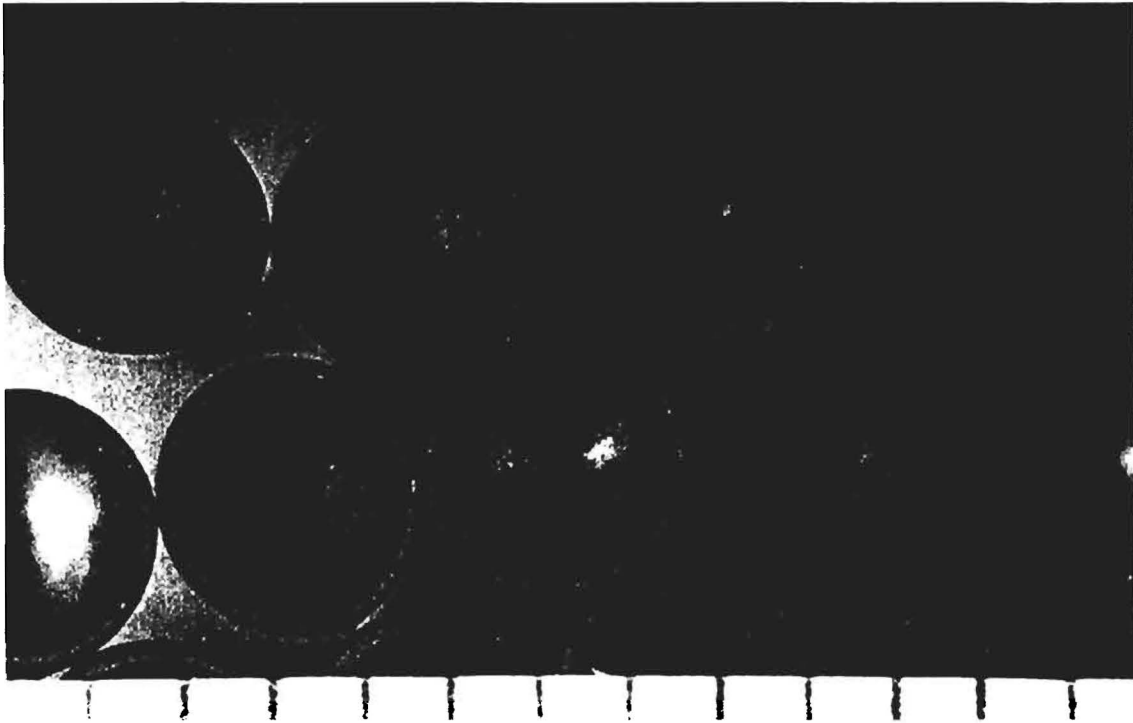


Figure 1.1.1 Thin-Walled Spheres Formed by the Coaxial Nozzle Process Showing Monosized Distribution and Uniform Wall Thickness.

became the basis of Phase III. Successful bonding techniques and mechanical modeling resulted but thermal conductivities were higher than desired for insulating activities. In addition, considerable interest had been expressed by industry for the technology. Thus the final Phase IV concentrated on methods to reduce thermal conductivity by a variety of techniques and technology transfer through individualized visits. This program resulted in three Ph.D. theses and 10 M.S. theses and they are listed in the appropriate technical sections below.

Technically, the program was divided into three distinct areas; (1) processing of hollow spheres including slurry rheology, fluid dynamic modeling, and aqueous gelling technology, (2) mechanical testing and modeling of individual spheres and monolithic foams and (3) thermal conductivity of spheres and foams and efforts to reduce conductivity. In addition, efforts to produce and characterize metal sphere foams were conducted under this program and high permeability applications dictated characterization and control of permeability through the high porosity foams.

Theses completed under this program grouped in each technical area as follows:

#### Coaxial Nozzle Formation of Hollow Spheres

T.J. Hwang, Ph.D. Thesis, June, 1989, "A Model for Viscosity of Organic Based Oxide Dispersions."

P.R. Chu, Ph.D. Thesis, June, 1991, "A Model for Coaxial Nozzle Formation of Hollow Spheres from Liquids."

C.M. Moore, M.S. Thesis, June, 1991, "Organic Gels from Injection Molding of Powders."

#### Mechanical Properties of Hollow Spheres and Foams

V. Munne, M.S. Thesis, September, 1988, "Monolithic Structures Foamed from Phosphate Bonded Hollow Microspheres."

M.K. Adicks, M.S. Thesis, March, 1989, "Strength Characterization of Thin-Wall Hollow Ceramic Spheres from Slurries."

J.H. Chung, Ph.D. Thesis, June, 1991, "Compressive Mechanical Behavior of Thin Wall Ceramic Spheres and Sphere Cellular Monoliths."

A.S. Jensen, M.S. Thesis, Dec., 1992, "Phosphate Bonding of Ceramic Hollow Sphere Foams."

#### Thermal Conductivity of Hollow Spheres and Foams

M.J. Shapiro, M.S. Thesis, March, 1988, "Thermal Conductivity of Thin Wall Hollow Ceramic Spheres."

S.D. Furlong, M.S. Thesis, December, 1990, "Reduction of Radiative Thermal Conductivity in Thin-Wall Hollow Ceramic Spheres Using Scattering Phases."

T.R. Ford, M.S. Thesis, June 1991, "Thermal Conductivity of Bonded Hollow-Sphere Monoliths."

G.E. Carlson, M.S. Thesis, August 1992, "Thermal Conductivity and Infrared Reflectance of Hollow Glass Spheres."

#### Syntactic Metal and Metal Matrix Foams

S.A. Rickles, M.S. Thesis, March, 1989, "Microstructural and Compressive Properties of Metal/Ceramic Syntactic Foam."

R. Clancy, M.S. Thesis, December, 1991, "Nickel and Nickel Alloy Hollow Spheres."

#### High Permeability Applications for Hollow Sphere Foams

L.A. Touryan, M.S. Thesis, December, 1992, "Permeability of Point Contact Bonded Hollow Sphere Foams."

## 2.0 COAXIAL NOZZLE FORMATION OF HOLLOW SPHERES

### 2.1 HOLLOW SPHERE FORMATION WITH ACETONE SLURRIES

#### 2.1.1 BACKGROUND

Prior to the start of this program, a method to form thin-wall hollow spheres from a variety of conventional ceramic powders dispersed in water had been demonstrated. However, at that time, the liquid spheres were collected on paper, several centimeters below the nozzle and on landing the spheres were distorted into flat bottomed ellipsoids with a wall thickness at the bottom four times greater than the top. This thickness difference was caused by the rapid deceleration on landing resulting in run-off from the top to the bottom. In addition, the fall distance was insufficient to allow spheridization and each ellipsoid was connected to the next by a stringer. The initial project objective therefore was to evaluate means to dry and recover the moisture-laden free-falling spheres, after the stringers had resorbed and the shells had rounded to spheres from surface tension forces. A variety of methods were considered including; microwave drying, hot air furnaces, and direct infrared radiant heating. The microwave drying approach was considered most attractive because the energy would be absorbed directly in the walls of the spheres. Several suppliers of microwave drying equipment were contacted and a series of experiments were performed to assess the feasibility of drying the free-falling, thin-wall spheres with microwave energy. Unfortunately, the small volume occupied by the relatively widely spaced falling spheres resulted in inefficient heating using conventional microwave frequencies and wave guides. Therefore, work on microwave drying was abandoned.

Other drying schemes were considered along with process and changes in slurry composition that would provide faster drying for the free-falling spheres. Dispersion of powders in a high volatility organic fluid was the most attractive alternative for several reasons. For example, acetone has a much larger vapor pressure, smaller heat of vaporization, and a lower surface tension and density than water. Initial testing of  $\text{Al}_2\text{O}_3$  powders dispersed in acetone demonstrated that a very uniform stream of spheres could be blown for short periods at room temperature, although the high fluid evaporation rate lead to clogging of the coaxial blowing nozzle.

The merits of dispersions made with acetone were readily apparent when, acetone-based shells dried sufficiently to bounce on a soft landing surface after 30 to 40 feet of free-fall, whereas, water-based spheres splattered on impact. Recovery of the partially dried acetone-based bubble streams was attempted using a variety of methods including deflection off inclined surfaces, horizontal air jets to blow spheres for roll-out on flat surface, and heating using an infrared furnace. All of the spheres

collected using these approaches experienced damage on collision with adjacent spheres and/or impact with a solid surface.

Success was achieved by designing an updraft drying and recovery system consisting of a vertical tube tower, approximately 3.2 meters tall and 30 cm in diameter, combined with an air blower and sphere-forming nozzle assembly. The system was constructed and tested. When the updraft air velocity and sphere diameter and weight are properly balanced, the residence time necessary for adequate drying (4 to 5 sec) can be maintained in the tower and a "soft landing" is achieved without visually apparent mechanical damage to the shells. Recent runs using this facility have produced the best defect-free, high strength, thin-walled  $\text{Al}_2\text{O}_3$  spheres achieved to date.

The major efforts of this part of the program have been 1) analysis of the rheology of alumina/acetone dispersions containing varying amounts of methyl methacrylate which acts as a dispersant and binder, 2) development of a sphere recovery system which provides adequate residence time and a soft landing. The following sections describe the procedures and terminology used to characterize the pseudoplasticity and Newtonian behavior of the acetone-based slips, the influence of the organic binder on slip rheology, and the recovery system that yielded virtually "flaw-free", high strength, thin-walled  $\text{Al}_2\text{O}_3$  spheres.

### 2.1.2 RHEOLOGY OF ACETONE-BASED DISPERSIONS

The rheology of alumina/acetone slips has been investigated to provide suitable dispersion for production of hollow polycrystalline spheres. It is necessary that the alumina powder be well dispersed to yield a reproducible process and to permit a high solids volume content which minimizes the quantity of solvent to be removed. In addition, the slips must possess a viscoelastic and film forming character sufficient for blowing and the hollow spheres formed must be strong enough for recovery. For these purposes, methyl methacrylate, Dupont\* Elvacite, resins were added to the dispersions. Elvacite 2008 was added as a dispersant and a binder, while Elvacite 2041 served as a binder and a rheology modifier. (In the following text, the additives will be simply referred to as "2008" or "2041") To characterize the rheology of these dispersions, the viscosity was measured with a Brookfield LV Viscometer at shear rate between  $0.1\text{-}50\text{ sec}^{-1}$ .

Due to the use of organic polymers, the dispersions exhibit pseudoplasticity. This property can be described by the power law (also known as Ostwald-deWaele equation),

$$\tau = K\dot{\gamma}^n \quad (2.1.1)$$



where  $\tau$  is shear stress,  $\dot{\gamma}$  is shear rate,  $K$  is the consistency index and  $n$  is the flow behavior index. The value of  $n$  is less than 1 for pseudoplastic flow, and decreases as the degree of pseudoplasticity increases. If  $n$  is close to 1, the liquid is Newtonian. The power law equation can be related to viscosity,  $\eta$ , by:

$$\eta = K\dot{\gamma}^{(n-1)} \quad (2.1.2)$$

Transformed for linear plotting, this equation is rewritten as

$$\log \eta = \log K + (n-1) \log \dot{\gamma} \quad (2.1.3)$$

The value of  $\dot{\gamma}$  is not accurately known since  $\dot{\gamma}$  varies with distance from the rotating spindle thus causing a variation of  $\eta$ , for non-Newtonian liquids. However, to a first approximation,  $\dot{\gamma}$  can be treated as in a Newtonian liquid so that

$$\dot{\gamma} = \frac{2\pi r R}{dr} = 2\pi R, \quad (2.1.4)$$

where  $r$  is the radius at which  $\dot{\gamma}$  is desired to be known and  $R$  is the rotational speed of the spindle. Therefore equation (2.1.3) can be transformed to

$$\log \eta = \log K + (n-1) \log 2\pi + (n-1) \log R. \quad (2.1.5)$$

The rheology of additional alumina/acetone slips as well as additional ceramic materials have been and will be studied by characterizing  $\eta$  and  $n$  for various compositions in order to improve the quality of the thin-walled spheres.

As stated above, the materials used for slip preparation were ALCOA\* A-3000  $\text{Al}_2\text{O}_3$ , acetone, plus Elvacite 2008 and Elvacite 2041. Used as a slip casting alumina, A-3000  $\text{Al}_2\text{O}_3$  powder has a mean particle size of 3  $\mu\text{m}$ , and a broad particle size distribution designed for slips. Elvacite 2008 is a low molecular weight binder and dispersant, which provides low viscosity at high solids content. Elvacite 2041 is a very high molecular weight binder which increases viscosity with small additions. The dispersions investigated had a fixed  $\text{Al}_2\text{O}_3$  content of 51 v/o based on the acetone plus alumina volumes. The slips were designated according to type of powder, solvent, and weight concentration of polymers based on powder content. For example, A-A-0.6 indicates  $\text{Al}_2\text{O}_3$  as the powder, acetone as the solvent, and 0.6 w/o of 2008, or A-A-1.2-0.67 indicates the same powder and solvent, but 1.2 w/o of 2008 and 0.67 w/o of 2041.

After weighing, the  $\text{Al}_2\text{O}_3$ , acetone and 2008 were mixed by rolling with alumina cylinders in a polyethylene jar on a ball mill rack at 70-90 RPM for 24 hours. Elvacite 2041 was added to the slip if needed and the mixture milled for an additional 24 hours. Viscosity was measured with the Brookfield LV viscometer using proper spindles at rotational speeds of 1.5 to 60 RPM.

The viscosities of dispersions were plotted as  $\log \eta$  vs.  $\log R$  as shown in Figures 2.1.1 to 2.1.4 in accordance with equation 2.1.5. All slips were pseudoplastic as shown by the negative slope,  $(n-1)$ , in Figures 2.1.1-2.1.4. The flow behavior as indicated by  $n$  values, were calculated along with viscosities at 30 RPM. It can be seen that  $n$  values increase with 2008 concentration indicating that the slips approach a Newtonian fluid as the powder becomes well dispersed.

The effect of 2008 concentration on viscosity is shown in Figure 2.1.5. These viscosity curves all show minimum viscosity around 1.7-2.0 w/o 2008. This minimum point is indicative of monolayer adsorption of the polymer on the alumina particles. For slips without 2041, the increase of viscosity as the 2008 content was increased beyond the minimum may be due to excess 2008 going into solution. The rate of viscosity increase in this range should be equal to the rate of viscosity increase for a powder free 2008/acetone solution. Therefore, viscosities of 2008/acetone solutions were measured for comparison to slip viscosities. A comparison between slips and solutions was made by converting the 2008 concentration in the slips to a w/o concentration based on solvent content,  $C$ . The viscosity increase rate,  $[(\log \eta_1 - \log \eta_2)/(C_1 - C_2)]$ , for the alumina/acetone slip in the range of 12.21-20.71 w/o 2008 was 0.051 and for the 2008/acetone solutions in the range of 20-30 w/o 2008, the rate was; 0.067. There is reasonable agreement between the two rates which indicates; that after monolayer adsorption on the powder has been achieved, additional 2008 in solution increases the viscosity of slip at the same rate as for powder free acetone.

For fixed 2008 concentrations, the additions of 2041 produced large viscosity increases as would be expected for a high molecular weight polymer, Figure 2.1.6. Addition of 0.67 w/o 2041 to the slips raised viscosity about one order of magnitude, but this effect was not linear as more 2041 polymer was added. If comparison of  $n$  for slips at the same 2008 content are made, it is evident that the 2041 also increases the pseudoplasticity along with the viscosity.

### 2.1.3 SPHERE RECOVERY SYSTEM

This section describes the continuing evaluation of a sphere recovery system capable of high volume collection. The recovery techniques reported below have all utilized

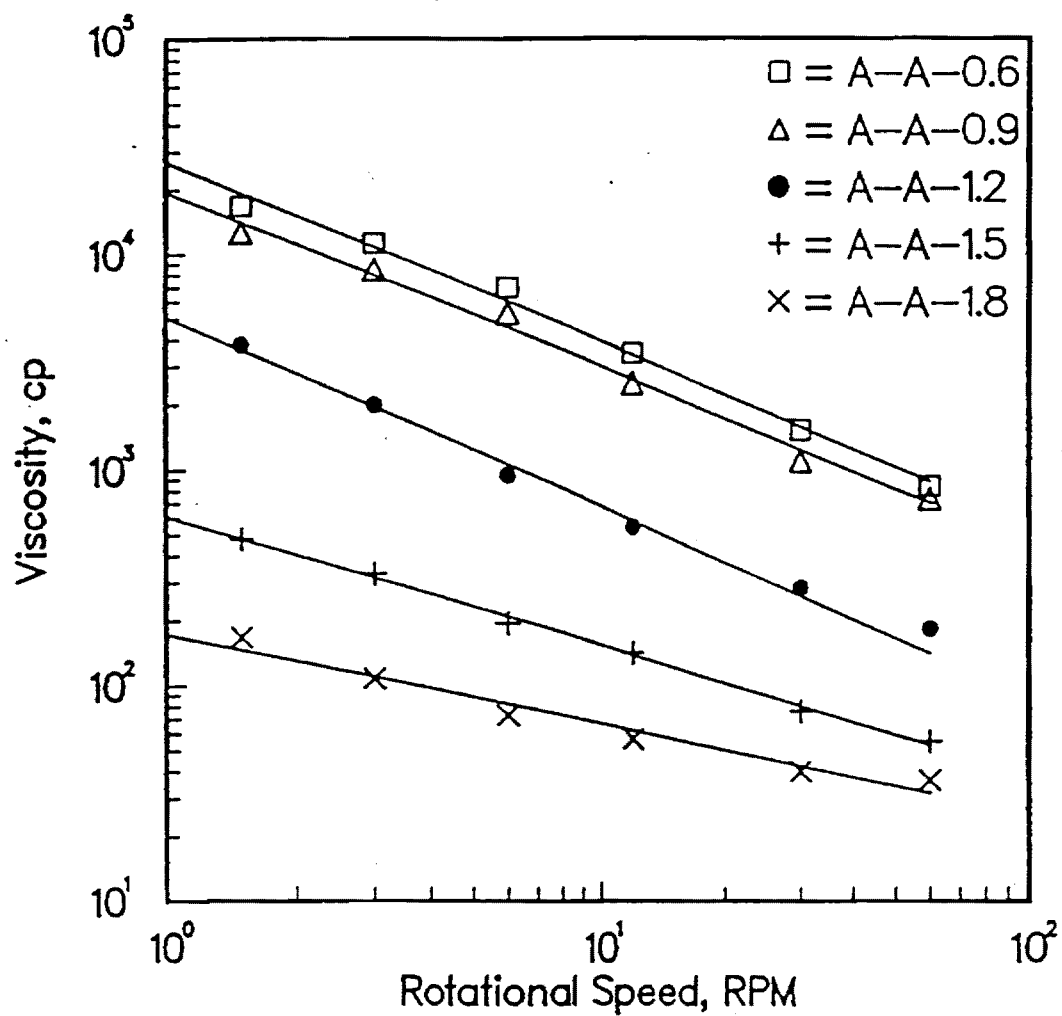


Figure 2.1.1

Viscosity of Alumina/Acetone Slips vs. Rotational Speed for Various PMMA Concentrations of 2008 Polymer.

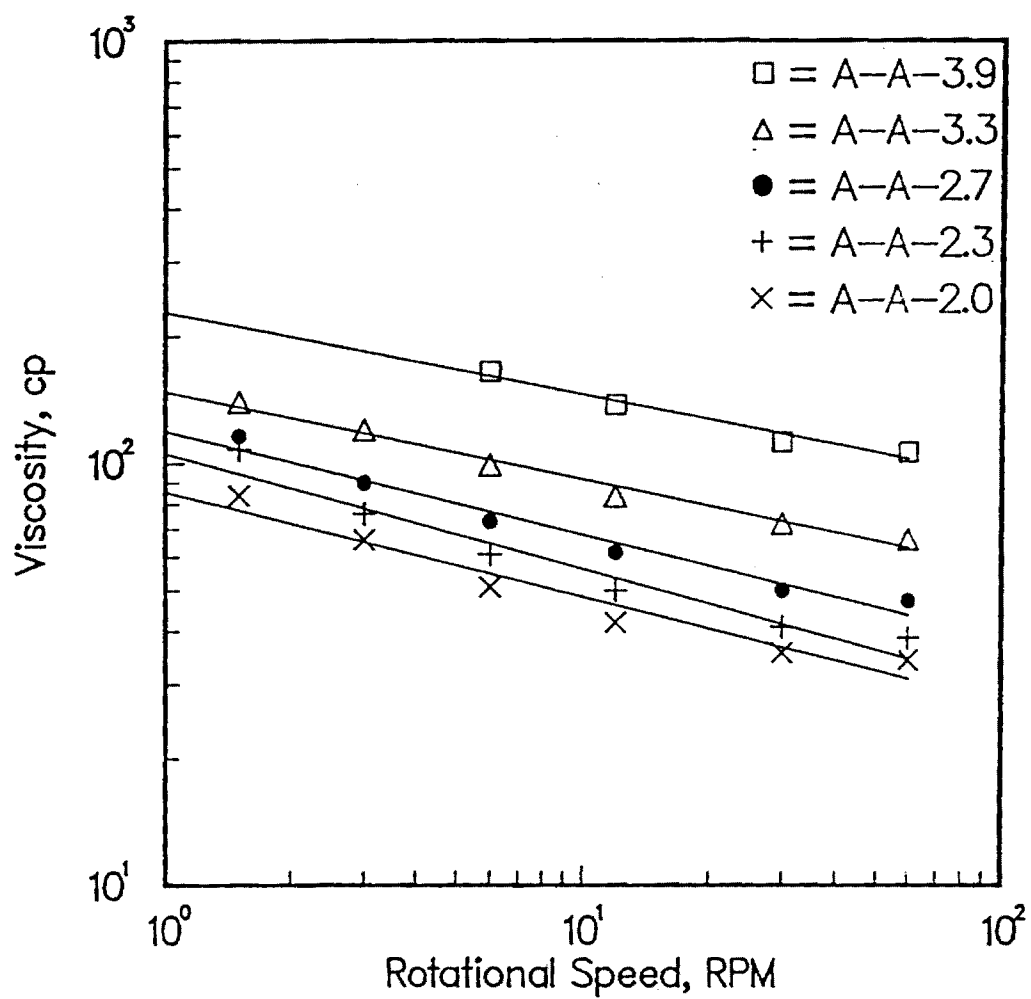


Figure 2.1.2

Viscosity of Alumina/Acetone Slips vs. Rotational Speed for Various PMMA Concentrations for 2008 Polymer.

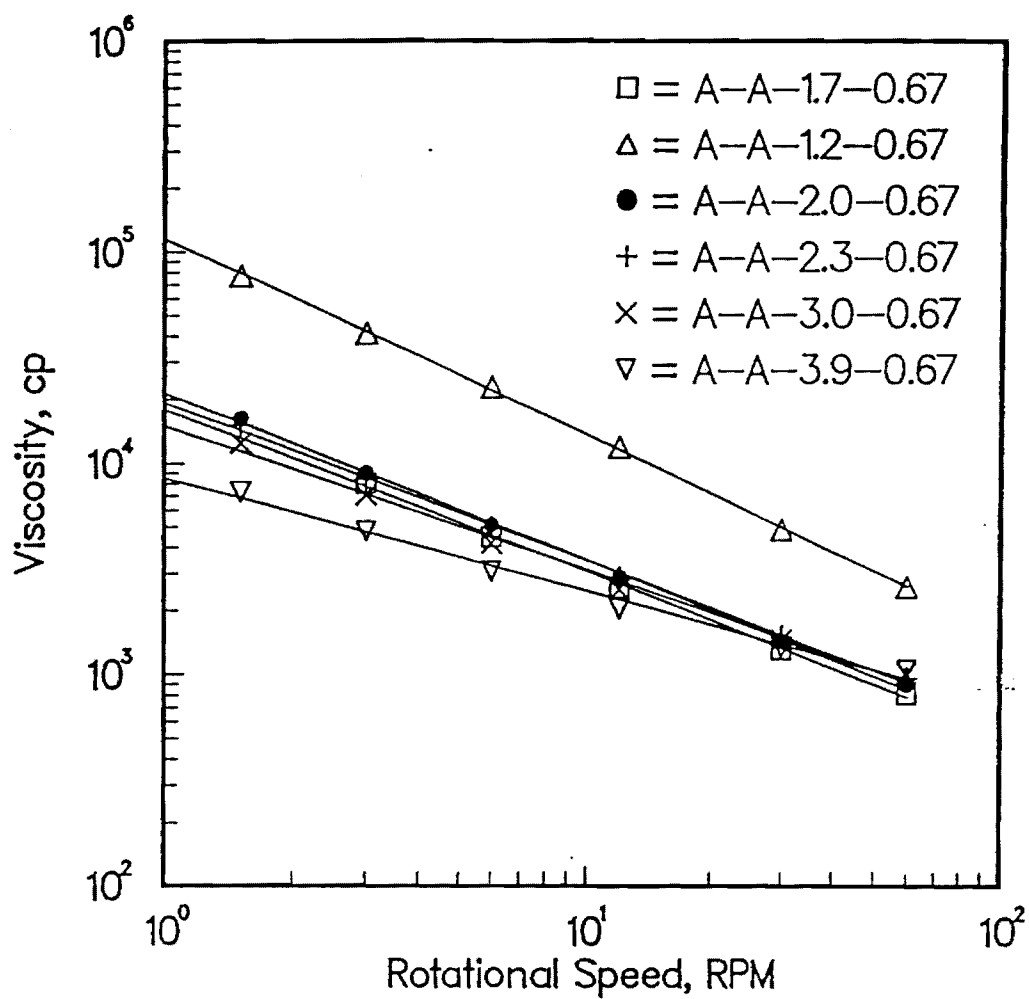


Figure 2.1.3

Viscosity of Alumina/Acetone Slops vs. Rotational Speed for Various PMMA 2008 Concentrations at a 2041 Concentration of 0.67 v/o.

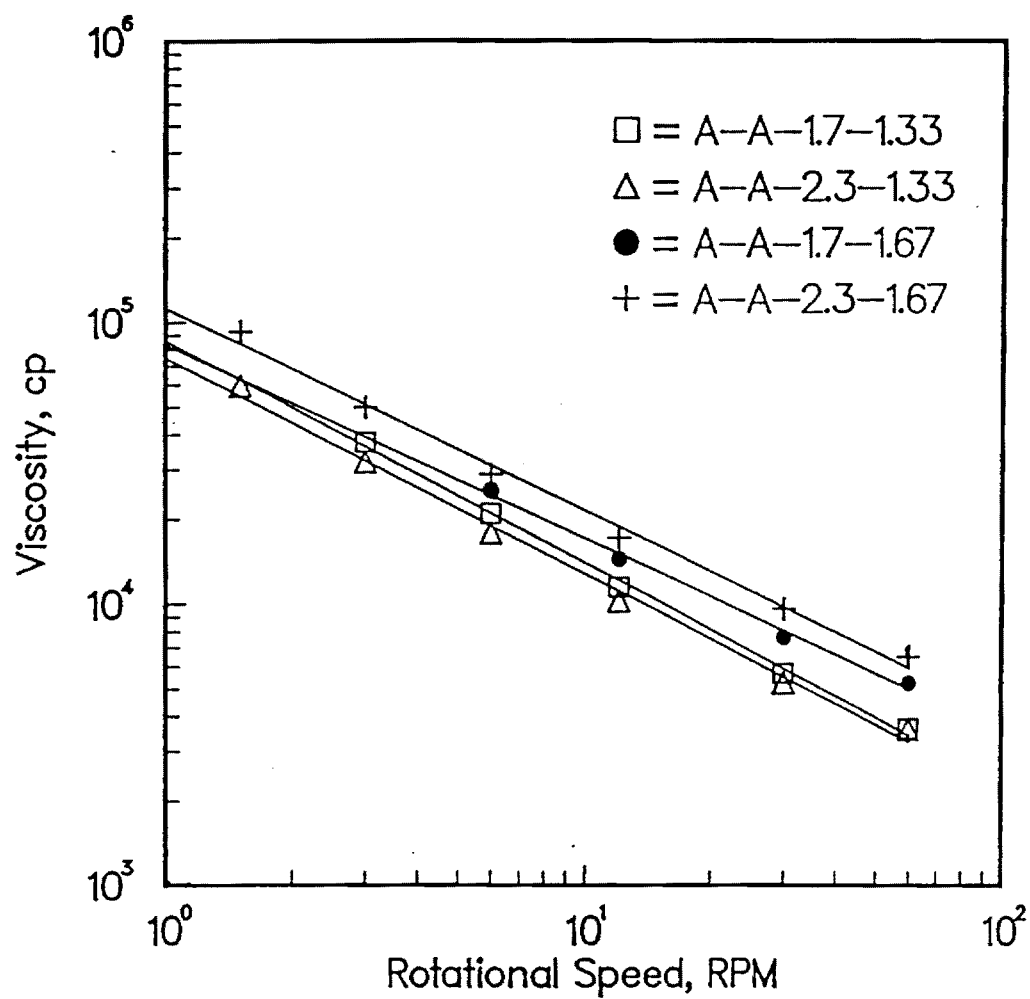


Figure 2.1.4

Viscosity of Alumina/Acetone Slips vs. Rotational Speed for Various PMMA 2008 Concentrations at 2041 Concentrations of 1.33 & 1.67 w/o.

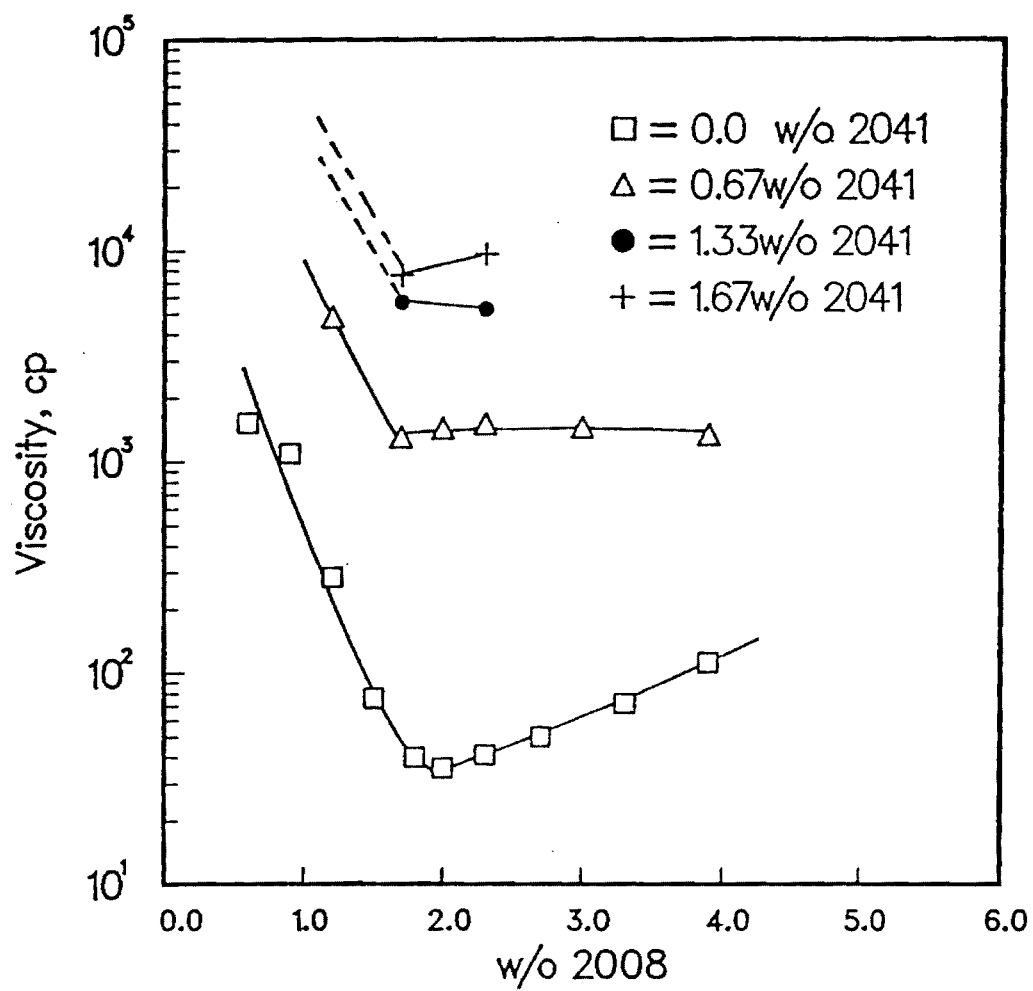


Figure 2.1.5

Plot of Viscosity at 30 RPM vs Elvacite 2008 Concentration Based on Solids Content.

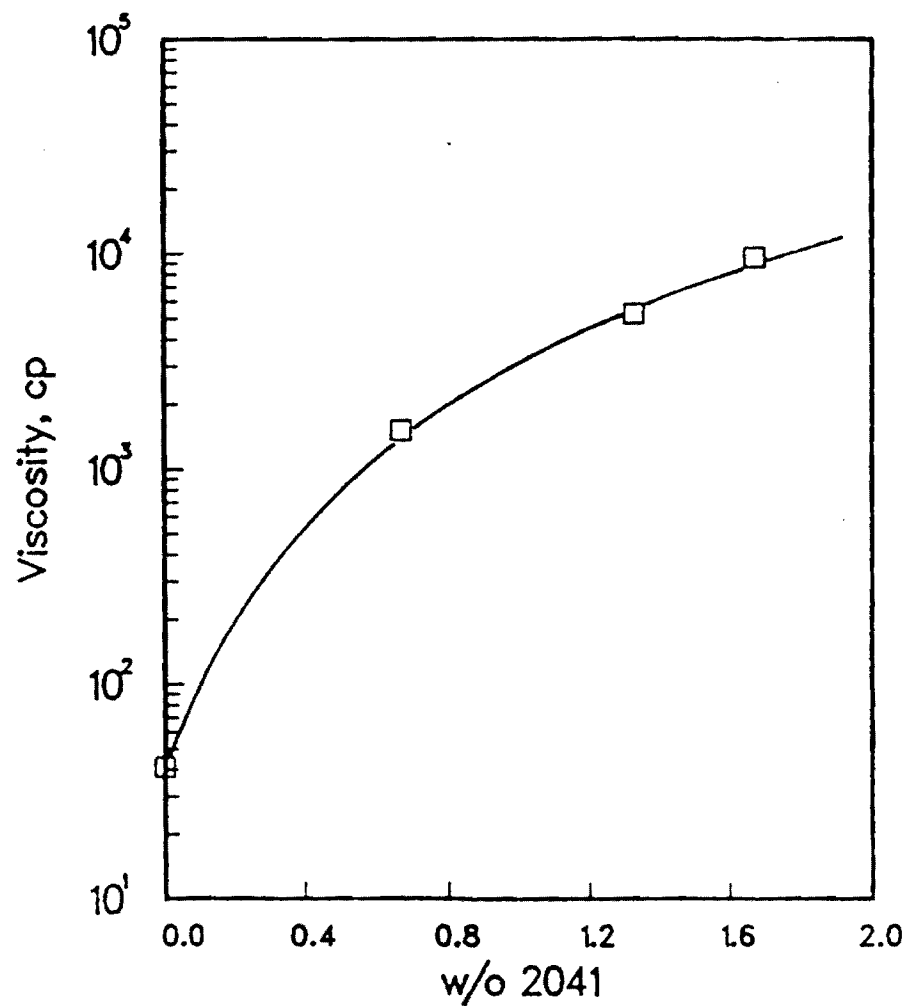


Figure 2.1.6 Effect of 2041 Content on Viscosity (304PM) of Alumina/Acetone Dispersions with 2008 Concentration Fixed at 2.3 w/o.



upward flowing air in an effort to increase the residency time for decreasing the free-falling rate of descent to enable a "soft damage-free landing" for the thin-walled product. The most successful design tested consists of a 3.2 meter tall stack of three plexiglass tubes 30 cm in diameter joined on the upper end with a chamber containing the coaxial sphere-forming nozzle, a smaller diameter tube to contain a saturated acetone atmosphere to facilitate sphere-formation and ducting to a high volume air blower. A photograph of the components at the top of the recovery tower is shown in Figure 2.1.7. Air is drawn in at the base of the tower to develop the updraft necessary to retard the decent rate of the free-falling spheres. At the base of the tower the sufficiently dried spheres land on an inclined screen and roll into a collection box. A process diagram describing the major steps for the manufacture of fired hollow ceramic sphere is shown schematically in Figure 2.1.8. The updraft drying and recovery system described above has produced symmetrical, damage-free, thin-walled microspheres. Future modifications planned for this system include (a) a larger capacity blower to increase the updraft air velocity to handle wider ranges of sphere diameters and densities, (b) an improved air intake geometry to provide more laminar flow inside the tube, (c) a larger diameter (low air velocity) chamber between the drying tower and blower to "drop-out" the fine, light weight  $\text{Al}_2\text{O}_3$  particles carried to the blower and, (d) the evaluation of intake deflectors (wings) at the base of the tower that will generate a mild vortex motion in the raising air to help contain the spheres in the center of the tower.

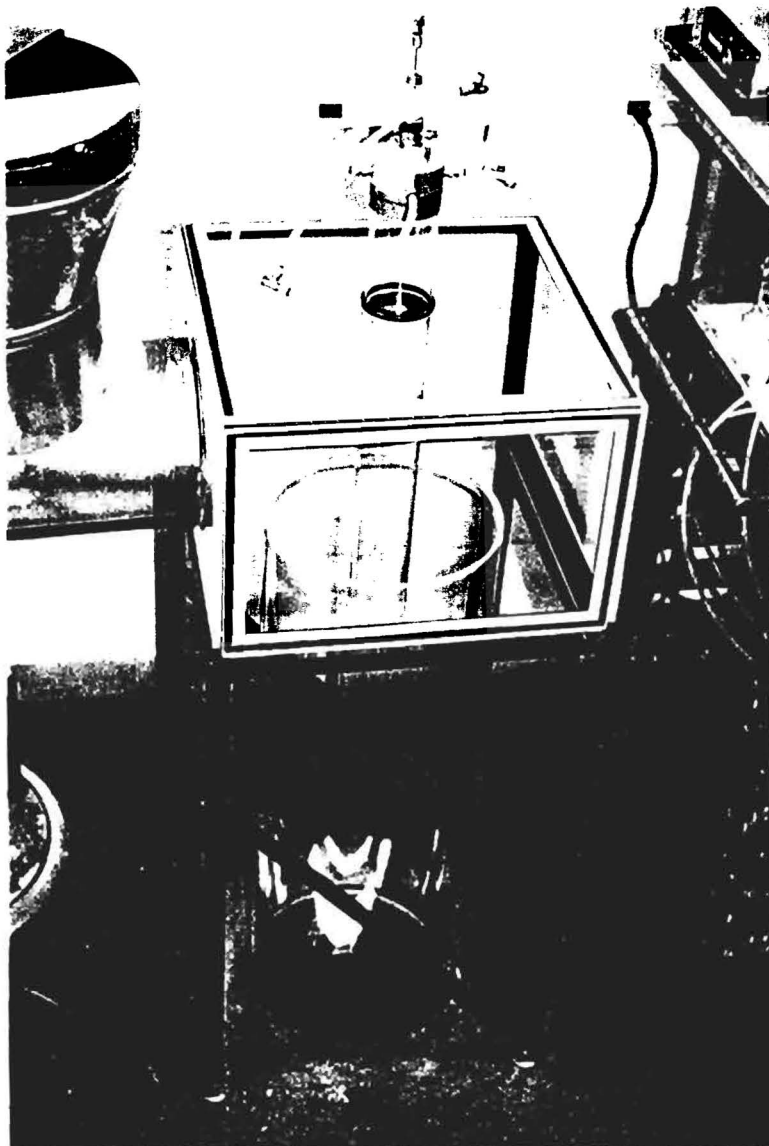


Figure 2.1.7

Photograph of Components at the Top of the Sphere Recovery Tower.

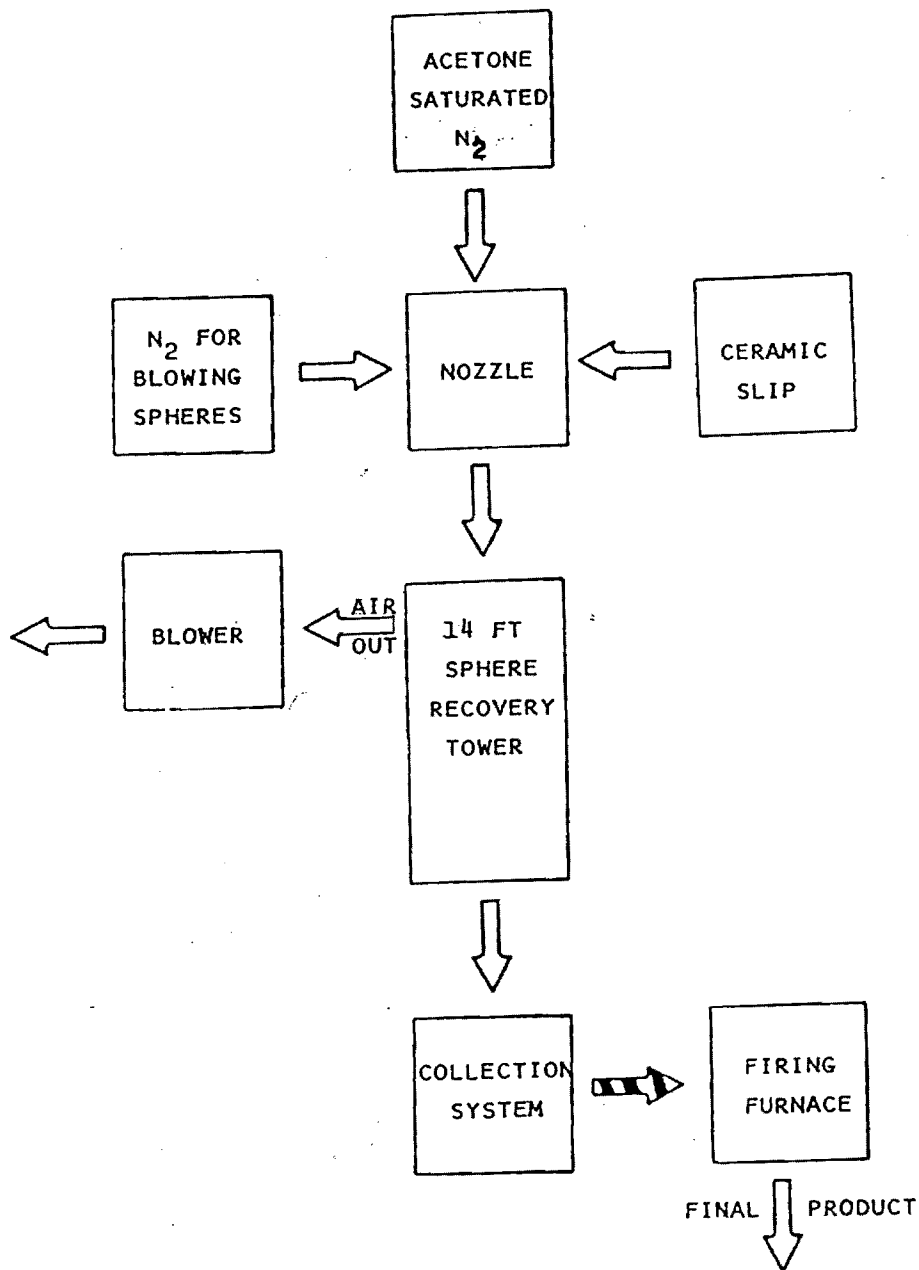


Figure 2.1.8

Schematic Process Diagram, Incorporating the 3.2 m Tall Sphere Recovery Tower, for the Manufacture of Low Density Ceramic Spheres.

## 2.2 VISCOSITY-SOLIDS RELATIONSHIP FOR ACETONE SLURRIES

The viscosity-solids concentration relation of alumina and zirconia suspensions in acetone has been investigated because these are the primary sphere forming systems. The addition of poly(methyl methacrylate), PMMA, provided steric stabilization to these slurries. Hence, the effective solids concentration was greatly different from the true solids concentration due to the adsorbed PMMA layer on the solids surface. A model was proposed to account for the thickness of the flexible adsorbed layer by considering the thickness changes with solids concentration. In this study, first, the adsorption behavior of PMMA onto alumina and zirconia surfaces was characterized by the adsorption isotherms. The adsorption isotherms conformed well to the BET and the Langmuir equations. From these isotherms, the monolayer adsorption and the PMMA equilibrium concentration of the liquid phase in the oxide suspensions were calculated. Because a constant layer thickness was found to be inadequate for describing the increase of solids content by the adsorbed PMMA layer, an equation was proposed to account for the variation of the layer thickness with solids content. The viscosity-solids content relationships were compared with Mooney's, Eilers', and Krieger and Dougherty's equations. It was found that viscosity could be expressed by the Eilers and the Krieger and Dougherty equations but not by the Mooney equation. Values for maximum volume fraction and intrinsic viscosity were obtained from the calculations accordingly. The maximum volume fraction values were found to increase with the surface average particle size, whereas the intrinsic viscosities were lowered as the surface area average particle size increased. The deviations of the intrinsic viscosity and the maximum volume fraction from theoretical values were explained by the presence of non-spherical particles and agglomerates.

The objective of this work was to study and model the viscosity of non-aqueous, steric, stabilized dispersions of ceramic powders as a function of solids concentration. The effects of the particle size, the surface area of the solids, the adsorbed polymer layer on ceramic particles, the intrinsic viscosity and the maximum solids concentration of the dispersions were also to be investigated. This study could provide guidelines for the property and viscosity controls of nonaqueous ceramic dispersions.

There have been many studies in the literature pertaining to the viscosity-concentration relation of ceramic suspensions. However these studies investigated the dispersions of uniform spheres, and corrections were made only for monodispersed particles coated with small molecules of constant layer thickness, whereas it was of interest here to examine the viscosity of concentrated suspensions of polydispersed particles. Moreover, a correction model for the apparent solids concentration was proposed to account for a flexible polymer layer adsorbed on the steric stabilized particles, which varies in thickness with crowding. In this study, the ceramic powders used were aluminum oxide and zirconium oxide. Acetone and PMMA

have been chosen for their effectiveness as a volatile solvent and a deflocculant, respectively, in the fabrication process of ceramic thin-wall hollow spheres. The role of PMMA in the oxide-acetone system is as a binder as well as to sterically stabilize the dispersion through adsorption at the solid/liquid interface. Therefore, an investigation of the adsorption isotherms of PMMA on oxides was also conducted to provide the information about the dispersibility of the slurries, and to calculate, indirectly, the apparent solids concentration and the viscosity of liquid phase.

### **2.2.1 SLURRY PREPARATION AND ADSORPTION/VISCOSITY PROCEDURES**

For this study, oxide powder/acetone suspensions of various solids concentrations, were stabilized by the addition of poly(methyl methacrylate) (PMMA), and were prepared for rheological evaluation. In order to examine the effects of particle size and size distribution of the powder on the rheological behavior, two types of commercially available alumina of the same chemical properties but different physical properties were used. Partially stabilized zirconia was also examined for comparison of the effects of the adsorbed PMMA layers at the solids/liquid interface on the rheological behavior of the suspensions. Adsorption experiments for PMMA on powders were conducted in order to provide information on dispersibility of the suspensions and for viscosity modeling.

**Materials** - The ceramic powders used in this study were aluminum oxide and partially stabilized zirconia (PSZ). Two types of commercially available aluminum oxide, A1000 and A3000 from ALCOA, were chosen. The PSZ powder was HSY3 grade with 5.4 w/o  $Y_2O_3$  as a stabilizer. These powders are described in Table 2.2.1.

The crystallites of Bayer alumina powders are often in the form of thin hexagonal plates in which the basal plane is parallel to the platelet surfaces. However, the powders may lose the plate-like morphology during ball milling subsequent to their calcination. Scanning electron micrographs of A3000 and A1000 alumina showed that the larger particles possess a platey morphology while the shapes of the other particles are irregular. Also from the particle size distributions, Figure 2.2.1, that A3000 has larger particle size and broader size distribution than A1000.

The scanning electron micrograph of HSY3 zirconia, showed many agglomerates consisting of sub-micron particles. These agglomerates may change the shape of the size distribution curve. This may explain why the serigraph curve of HSY3, Figure 2.2.2, does not show a substantial portion of those sub-micron particles, as indicated by the scanning electron micrograph of HSY3.

The polymer used in this study was Elvacite 2008 grade poly(methyl methacrylate) from DU PONT. The molecular weight of Elvacite 2008 is about 25,000, according

Table 2.2.1 Specifications of Alumina and Partially-Stabilized-Zirconia Powders.

Grade	Alumina		PSZ
	XA3000	XA1000	HSY3
Supplier	ALCOA <sup>1</sup>	ALCOA	Zirconia Sales <sup>2</sup>
Purity, %	99.7	99.7	99.6 <sup>3</sup>
Density, g/cc	3.98	3.98	6.05
Surface Area <sup>4</sup> , $m^2/g$	3.99	9.01	6.52
Average Particle Size <sup>5</sup> , $\mu m$	3.0	0.5	0.7

<sup>1</sup>Aluminum Company of America, Pittsburgh, Pa.

<sup>2</sup>Zirconia Sales (America), Inc., agent for Daiichi Kigenso, Osaka, Japan

<sup>3</sup> $ZrO_2 + Y_2O_3$

<sup>4</sup>Measured by Micromeritics Materials Analysis Lab using FlowSorb II

<sup>5</sup>Sedigraph median, data provided by suppliers

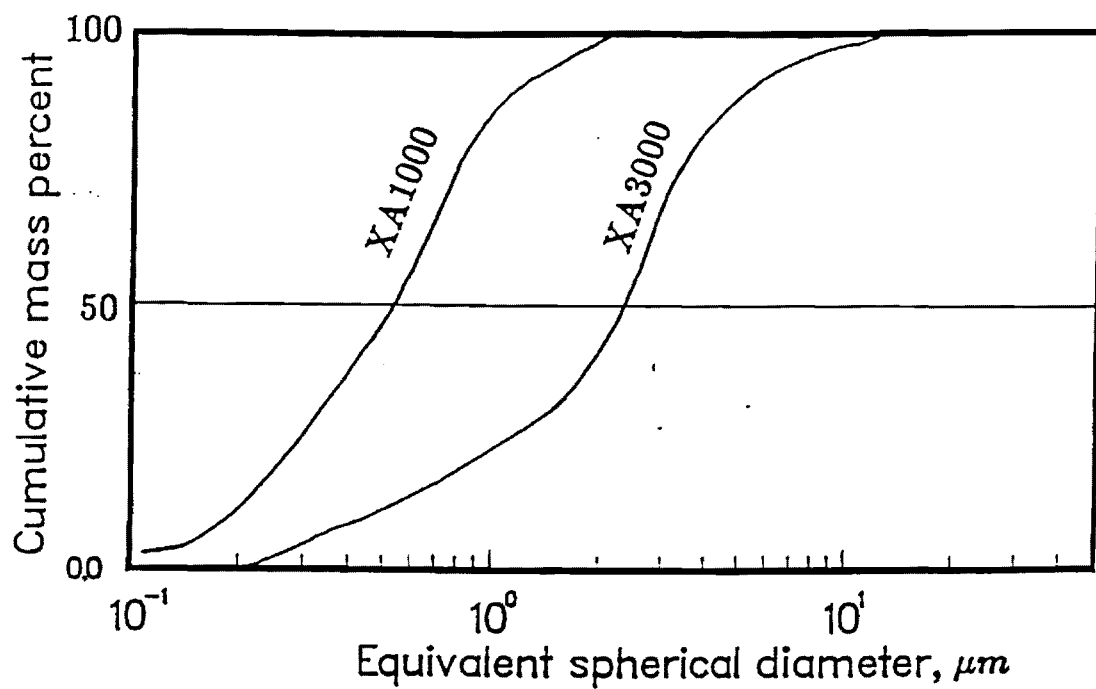


Figure 2.2.1 Particle Size Distribution of XA3000 and XA1000.

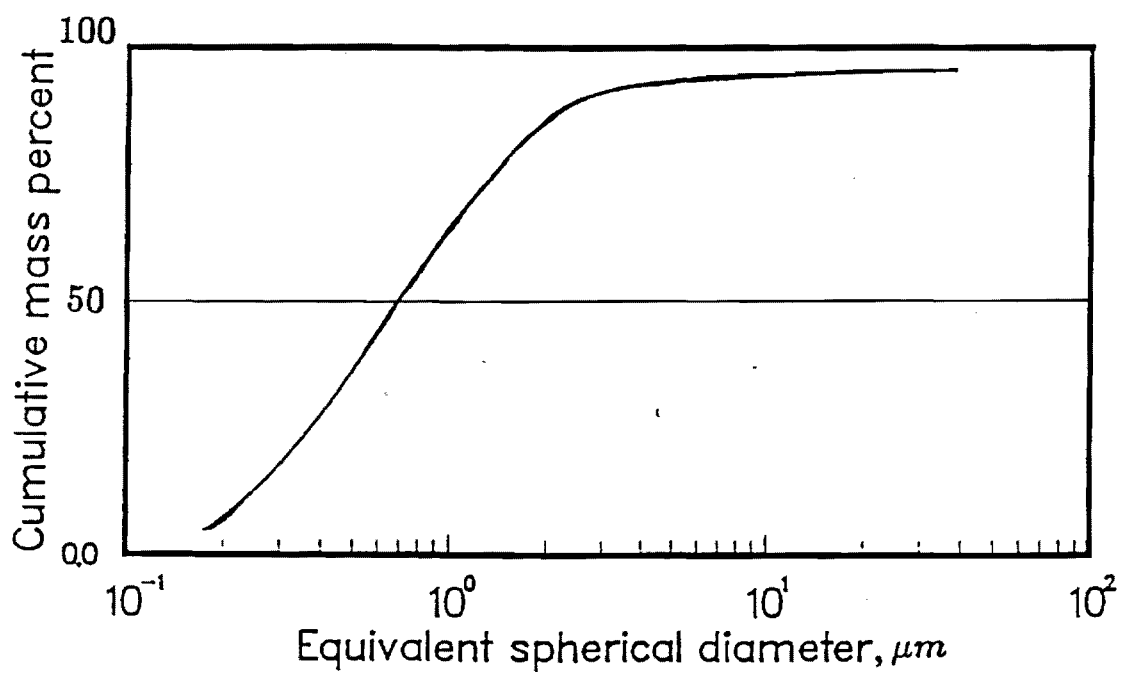


Figure 2.2.2 Particle Size Distribution of HSY3.

to the manufacturer's information. It was further analyzed with Gel Permeation Chromatography (GPC) for molecular weight distribution. The results indicated a weight average molecular weight,  $M_w$ , of 33,000, a peak molecular weight,  $W_p$ , of 41,500, a number average molecular weight,  $M_n$ , of 19,000, a Z average molecular weight,  $M_z$ , of 48,100, and a polydispersity,  $M_w/M_n$ , of 1.74.

The solvent was acetone ( $\text{CH}_3\text{COCH}_3$ ). It has a molecular weight of 58.08, a density of 0.79 g/cc at 20°C and a solubility parameter of 10, which makes acetone a good solvent for PMMA (solubility parameter = 9.5) [60]. Acetone was chosen as the solvent for this study because it is used in the production of ceramic thin-wall hollow spheres due to its high evaporation rate (evaporation rate = 1160 relative to n-BuOAc = 100). In the experiments, acetone was obtained in spectroanalyzed grade from Fisher Scientific Co.

**Dispersion Preparation** - The dispersions were prepared by mixing the batches of materials in 250 ml Nalgene bottles with zirconia mill balls for at least twenty four hours at room temperature. The twenty-four hour milling time was suggested to be sufficient for attaining adsorption equilibrium [44]. The volume of each slurry was about 50-70 ml. All the weighing operations for viscosity experiments were performed with a Sartorius analytical balance (model 1264MP) with an accuracy of 5mg, whereas those for isotherm experiments were performed with an August Sauter analytical balance having an accuracy of ~1 mg.

**Adsorption Experiments** - In the adsorption experiment, the solids concentrations of dispersions were 30 v/o (volume percent) for A1000 alumina and HSY3 zirconia, and 20 v/o for A3000 alumina. These concentrations were used to allow the slurries to flow easily during mixing. The original PMMA concentrations ranged from 2 w/o to 22 w/o.

After the dispersions were prepared, a typical adsorption experiment was conducted as follows: First, the dispersions were centrifuged at 1000-5000 RPM for a period of time ranging from 10 to 30 minutes depending on the powder property (e.g. finer powders require longer sediment time). The resulting clear supernatant solutions were removed for analysis. Next, the indices of refraction of these solutions were measured with the Abbe refractometer (American Optical, model 10450). For the purpose of quantitative analysis, appropriate calibration curves of refractive index versus PMMA concentration were constructed using a series of Elvacite 2008/acetone solutions of known concentrations. A typical refractive index curve is shown in Figure 2.2.3. The indices of refraction of these standard solutions were measured together with the samples of unknown concentration to eliminate the effects of refractometer and temperature fluctuations. Then, the concentrations of solutions were determined from



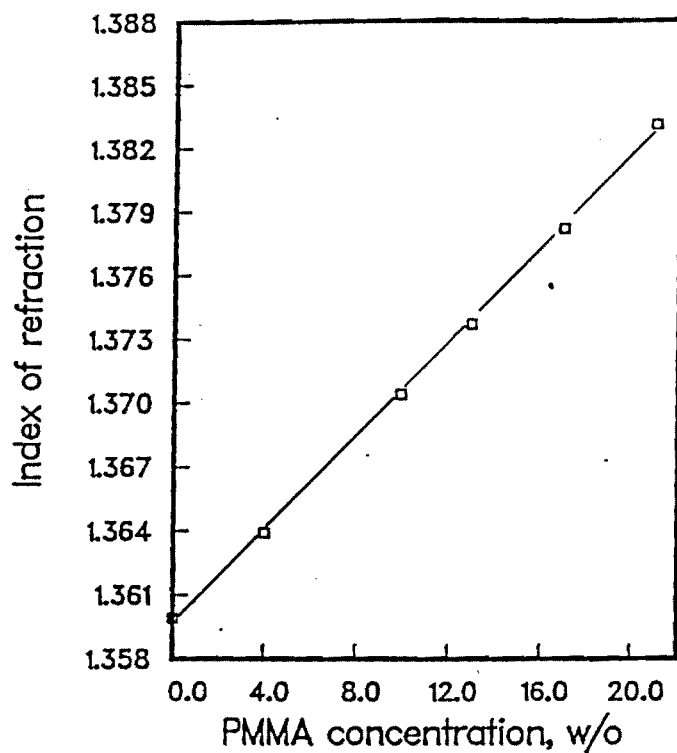


Figure 2.2.3

The Calibration Curve of the Refractive Index Versus Solution Concentration for PMMA/Acetone Solution - Used for Adsorption Analysis from HSY3, Temperature =  $18.1^{\circ} \pm 0.2^{\circ}\text{C}$ .

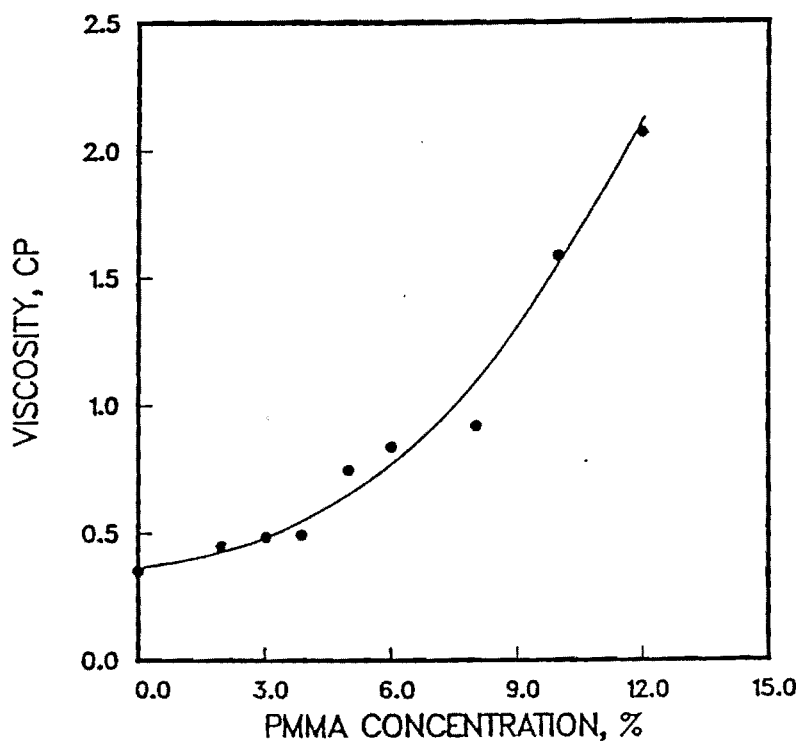


Figure 2.2.4

The Calibration Curve of the Viscosity of PMMA Solution Versus PMMA Concentration.

that specific calibration curve. These concentrations are the equilibrium concentrations of adsorption. The difference between the equilibrium and the original concentration gives the amount of adsorbed PMMA. Finally, the adsorption isotherm is plotted for the adsorbed amount as a function of equilibrium concentration.

**Viscosity Measurements** - These experiments were designed with high solids concentration in an attempt to simulate practical ceramic slurry preparation. The lowest concentrations were 29.04 v/o for alumina slurries and 28 v/o for HSY3 zirconia ones. The highest concentrations were 58.88 v/o for XA3000, 43.86 v/o for XA1000 and 39 v/o for HSY3 zirconia dispersions. The high concentration slurries were too thick to provide a reliable viscosity measurement due to the limitation of the viscometer and the poor workability of concentrated slurries. The solids concentration of the dispersions,  $\phi$ , termed the true volume fraction here, was calculated as follows:

$$\phi = \frac{V}{V + V_a + V_p} \quad (2.2.1)$$

where  $V$ ,  $V_a$  and  $V_p$  are the volumes of the powder, acetone, and PMMA, respectively. For each composition three dispersions were prepared and measured for viscosity. To determine the viscosity of the equilibrium liquid phase in the ceramic dispersions, a series of PMMA/acetone solutions of known concentration were also prepared for viscosity measurement. From the viscosity measurements of these PMMA solutions, a calibration curve was plotted as solution viscosity versus PMMA concentration, Figure 2.2.4.

The viscometer used here was the HAAKE viscometer. It is a Searle type coaxial cylinder viscometer which provides shear rates up to 2700 1/s and shear stress up to 1200 Pa. A desired measuring range can be set up by selecting an appropriate sensor system (including a sensor and a beaker). The geometry of the sensor (the bob) and the beaker (the cup) are designed to have a very low  $R_c/R_b$  ratio (1.02 - 1.14) and to trap air on the bottom of the sensor to eliminate end effect for precision measurements. The process is controlled through a Rotovisco RV20 and an IBM personal computer. This system provided continuous measurement and recording of shear rate, shear stress, viscosity and temperature. In addition, the temperature of the measuring unit was regulated by a HAAKE Circulator, a circulating water bath with thermal elements and a thermal set.

During viscosity measurement, the beaker was covered with a stainless steel plate designed to prevent volatile solvent evaporation. The sensors used here were SV1 for high-viscosity samples ( $> 400cp$ ), MV1 and MV2 for medium-viscosity, and NV for low-viscosity slurries and for all the PMMA/acetone solutions ( $< 10cp$ ). The samples were measured in the following manner: The shear rate was increased at a given rate

from zero to a shear rate at which shear thickening flow behavior was observed. Then the shear rate was returned to zero. All the measurements were performed at  $20^{\circ} \pm 0.2^{\circ}\text{C}$ .

### 2.2.2 ADSORPTION ISOTHERMS AND VISCOSITY-SOLIDS MODEL

Adsorption isotherms of PMMA onto alumina and zirconia powders were constructed. From the Langmuir and BET analyses of the isotherms, the conformations of the adsorbed PMMA layers were investigated. Furthermore, analyses of the isotherms provided an estimate of the apparent solids concentration, and allowed calculation of the viscosity of liquid phase, both which were important in viscosity modeling. Results of the viscosity measurements of the alumina and zirconia suspensions are presented as relative viscosity as a function of apparent solids concentration and are compared with the most common viscosity-concentration relationships applied to powder dispersions: the Mooney, the Eilers and the Krieger-Dougherty equations.

**Adsorption Isotherms** - The isotherms obtained under ambient condition for the adsorption of PMMA from acetone onto alumina and zirconia powders are seen in Figures 2.2.5 and 2.2.6. They are plotted as weight of PMMA adsorbed on per 100 grams of powder,  $N$ , versus equilibrium PMMA concentration,  $C$ .

A generalized form of the Langmuir adsorption model was developed by Brunauer, Emmett, and Teller in 1938 to include multilayer adsorption [59]. Basically, the BET model is a Langmuir adsorption in the first layer with liquid-like condensation on molecules adsorbed in the first layer. The assumptions made were:

1. in all layers except the first, the heat of adsorption is equal to the molar heat of condensation  $qL$ ;
2. in all layer except the first, the evaporation-condensation conditions are identical;
3. when the concentration becomes equal to the saturation concentration, the adsorbate condenses to a bulk liquid on the surface of the solid, i.e. the number of layers becomes infinite.

Hence, a linear form of the BET equation for polymer adsorption on solid surface is given as

$$\frac{C}{N(1-K)} = \frac{1}{N_m K} + \left( \frac{K-1}{N_m K} \right) C \quad (2.2.2)$$

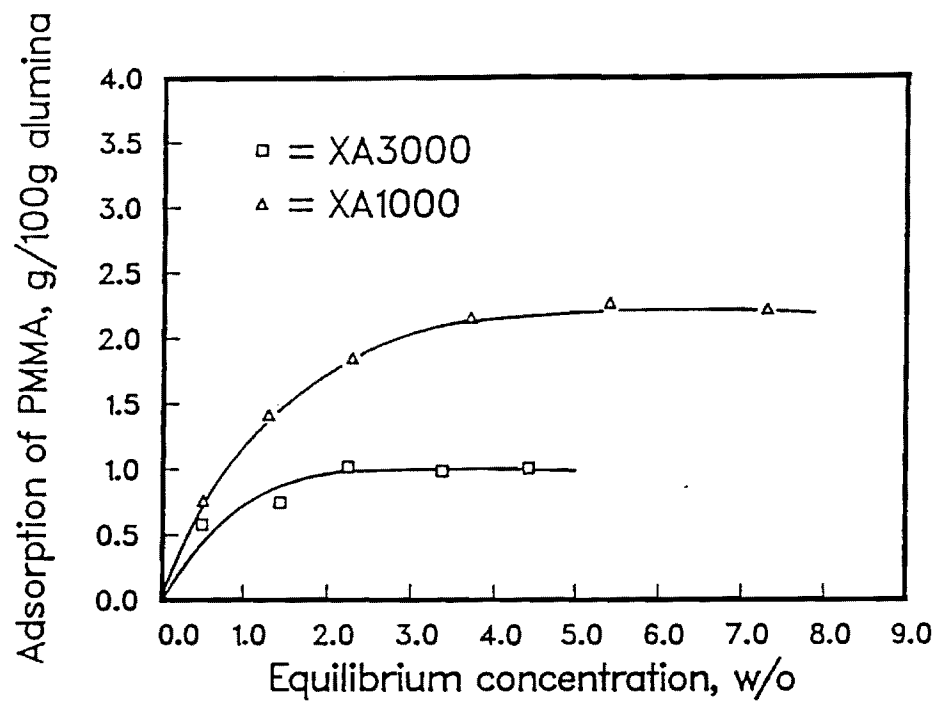


Figure 2.2.5

Adsorption Isotherms of PMMA onto XA1000 and XA3000 Alumina from Acetone.

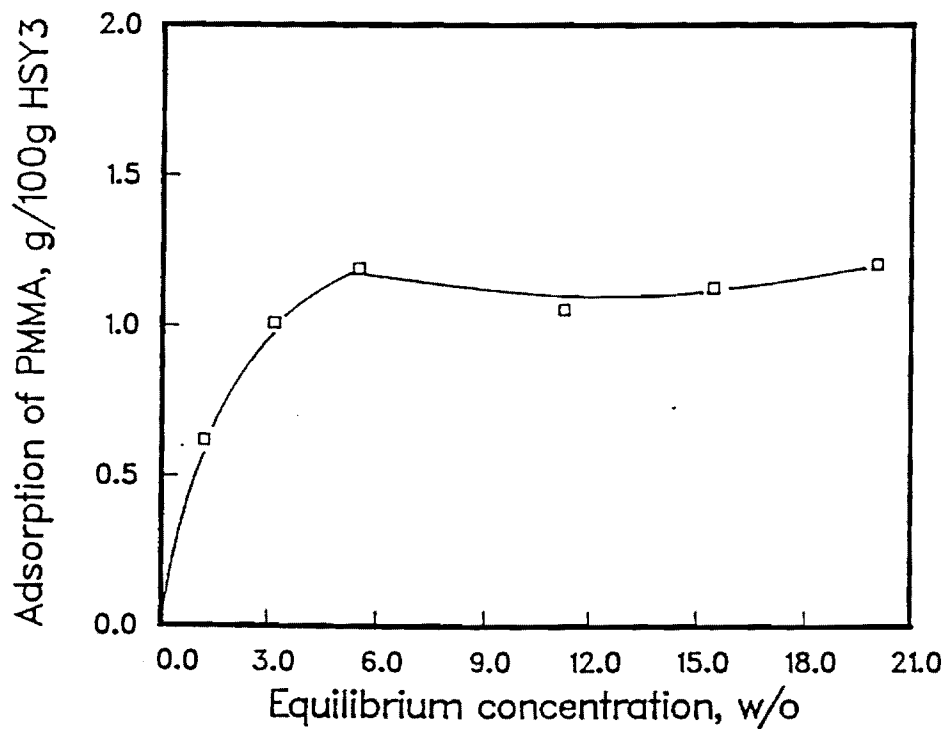


Figure 2.2.6

Adsorption Isotherm of PMMA onto HSY3 Zirconia from Acetone.

where  $C$  is the equilibrium solute concentration,  $N$  is the amount adsorbed per unit weight of solid,  $N_m$  is amount adsorbed in a monolayer, and  $K$  is a system constant.

Likewise, the values of  $N_m$  and  $K$  can be calculated from the plot of the left hand side of Eq. (2.2.2) versus concentration  $C$ . The parameter  $K$  is practically taken as  $K = \exp[(q^{st} - q_L)/RT]$ , where  $(q^{st} - q_L)$  is the net heat of adsorption;  $q_L$  the heat of condensation for gas;  $q^{st}$  the differential heat of adsorption of the monolayer on solid surfaces. In addition, an important factor for successful application of the BET equation is that the  $K$  value should be high enough to ensure the separation of monolayer and multilayer formation [59]. On the other hand, it should be low enough to eliminate appreciable localization of the adsorbate molecules. The net result of these two opposing requirements for  $K$  value is that  $K$  should have an optimum value.

In gaseous adsorption, the BET equation fails in the low pressure region. Brunauer et al adduce energetical non-uniformity as the reason[59]. In adsorption from solutions, however, a smoothing out of the surface non-uniformity occurs[57] when the solid surface is covered with solvent because the high energy regions are made relatively inaccessible to solute by their firm retention of solvent molecules. Consequently, the values of  $N_m$  may not be representative of a close packed solute monolayer.

**BET Analysis of Adsorption Isotherms** - BET plots of adsorption of PMMA onto A1000, A3000 and HSY3 are shown in Figure 2.2.7. They were plotted as  $C/N(1-K)$  versus  $C$  and least squares lines, which are described in Table 2.2.2, were drawn through the data points. From the slopes ( $s$ ) and intercepts ( $i$ ) of these straight lines, the monolayer adsorption capacity  $N_m$  and the constant  $K$  were determined;

$$N_m = \frac{1}{s + i} \quad (2.2.3)$$

$$K = \frac{s}{i} + 1 \quad (2.2.4)$$

and listed in Table 2.2.2.

The  $N_m$  values for A1000 and A3000 agree well with the plateau level adsorption in their isotherms. However, the  $N_m$  for HSY3 is much lower than the plateau adsorption. This deviation may have resulted from experimental errors. Furthermore, in the analysis on the relation between  $N_B$  from the "Point B"<sup>1</sup> and  $N_m$  from the BET equation, several workers have noted that *satisfactory agreement between the two quantities may not be achieved unless the BET equation is applied over a range of the isotherm*

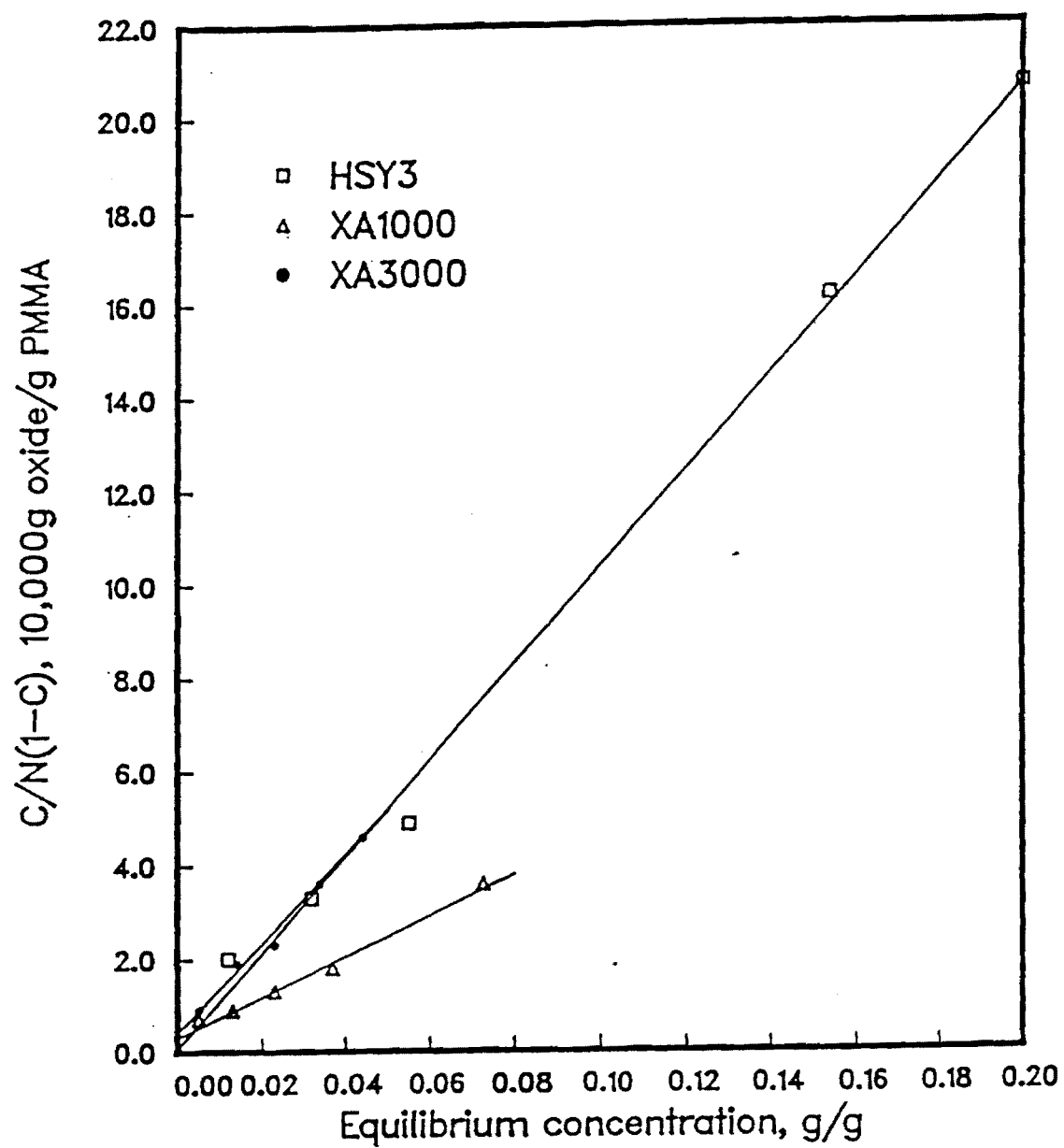


Figure 2.2.7 BET Plot for the Adsorption of PMMA onto XA1000, XA3000 and HSY3.

Table 2.2.2 Analysis of Adsorption Isotherms by BET Theory.

(a) Fitting of Experimental Data to the BET Equation

Oxides	Best fit equation	R
XA1000	$\frac{C}{N(1-C)} = 0.427C + 3.50 \times 10^{-3}$	0.992
XA3000	$\frac{C}{N(1-C)} = 0.948C + 4.19 \times 10^{-3}$	0.992
HSY3	$\frac{C}{N(1-C)} = 1.032C + 0.53 \times 10^{-3}$	0.999

(b) Adsorption Analysis Using the BET Equation

Oxides	$N_m$ , g/100g oxide	$K$
XA1000	2.323	123.14
XA3000	1.050	227.31
HSY3	0.968	1948.17

(c) Heat of Adsorption and  $N_{m,area}$

Oxides	Heat of adsorption, cal/mol	$N_{m,area}$ , mg/m <sup>2</sup>
XA1000	2850.0	2.58
XA3000	3213.1	2.63
HSY3	4485.1	1.48

(d) Area Occupied by One PMMA Molecule Adsorbed on Oxide Surface

Oxides	$a_{m,BET}$ , Å <sup>2</sup>	$a_{m,L}$ , Å <sup>2</sup>
XA1000	1610.27	1308.05
XA3000	1577.43	1308.05
HSY3	2790.67	1308.05

which contains Point B[59]. Therefore, insufficient data points in the isotherm might cause the deviation of  $N_m$  from  $N_B$  in this study.

*'Point B: the point of inflection in the Langmuir type of adsorption isotherm, that is, the point at which the linear plateau portion begins. It is sometimes used as an indicator of the completion of the monolayer.'*

Furthermore, an estimate of the net heat of adsorption,  $(q^{st} - q_L)$ , was obtained by the following equation:

$$q^{st} - q_L = RT \ln K \quad (2.2.5)$$

by using  $R = 1.987 \text{ calK}^{-1}\text{mol}^{-1}$ ,  $T = 298^\circ\text{K}$  and each  $K$  in Table 2.2.2. The results were listed in Table 2.2.2 along with the  $N_{m,area}$  values. The values for heat of adsorption of PMMA on alumina and zirconia range from 2.9 kcal/mol to 4.5 kcal/mol. In the literature, values of heat of adsorption of 2.0 and 1.7 kcal/mol have been found for adsorption of naphthalene and  $\alpha$ -methyl naphthalene onto silica gel from n-heptane[58]. Higher values of 5-10 kcal/mol were also found for the heat of adsorption of aliphatic alcohols from benzene onto alumina. Therefore, equation (2.2.5) is considered to be able to provide a feasible computation of the heat of adsorption. The  $N_{m,area}$  value for the adsorption on HSY3 was lower than those on alumina. Again, it may result from either one of the following two phenomena. First, the area occupied by one PMMA molecule on the HSY3 surface is larger than on the alumina surface; or the surface coverage on the former is lower than the latter. Since the heat of adsorption for PMMA adsorbed by HSY3 zirconia is considerably higher (indicating a stronger affinity of PMMA molecules for HSY3 zirconia than for alumina), more segments in one polymer molecule may lie on the zirconia surface than extend into the liquid. Consequently, each molecule occupies more surface area, that is, fewer PMMA molecules are adsorbed per unit surface area of zirconia-yielding lower  $N_{m,area}$ .

Since the poly(methyl methacrylate) may attach on basic sites of oxides by acidic methacrylate groups, the PMMA molecules are adsorbed on solids at multiple points of attachment. Parts of PMMA segments may lie in the layer immediately adjacent to the surface, which are called "trains", and other segments may extend into the bulk solution, called "loops" or "tails" [39]. It was suggested that as polymer concentration increases, the fraction of segments in "trains" should decrease and cross-linking of polymers occurs[36,39]. Since the PMMA concentration ranges are high in this study, there may be more segments in "trains" on zirconia than on alumina, and the polymer molecules may be more highly entangled.

The average area occupied by a molecule of adsorbate in the completed monolayer,  $a_m$ , can be estimated from the monolayer adsorption or from the geometrical



calculation of the molecules. By comparing the results from these two different computations, one can approximate the conformation of the adsorbed layer.

The values of  $a_m$  from the monolayer adsorption, termed  $a_{m,BET}$  here, were calculated by

$$a_{m,BET} = A \times \frac{M}{N_m} \times \frac{1}{L} \times 20^{20} \quad (2.2.6)$$

where  $A$  is the specific  $N_2$  surface area of the adsorbent in  $m^2/g$ ,  $M$  is the molecular weight of the polymer,  $N_m$  is in grams of polymer per gram of solid, and  $L$  is the Avogadro constant. For  $M$ , the average molecular weight of 25,000 was used. The resultant  $a_{m,BET}$  values, in  $\text{\AA}^2$ , are listed in Table 2.2.2.

The  $a_m$  value was also obtained by assuming that the arrangement of the adsorbed molecules on the surface is the same as it would be on a plane surface immersed in the bulk liquid of the adsorbate without disturbing the pre-existing arrangement. Therefore, the area occupied by one PMMA molecule of density of 1 g/cc, termed  $a_{m,L}$ , is

$$\begin{aligned} a_{m,L} &= 1.091 \left( \frac{M}{\rho L} \right)^{2/3} \times 10^{16} \\ &= 1308.05 \text{\AA}^2 \end{aligned} \quad (2.2.7)$$

where 1.091 is the packing factor for 12 nearest neighbors in the bulk and six on the plane surface[59]. Since the  $a_{m,L}$  value represents the area of adsorbent occupied by a molecule with a cubic form, the divergence between  $a_{m,BET}$  and  $a_{m,L}$  indicates that the shape of the adsorbed molecule is deviated from cubic. The  $a_{m,BET}$  value of each PMMA/oxide system are higher than the  $a_{m,L}$  value. Hence, more of the segments in the adsorbed polymer molecule apparently lie on the surface of the solid than are solvated into the liquid medium. The higher  $a_{m,BET}$  value for HSY3 compared to those for alumina further prove that the stronger affinity of PMMA for HSY3 zirconia results in a thinner layer of the adsorbed molecules on the HSY3 surface.

**Viscosity-Solids Content Relation of Slurry** - In general the dispersions prepared in this study exhibited Newtonian flow behavior at low solids content. As the concentration increased, the flow behavior became strongly dependent on the shear rate. A typical viscosity-shear rate flow curve in this analysis could be divided into three continuous stages: pseudoplastic (shear thinning) flow at low shear rates, Newtonian flow at medium shear rates, and shear thickening (dilatant) flow at high shear rates. At low solids content, the Newtonian range extended to high shear rate. As solids content increased, the Newtonian portion became progressively narrower and finally disappeared producing a minimum in the flow curve.

Although it was not shown in the flow curve here, the presence of Newtonian behavior at sufficiently low shear rate was of little doubt. This low-shear Newtonian behavior occurs due to the absence of sufficient forces to break up agglomerates or affect particle alignment[63]. In the range of slightly higher shear rates, the flowing particles either align or weak agglomerates are progressively broken due to the imposed shear[63]. Therefore, shear-thinning flow behavior emerges. As the shear stresses increase to levels at which the size of the aggregates has been reduced to a minimum, the flow should become Newtonian (constant viscosity). Above a particular shear rate, the flow becomes dilatant. This is due to the hindered rotation and mutual particle interference[6]. The dilatant behavior might also result from the turbulent flow in the viscometer at high shear rate[7]. Above the turbulent point, the kinetic energy of flow is diverted to nonstreamline phenomena so that more stress is required for an arbitrary increase in the shear rate than for laminar flow. This phenomenon may be misinterpreted as dilatancy.

According to the mechanisms explained above, one can conclude that the Newtonian range in the viscosity-shear rate curve indicates minimal particle-particle interaction in the sheared suspensions. Therefore, the minimum viscosity in the flow curve was recorded and used in modeling viscosity relationships. The results are seen in Tables 2.2.3 to 2.2.5.

To compute the relative viscosity of the suspension, first, the BET equation obtained previously, Table 2.2.2, was used to calculate the PMMA equilibrium concentration in the liquid phase in the suspension, as shown in the third column in Tables 2.2.3-2.2.5. Then, the viscosity of the liquid phase (PMMA/acetone solution) was determined by interpolating from a calibration curve of solution viscosity versus PMMA concentration, Figure 2.2.4, and the solution viscosity was listed in the fourth column in Tables 2.2.3-2.2.5. Finally, the relative viscosity,  $\eta_r$ , was obtained as the ratio of the viscosity of the suspension to that of the equilibrium liquid medium, Tables 2.2.3-2.2.5. Furthermore, the standard deviation of the relative viscosity,  $\sigma_{\eta_r}$ , was calculated from multiple samples and the results are listed in Table 2.2.6 along with the average relative viscosity. In general, standard deviations for relative viscosity were less than 9% of the average viscosity.

**Comparison of Viscosity Results with Classic Equations** - The simple viscosity-concentration functions were tested by fitting them to the data of Tables 2.2.3-2.2.5, by adjustment of the parameters  $[\eta]_0$  and  $\phi_{max}$ . These three equations are:

Table 2.2.3                      Viscosity of XA1000 Dispersion and Calculation of the Relative Viscosity

Volume fraction	Viscosity, cp	Liquid phase		$\eta_r$
		conc., g/g	viscosity, cp	
.2904	15.45	.0851	1.095	14.1
.3396	28.29	.0824	1.018	27.80
.3889	80.38	.0861	1.124	71.51
40.87	110.82	.0808	.972	114.02
41.87	138.44	.0838	1.058	130.84
43.86	259.09	.0812	.983	253.45

Table 2.2.4                      Viscosity of XA3000 Dispersion and Calculation of the Relative Viscosity

Volume fraction	Viscosity, cp	Liquid phase		$\eta_r$
		conc., g/g	viscosity, cp	
.2904	4.13	.05032	.763	5.42
.3395	5.54	.05062	.764	7.24
.3889	10.77	.06186	.827	13.02
.4885	36.75	.0904	1.247	33.14
.5386	84.57	.1090	1.7813	51.7
.5587	196.2	.1175	2.025	91.5
.5888	584.69	.1316	2.254	269.8

Table 2.2.5                      Viscosity of HSY3 Dispersion and Calculation of the Relative Viscosity

Volume fraction	Viscosity, cp	Liquid phase		$\eta_r$
		conc., g/g	viscosity, cp	
.28	11.85	.0330	.4867	24.35
.30	15.25	.0332	.4874	31.375
.33	34.46	.0379	.4940	69.755
.35	50.75	.0336	.4894	103.70
.37	68.39	.0365	.4923	138.91
.39	115.28	.0396	.5174	222.81

Table 2.2.6                      Mean and Standard Deviation of the Relative Viscosity of XA1000, XA3000 and HSY3 Dispersions

XA3000			XA1000			HSY3		
$\phi$	$\bar{\eta}_r$	$\sigma_{n-1}$	$\phi$	$\bar{\eta}_r$	$\sigma_{n-1}$	$\phi$	$\bar{\eta}_r$	$\sigma_{n-1}$
.2904	5.42	.799	.2904	14.10	.213	.28	24.35	.0849
.3395	7.24	1.937	.3396	27.80	.431	.30	31.375	.1626
.3889	13.02	1.890	.3889	71.51	.389	.33	69.755	9.27
.4885	33.14	1.690	.4087	114.02	4.476	.35	103.7	.0283
.5386	51.70	3.224	.4187	130.84	3.366	.37	138.91	7.76
.5587	91.50	2.793	.4386	263.45	8.754	.39	222.81	77.35
.5888	214.69	26.98						

Eilers' equation:

$$\eta_r = \left( 1 + \frac{[\eta]_i \phi}{2 \left( 1 - \frac{\phi}{\phi_{max}} \right)} \right)^2 \quad (2.2.8)$$

Mooney's equation:

$$\eta_r = \exp \left( \frac{[\eta]_i \phi}{1 - \frac{\phi}{\phi_{max}}} \right) \quad (2.2.9)$$

and Krieger-Dougherty's equation:

$$\eta_r = \left( 1 - \frac{\phi}{\phi_{max}} \right)^{-[\eta]_i \phi_{max}} \quad (2.2.10)$$

Here  $\phi$  is the solids content,  $[\eta]_i$  is the intrinsic viscosity, and  $\phi_{max}$  is the maximum solid volume fraction at which  $\eta \rightarrow \infty$ . It was not unexpected that the experimental results did not agree with any of the equations above because of the increase in the effective solids content from adsorption of PMMA on the oxide surface. To provide a realistic solids load effect, the solids content had to be corrected for the thickness of the adsorbed PMMA layer.

Traditionally, the apparent volume fraction,  $\phi_{app}$ , is calculated from the original volume fraction  $\phi_o$ , the diameter of the suspension particle  $D$ , and the thickness of the adsorbed layer  $\Delta$  by [22,64].

$$\phi_{app} = \phi_o \left( 1 + 6 \frac{\Delta}{D} \right) \quad (2.2.11)$$

Equations 2.2.8, 2.2.9, and 2.2.10 can then be modified by substituting  $\phi_{app}$  for  $\phi$  using Eq. (2.2.11).

Usually, when  $\phi$  is corrected to  $\phi_{app}$  with Eq. (2.2.11), the layer thickness is considered a constant for a given powder/dispersant system. For sterically stabilized dispersions, the adsorbed layer thickness,  $\Delta$ , can be estimated from the monolayer adsorption and from the radius of gyration of PMMA in acetone. These two methods are described in the following.

**Calculation of  $\delta_1$  from Monolayer Adsorption** - For a close packed monolayer, the layer thickness, denoted  $\delta_1$  here, can be calculated from monolayer adsorption,  $N_{m,area}$  (listed in Table 2.2.2), and the density of PMMA in the adsorbed layer,  $\rho$ , by

$$\delta_1 = \frac{N_{m,area}}{0.94\rho} \quad (2.2.12)$$

where 0.94 is the close packing factor. The density of PMMA in the adsorbed layer is not known and thus it was assumed to be 1 g/cc, which is the density of the PMMA powder. Accordingly, the  $\delta_1$  values for PMMA on A1000, A3000, and HSY3 are calculated to be 27.4 Å, 28.0 Å and 15.8 Å respectively.

**Calculation of  $\delta_2$  from Radius of Gyration** - In many cases, the thickness of the adsorbed polymer layer is generally of the order of the diameter of the free coil in solution[39,48,49,50], and computation of the radius of gyration will yield an estimate of the thickness of the layer. The radius of gyration, which is a statistical approach to polymer chain dimensions, is calculated from the Flory-Fox relation[49]

$$(\bar{S}^2)^{1/2} = \left( \frac{M_w[\eta]}{\Phi} \right)^{1/3} \quad (2.2.13)$$

where  $M_w$ , is the weight molecular weight of polymer,  $[\eta]$  is intrinsic viscosity, and  $\Phi$ , the Flory-fox hydrodynamic parameter, is equal to  $3.2 \times 10^{23} \text{ ml/mole.cm}^3$ . The intrinsic viscosity of Elvacite 2008 in acetone was calculated from two parameters,  $K$  and  $a$ , by

$$[\eta] = KM_w^a \quad (2.2.14)$$

According to the *Polymer Handbook*[65], at 25°C, the average values of  $K$  and  $a$  for PMMA at a molecular weight of  $2 \sim 740 \times 10^4$  are  $6.77 \times 10^{-3} \text{ ml/g}$  and 0.71 respectively - measured with light scattering method. Therefore, the  $[\eta]$  value is equal to 10.928 ml/g for  $M_w = 33,000$ , and the radius of gyration is calculated to be 104Å. In this case, the adsorbed PMMA layer, denoted  $\delta_2$ , was approximated as 2x(radius of gyration), which becomes 208Å. The particle sizes of A1000, A3000, and HSY3 powder used in Eq. (2.2.11) were the surface area average diameter,  $D$ . They were calculated by

$$D = \frac{6}{\rho_p A} \quad (2.2.15)$$

where  $\rho_p$  is the density of the powder and  $A$  is the specific surface area of the powder. The resultant diameter values for XA1000, XA3000, and HSY3 are 1673.1A,

3778.6Å and 1521.1Å. Using both  $\delta_1$  and  $\delta_2$  for  $\Delta$  and the  $D$  values obtained above, the solids content was modified by using  $\phi_{app}$  from Eq. (2.2.11) and the viscosity was again fit to the Eilers, Mooney, and Krieger-Dougherty equations. It was found that the modified data using a constant layer thickness correction did not agree with any of the equations. Examples are shown in Figure 2.2.8 for A3000 dispersions. Furthermore, it was noted that for  $\Delta$  values varying between  $\delta_1$  and  $\delta_2$ , the experimental data would not fit either the Eilers, the Mooney, or the Krieger-Dougherty functions simply by employing the correction made with Eq. (2.2.11). The curves also showed that the increases of  $\phi$  from  $\phi_o$  to  $\phi_{app}$  were less at high solids content than at low solids content in order to fit those viscosity-concentration functions. This indicates that the adsorbed layer may not be of constant thickness as  $\phi$  increases. Therefore, a model considering varying layer thickness was developed and is described in the following section.

**Model For Calculation of Apparent Volume Fraction** - The basic concept of the model for modification of the apparent volume fraction is that the thickness of the adsorbed polymer layer is not constant but varies with the solids concentration. Since the PMMA chain molecule is flexible and of a rather high molecular weight, its effective dimension in acetone can be greatly decreased under compression which probably occurs at high solids content where interparticle space is smaller than the double PMMA dimension (freely extending) in acetone. Therefore, the adsorbed PMMA layer was considered to extend fully into the liquid medium in dilute suspensions, and to be progressively compressed toward the solids surface as the solids concentration increases.

Based on the concept described above, the thickness of the adsorbed layer has two limits. The upper limit,  $\delta_{max}$  exists when the adsorbed polymer chain can extend freely into the liquid phase. This can be approximated by the radius of gyration of PMMA in acetone, i.e.  $\delta_{max} = \delta_2$  as calculated in the previous section. The lower limit of the layer thickness,  $\delta_{min}$ , would be reached when the adsorbed polymer molecules coil or lie on the solids surface. This occurs as the solids fraction  $\phi$  reaches  $\phi_{max}$ . This thickness can be calculated from the monolayer adsorption for complete surface coverage, that is,  $\delta_{min} = \delta_1$ . As a summary, the boundary conditions are: when the solids fraction  $\phi$  equals  $\phi_{max}$ , the layer thickness becomes  $\delta_{min}$ ; as  $\phi$  decreases, the layer thickness approaches  $\delta_{max}$  and after  $\phi$  is lower than an arbitrary solids fraction, the layer thickness becomes constant and is equal to  $\delta_{max}$ .

According to the boundary conditions above, an equation was developed to modify the solids concentration for the layer thickness between  $\delta_{max}$  and  $\delta_{min}$ :

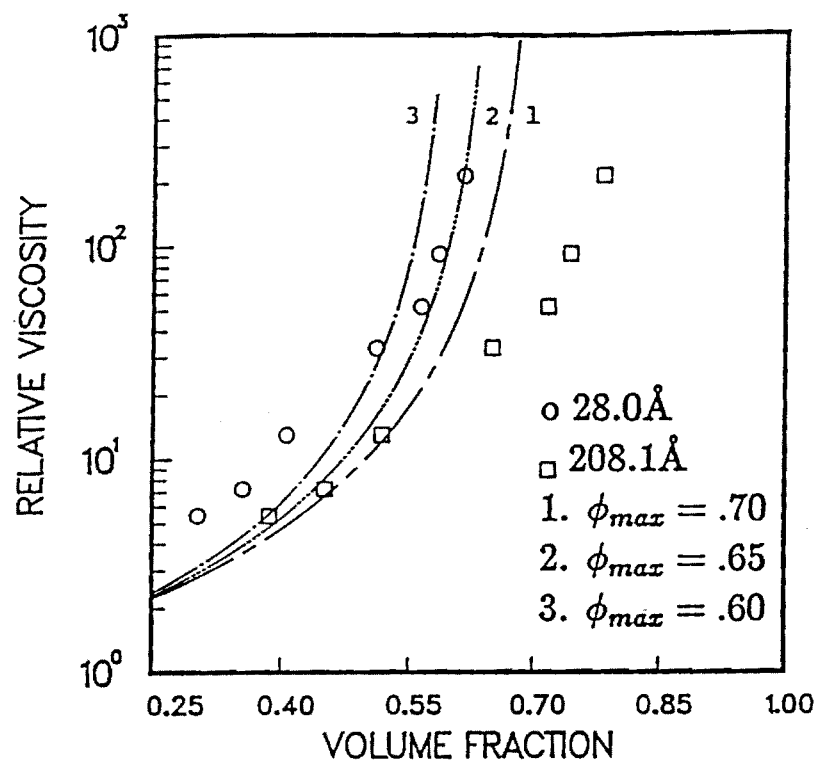


Figure 2.2.8

Comparison of the experimental results with the Eilers equation for  $[\eta]_f = 2.5$ ,  $\phi_{max} = 0.7$  (curve 1),  $\phi_{max} = 0.65$  (curve 2), and  $\phi_{max} = 0.6$  (curve 3); the volume fraction of XA3000 slurry was corrected for the thickness of the adsorbed layer for  $\Delta = 28\text{Å}$  and  $\Delta = 208.13\text{Å}$ , using Eq. 2.2.8.

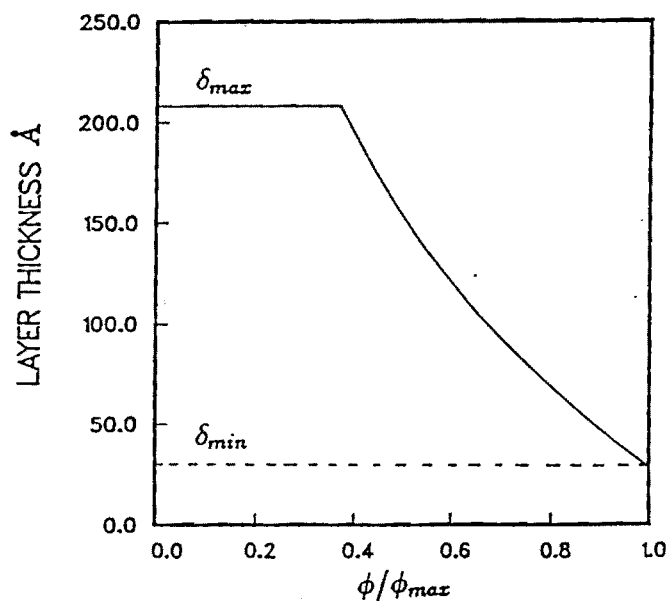


Figure 2.2.9

Thickness of Adsorbed Polymer Layer Versus Solids Volume Fraction.



$$\phi_{app} = \phi \left\{ \frac{D + 2 \left[ \left( 1 - \ln \left( \frac{\phi_{max}}{\phi} \right) \right) \delta_{min} + \ln \left( \frac{\phi_{max}}{\phi} \right) \delta_{max} \right]}{D} \right\}^3 \quad (2.2.16)$$

Equation (2.2.16) reduces to  $\phi_{app} = \phi(1 + 2\delta_{min}/D)^3$  at  $\phi = \phi_{max}$ , and becomes  $\phi_{app} = \phi(1 + 2\delta_{max}/D)^3$  when  $\ln(\phi_{max}/\phi) \geq 1$  (i.e.  $\phi \leq \phi_{max}/e$ ). In other words, the layer thickness is a constant,  $\delta_{max}$ , when solids content,  $\phi$ , is no greater than an arbitrary solids content,  $\phi_{max}/e$ . This arbitrary solids content is believed to be a function of the nature of the suspension powders, as is implied by  $\phi_{max}/e$ . Because the value of  $\phi_{max}$  is not readily available, the solids content corresponding to the onset of the compression of adsorbed PMMA layer can not be known in advance.

The proposed variation of layer thickness with solids content, Figure 2.2.9, suggests that the compression rate of the adsorbed layer is decreasing as solids content increases. This is explained physically by the increasing difficulty in compressing the adsorbed layer as the adsorbed layer becomes denser.

**Experimental Result Modified with Flexible Layer Model** - The experimental data was fit to Eq. (2.216) and one of the viscosity-concentration functions simultaneously. This process provided unique values for  $[\eta]_t$  and  $\phi_{max}$ .

For the best fit Mooney equation the resultant  $[\eta]_t$  and  $\phi_{max}$  values were not reasonable. For example, the data required  $[\eta]_t = 2.0$  and  $\phi_{max} = 0.96$  for XA3000 suspensions with a standard deviation of 10.64. Since the upper limit on  $\phi_{max}$  is 0.74 (for uniform spheres, whereas for polydisperse particles, the highest  $\phi_{max}$  ever reported is 0.82) and the lower limit on  $[\eta]_t$  is 2.5 (for rigid particles), it must be concluded that the Mooney equation is unsuitable here. However, both the Eilers equation and the Krieger-Dougherty equation fit the data with realistic values of  $[\eta]_t$  and  $\phi_{max}$ . The  $[\eta]_t$ ,  $\phi_{max}$  values and the standard deviation from the best fit,  $\delta$ , are listed in Table 2.2.7. The experimental data with the solids fraction modified by Eq. (2.2.16) are plotted in Figures 2.2.10 and 2.2.11. The curve drawn through the data points are the Eilers equation and the Krieger-Dougherty equation using the  $[\eta]_t$  and  $\phi_{max}$  values in Table 2.2.7.

Both the Eilers and Krieger-Dougherty equations provide equally good agreement (almost the same  $\delta$ ) with the experimental data. One should bear in mind that the Krieger-Dougherty equation was derived as a modification of Mooney's functional analysis while Eilers obtained his equation empirically. Furthermore, the  $[\eta]_t$  and  $\phi_{max}$  values obtained from the Eilers equation are, generally, very close to those from the Krieger-Dougherty equation.

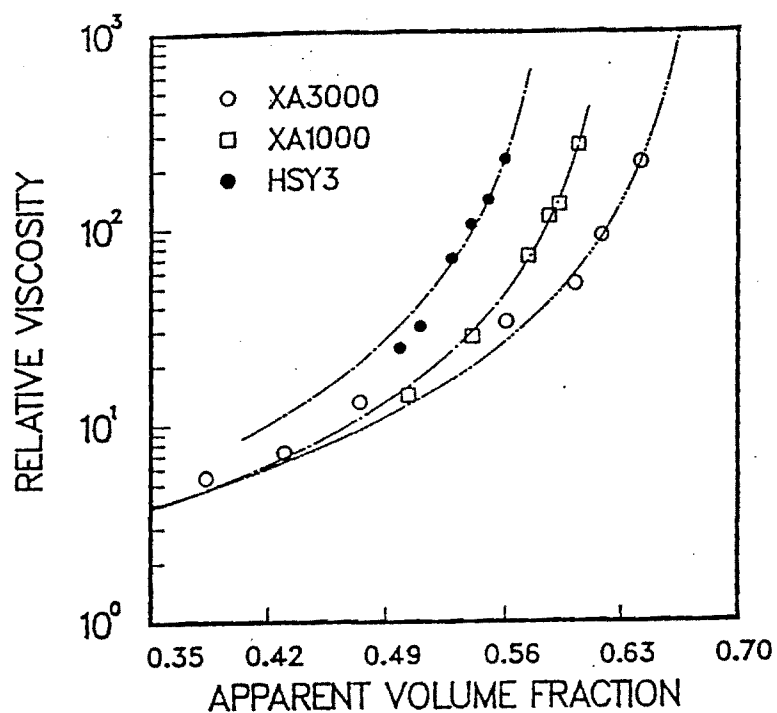


Figure 2.2.10

Relative Viscosity Versus Apparent Viscosity Calculated from Eq. 2.2.16 and the Eilers Equation.

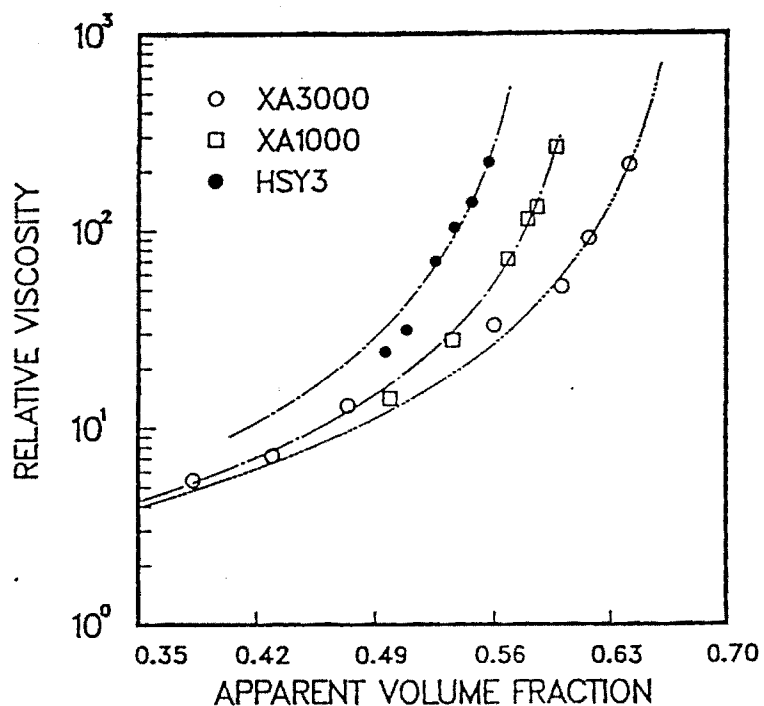


Figure 2.2.11

Relative Viscosity Versus Apparent Viscosity Calculated from Eq. 2.2.16 and the Krieger-Dougherty Equation.

Table 2.2.7

The values of  $[\eta]_t$ ,  $\phi_{max}$  and  $\sigma$  for XA1000, XA3000 and HSY3 for the Eilers and the Krieger-Dougherty Equations.

Oxides	Eilers'			Krieger-Dougherty's		
	$[\eta]_t$	$\phi_{max}$	$\sigma$	$[\eta]_t$	$\phi_{max}$	$\sigma$
XA3000	2.68	0.685	4.64	2.80	0.682	4.55
XA1000	2.42	0.634	5.73	2.81	0.624	5.69
HSY3	3.05	0.597	8.18	3.22	0.592	8.36

For the A1000 system, the reason that the  $[\eta]_f$  values from the Eilers equation are a little lower than 2.5 and greatly different from that of the Krieger-Dougherty equation is not clear. However, two possibilities were considered:  $\phi_{max}$  and experimental error in viscosity. Since the quantity of  $\phi_{max}$  used in correcting the solids content has a greater effect on  $\phi_{app}$  at low solids concentration than at high solids concentration, an error in  $\phi_{max}$  will result in an aberration in  $[\eta]_f$ , but would have little effect on  $\phi_{max}$ . Therefore, a better estimate of  $\phi_{max}$  would likely yield a more reliable  $[\eta]_f$  value. In addition, there is a distinct possibility that the deviation might be attributed to experimental error, which was relatively more significant at low viscosities (low solids content) than at high viscosities. The errors in viscosity at low solids content affect regression and thus generate errors in  $[\eta]_f$ .

Theoretically,  $[\eta]_f$  is equal to 2.5 for dilute suspension of spherical particles. By examining the SEM photographs of the alumina and zirconia powders, it was clear that most of the particles were not spheres and that there were noticeable quantities of aggregated fine particles in the HSY3 zirconia powders. The non-spherical particles and particle agglomeration both contribute to the higher  $[\eta]_f$  values here. The extraordinarily high  $[\eta]_f$  for HSY3 zirconia may be mainly the result of the presence of the hard agglomerates which were not broken down during milling.

### 2.2.3 CONCLUSIONS

Poly(methyl methacrylate) contributes to the dispersibility of alumina and zirconia powders in acetone by adsorbing at the solids/liquid interface. Both the BET and Langmuir equations could adequately describe the adsorption isotherms of PMAA on alumina and zirconia. By calculating the monolayer adsorption,  $N_m$  from the BET or the Langmuir equations, the conformations of the adsorbed PMMA layer can be compared between alumina and zirconia. The analysis of adsorption isotherms of PMMA on A1000, A3000 and HSY3 provided an estimation of the adsorbed layer thickness and allowed calculation of the PMMA concentration in the equilibrium liquid phase in suspensions. Instead of the true solids concentration, the apparent solids concentration should be used to account for the adsorbed PMMA layer during viscosity-concentration modeling. The traditional equation  $\phi_{app} = \phi(1 + 6\Delta/D)$  is not sufficient in describing the volume change of the solids due to the adsorption of the flexible PMMA on powders. Therefore, an equation which considers the layer thickness varying with the solids concentration was used:

$$\phi_{app} = \phi \left\{ \frac{D + 2 \left[ \left( 1 - \ln \left( \frac{\phi_{max}}{\phi} \right) \right) \delta_{min} + \ln \left( \frac{\phi_{max}}{\phi} \right) \delta_{max} \right]}{D} \right\}^3 \quad (2.2.17)$$

The layer thickness at  $\phi = \phi_{max}$  is  $\phi_{min}$  which can be calculated from the monolayer adsorption assuming complete surface coverage of solids by PMMA. The maximum layer thickness,  $\phi_{max}$  is that which results when the polymer chains extend freely into the liquid medium. It was approximated by the radius of gyration of PMMA in acetone. The Mooney equation could not describe the viscosity-solids concentration relation of these PMMA/acetone/oxide slurries, with or without the correction for the thickness of the adsorbed layer. Both the Eilers equation,  $\eta_r = [1 + [\eta]_i \phi / 2(1 - \phi/\phi_{max})]^2$ , and the Krieger-Dougherty equation,  $\eta_r = (1 - \phi/\phi_{max})^{[\eta]_{max}}$ , were found to agree with the experimental data by correcting the apparent solids volume fraction with an equation which takes into account the variation in adsorbed layer thickness with solids content. The average intrinsic viscosity values for XA1000, XA3000, and HSY3 are all higher than 2.5, the intrinsic viscosity of dilute suspensions of spheres. This is likely due to the non-spherical shape of the particles and the presence of agglomerates in the suspensions. The values of apparent maximum volume fraction increases as the surface average particle size increases. They are apparently irrelevant to specific surface area alone or serigraph medium particle size. The effective volume fraction, the solids content plus adsorbed PMMA layer plus particle interaction range, can be computed as a function of the particle interaction distance,  $d$ .

#### 2.2.4 BIBLIOGRAPHY

- [1] J. C. Williams. *Ceramic Fabrication Processes*. Academic Press Inc., New York, N. Y., 1976.
- [2] D. W. Richerson. *Modern Ceramic Engineering*. Marcel Dekker Inc., New York, N. Y., 1982.
- [3] I. M. Krieger. Flow properties of latex and concentrated solutions. In R. H. Marchessault, editor, *Surfaces and Coatings Related to Paper and Wood*, chapter 2, Syracuss University Press, 1967.
- [4] I. M. Krieger and T. J. Dougherty. A mechanism for non-newtonian flow in suspensions of rigid spheres. *Trans. Soc. Rheology*, 3:137, 1959.
- [5] T. Ree and H. Eyring. Theory of non-newtonian flow. I. solid plastic system. *J. Appl. Phys.*, 26:793, 1955.

- [6] James S. Reed. *Introduction to the Principles of Ceramic Processing*. John Wiley & Sons, New York, 1988.
- [7] J. R. Van Wazer and et al. *Viscosity and Flow Measurement*. Interscience Publishers, 1963.
- [8] H. Van Olphen. *An Introduction to Clay Colloid Chemistry*. John Wiley & Sons, New York, N. Y., 2nd edition, 1977.
- [9] P.S. Williams. Some effects on the flow of concentrated suspensions of variations in particle size and shape. *Discuss. Faraday Soc.*, 16:13, 1961.
- [10] R.L. Peek Jr. and D. A. MacLean. Some physical concepts in theories of plastic flow. *J. Rheology*, 2:370, 1931.
- [11] Ir. R. Rutgers. Relative viscosity of suspensions of rigid spheres in newtonian liquids. *Rheologica Acta*, 2:202, 1962.
- [12] T. L. Smith. Rheological properties of dispersions of particulate solids in liquid media. *J. of Paint Technology*, 44:71, 1972.
- [13] A. Einstein. Eine neue bestimmung der moleculdimensionen. *Ann. Physik*, 19:289, 1909.
- [14] A. Einstein. *Investigation of the Brownian Movement*. Dover, New York, 1956.
- [15] R. J. Farris. Prediction of the Viscosity of multimodal suspensions from unimodal viscosity data. *Trans. Soc. Rh.* 12:281, 1968.
- [16] von F. Eirich, M. Bunzi, and H. Margaretha. Untersuchungen über die viskosität von suspensionen und losungen. 4. über die viskosität von kugelsuspensinen. *Kolloid-Z*, 74:114, 1936.
- [17] D. Quemada. Rheology of concentrated disperse systems ii. a model for nonnewtonian shear viscosity in steady flows. *Rheol. Acta*, 17:632, 1978.
- [18] H. L. Goldsmith and S.G. Mason. The microrheology of suspensions. In F. R. Eirich, editor, *Rheology*, Academic Press, 1967.
- [19] R. Manley and S. G. Mason. Particle motions in sheared suspensions. ii. collisions of uniform spheres. *J. of Colloid Sci.*, 7:354, 1952.

- [20] T. Gillespie. The effect of aggregation and liquid penetration on the viscosity of dilute suspensions of spherical particles. *J. of Colloid Sci.*, 18:32, 1963.
- [21] M. Mooney. The viscosity of a concentrated suspension of spherical particles. *J. of Colloid Sci.*, 6:162, 1951.
- [22] F. L. Saunders. Rheology properties of monodisperse latex system, I. concentration dependence of relative viscosity. *J. of Colloid Sci.*, 16:13, 1961.
- [23] C. Parkinson, S. Matsumoto, and P. Sherman. The influence of particle-size distribution on the apparent viscosity of non-newtonian dispersed systems. *J. of Colloid and Interface Sci.*, 33:150, 1970.
- [24] S. Matsumoto and P. Sherman. The viscosity of microemulsions. *J. of Colloid and Interface Sci.*, 30:525, 1969.
- [25] V. Vand. Viscosity of solutions and suspensions, ii. experimental determination of the viscosity-concentration function of spherical suspensions. *J. Phys. Colloid Chem.*, 52:300, 1948.
- [26] H. L. Frisch and R. Simha. The viscosity of colloidal suspensions and macromolecular solutions. In F. R. Eirich, editor, *Rheology*, Academic Press, 1956.
- [27] D. J. Thomas. Transport characteristics of suspensions, viii. a note on the viscosity of newtonian suspension of uniform spherical particles. *J. of Colloid Sci.*, 20:267, 1965.
- [28] H. Eilers. Die viskosität von emulsionen hochviskoser stoffe als funktion der konzentration. *Kolloid-ZZ Polym.*, 97:313, 1941.
- [29] R. F. Fedors. Relationships between viscosity and concentration for newtonian suspensions. *J. of Colloid and Interface Sci.*, 46:545, 1974.
- [30] R. Simha. The influence of brownian movement on the viscosity of solutions. *J. Phys. Chem.*, 44:25, 1940.
- [31] M. E. Woods and I. M. Krieger. Rheological studies on dispersions of uniform colloidal spheres. *J. of Colloid and Interface Sci.*, 34:91, 1970.

- [32] S. G. Mason. Flow properties of model systems. In R. H. Marchessault, editor, *Surfaces and coatings related to paper and wood*, chapter 1, Syracuss university Press, 1967.
- [33] S. H. Maron and S. M. Fok. Rheology of synthetic latex, v. flow behavior of low-temperature gr-s latex. *J. of Colloid Sci.*, 10:482, 1955.
- [34] S. H. Maron and A. E. Levy-Pascal. Rheology of synthetic latex, vi. the flow behavior of neoprene latex. *J. of Collotd Sci.*, 10:494, 1955.
- [35] J. G. Brodnyan. The dependence of synthetic latex viscosity on particle size and size distribution. *Trans. Soc. Rheology*, 12:357, 1968.
- [36] Y. S. Lipatov and L. M. Sergeeva. *Adsorption of Polymers*. John Wiley & Sons, 1974.
- [37] James E. Funk and Dennis R. Dinger. Slip control using particle-size analysis and specific surface area. *Amer. Cer. Soc. Bull.*, 67:890, 1988.
- [38] R. E. Johnson, Jr. and W. H. Morrison, Jr. *Ceramic poulder dispersion in nonaqueow systems*, page 323. Volume 21 of *Advances in Ceramics*, The Amer. Cera. Soc., 1987. *size distribution. Trans. Soc. Rheology*,
- [39] B. Vincent. The effect of adsorbed polymers on dispersion stability. *Advanced Colloid Interface Sci.*, 4:193, 1974.
- [40] G. D. Parfitt. Fundamental aspects of dispersion. In G. D. Parfitt, editor, *Dispersion of Powders in Liquids*, chapter 1, John Wiley & Sons, New York, N. Y., 1973.
- [41] M. J. Vold. The effect of adsorption on the van der waals interaction of spherical particles. *J. of Colloid Sci.*, 16:1, 1961.
- [42] J. Th. G. Overbeek. Recent developments in the understanding of colloid stability. In *Colloid and Interface Science*, page 431, Academic Press Inc., 1977.
- [43] D. H. Napper. Steric stabilization. In *Colloid and Interface Science*, page 413, Academic Press Inc., 1977.
- [44] P. M. Heetjes and et al. Some aspects of adsorption processes occurring on titanium dioxide particles. *Progress in Organic Coatings*, 7:141, 1979.



- [45] P. M. Heertjes and C. I. Smits. The influence of adsorbed layer on the rheology behavior of titanium dioxide dispersions. *Powder Tech.*, 17:197, 1977.
- [46] G. J. Fleer and J. M. H. M. Scheutjens. Interaction between adsorbed layers of macromolecules. *J. of Colloid and Interface Sci.*, 111:504, 1986.
- [47] T. Sato and R. Ruch. *Stabilization of Colloidal Dispersion by Polymer Adsorption*. Marcel Dekker Inc., 1980.
- [48] F. Rowland and et al. *Chemistry and Physics of Interfaces*, page 110. Amer. Chem. Soc. Publication, Washington, D. C., 1965.
- [49] E. C. Rothstein. *Role of the Adsorbed resin layer in the dispersion of pigmented alkyd systems*. Technical Report, Federation of Soc. for Paint Tech., 1964.
- [50] J. Klein. Surface interaction with adsorbed macromolecules. *J. of Colloid and Interface Sci.*, 111:305, 1986.
- [51] G.J. Howard and C. C. Ma. Steric stabilization of surface-coated titanium dioxide pigments by adsorbed methyl methacrylate copolymers. *J. Coatings Tech.*, 51:47, 1979.
- [52] F. M. Fowkes, M. J. Marmo, M. A. Mustafa, H. Jinnal, and J. A. Manson. Acid-base interaction in filler-matrix systems. *Ind. Eng. Chem., Prod. Res. Dev.*, 15:206, 1976.
- [53] E. C. Rothstein. Nature of pigment surfaces. In T. C. Patton, editor, *Pigment Handbook*, page 131, John Wiley & Sons, New York, 1973.
- [54] F. M. Fowkes. *Dispersions of ceramic powders in organic media*, page 411. Volume 21 of Advances in Ceramics, The Amer. Cera. Soc., 1987.
- [55] G.D. Parfitt and C.H.Rochester. *Adsorption of small molecules*, page 3. Academic Press Inc., 1983.
- [56] C. H. Giles and et al. A general treatment and classification of the solute adsorption isotherm, I. theoretical. *J. of Colloid and Interface Sci.*, 47:755, 1974.
- [57] E. S. Tormey and et al. Adsorption of dispersants from nonaqueous solutions. *Material Sci. Res.,(Eng)*, 14:121, 1981.

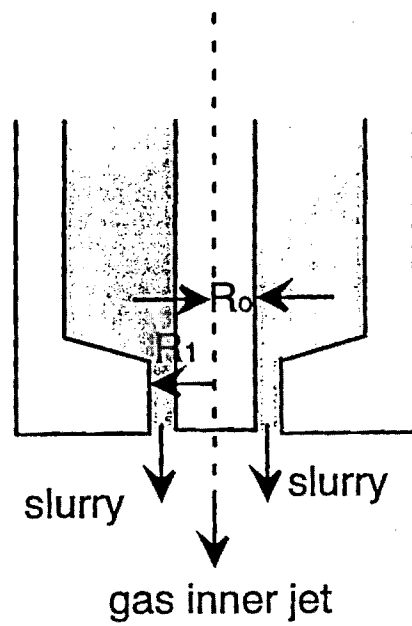
- [58] J. J. Kipling. *Adsorption from Solution of Non-electrolytes*. Academic Press, London, 1965.
- [59] S. J. Gregg and K. S. W. Sing. *Adsorption, Surface Area and Porosity*. Academic Press Inc., 2 edition, 1982.
- [60] F. Rodriguez. *Principles of Polymer Systems*. Hemisphere Publication Corp., 2 edition, 1982.
- [61] Ellen S. Tormey. *The Adsorption of Glyceryl Esters at the Alumina/Toluene Interface*. PhD thesis, Massachusetts Inst. of Tech., August 1982.
- [62] Joe K. Cochran and T. J. Hwang. Bet analysis of adsorption of pmma on oxides in acetone. 91st ACS Annual Meeting, Symposium on Colloidal Processing and Forming of Ceramics, April 1989.
- [63] A. B. Metzner and M. Whitlock. Flow behavior of concentrated (dilatant) suspensions. *Trans. Soc. Rheology*, 2:239, 1958.
- [64] M. Mooney and W. A. Hermonat. Effect of swelling or of an adsorbed layer on the viscosity of a suspension of spherical particles. *J. of Colloid Sci.*, 10:121, 1955.
- [65] J. Brandrup and E. H. Immergut, editors. *Polymer Handbook*. John Wiley & Sons, 2 edition, 1975.

## 2.3 MODEL FOR FORMATION OF HOLLOW SPHERES

Thin wall hollow liquid spheres are fabricated by the coaxial nozzle process by extruding a liquid through an annular-cross-section nozzle with a gas jet providing a ballooning effect. This process produces monosized hollow spheres at constant, precise rates or frequencies for a fixed set of conditions. A model based on fluid continuum concepts and dynamic equations (equations of motion) was derived to describe liquid hollow sphere formation. This model resulted in mathematical expressions to calculate hollow sphere formation frequency, based on liquid and gas flow rates, liquid viscosity, surface tension, density, and jet dimensions. At high liquid flow rates, a critical condition for hollow sphere closure was postulated which permitted prediction of the sphere formation cycle. At higher liquid flow rates, the model frequencies agree with experimental frequencies reasonably well. However the model was insufficient to predict frequencies at lower liquid flow rate because the critical condition of bubble formation could not be clearly defined for the lower liquid flow rate situation.

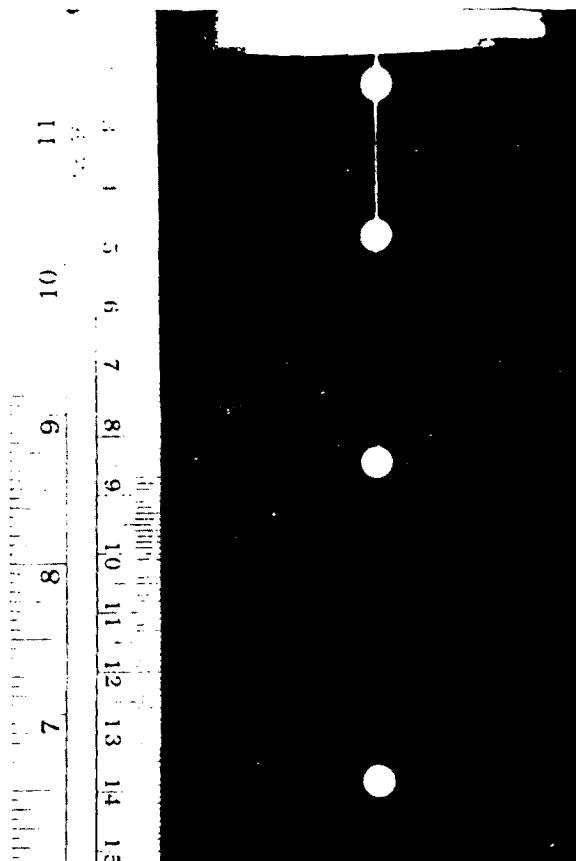
The coaxial nozzle is named because the nozzle consists of two coaxial tubes where the inner tube injects gas (this is termed inner jet) and a slurry flows in the annular opening between the inner jet and outer tube, as shown in Figure 2.3.1(a). Figure 2.3.1(b) shows sphere formation with a coaxial nozzle from a 55 v/o alumina slurry. The hollow spheres manufactured by coaxial nozzle technique have very narrow size distribution, Figure 2.3.2(a). This technique is unique in that not only does it accommodate any composition because it is a powder process, but it also allows tailoring of thermal conductivities using additives such as pores and pacifiers in the sphere walls<sup>1,4</sup>. The process is practical in that over 300 tons of ceramic spheres have been made by the process for several applications over the last few years. For practical reasons, high quality spheres, i.e. monosized with uniform wall thickness, are desired because increased perfection enhances both mechanical and insulation performance. Uniformity in the sphere wall thickness also eliminates anisotropic mechanical and thermal properties. Unfortunately, this process has not been shown to produce sphere with a uniform wall thickness<sup>2</sup> (Figure 2.3.2(b)) and therefore improvements are desired. Improved sphere quality is probable when the sphere forming process is fully understood. Therefore, the objective of this study was to investigate the mechanism of hollow liquid sphere formation using a coaxial nozzle technique.

Two models for sphere formation from liquid existed previously. The earliest model, the capillary model<sup>9-12</sup>, was based on capillary waves developed on a liquid jet surface due to surface tension of the liquid. This was used to describe solid liquid sphere formation as early as the end of the last century. More recently, research conducted in the Jet Propulsion Laboratory, California Institute of Technology resulted in a hollow



Typically,  $R_o = 14 \text{ mil}$   
 $R_1 = 25 \text{ mil}$

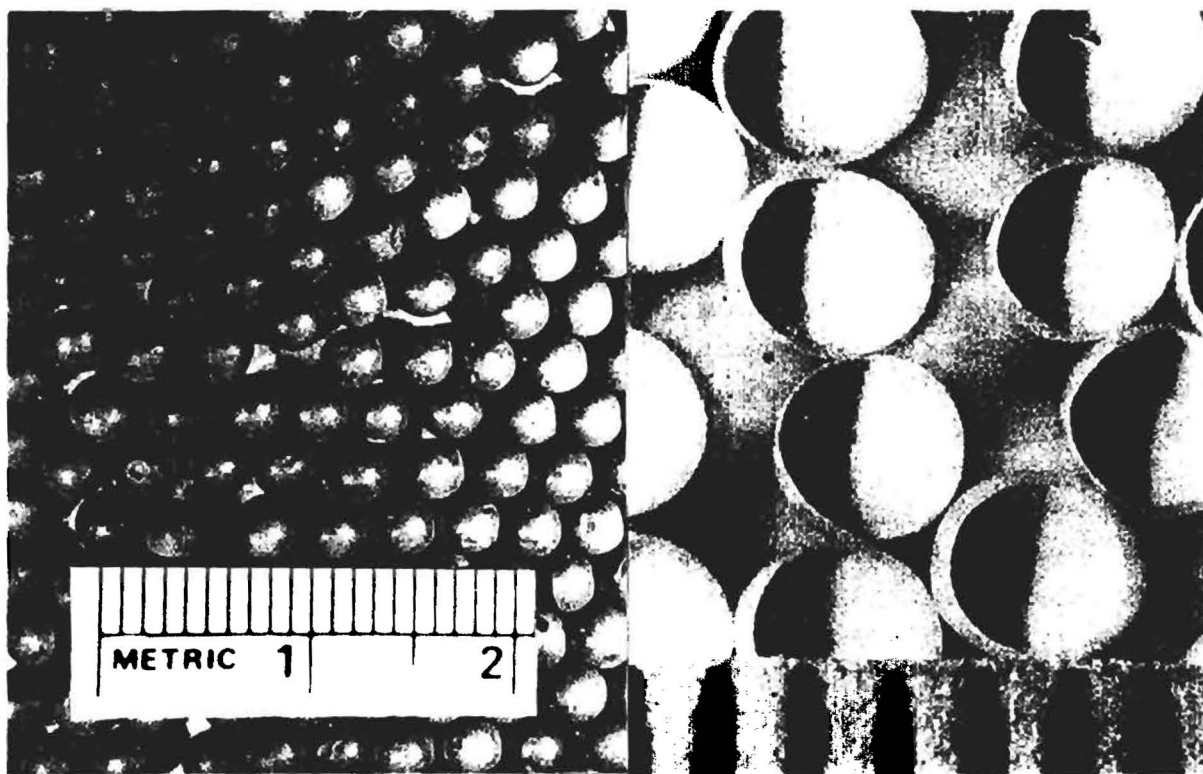
(a)



(b)

Figure 2.3.1

(a) Cross Section of a Coaxial Nozzle. (b) Hollow Alumina Spheres Formation with Coaxial Nozzle from Alumina Slurry.



(a)

(b)

Figure 2.3.2

(a) Hollow Ceramic Spheres with Narrow size Distribution. (b) Sphere Wall Thickness Variation.

sphere formation scheme<sup>13</sup>. This model started with the continuity equation and kinematic relations, and incorporated the assumption of capillary waves growing on the liquid jet surface.

An easily applied model, involving few assumptions, was established in this study. In the model, a balance is established between the interior gas pressure, the viscous stress in the liquid shell, and surface tension. The sphere formation process was divided into two regions, high and low, based on liquid flow rate. As can be seen later, the model predictions agreed with experimental results reasonably well at high liquid flow rates. At low liquid flow rates, sphere formation was not predicable by this model because the critical closure mechanism postulated here must not be valid at low liquid flow rates.

### 2.3.1 EXPERIMENTAL SPHERE FORMATION

To test the model derived below, hollow spheres were formed by flowing silicone fluid through the annular opening of a coaxial nozzle and the ballooning effect was provided by a  $N_2$  gas jet flow through the center tube in the nozzle. The liquid flow rate was controlled by gas pressure, which will be termed cell pressure, in a liquid reservoir connected to the nozzle. The liquid exited the nozzle with the configuration shown in Figure 2.3.3. The hollow liquid jet initially forms a cylindrical liquid tube with a inner radius,  $R_o = 0.014$  in., equal to nozzle inner radius and a thickness,  $\delta = R_i - R_o = 0.012$  in., equal to the width of the annular opening of the nozzle. Due to the flowing  $N_2$  gas jet, the cylindrical liquid shell gradually expands into a spherical shell at the end of the liquid tube. The sphere formation frequency (number of hollow liquid spheres formed per minute) was measured by a Ametec stroboscope. Cell pressure (or liquid flow rate  $Q_l$ ) and inner jet flow rate  $Q_g$  were varied to obtain diverse sphere formation frequencies. Silicone viscosity standard fluid was used in the preliminary hollow liquid sphere formation experiments. The silicone oil was purchased from Brookfield Engineering Laboratories, Inc. and exhibit newtonian behavior with a viscosity of 0.993 poise and a surface tension of 23 dyne/cm.

### 2.3.2 MODEL OF HOLLOW SPHERE FORMATION

Liquid hollow sphere formation from a coaxial nozzle usually follows the sequence described in Figure 2.3.4. A hollow cylindrical liquid tube produced by flow of the liquid through the nozzle closes at a distance below the nozzle at which point a spherical shell is generated due to the inflation pressure of the gas jet. The length of the cylinder appears to be controlled partially by liquid flow rate  $Q_l$ . Longer cylindrical cavities were observed at higher liquid flow rates, as shown in Figure 2.3.4(a). As  $Q_l$  decreased, cylindrical cavities became shorter and eventually disappeared, Figure 2.3.4(b). Similar phenomena were also found by Bennie and Squire<sup>19</sup> and Baird and

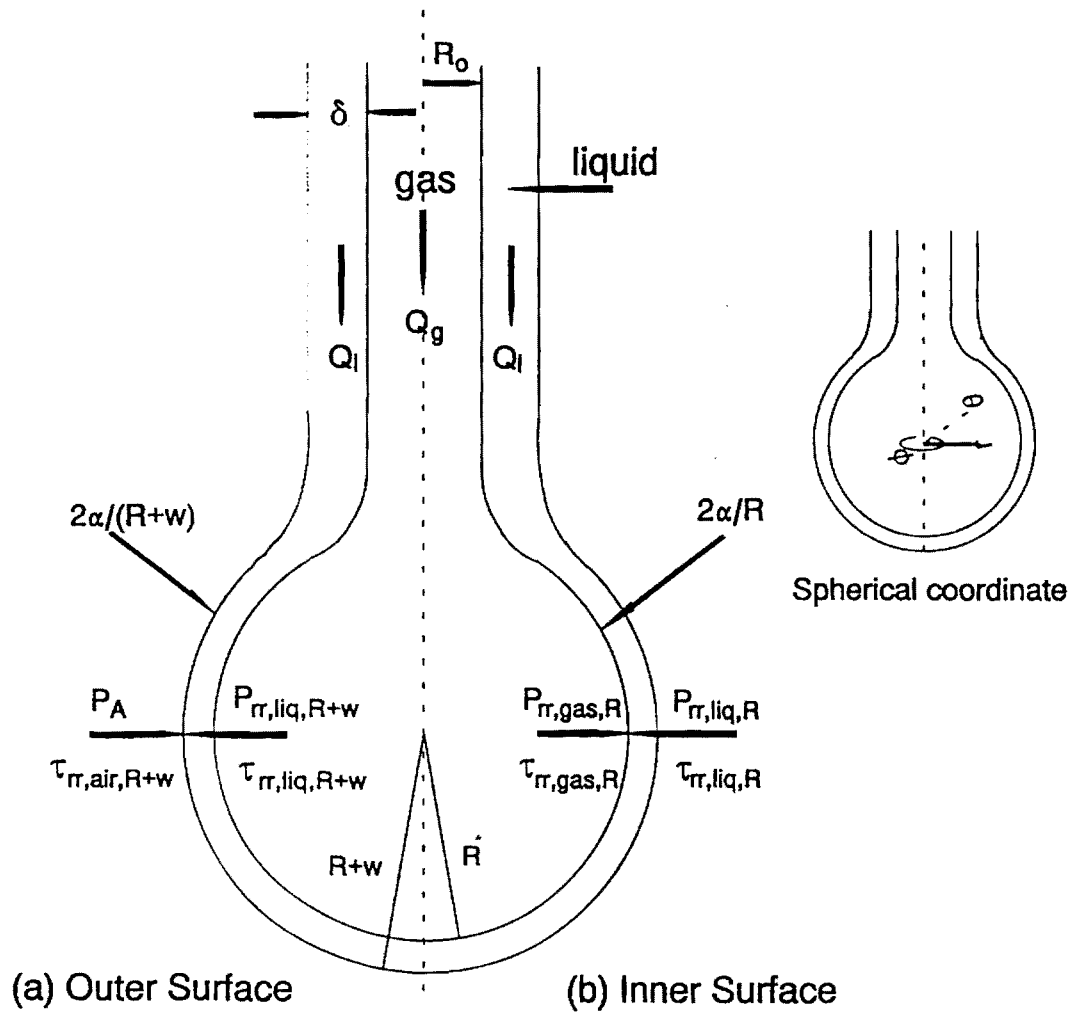
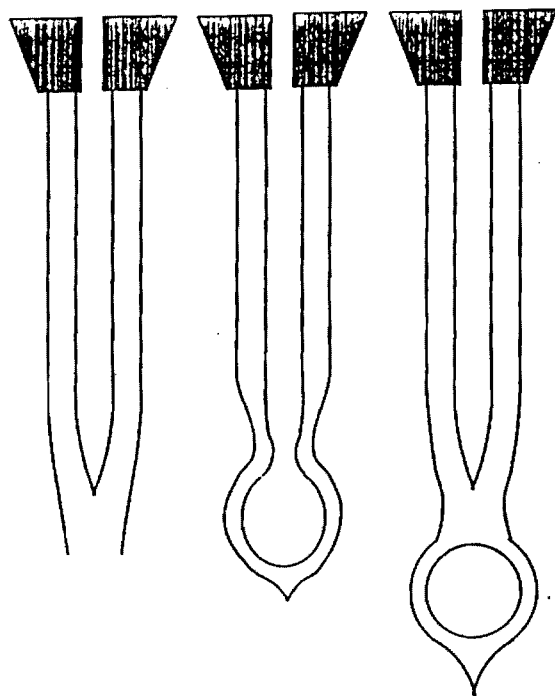
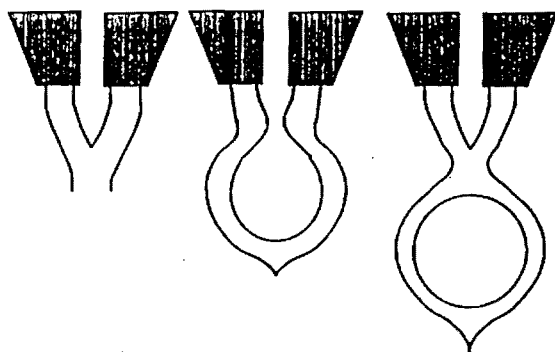


Figure 2.3.3 The Geometry and Stresses on (a) the Outer Surface and (b) the Inner surface of Hollow Sphere Formation.



(a) at higher liquid flow rates



(b) at lower liquid flow rates

Figure 2.3.4. Schematic Description of Sphere Formation for (a) Higher and (b) Lower Liquid Flow Rates.



Davison<sup>20</sup>. They attributed this to the fact that the length of the center cavities was affected by the vertical curvatures of the cavities which could be altered by the velocities of the liquid jet.

In addition to the different forming configuration, sphere formation frequencies were also influenced distinctly by liquid flow rate. As can be seen from Figure 2.3.5, at higher liquid flow rates, for example  $Q_l \geq 1.25$  cc/s, the dependency of frequency on gas flow rate is more dominant than at lower liquid flow rates. The variations in sphere formation configuration and frequency vs. flow rate tendency suggested that separate sphere formation mechanisms should be considered for higher  $Q_l$  and lower  $Q_l$ .

**Model** - The driving force for growth of a liquid hollow sphere comes from the gas pressure inside the sphere. Expansion rate of the shell is controlled by the balance between the stresses caused by the gas pressure inside the shell, the viscous stress due to the liquid motion, and the surface tension. By establishing and solving stress balance equations, the expansion rate (or radius vs time relationship) of the hollow sphere can be determined.

To simplify the problem, the system was decoupled into two parts, a cylindrical and a spherical cavity, Figure 2.3.3. The cylindrical cavity appeared to maintain approximately the same configuration and dimensions during sphere formation and thus was independent of time as will be presented later. This implied that the amount of liquid in the sphere was constant during the expansion and as the spheres increase in size, the sphere wall thickness became thinner due to stretching. However, in actuality, the boundary between the cylinder and the sphere cannot be distinct. As the sphere grows, the center of the sphere must move toward the cylinder and incorporate some of the liquid from the cylinder (meaning the amount of the liquid in the sphere did not remain constant). This variation in the amount of liquid in the sphere was not considered in the model because the sphere expands at such a fast rate that radial expansion and the thinning of the wall thickness is assumed to be the dominate mechanism, and the effects of increasing the amount of the liquid in the sphere is assumed negligible. The motion of liquid shell can be expressed in terms of the following velocity tensor<sup>21</sup>,  $v_i$ ,

$$v_i \rightarrow (v_r, v_\theta, v_\phi) \rightarrow (v_r, 0, 0) \quad (2.3.1)$$

Because the sphere only grows in the  $r$  direction,  $v_\theta = v_\phi = 0$ . The sphere was assumed to be symmetric about the  $\theta$  and  $\phi$  axes, therefore  $v_r = f(r) \neq f(\theta, \phi)$ . This assumption idealized the process and assumed a spherical geometry from the initiation of sphere formation. In the actual sphere formation process, the bubbles appear as ellipsoids

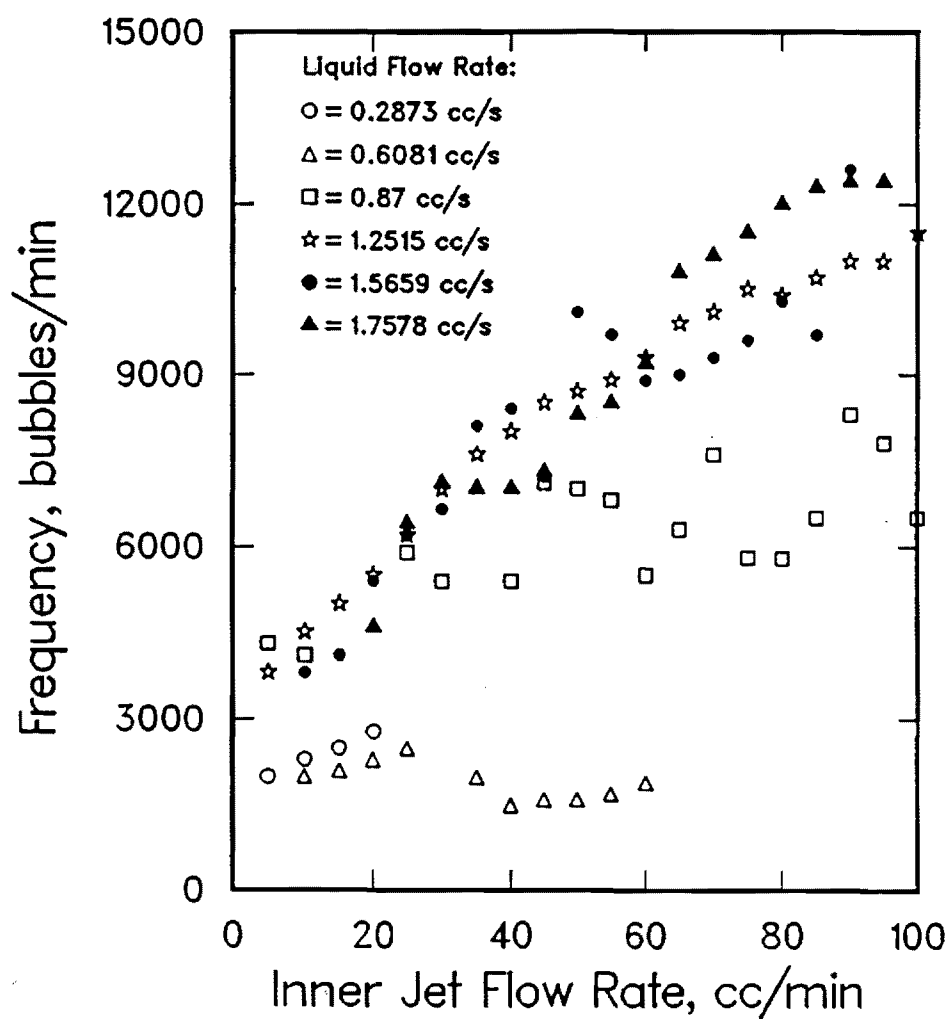


Figure 2.3.5. Frequency vs. Inner Jet Gas Flow Rate for Silicone Fluid ( $\mu = 0.993$  poise,  $\alpha = 23$  dyne/cm,  $\rho = 0.97$  g/cm<sup>3</sup>) at a Variety of Liquid Flow Rates.

rather than spheres and  $\mathbf{v}_r$  would be a function of  $r$  and  $\theta$ . As bubbles increased in size, the non-symmetry of  $\mathbf{v}_r$  about  $\theta$  appeared to be gradually eliminated and the assumption that  $\mathbf{v}_r = f(r)$  only became more valid. Hence the assumption that  $\mathbf{v}_r$  was symmetric about both  $\theta$  and  $\phi$  seemed acceptable and allowed an idealized and less complicated sphere formation model.

By applying the following continuity equation<sup>21</sup> and boundary conditions,

$$\text{Continuity Equation: } \frac{1}{r^2} \frac{\partial}{\partial r} (r^2 \mathbf{v}_r) = 0 \quad (2.3.2)$$

where  $R$  was instantaneous sphere inner radius,  $\mathbf{v}_r$  can be solved as,

$$\text{Boundary Condition: } \mathbf{v}_r|_{r=R} = \frac{dR}{dt} = \dot{R} ; \quad \text{at } r=R \quad (2.3.3)$$

$$\mathbf{v}_r = \frac{\dot{R} R^2}{r^2} \quad (2.3.4)$$

Equation (2.3.4) was valid for  $r$  ranges from the sphere inner radius,  $R$ , to an outer surface radius,  $R+w$ . Therefore the velocity tensor for a growing hollow sphere, equation (2.3.1), could be rewritten as,

$$\mathbf{v}_i \rightarrow \left( \frac{\dot{R} R^2}{r^2}, 0, 0 \right) \quad (2.3.5)$$

**Stress Balance** - Figure 3 indicates that stresses on the spherical shell included hydrostatic pressures,  $P$ , normal viscous stress,  $\tau$ , and stresses caused by surface tension,  $\alpha$ . The balance between the these stresses for inner and outer surfaces can be presented as:

$$\text{Inner Surface: } -P_{liq,R} + \tau_{rr}|_{liq,R} + P_{gas,R} = \alpha \frac{2}{R} \quad (2.3.6)$$

$$\text{Outer Surface: } -P_A + P_{liq,R+w} - \tau_{rr}|_{liq,R+w} = \alpha \left( \frac{2}{R+w} \right) \quad (2.3.7)$$

The total stress balance is the summation of equation (2.3.6) and

$$\Delta P + (P_{liq,R+w} - P_{liq,R}) + (\tau_{rr}|_{liq,R} - \tau_{rr}|_{liq,R+w}) = 2\alpha \left( \frac{1}{R} + \frac{1}{R+w} \right) \quad (2.3.8)$$

(2.3.7), where  $\Delta P$  replaced  $(P_{gas,R} - P_a)$  and is the pressure difference inside and outside the shell. Liquid hydrostatic pressure difference,  $(P_{liq,R+w} - P_{liq,R})$ , and liquid viscous stress difference,  $(\tau_{rr}|_{liq,R} - \tau_{rr}|_{liq,R+w})$ , are solved from the rate-of-deformation tensor, the viscous stress, and the dynamic equation<sup>21,22</sup> as presented below.

For a bubble expanding according to the velocity vector of equation (2.3.5), the rate-of-deformation tensor is derived as,

$$\Delta_{ij} \Rightarrow \begin{vmatrix} -4\frac{\dot{R}R^2}{r^3} & 0 & 0 \\ 0 & 2\frac{\dot{R}R^2}{r^3} & 0 \\ 0 & 0 & 2\frac{\dot{R}R^2}{r^3} \end{vmatrix} \quad (2.3.9)$$

The general expression for viscous stress tensor is  $\tau_{ij} \Rightarrow \eta(\Delta_{ij} + \Delta_{ji})$ . For a newtonian fluid the coefficient,  $\eta$ , does not depend on  $\Delta_{ij}$  and viscosity,  $\mu$ , is constant. Thus the viscous stress tensor becomes,

$$\tau_{ij} \Rightarrow \begin{vmatrix} -4\mu\frac{\dot{R}R^2}{r^3} & 0 & 0 \\ 0 & 2\mu\frac{\dot{R}R^2}{r^3} & 0 \\ 0 & 0 & 2\mu\frac{\dot{R}R^2}{r^3} \end{vmatrix} \quad (2.3.10)$$

Using  $\tau_{rr}$  component and replacing  $r$  with  $R$  and  $R+w$ , the viscous stress difference in equation (2.3.8) could be solved,

$$\tau_{rr}|_{liq,R} - \tau_{rr}|_{liq,R+w} = -4\mu \frac{\dot{R}}{R} \left( 1 - \frac{R^3}{(R+w)^3} \right) \quad (2.3.11)$$

The liquid hydrostatic pressure difference,  $(P_{liq,R+w} - P_{liq,R})$ , is acquired by solving the  $r$ -component dynamic equation<sup>19,20</sup>,

$$\rho \left( \frac{\partial v_r}{\partial t} + v_r \frac{\partial v_r}{\partial r} \right) = -\frac{\partial P}{\partial r} + \left( \frac{1}{r^2} \frac{\partial}{\partial r} (r^2 \tau_{rr}) - \frac{\tau_{\theta\theta} + \tau_{\phi\phi}}{r} \right) \quad (2.3.12)$$

and for a newtonian fluid,

$$P_{liq,R+w} - P_{liq,R} = -\rho \left[ (\ddot{R}R + 2\dot{R}^2) \left( 1 - \frac{R}{R+w} \right) - \frac{\dot{R}^2}{2} \left( 1 - \frac{R^4}{(R+w)^4} \right) \right] \quad (2.3.13)$$

where  $\rho$  was the liquid density. The sphere inner radius inflation rate,  $\dot{R}$ , depends on the volumetric flow rate of the gas into the sphere which is dependent on the instantaneous pressure inside the sphere. Because the pressure difference inside and outside the cavity was on the order of less than a few percent of the atmosphere pressure (the pressure outside the cavity), it should be reasonable to assume the gas volume flow rate into the sphere was equal to the metered inner jet gas flow rate which was calibrated at atmosphere pressure. Therefore the sphere inner radius inflation rate,  $\dot{R}$ , was related to inner jet flow rate,  $Q_g$ , in the following fashion,

$$\dot{R} = \frac{Q_g}{4\pi R^2} \quad (2.3.14)$$

Combining equation (2.3.8), (2.3.11), (2.3.13), and (2.3.14), the stress balance in a growing liquid shell becomes,

$$\Delta P + \frac{\rho Q_g^2}{32\pi^2 R^4} \left[ 1 - \left( \frac{R}{R+w} \right)^4 \right] - \mu \frac{Q_g}{\pi R^3} \left[ 1 - \left( \frac{R}{R+w} \right)^3 \right] = \frac{2\alpha}{R} \left( 1 + \frac{R}{R+w} \right) \quad (2.3.15)$$

**Critical Condition** - The stress balance in, equation (2.3.15), presents the relationship between the pressure inside the hollow sphere (which was expressed as pressure difference across the spherical shell,  $\Delta P$ ) and instantaneous inner sphere radius,  $R$ .

Equation (2.3.15) can also be rearranged to predict  $\Delta P$  vs time,  $t$ , if  $R$  is expressed by the following relationship,

$$t = \frac{4/3\pi R^3}{Q_g} \quad (2.3.16)$$

Once the pressure drop across the shell,  $\Delta P$ , is known as a function of time, a mechanism can be proposed based on the pressure distribution inside the spherical cylindrical which leads to the closing of the separation at the neck between the cylinder and the sphere. As shown in Figure 2.3.6, between the two pressures in the cylinder,  $\Delta P_{cav}$  (which is approximately constant due to the unchanged cylindrical configuration) and in the sphere,  $\Delta P$ , there should exist a transition zone to allow the pressure to change gradually from  $\Delta P_{cav}$  to  $\Delta P$ . Therefore the pressure in the transition zone,  $\Delta P_{tran}$ , would range between  $\Delta P_{cav}$  and  $\Delta P$  at any point of time. The pressure  $\Delta P_{tran}$  must determine the two curvatures and thus the shape of this neck area. When  $\Delta P$  and consequently  $\Delta P_{tran}$  become smaller than  $\Delta P_{cav}$ , the liquid shell at the transition area should exhibit a neck because negative curvature develops. The necking effect increases with decreasing  $\Delta P$  and  $\Delta P_{tran}$  because of increased negative curvature until the neck collapses. This argument suggests that the critical condition  $\Delta P_{cav} = \Delta P_{tran} = \Delta P$  triggers the development of the neck and the collapse of the neck. Because the collapse is observed to occur very rapidly, it is reasonable to assume that bubbles stop growing when the following critical condition is satisfied, where  $\delta$  is the annular width of nozzle between the inner and outer radii or the thickness of the cylindrical tube. If  $\Delta P_{cav}$  from equations (2.3.17) and  $\Delta P$  from equation (2.3.15) are plotted vs time, Figure 2.3.7, the intersection defines the critical condition for sphere closure, and  $t_b$  defines the time period for sphere formation. Please note that sphere formation frequency is the reciprocal of the critical time,  $f = 1/t_b$ .

$$\Delta P = \Delta P_{cav} = \alpha \left( \frac{1}{R_o} + \frac{1}{R_o + \delta} \right) \quad (2.3.17)$$

Most of the variables involved in the process of determining  $\Delta P$  vs  $R$ , equation (2.3.15), can be experimentally measured, such as liquid density  $\rho$ , liquid viscosity  $\mu$ , liquid surface tension  $\alpha$ , and inner gas flow rate  $Q_g$ . The instantaneous spherical shell thickness,  $w$ , however can only be calculated from liquid flow rate,  $Q_l$ , when sphere formation frequency ( $1/t_b$ ) is known. Thus, calculation of  $Q_l$  and  $t_b$  must be resolved by a iterative method. Assuming that the volume of liquid per sphere is constant during the sphere formation, the spherical shell thickness,  $w$ , is approximately equal to volume of liquid per bubble,  $Q/f_{assumed}$ , divided by surface area of the spheres, or,

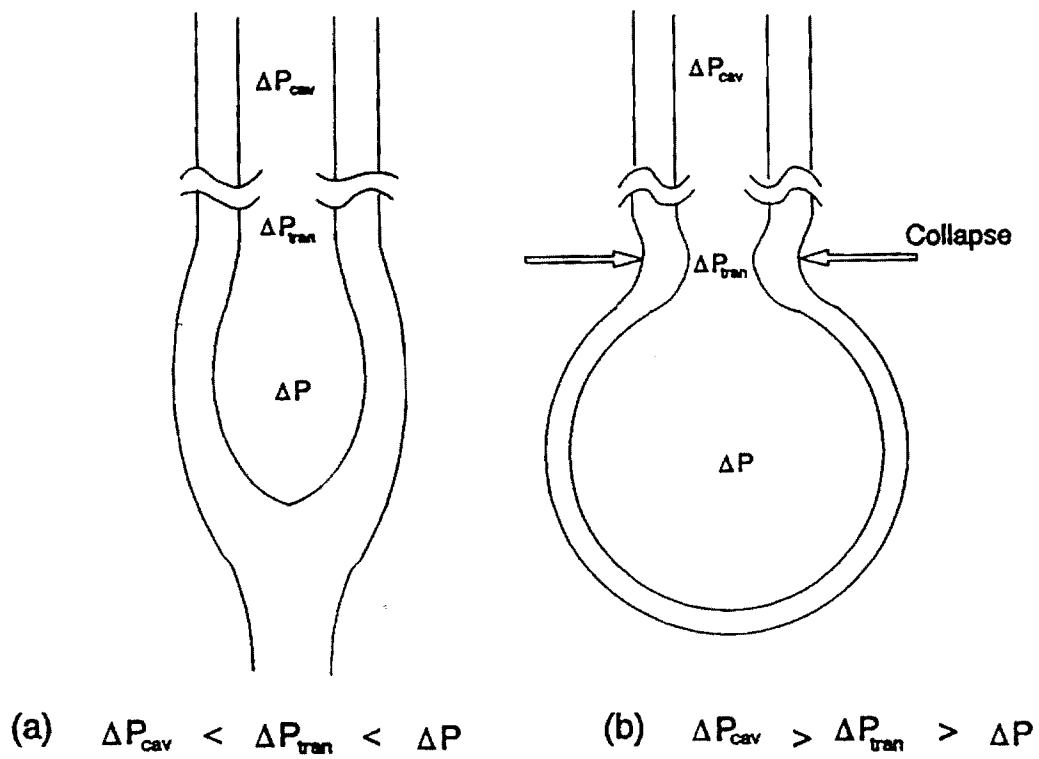
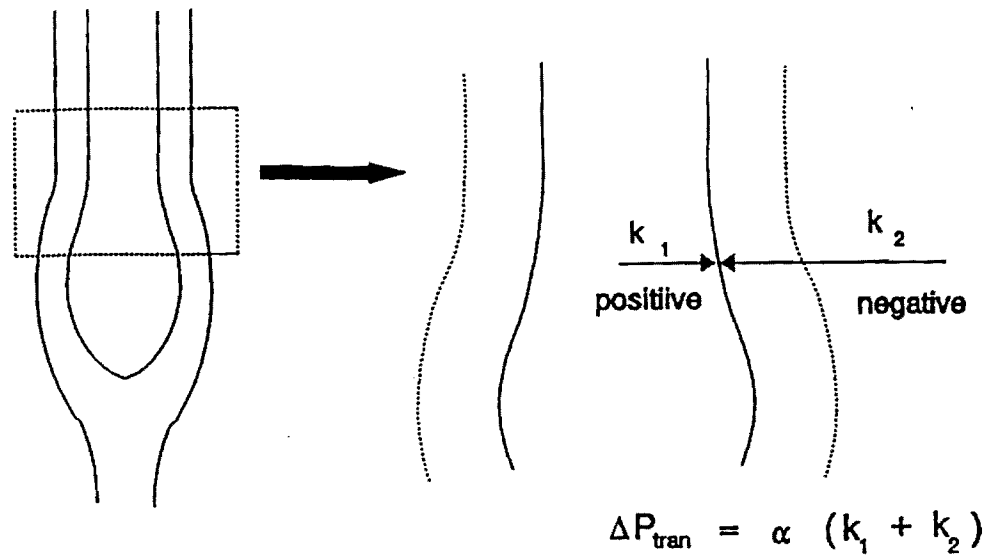


Figure 2.3.6. The Pressure in the Transition Zone of the Cavity Affect the Magnitude of the Negative Curvature.

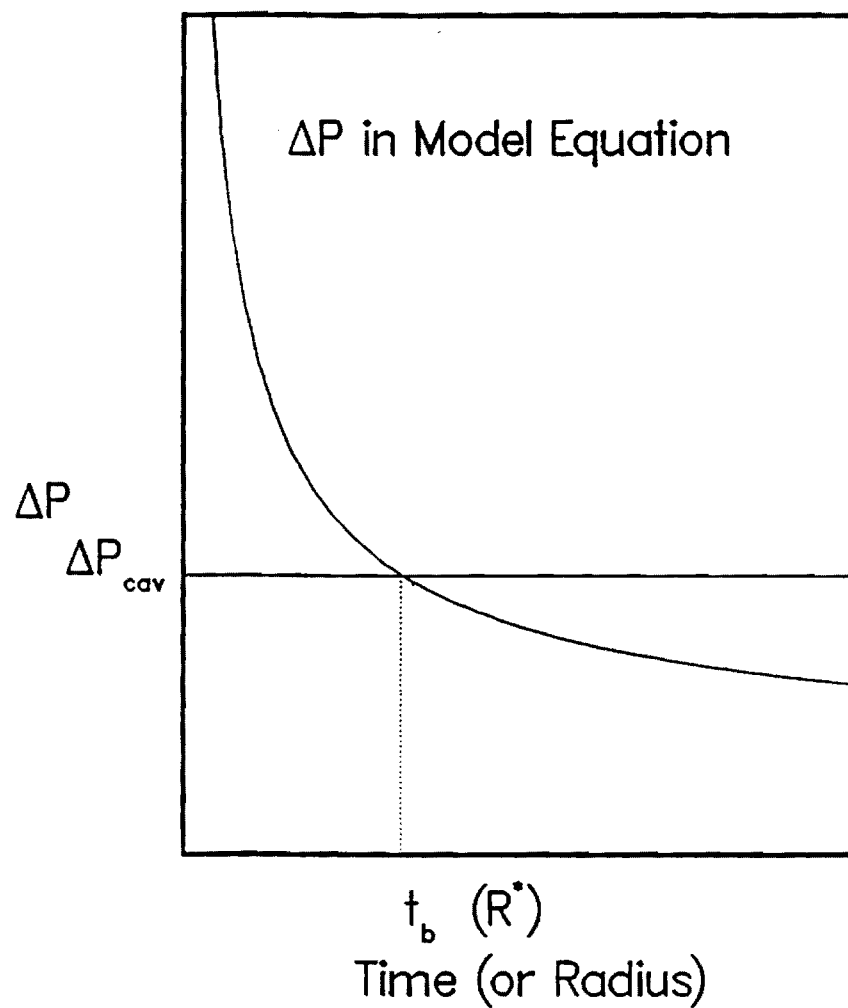


Figure 2.3.7. The Pressure Inside the Cavities as a Function of Time and the Critical Condition.



$$w = \frac{Q_i}{4\pi R^2 f_{assumed}} \quad (2.3.18)$$

This  $w$ , calculated by a assumed frequency, was then used to calculate  $\Delta P$ , equation (2.3.15), and obtain the calculated frequency  $1/t_b$ . If the assumed frequency,  $f_{assumed}$ , and calculated frequency,  $f$ , did not agree, the calculation is repeated with another assumed frequency. An appropriate number of iterations are completed until an acceptable agreement between the assumed and calculated frequencies is achieved. A sample demonstration of this operation is shown in Figure 2.3.8.

One concern presented by this model centered on the flow of inner jet gas. From Figure 2.3.7, it is obvious that at initiation of hollow sphere formation, the pressure in the spherical cavity is greater than that in the cylindrical cavity. This required the inner jet gas to flow from a low pressure region (cylindrical tube) to a high pressure region (hollow sphere). It is possible that the inner jet possesses enough momentum to carry the gas down stream in the hollow cylinder until hindered by an obstacle, in this situation the closed end of the cylindrical liquid shell. The accumulation of the inner jet gas caused the expansion at the closed end. In addition, the momentum of the annular liquid jet provides a retarding force to prevent expansion of the cylindrical tube, particularly near the nozzle and at high liquid flow rates as demonstrated by Baird and Davidson<sup>20</sup>.

In addition to the momentum of both the inner jet gas and the annular liquid jet, equilibrium of pressures in the cavities must be considered. Although the system was divided into two cavities when the model was derived, the two cavities were physically connected and the pressures inside the two must have the tendency to reach an equilibrium. Either the cylindrical cavity must decrease in size to raise  $\Delta P_{cav}$  or the spherical cavity must increase in size to reduce  $\Delta P$ . The former was not possible because of the continuous feeding of the inner jet gas. Therefore the spherical cavity would have to grow to reduce the pressure inside the sphere and consequently to eliminate the difference between  $\Delta P_{cav}$  and  $\Delta P$ . Consequently, the sphere formation process is basically the competition between the inner jet momentum which carries the gas down stream and the pressure distribution in the cavities which retard the gas flow toward the closed end. If the pressure distribution was the energy barrier for a reaction (growth of bubbles), inner jet must have enough energy (*i.e.* velocity) to overcome the energy barrier to activate the reaction. This might help to explain the observation that when  $Q_g$  was too low there would be no hollow spheres produced.

	Assumed Frequency (bubbles/min)	Calculated Time Period (sec/bubble)	Calculated Frequency (Bubbles/min)
First Trial	$f_1 = 15000$	$t_1 = 0.0061$	9800
Second Trial	$f_2 = 5000$	$t_2 = 0.0067$	9000
Third Trial	$f_3 = 9200$	$t_3 = 0.0064$	9300

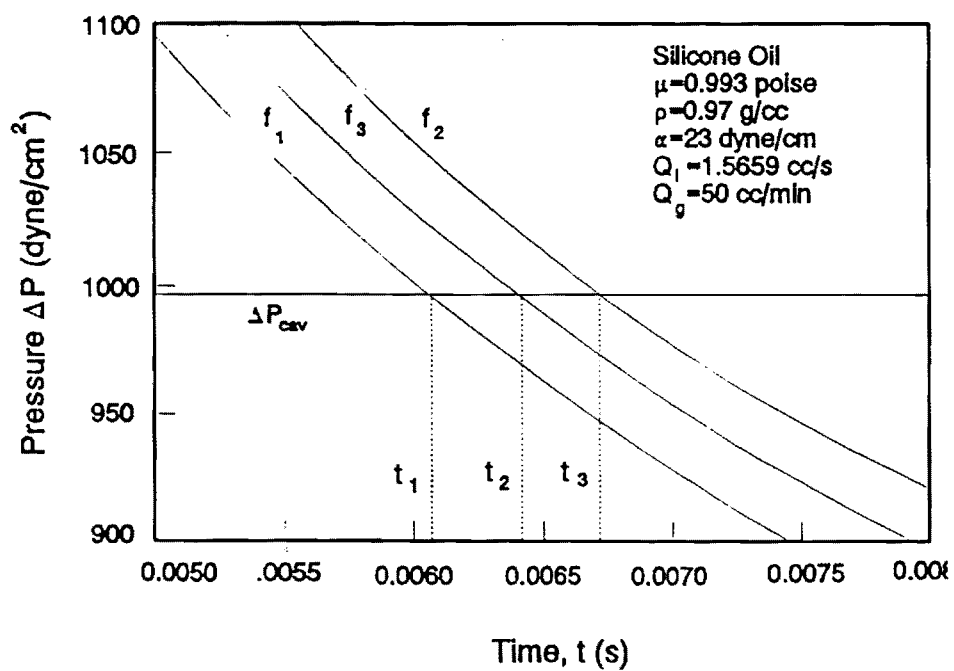


Figure 2.3.8. Iterative Method Used to Calculate Correct Frequency.

### 2.3.3 PREDICTION OF SPHERE DIMENSIONS AND VERIFICATION

One purpose of an accurate hollow sphere formation model is that, by predicting sphere formation frequency,  $f$ , one can predict other characteristics of the hollow spheres such as diameter,  $d$ , wall thickness,  $th$ , and liquid sphere density,  $\rho$ , with the following relationships,

$$d = 2 \left[ \frac{3(Q_l + Q_g)}{4\pi f} \right]^{\frac{1}{3}} \quad (2.3.19)$$

$$th = \left[ \frac{3(Q_l + Q_g)}{4\pi f} \right]^{\frac{1}{3}} - \left[ \frac{3Q_g}{4\pi f} \right]^{\frac{1}{3}} \quad (2.3.20)$$

$$\rho_{bubble} = \frac{Q_l/f}{(Q_l + Q_g)/f} \cdot \rho = \frac{Q_l}{Q_l + Q_g} \cdot \rho \quad (2.3.21)$$

These parameters have been intensively addressed and it was demonstrated<sup>23</sup> that the establishment of the model allows for tailoring of the process to meet the specification requirements of the final products.

Verification of the model is shown in Figure 2.3.9. The model (solid curves) agree well with experimental data for higher liquid flow rate ( $Q_l \geq 1.25$  cc/s). However, at lower  $Q_l$ , or lower  $Q_l/Q_g$  ratios, model calculations deviates from the experimental frequencies. This deviation might be explained by the fact that at lower  $Q_l$ , or lower  $Q_l/Q_g$  ratios, the cylindrical part of the cavity became less obvious or even disappeared. Consequently the definition of critical condition (which was closely related to the existence of the cylindrical cavity) became ambiguous and eventually led to invalidity of the model.

### 2.3.4 CONCLUSIONS

The experiments presented here with newtonian silicone oil have shown that coaxial nozzle hollow sphere formation was divided into high  $Q_l$  region and low  $Q_l$  region. At high  $Q_l$  region inner jet gas flow rate dominated the process. Sphere formation frequency increased with increasing inner jet gas flow rate. At low  $Q_l$  region the influence of inner jet gas flow rate on frequency disappeared. Frequency remain approximately the same in spite of changing inner jet flow rate. A mathematic model was derived which predicted newtonian liquid hollow sphere formation to a reasonable

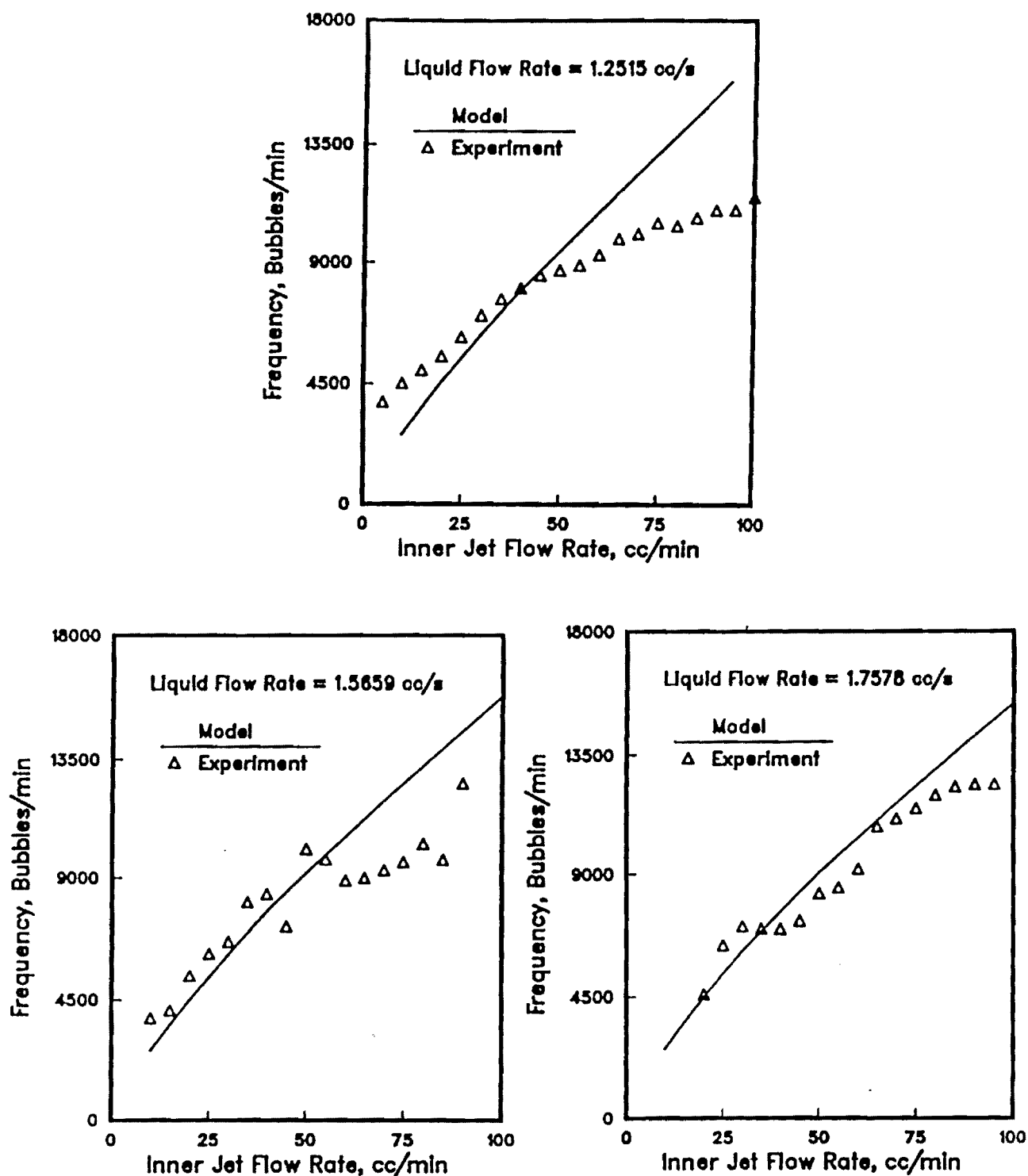


Figure 2.3.9. Comparison of Experimental Results and Model Calculations of Frequency vs. Inner Jet Flow Rate for Silicone Fluid ( $\mu = 0.993$  poise,  $\alpha = 23$  dyne/cm,  $\rho = 0.97$  g/cm<sup>3</sup>) for High Liquid Flow Rates.

extend at high  $Q_l$  region. The current model does not predict the sphere formation frequency at lower liquid flow rate range because the critical condition for the hollow sphere formation could not be defined at low liquid flow rates. It should be noted that experiments were also conducted with high solids loaded alumina slurries and experimental testing confirmed that the model presented here has the same accuracy as for the silicon oil data.

Thus, the model appears to describe the process accurate over the regions where it applies.

### 2.3.5 GLOSSARY

$R_o$	:	inner radius of cylindrical cavity
$\delta$	:	wall thickness of cylindrical cavity
$R$	:	instantaneous inner radius of the hollow sphere
$w$	:	spherical shell thickness
$\dot{R}$	:	expansion rate of inner radius of sphere, $= \partial R / \partial t$
$R^*$	:	sphere inner radius at critical condition
$Q_g$	:	gas flow rate
$Q_l$	:	liquid flow rate
$\rho$	:	liquid density
$\alpha$	:	liquid surface tension
$\mu$	:	liquid viscosity
$t_b$	:	time period of sphere formation
$f$	:	hollow sphere formation frequency
$P_A$	:	$= P_{air, R+w}$
$P_{air, R+w}$	:	hydrostatic pressure of atmospheric air
$P_{liq, R+w}$	:	hydrostatic pressure of liquid at outer surface of sphere
$P_{liq, R}$	:	hydrostatic pressure of liquid at inner surface of sphere
$P_{gas, R}$	:	hydrostatic pressure of gas inside the sphere
$\tau_{rr} \Big _{air, R+w}$	:	viscous stress due to atmospheric air
$\tau_{rr} \Big _{liq, R+w}$	:	viscous stress due to liquid at outer surface of sphere
$\tau_{rr} \Big _{liq, R}$	:	viscous stress due to liquid at inner surface of sphere
$\tau_{rr} \Big _{gas, R}$	:	viscous stress due to gas inside the sphere
$\Delta P$	:	pressure difference across the spherical shell
$\Delta P_{cav}$	:	pressure difference across the cylindrical shell
$\Delta P_{tran}$	:	pressure difference across the liquid shell at the transition zone.

### 2.3.6 REFERENCES

1. A.T. Chapman, J.K. Cochran, T.R. Ford, S.D. Furlong, and D.L. McElroy, "Reduction of High Temperature Thermal Conductivity of Thin-Wall Ceramic Spheres," *Insulation Materials: Testing and Applications*, 2, ASTM STP 1116, R.S. Graves and D.C. Wysocki, Eds, American Society of Testing and Materials, Philadelphia, pp.465-76, 1991.
2. M.K. Adicks, *Strength Characterization of Thin-Wall Hollow Ceramic Spheres From Slurries*, MS Thesis, Georgia Institute of Technology, School of Ceramic Engineering, March 1989.
3. M.J. Shapiro, *Thermal Conductivity of Thin Wall Hollow Ceramic Spheres*, MS Thesis, Georgia Institute of Technology, School of Ceramic Engineering, March 1988.
4. S.D. Furlong, *Reduction of Radiative Thermal Conductivity in Thin-Wall Hollow Ceramic Spheres Using Scattering Phases*, MS Thesis, Georgia Institute of Technology, School of Materials Engineering, Dec. 1990.
5. T.R. Ford, *Thermal Conductivity of Bonded Hollow-Sphere Monoliths*, MS Thesis, Georgia Institute of Technology, School of Materials Engineering, June 1991.
6. R.B. Clancy, J.K. Cochran, and T.H. Sanders, "Fabrication of Thin-Wall Hollow Nickel Spheres and Low Density Syntactic Foams," *Proceedings of Second International Conference on Light Weight Alloys*, TMS Annual Meeting, New Orleans, LA, Feb. 1991.
7. R. Meyer Jr., H. Weitzing, Q. Xu, Q. Zhang, and R.E. Newnham, and J.K. Cochran, "PZT Hollow-Sphere Transducers", to be published in *Bulletin Am. Ceram. Soc.*, June 1994.
8. L.B. Torobin, *Method for Making Hollow Porous Microspheres*, US Patent No. 4,671,909, Jun. 9. 1987.
9. A. Ziabicki and R. Takserman-Krozer, "Formation and Breakage of Liquid Threads. I. Mechanism," *Roczniki Chemii Ann. Soc. Chim. Polonorum*, 37, pp. 1503, 1963.
10. L. Rayleigh, "On the Instability of a Cylinder of Viscous Liquid under Capillary Force," *Phil. Mag. S. 5*, Vol. 34, No. 207, Aug. 1892.

11. A. Ziabicki and R. Takserman-Krozer, "Formation and Breakage of Liquid Threads. III. Capillary Break-up of A Steady Viscous Jet," *Roczniki Chemii Ann. Soc. Chim. Polonorum*, **37**, pp. 1607, 1963.
12. A. Ziabicki and R. Takserman-Krozer, "Formation and Breakage of Liquid Threads. IV. Effect of Rheological Behavior on the Length of Liquid Threads," *Roczniki Chemii Ann. Soc. Chim. Polonorum*, **38**, pp. 465, 1964.
13. C.P. Lee and T.G. Wang, "A Theoretical Model for the Annular Jet Instability," *Phys. Fluids* **29**(7), July 1986.
14. R.J. Calliger, R.J. Turnbull, and C.D. Hendricks, "Hollow Drop Production by Injection of Gas Bubbles into a Liquid Jet", *Rev. Sci. Instrum.*, **48**[7] 846-51, 1977.
15. James M. Kendall, "Experiments on Annular Liquid Jet Instability and on the Formation of Liquid Shells", *Phys. Fluids*, **29** [7], 2086-94, 1986.
16. N.K. Kim, K. Kim, D.A. Payne, and R.S. Upadhye, "Fabrication of Hollow Silica Aerogel Spheres by a Droplet Generation Method and Sol-Gel Processing", *J. Vac. Sci. Technol.* **A7**[3] 1181-4, 1989.
17. K.Y. Jang, K. Kim, and R.S. Upadhye, "Study of Sol-Gel Processing for Fabrication of Hollow Silica-Aerogel Spheres", *J. Vac. Sci. Technol.* **A8**[3] 1732-5, 1990.
18. K. Kim, K.Y. Jang, and R.S. Upadhye, "Hollow Silica Spheres of Controlled Size and Porosity by Sol-Gel Processing", *J. Am. Ceram. Soc.*, **74**[8] 1987-92, 1991.
19. A.M. Bennie and H.B. Squire, "Liquid Jets of Annular Cross Section," *Engineer*, **171**, pp.236-38, 1941.
20. M.H.I. Baird and J.F. Davison, "Annular Jet - I. Fluid Dynamics," *Chemical Eng. Science*, **17** pp.467, Pergamon Press Ltd, London, 1962.
21. S. Middleman, *Fundamentals of Polymer Processing*, McGraw-Hill, Inc. New York, 1977.
22. R.B. Bird, W.E. Stewart and E.N. Lightfoot, *Transport Phenomena*, John Wiley and Sons, Inc.

23. P.R. Chu, *A Model for Coaxial Nozzle Formation of Hollow Spheres from Liquid*, PhD Thesis, Georgia Institute of Technology, School of Materials Engineering, June, 1991.



## 2.4 GEOMETRICAL CHARACTERISTICS OF THIN WALL HOLLOW SPHERES

This section characterizes the sphere geometry from the coaxial nozzle process and demonstrates that this produces thin-wall hollow spheres which have a size uniformity seldom achieved by high volume manufacturing processes. To demonstrate the capabilities of the process, spheres were blown from the same slip under two sets of conditions; (1) 40 psi on the slip and 20 cc/min blowing gas flow rate (40-20) and (2) 20 psi with a blowing gas rate of 40 cc/min (20-40). Note that the ranges for both these variables are much greater than those values used here. The hollow sphere parameters presented below, Table 2.4.1, are not the limitation of the process but are presented to demonstrate the degree of perfection of size distribution and sphericity achievable at this time. As the process continues to improve, degree of perfection will increase. The measurements and distributions presented are for randomly selected spheres from the two conditions.

Table 2.4.1. Characteristics of Thin Wall Hollow Spheres Fabricated Under Two Blowing Conditions.

Parameter	<u>Blowing Conditions</u>	
	40-20	20-40
Green Bulk Density (g/cc)	0.51	0.20
Fired Bulk Density (g/cc)	0.61	0.25
Fired Sphere Density (g/cc)	1.07	0.41
Wall Thickness Fired ( $\mu\text{m}$ )	112	56
Diameter ( $\mu\text{m}$ )	2502 $\pm$ 71	3169 $\pm$ 83
Aspect Ratio a	1.11 $\pm$ 0.05	1.08 $\pm$ 0.02
Shape Factor b	1.04 $\pm$ 0.02	1.03 $\pm$ 0.02

a Due to measurement error, the aspect ratio (max dia/min dia) for perfect spheres was 1.05 for 40-20 and 1.04 for 20-40.

b Shape Factor =  $P^2/4\pi A$  where P = perimeter and A = area.  
Shape Factor for Spheres = 1.00, Hexagons = 1.10, Squares = 1.27 and Triangles 1.65.

For the higher slip pressure (or liquid flow rate) and lower blowing gas flow rate (40-20), spheres of smaller size were produced compared to a lower slip flow rate and higher gas flow rate (20-40) as shown in Figure 2.4.1. As the ratio of gas to slip flow rate increased, spheres were larger and had a smaller wall thickness as would be expected, Figure 2.4.2. After recovery and drying, the bulk density of the green product as measured by weighing ~100 cc of tapped spheres was 0.51 and 0.20 g/cc (31.8 and 12.5 lb/ft<sup>3</sup>), respectively. After firing at 1650°C for 2 hours, the A-3000 alumina sphere walls were impervious as indicated by boiling in water and the spheres increased in bulk density to 0.61 and 0.25 g/cc (38.1 and 15.6 lb/ft<sup>3</sup>), respectively.

Sphere diameters, aspect ratios, and shape factors were measured using a video camera interfaced to an image analyzer. At a magnification of 11x, four spheres at a time could be measured. For each sphere, the diameter in eight directions, the perimeter, and the cross sectional area were recorded. For each blowing condition, 64 randomly selected spheres were quantified. As reported in Table 2.4.1 and shown in Figure 2.4.3, the average diameters for the two conditions were 2.50 and 3.17 mm with one standard deviation for the distributions of 2.8% and 2.6%, respectively. This provides a 3 $\sigma$  limit of ~8% which is well under the 10% target for diameter variation suggested in the work statement.

Spherodicity was measured with two techniques, aspect ratio and shape factor, by the image analyzer. The aspect ratio measured for each sphere was the maximum of the eight diameters divided by the minimum diameter. Because the sphere image was digitized from a video camera, the viewed area was divided into 256 x 256 pixels. Each diameter measurement had an error of  $\pm 1$  pixel. This provided a diameter measurement error of 2.5% for the small spheres and 2.0% for the large spheres. Because of the error, perfect spheres would have average aspect ratios of 1.05 and 1.04 for the small and large spheres, respectively. The measured average aspect ratios for 40-20 and 20-40 were 1.11 and 1.08, respectively (Figure 2.4.4) which provided deviations of 6% and 4% from spherodicity, respectively. Although, the 6% and 4% deviations are above the desired value of 2%, it must be noted that aspect ratio is the most severe measurement of spherodicity that can be applied. As residence time in the recovery tower is increased, so also should spherodicity. A more moderate measure of spherodicity was the shape factor which is  $P^2/4\pi A$  where P is the measured perimeter and A the cross sectional area of the projected sphere. Shape factor for a perfect sphere is 1.00; for a hexagon, it is 1.10; and a square has a factor of 1.27. Shape factors on average were 1.04 and 1.03 for the small and large spheres, respectively. Standard deviations for the shape factors were only 2%. By this techniques, deviations from spherodicity were minimal.

Using the average diameter for each distribution to calculate individual sphere volume and the average individual sphere weight from 100 spheres, the true sphere density

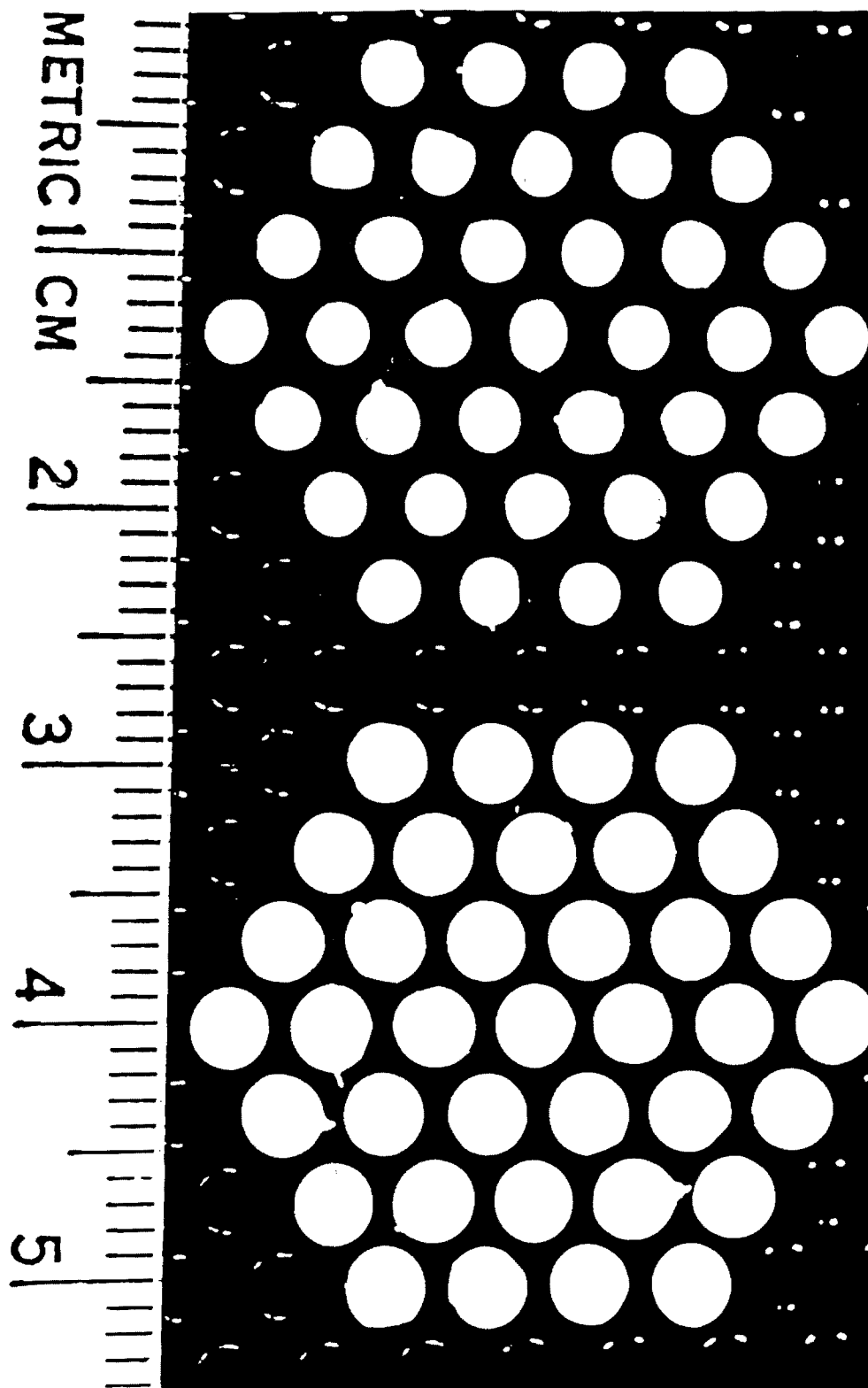


Figure 2.4.1 Photographs of Fired, Thin-Wall, Alumina, Spheres Formed at Blowing Conditions (a) 40-20 and (b) 20-40.

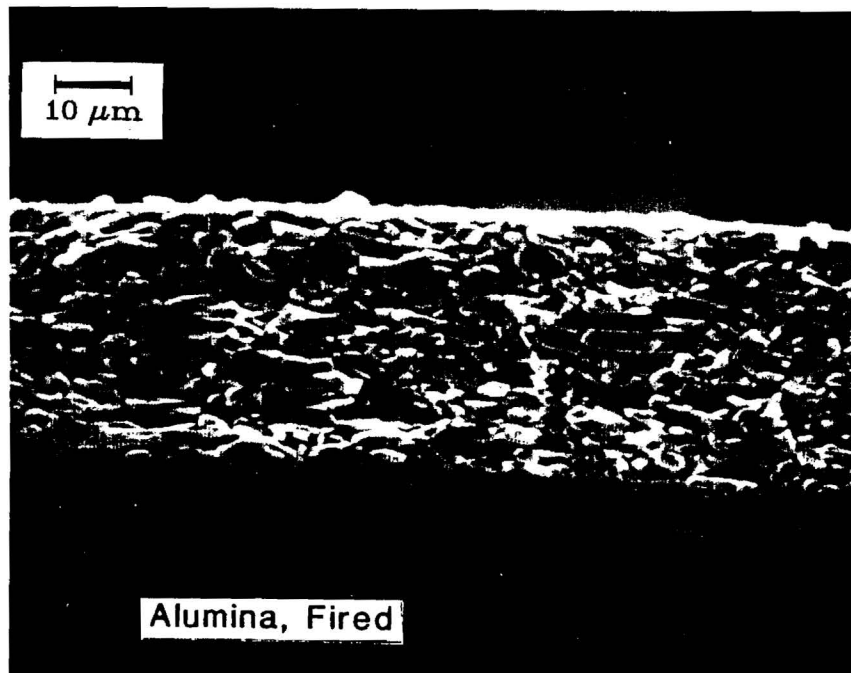
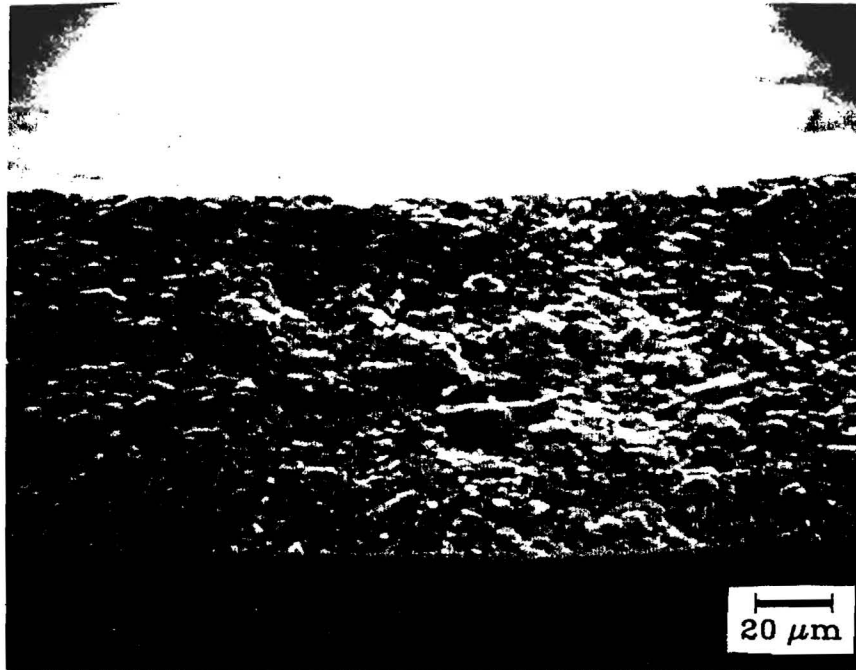
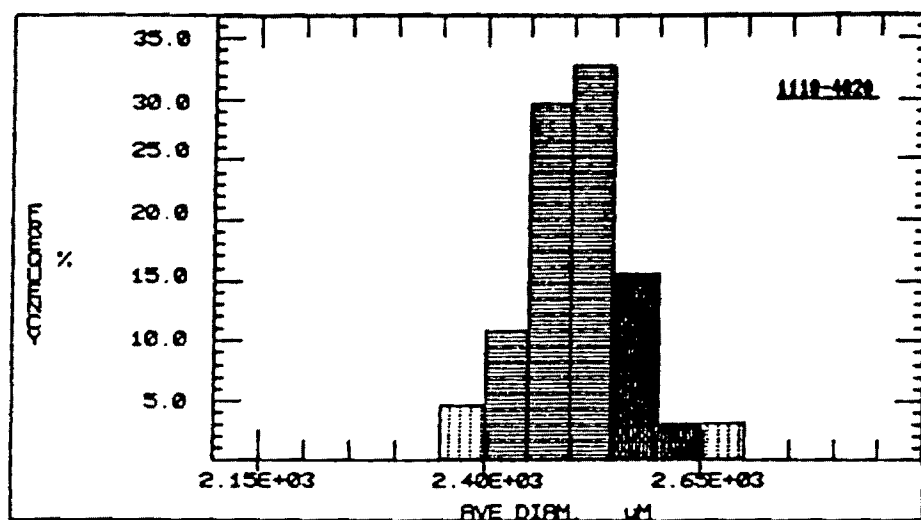
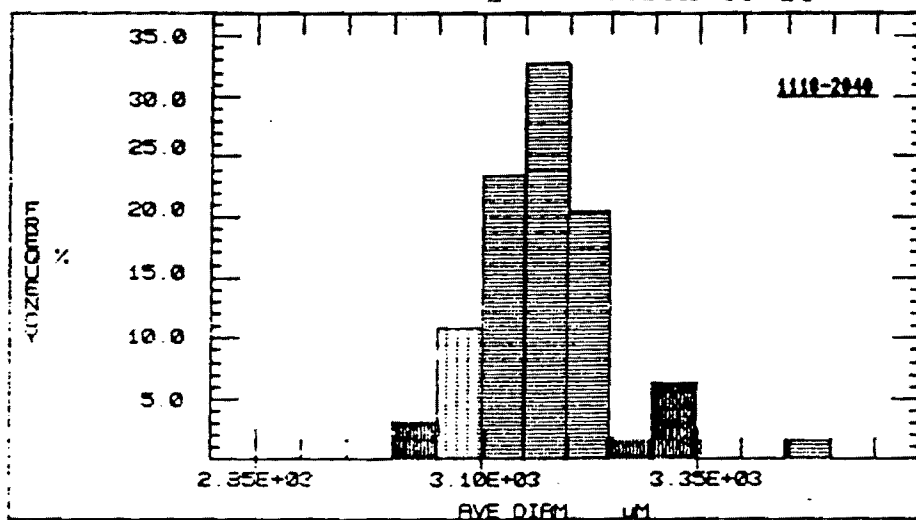


Figure 2.4.2

Cross-section of Sphere Walls for Polycrystalline Alumina Spheres Fired at 1650°C, (a) 40-20 and (b) 20-40.

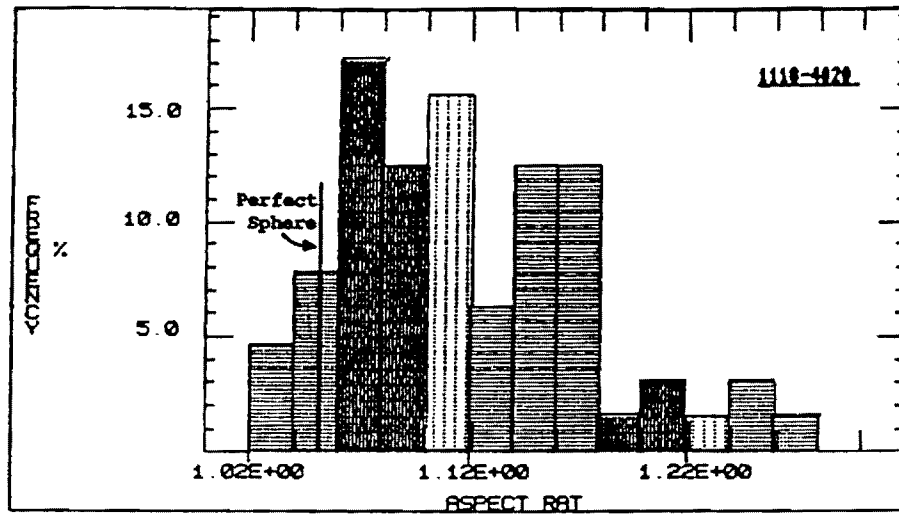


(a) Blowing Condition 40-20

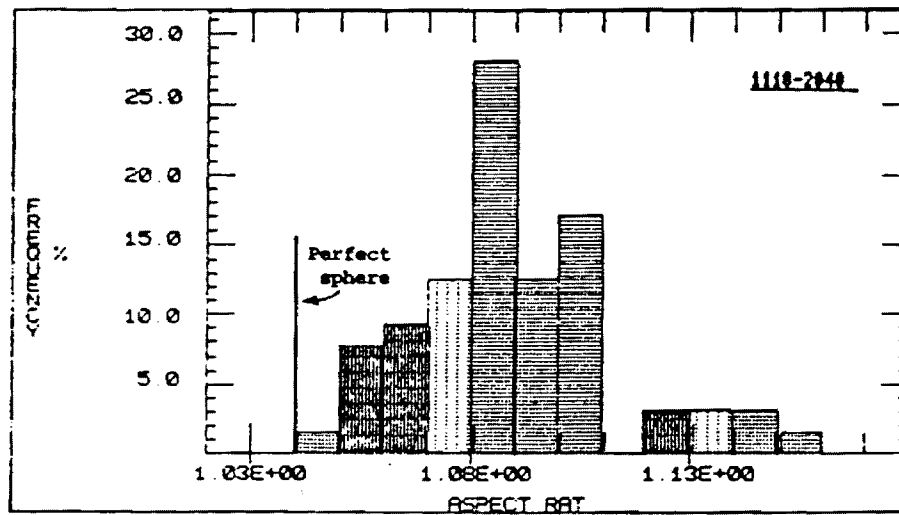


(b) Blowing Condition 20-40

Figure 2.4.3 Diameter Distributions for 64 Randomly Selected Thin Wall Hollow Alumina Spheres.



(a) Blowing Conditions 40-20



(b) Blowing Condition 20-40

Figure 2.4.4 Aspect Ratio Distributions for 64 Randomly Selected Thin Wall Hollow Alumina Spheres.

was calculated to be 1.07 and 0.41 g/cc for the small and large spheres, Table 2.4.1. Based on an alumina wall density of 3.98, the average wall thicknesses were calculated to be 112 and 56  $\mu\text{m}$ , respectively, see Table 2.4.1. The thicknesses from the wall cross section micrographs of Figure 2.4.2 agree well with these values. Statistical analysis of wall thickness variation has not yet been completed but techniques using the image analyzer are under development.

From the above analysis, it can be seen that the thin walled spheres being produced by the coaxial nozzle process have a uniformity seldom achieved by a bulk production process. As process controls are varied and improved, not only will the range of diameter and densities increase but distributions and deviations from sphericity will approach a true monodispersed state.

## 2.5 FORMING SPHERES FROM AQUEOUS SLURRIES

Formation of hollow spheres from acetone based slurries has been very successful and at the time of this report over 300,000 lbs of spheres/year are being manufactured for automotive applications. However, because of concerns for organic emissions and the limitations that are legislated, a real need exist to convert the process to water based operation. A major effort has been made to use naturally occurring gums to gel the slurry systems and provide the necessary rigidity in the free falling spheres to survive a landing on a hard surface. Carrageenan was identified as the gum possessing the optimum properties for the sphere forming and collecting process. The typical gelling and melting characteristics of this class of material is shown in Figure 2.5.1 where the viscosity versus cycling temperature are plotted. After the initial gum solution and slurry processing, the dispersions containing the gelling agent are heated to high temperature ( $\sim 80^{\circ}\text{C}$ ) to provide a low viscosity slurry for forming the sphere. Once the spheres are formed by the coaxial nozzle technique, they are rapidly cooled to below  $50^{\circ}\text{C}$  to initiate the gelling process. Most encouraging was the demonstration that, indeed, the aqueous-based systems could be gelled during the 3 to 5 second free-fall residence time and the sphere wall developed adequate strength to maintain a "sphere-like" geometry during landing.

At present the sphere forming characteristics of the aqueous slurries have not matched the quality or low densities of acetone-based systems. For example, the slurries containing carrageenan must employ 3 to 4 w/o of the gum to provide enough gel strength to maintain the shape during free-fall and survive the landing. Unfortunately these slurries, with a high volume loading of solids ( $\text{Al}_2\text{O}_3$  powder), are very viscous and do not possess the film-forming capacity of the organic systems. As a result the typical density of the aqueous processed spheres is 40-50 lbs/ft<sup>3</sup> compared to 20-30 lbs/ft<sup>3</sup> for the acetone derived spheres. Photographs comparing spheres formed from both acetone and aqueous/carrageenan slurries are showing the raisin like surface of the aqueous spheres, Figure 2.5.2. Because of the softer wall and landing damage, the sphericity of the aqueous spheres do not match that of the organic base spheres. Work should be continued on aqueous systems and the gelling concept because of the economic attractiveness of the water-based systems.

### 2.5.1 PROPERTIES OF POLYSACCHARIDES

Polysaccharides exhibit a behavior known as gel thermoreversibility [5], Figure 2.5.1. To gel a polysaccharide, it is first dispersed in water. The dispersion is brought to an elevated temperature and, just prior to boiling, the polysaccharide goes into solution. The solution exhibits a relatively low apparent viscosity. On cooling, the polysaccharide solution gels. This gel can be reheated and put back into solution, resulting again in a low apparent viscosity. The cycle of converting gel to fluid and



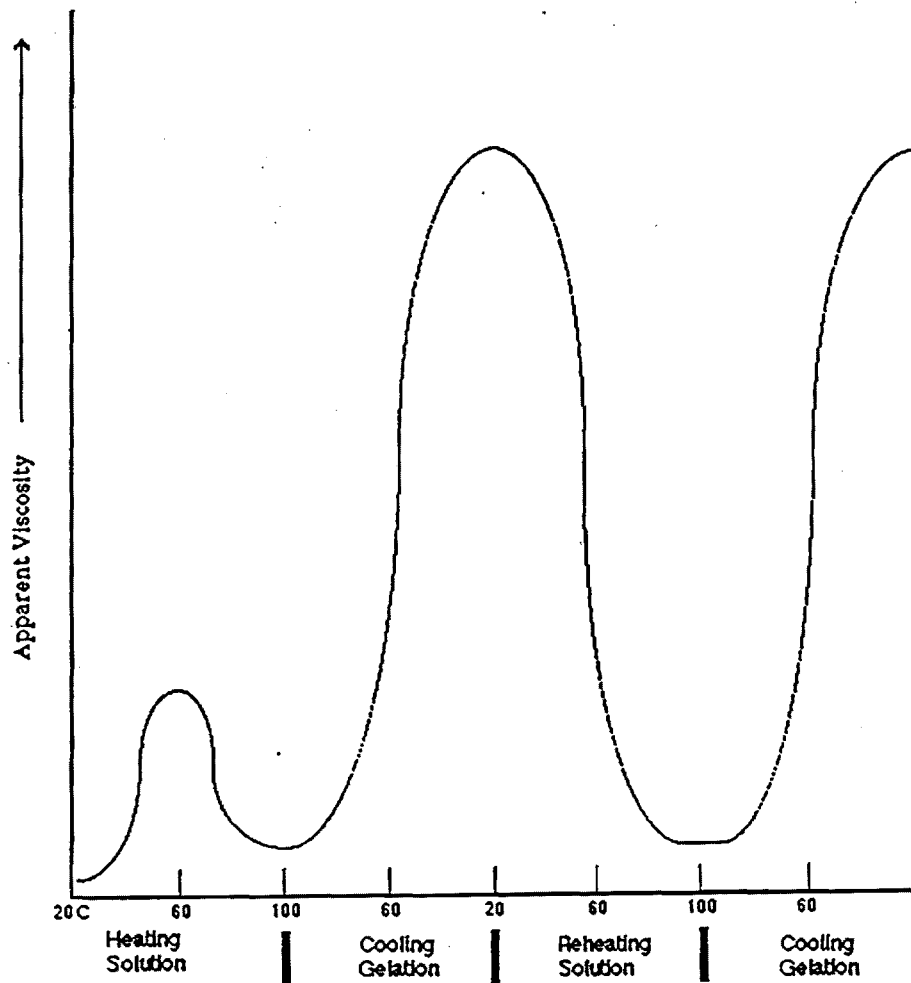
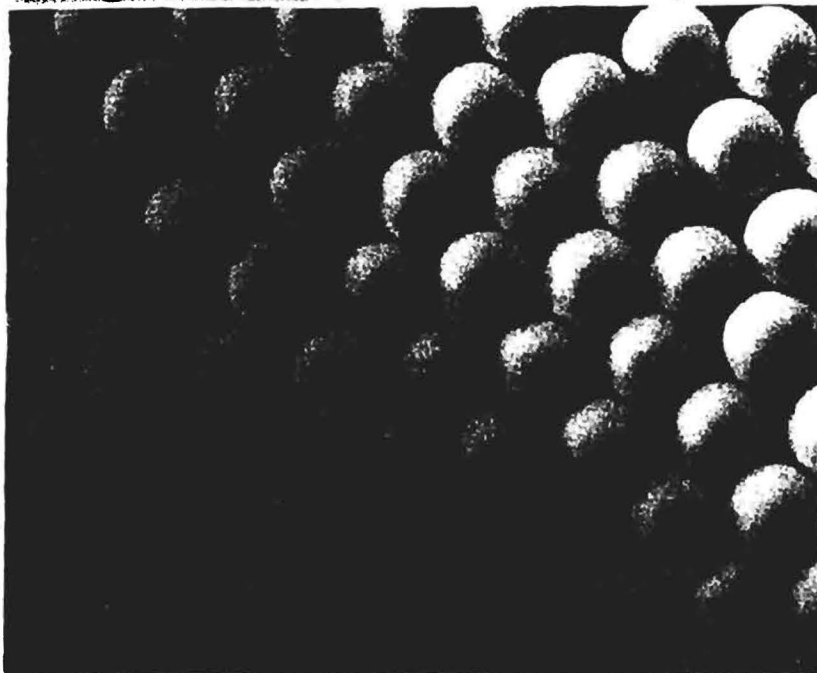


Figure 2.5.1 Gel Thermoreversibility, Describes Repeated Low Viscosity Solutions at High Temperatures and Solid Gels at Low Temperatures

### Organic Based Alumina Aerospheres



### Water based Alumina Aerospheres

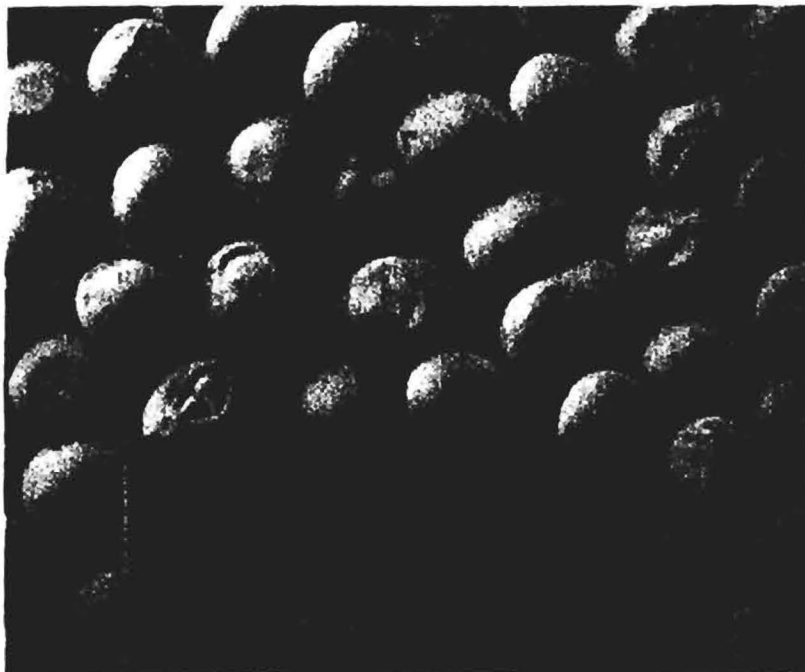


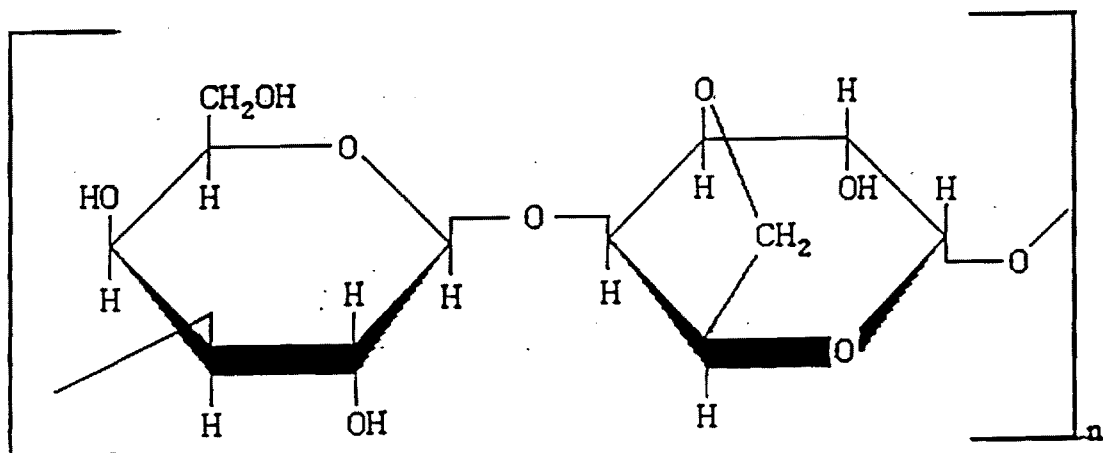
Figure 2.5.2 Comparison of Hollow Spheres From (A) Acetone Based Slurries and (B) Aqueous Based Slurries Using Carrogeenan as the Gelling Agent

fluid to gel can be repeated many times. The average molecular weights of two most used polysaccharides, agar and carrageenan, are on the order of 100,000 [2] and 250,000 [22], respectively. The viscosity of the polysaccharides are very high due to their unbranched linear polymer structure and the negative repulsion that is produced along the chain by the ester sulfate groups. For carrageenan, this repulsion keeps the polymer rigid. The hydrophilic nature of the polymer causes a layer of immobilized water to be maintained [3] which results in a viscous fluid. Addition of cations, in the form of salts, decrease the viscosity of carrageenan at elevated temperatures, by reducing the effect of the negative charge by the sulfate group [3]. Polysaccharides exhibit a characteristic that is termed "pseudoplastic" and often referred to as shear thinning [5,23]. Pseudoplasticity in polysaccharides is due to the alignment of the polymer molecules in a manner that reduces the resistance of flow [8]. This results in an apparent decrease in viscosity as shear is increased.

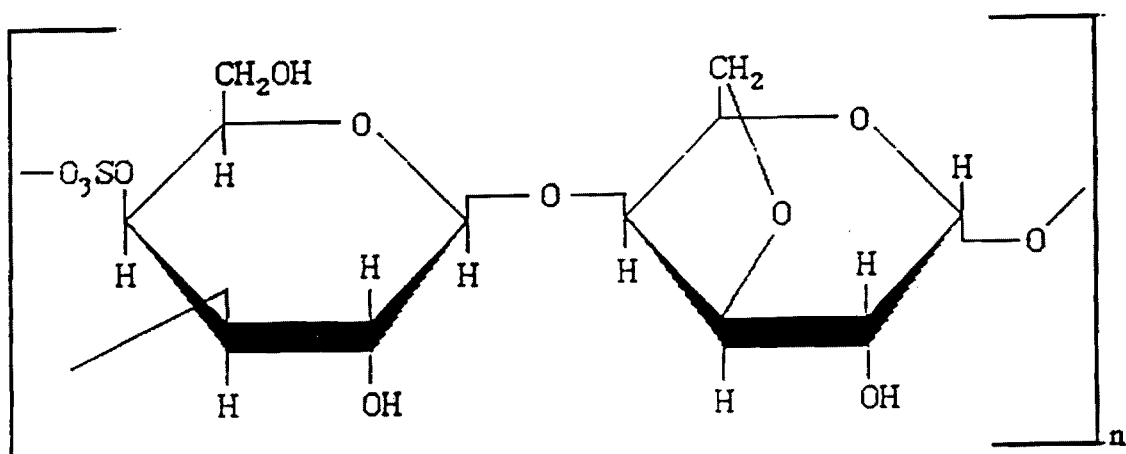
After identifying the "idealized" structure of agar, it was determined that the fraction of agar with the greatest gelling capacity could be separated from a normal distribution of the product. This "high gelling" fraction was termed agarose [17], Figure 2.5.3(A) [1,2,24]. Carrageenan also can be separated by precipitation and centrifuge methods. To date, six different types, of carrageenan have been identified, three of which, kappa, iota and lambda, are available commercially [3,17,22,25]. Lambda carrageenan does not gel but proves to be an excellent dispersant for heavy particles [5,22]. Iota carrageenan forms elastic syneresis free gels, that is, a gel that does not weep or exude water upon gelation [4,5,26]. Kappa carrageenan, which usually has traces of calcium ions, form rigid or, as commonly referred to in the industry, brittle gels [5,22,26], Figure 2.5.3(B) [3,22,24,27]. Kappa carrageenan also exhibits syneresis. Iota gels are the only ones that have "rehealing" properties; if the gel is broken, the polymer molecules can eventually reform. Reformation of a gel is referred to as thixotropy [3, 26] .

The process of gelation for kappa carrageenan and agarose has been drawn from the verbal description in reference [17]. The differences between the two may seem slight, but actually are of major influence to final gel strength. For kappa carrageenan, small levels of masking residue from the production process cause portions of the molecular chain to kink. Therefore, a double helix formation produced by two polymer chains is interrupted at the kink, allowing the polymers to form additional double helices with other chains [3,17]. Agarose, on the other hand, can only form single pairs of double helices [17]. The formation of the double helices are the result of hydrogen bonding between the two polymer chains [4]. In both cases, the helices "trap" water and hold it in place forming the gel.

Kappa carrageenan has the added ability to trap water through aggregation. Aggregation is the formation of "super junctions" [24] between two or more helices,



(A)



(B)

Figure 2.5.3 Idealized Molecular Structure of (A) Agarose and (B) Kappa Carrageenan

due to the attraction caused by the potassium and calcium ions, which are usually present in the carrageenan. The ester sulfates along the kappa carrageenan molecule provide attachment points for the calcium ions. This aggregation of the polymer helices causes syneresis and contributes to dramatically increasing the gel strength. The process of aggregation can be enhanced through further addition of calcium ions and certain other types of cations in the solution [4,5,26,27]. Cesium ions are more efficient than sodium ions in their ability to form junction zones. This is apparently due to an observed selectivity by the molecule, which results in more bonding sites [29,30]. Agar's gel strength is not affected by ions dispersed in the water; hence its helices cannot be aggregated. The inability to aggregate the agar helices is most likely due to the lack of sulphates associated with the molecule. The sulfates are theorized to be points of attachment for the cations in kappa carrageenan [27].

### 2.5.2 MEASUREMENT OF GEL STRENGTH AND VISCOSITY

A comparison of the most promising polysaccharides were tested for gel strength and fluid viscosity. It should be noted that there is no standard for measuring gel strengths [26]. This is probably due to the fact that the principal consumer of gels is the foods industry which is more interested in the texture as felt by the mouth, rather than in the actual strength of the gel in engineering terms. The most common form of measuring gel strengths is to impinge the gel surface with a 1 cm<sup>2</sup> diameter plunger, which is subsequently forced into the gel. The force required to break the gel at room temperature is measured in units of grams/cm<sup>2</sup> [1,23].

**Preparation of Gels** - The polysaccharide test samples to be measured for their gel strength were made in the following manner. Polyethylene containers, 250 ml, with air tight threaded caps were filled with 200 grams of tap water. Specified weights of ion species, such as K<sub>2</sub>CO<sub>3</sub>, were added to the water. The polysaccharide was weighed and added to the solution and, after sealing the container, was shaken vigorously. The container was placed into a boiling water bath and agitated occasionally until all the gel powder had gone into solution. It was determined the polysaccharide had gone into solution when there were no visible clumps and the viscosity had decreased dramatically. The solution was poured into 250 ml sealable molds (cups with lids) and was allowed to gel on cooling to room temperature. For kappa carrageenan, the gel temperature is dependent on the concentration of cation species in solution and to a lesser degree the concentration of kappa carrageenan in solution. The larger the concentration of cations and kappa carrageenan, the higher the gelation temperature. Usual gelation temperatures for kappa carrageenan fall in the range of 20 to 80°C [3]. For agarose, the gel temperature is dependent on the concentration of agarose in solution. The higher the concentration of agarose, the higher the gel temperature. Usual gelation temperatures for agarose fall in the range of 30 to 45°C [2].

**Gel Strength Measurements** - A Universal Instron Testing machine, used in compressive mode was used to test gel strengths. The gels were placed on a precalibrated load cell, usually in the cup, unless the surface of the gel was defective. If there was entrained air at the surface due to an accelerated gelation rate, the gel was removed from the cup and set inverted, on the load cell. The force required to break the gels was read off of a strip chart in g/cm<sup>2</sup> using a cross head speed of 0.1 cm/min and a plunger with 1 cm<sup>2</sup> surface area. The edges of the plunger were polished to eliminate sharp edges to prevent prematurely rupturing the gel. Gel strength tests were conducted on agar (S-100 [31]) and kappa carrageenan (Gelcarin® GP 911 [28]). A series of tests were conducted on kappa carrageenan (911) with varying concentrations of specific cations to determine cation effect on gel strength. Note, there is no increase of gel strength on agar when cations are added because of the lack of ester sulfate groups. Hence, many more tests were conducted on kappa carrageenan than on agar.

**Gel Viscosity Measurements** - To measure viscosities of gel solutions, the same steps were repeated in preparation of the gels, up to the point that the dispersed polysaccharide went into solution in the hot water bath. Samples were placed directly into a preheated HAAKE viscometer of the Searle coaxial cylinder type. The viscometer was controlled through a Rotoviscometer RV20 and an IBM personal computer [32]. Solutions with low viscosities and high viscosities were measured with spindles NV and MVII, respectively. It was recommended that viscosity measurements of polysaccharides be conducted at temperatures greater than 75 °C [3] to stay well above solution temperatures. Hence, the temperature of the samples was maintained at 90°C + /-0.4 during these measurements. Temperature of the gel solution samples was controlled by a HAAKE circulator, a circulating water bath with thermal elements, and a temperature control monitor [32]. During viscosity measurements, the samples were covered with a stainless steel disc which had a hole in the center for the spindle and a rubber ring that fit close to the spindle to prevent evaporation of the water. Evaporation had to be prevented in order to maintain the proper concentration of the polysaccharide in solution. The shear rate was increased at a predetermined rate from zero to 1100 1/sec for spindle NV, zero to 450 1/sec for spindle MVI 1.

**Slurry Preparation** - Kappa carrageenan was chosen as the binder for attempts to fabricate aqueous based hollow spheres. Slurry preparation entailed weighing the water, adding 0.5 wt% of a dispersant (Darvan 811 a 43% solution sodium polyacrylate), based on powder weight, and adding potassium ions, in the form of K<sub>2</sub>CO<sub>3</sub>, based on weight percent in the water. The mixture was shaken to place the potassium ions into solution. Alumina, A3000 from Alcoa, with a particle density of 3.98 g/cm<sup>3</sup>, was weighed to produce a known solids volume in water. The slip was ball milled overnight using 2 cm zirconia cylinders. After milling, kappa carrageenan

(911) was added to the slip at a specific percent weight in water. The slip was mixed with a high shear blender to promote dispersion of the carrageenan particles. The sealed container was placed in a boiling water bath. The container was removed and shaken periodically for verification of polysaccharide solution.

### 2.5.3 GEL STRENGTH AND VISCOSITY OF CARRAGEENAN SLURRIES

Gel strength tests and viscosity measurements were conducted on agar and kappa carrageenan. Data and results for agar gels will not be presented here since carrageenan was selected for sphere formation. Kappa carrageenan was tailored, through the use of specific cations, for optimum strength and viscosity properties. The kappa carrageenan was then used as the binder for slurries in the formation in wall hollow spheres.

**Gel Strength Comparison** - Agar's gel strength of 1500 g/cm<sup>2</sup>, at 3 wt% concentration, was consistent with Fanelli et al. [1]. In an effort to produce stronger gels, the gel strength of agar (S-100) was measured as a function of concentration. Agar reached a strength of 2600 g/cm<sup>2</sup> at 5 wt% and the strength was approximately linear with concentration. Extrapolating to zero strength indicates that 0.5 wt% of agar is required to form a gel. For use as a binder, agar's gel strength was only half that of kappa carrageenan samples gelled with K<sup>+</sup> and Cs<sup>+</sup> at high concentrations. Therefore, agar was abandoned as a hollow sphere binder.

**Optimization of Kappa Carrageenan's Gel Strength** - Unlike agar, it is known that kappa carrageenan's gel strength can be enhanced through the use of certain cations. A list of suitable cations can be found in the foods industry literature. The list includes: potassium (K<sup>+</sup>), calcium (Ca<sup>++</sup>), sodium (Na<sup>+</sup>), and ammonia (NH<sub>4</sub><sup>+</sup>) [5,26,39]. One reference noted additional cations, Sr<sup>++</sup>, and Ba<sup>++</sup>, but did not say how effective they were in increasing the gel strength [3]. Therefore, varying concentrations of certain cations were put into solution and 3 wt% kappa carrageenan (911) was added to the solution. After going through the procedure outlined above, the solutions were gelled and strength determined, Figure 2.5.4. It was readily apparent that monovalent cations, in particular K<sup>+</sup> and Cs<sup>+</sup>, were superior in terms of improving gel strength. The monovalent cations are dimensionally larger than the divalent cations because the divalent nucleus has a larger contraction effect on the electron cloud, thereby making the cation dimensionally smaller. It is thought that the larger cations can be positioned between the helices more favorable and therefore are able to promote a larger aggregation effect. The gel strength difference between K<sup>+</sup> and Cs<sup>+</sup> were not very different, with K<sup>+</sup> having the slightly higher peak value at 0.42 molarity. A larger K<sup>+</sup> concentration was required to match the same strength produced by Cs<sup>+</sup>. For divalent cations at low concentrations (<0.1 M), Ba<sup>++</sup> exhibited the largest gel strength.

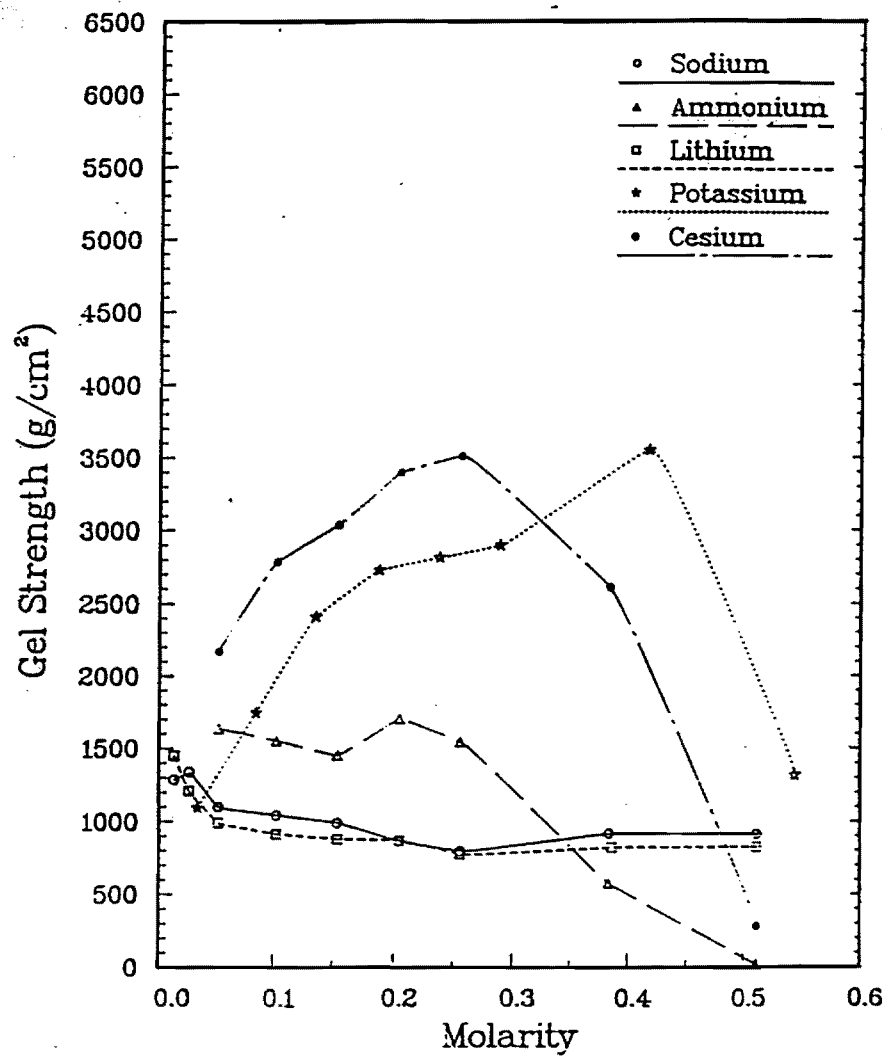


Figure 2.5.4 Monovalent Cations Dissolved at Specific Molarities in Water with 3 wt% Kappa Carrageenan



Again, cation size may be contributing because  $\text{Ba}^{++}$  was the largest of all the divalent cations tested. It was thought that a composition of  $\text{Ba}^{++}$  and  $\text{K}^+$  together would result in an increased gel strength. However, the effect was not statistically significant from  $\text{K}^+$  by itself. Therefore, potassium cations, due to their excellent gel strength properties, were used for the rest of the experiments involving kappa carrageenan.

In order to find the amount of potassium in kappa carrageenan that will produce optimum gel strengths, various weight percentages of  $\text{K}^+$ , based on water weight, were produced by dissolving the solid dry form of  $\text{K}_2\text{CO}_3$ . Weight percentages of kappa carrageenan (911), based on water weight, were dispersed in the water. As was expected, an increase in the amount of potassium, resulted in an increase in gel strength. Above some critical value of potassium, or any cation species, there is a decrease in gel strength, as can be seen in Figure 2.5.5. The drop in gel strength at 2% potassium, is due to a "salting out" [26] of the polysaccharide; that is, a major portion of the polysaccharide is prevented from going into solution at high salt concentrations. The maximum gel strength occurs in the range of 1.5% potassium; but this value exhibits the largest error, which means the predictability of the gel strength is not very good. It has been surmised that the quantity of potassium cations (1.5 wt%  $\text{K}^+$ ) is near the critical juncture. Some specimens were just beginning to salt out at 1.5 wt%  $\text{K}^+$ , while others were experiencing maximum strength. As a result of the unpredictability at 1.5% potassium, all tests conducted after this observation used 1% potassium. This provided sufficient gel strengths which could be expected with some certainty, without having to be tested.

A general trend of the gel strength versus kappa carrageenan concentration is also apparent in Figure 2.5.5 in addition to the  $\text{K}^+$  concentration effect. The gel strength was first examined using regression analysis at each carrageenan concentration curve based on the effect of  $\text{K}^+$  concentration. The potassium was thought to have a volume effect; and the  $\text{K}^+$  concentration raised to the 1/3 power provided a reasonable fit for all five carrageenan contents resulting in the general Equation (2.5.1), where n is equivalent to 1/3.

$$\sigma_g = C [\text{K}^+]^n \quad (2.5.1)$$

Where  $s_g$  is gel strength, C is a constant,  $[\text{K}^+]$  is potassium concentration, and n was 0.333. Similarly, the amount of kappa carrageenan (911) was expected to be related directly to gel strength and when C, in Equation (2.5.1), was analyzed versus carrageenan content, C could be approximated by 900(wt% carrageenan). Therefore, the combined effect of carrageenan and potassium concentration could be expressed as:

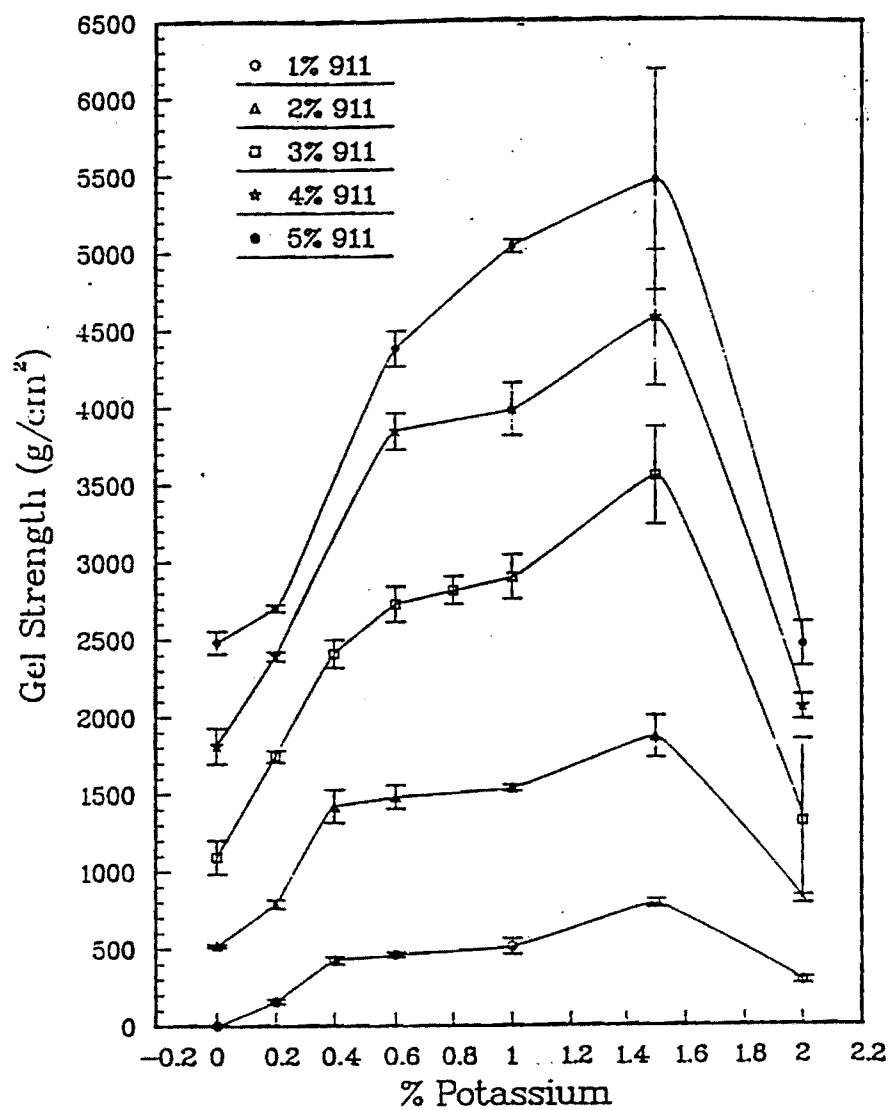


Figure 2.5.5

Gel Strength at Varying Concentrations of Potassium Ions in Aqueous Kappa Carrageenan Gels

$$\sigma_g = 900(\text{wt\% kappa carrageenan})(K^+)^{0.33} \quad (2.5.2)$$

The degree of fit can be seen in Figure 2.5.6, where Equation (2.5.2) is seen to slightly underestimate strengths at high carrageenan contents and overestimate at lower contents. The salting out occurred near the same level for all weight percentages of kappa carrageenan. Therefore, data points were eliminated at  $K^+$  concentrations above the maximum strength and not considered in arriving at this formulation.

**Viscosity of Carrageenan Solutions and Slurries** - The viscosity of kappa carrageenan was measured at two concentrations: 3, and 5 wt% in water, Figure 2.5.7. As anticipated, the addition of agar into water increased in viscosity as a function of the carrageenan concentration. This increase in viscosity was from  $\sim 30$  mPa.sec at 3 wt% to  $\sim 120$  mPa.sec at 5 wt%. Note the shear thinning as the shear rate is increased. This has been attributed to the breaking of bonds between the polymeric chains and alignment of chains with increased shear, which provides less resistance to flow [12]. As polymers get shorter, the molecular weight decreases. This results in an exponential decrease in viscosity [3] as expressed in power law rheology [12].

According to the manufacture [3], viscosity of carrageenan solutions can be decreased through the addition of cations into the polymer solution. A decrease in viscosity is due to a screening of the effective negative charge of the sulfur groups along the polymer chain which in turn, decreases the repulsive forces between neighboring chains, allowing them to slide by each other more easily. An increase in the amount of cations did not necessarily translate into a specific decrease in viscosity, as is shown in Figure 2.5.7.

There is an effect by the potassium cations on the viscosity, but it does not seem to be precisely predictable. For example, Figure 2.5.7(A), the 3 wt% carrageenan (911) has an expected maximum viscosity when no extra cations are introduced into the solution (0 wt% potassium). In Figure 2.5.7(B), at 5 wt% carrageenan (911) 1%  $K^+$  produces the minimum viscosity over the entire applied shear. Except for the decrease in viscosity shown for 3% kappa carrageenan, Figure 2.5.7(A), when  $K^+$  is added, the suggestion that  $K^+$  reduces viscosity was not observed. There appears to be no predictability for viscosity with  $K^+$  concentration. Agar and kappa carrageenan have approximately the same viscosity. Unlike agar, kappa carrageenan's viscosity can be affected, or possibly engineered upon further study, with variations in cation concentration.

Another test was conducted to see if the polysaccharide maintained a constant viscosity after repeated solution and gelling cycles. The viscosity was suggested not to change as thermoreversibility, the cycle of heating and cooling the gel, proceeds

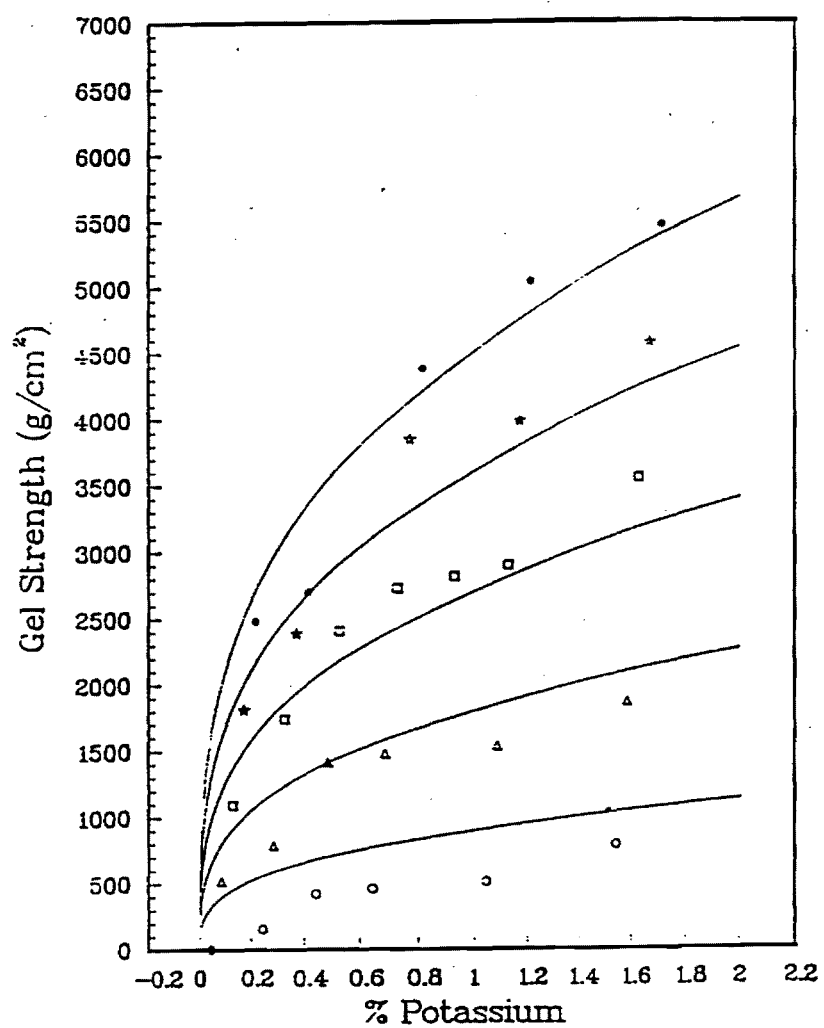


Figure 2.5.6 Curve-Fitting of Kappa Carrageenan Gel-Strengths in Figure (3.5.5), According to the Equation 2.5.2.

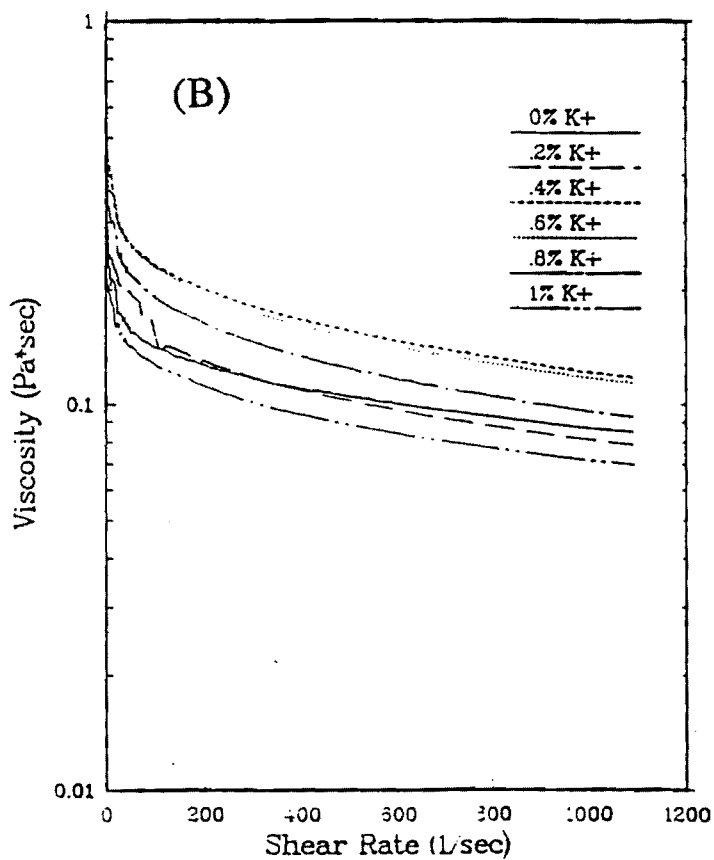
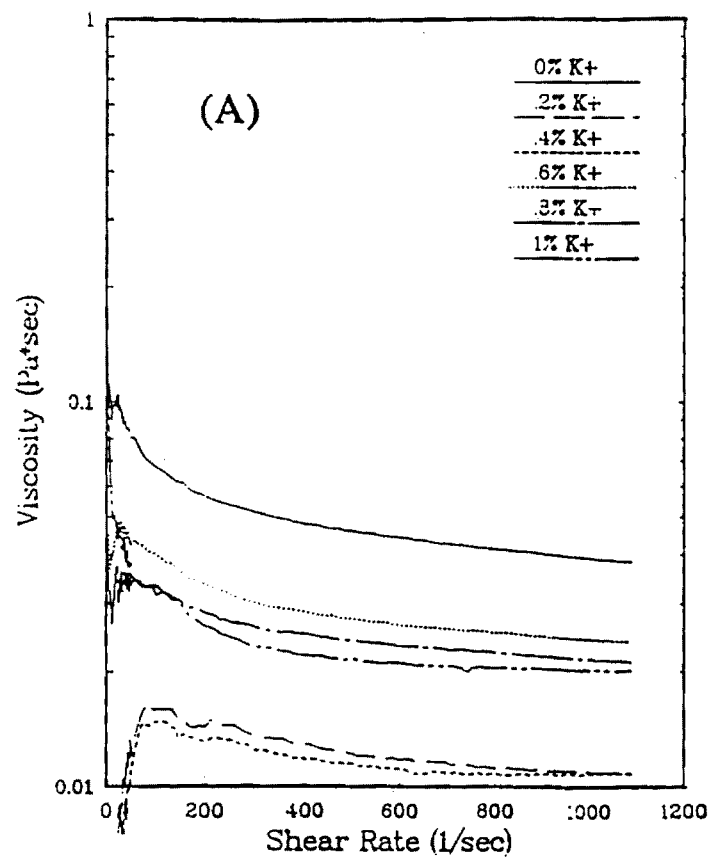


Figure 2.5.7

Viscosity of (A) 3 Weight % and (B) 5 Weight % Kappa Carrageenan in Water, with Specific Concentrations of K<sup>+</sup> Measured at 90 Degrees C.

[5]. But in fact, viscosity did vary based on a number of cycles of thermoreversibility for kappa carrageenan. A container of the polysaccharide was prepared and a small portion of it was used for one viscosity measurement. The container was immediately resealed, allowed to gel, and then reheated whereupon another sample was withdrawn for testing. A minimum amount of shaking was done from cycle to cycle. A decrease in viscosity of 25% measured at a shear rate of 600 1/sec for kappa carrageenan at 3, 4, and 5 wt% in water at 90 °C. Gel strength exhibited an approximate decrease of only 7%, measured from cycle to cycle. Thus, repeated cycling could be used for viscosity reduction without sacrificing strength in the gelled state.

Kappa carrageenan was selected over agar for slurry binder studies because of its superior gel strength and similar viscosities. Slips were prepared and viscosities were measured at 90 °C, Figure 2.5.8. Relative viscosities, comparing slurry to carrageenan solution viscosities, were low, and ranged from 4 to 8. Relative viscosity is defined as viscosity of the slip (solution containing the alumina particles) divided by the viscosity of the solution (kappa carrageenan, water, and cations). A low relative viscosity implies a negligible interaction between the alumina particles and the kappa carrageenan molecules. Therefore, high solids contents can be used with relatively high kappa carrageenan contents.

#### **2.5.4 CONCLUSIONS AND RECOMMENDATIONS**

Viscosities of kappa carrageenan solutions have been shown to be low enough to allow 40 vol% solids to be used for formation of hollow spheres, Figure 2.5.2. This demonstrates that powders can be readily dispersed in the system. Kappa carrageenan when tailored correctly, has greater gel strength than either agarose or agar, for the same concentration. In addition the much higher resolution temperature of carrageenan (70°C) compared to agar (50°C) allows gelled carrageenan slurries to be dried in a reasonable time period with out melting the gel. Manufacturers interested in the polysaccharides should investigate the potential of multiple gelation cycles to dramatically decrease slip viscosity without a significant decrease in gel strength. This would allow increased solid loads. Also the concentration of kappa carrageenan, and the effect of pH on the slip system, needs to be investigated further to obtain insight on the dispersiveness of ceramic particles to higher solids loading.

#### **2.5.5 FOOTNOTES AND BIBLIOGRAPHY**

1. A.J. Fanelli, R.D. Silvers, W.S. Frei, J.V. Burlew, and G.B. Marsh, "New Aqueous Injection Molding Process for Ceramic Powders," Journal of the American Ceramic Society, 72 [10] (1989) 1833-36.

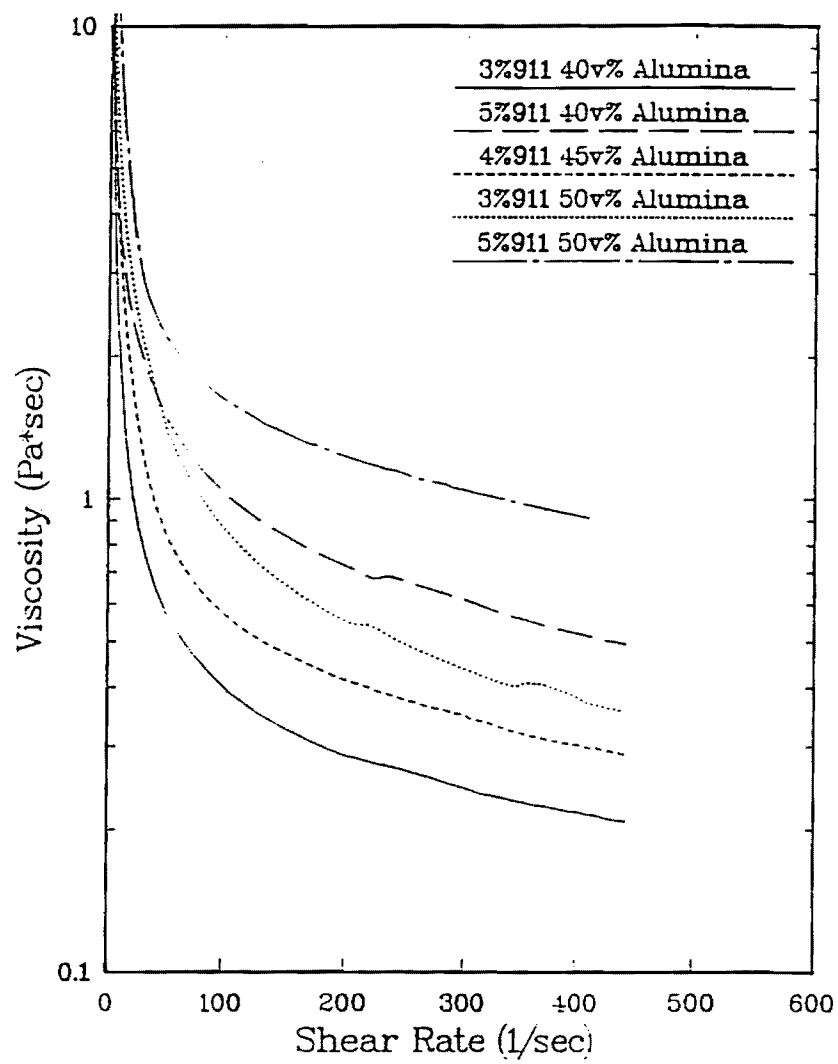


Figure 2.5.8 Viscosity of Alumina/Carragenan Slurries at 90° C.

2. H.H. Shelby and T.A. Selby, "Agar", Industrial Gums Polysaccharides and Their Derivatives, ed. R.L. Whistler, Academic Press, N.Y. (1959) 15-49.
3. FMC Corporation Staff, "General Carrageenan Application Technology, " G-31 ( 1988) 1- 18.
4. FMC Corporation Staff, "Carrageenan" (reprint of technical presentation), G-24 (1987) 1-11.
5. FMC Corporation Staff, Carrageenan Product Literature, (1988) 1-6. B.C. Mutsuddy, "Equipment Selection for Injection Molding," American Ceramic Society Bulletin, vol. 68 no. 10, (1989) 1796-1802.
7. M.J. Edirisinghe and J.R.G. Evans, "Review: Fabrication of Engineering Ceramics by Injection Molding. I. Materials Selection," Int. J. High Technology Ceramics, vol. 2, (1986) 1-31.
8. G.Y. Onoda, Jr., "The Rheology of Organic Binder Solutions," Ceramic Processing Before Firing, ed. G.Y. Onoda Jr. and L.L. Hench, John Wiley and Sons, (1978) 235-251.
9. M.J. Edirisinghe and J.R.G. Evans, "Properties of Ceramic Injection Molding Formulations," Journal of Materials Science, 22 (1987) 269 - 277 .
10. J.S. Reed, Introduction to the Principles of Ceramic Processing, John Wiley and Sons, N.Y. (1988) 285-289.
11. J.K. Wright, M.J. Edirisinghe, J.G. Zhang, and J.R.G Evans, "Particle Packing in Ceramic Injection Molding," Journal of the American Ceramic Society, 73 [9] (1990) 2653-2658.
12. Dr. J.K. Cochran; School of Materials Engineering, Georgia Institute of Technology: private communication (Feb.- May 1991).
13. M.J. Edirisinghe and J.R.G. Evans, "Review: Fabrication of Engineering Ceramics by Injection Molding. II. Techniques," Int. J. High Technology Ceramics, vol. 2, (1986) 249-278.
14. M.J. Edirisinghe and J.R.G. Evans, "Systematic Development of the Ceramic Injection Molding Process," Materials Science and Engineering, A109 (1989)17-26.



15. T. Zhang, Z. Jiang, J. Wu, and Z. Chen, "Influence of Rheological Behavior of Ceramic Mixes on Injection Molding of Ceramic Compacts," *Journal of the American Ceramic Society*, 73 [7] (1990) 21 71-75.
16. Dr. N. Hill; School of Materials Engineering, Georgia Institute of Technology: private communication (March 1991).
17. P.A. Sandford and J. Baird, "Industrial Unitization of Polysaccharides," *Molecular Biology*, ed. G.O. Aspinall, Academic Press, (1983) 411-490.
18. G.O. Aspinall, "Classification of Polysaccharides," *Molecular Biology*, ed. G.O. Aspinall, Academic Press, (1983) 411-490.
19. D.B. Smith, W.H. Cook and J.L. Neal, "Physical Studies on Carrageenin and Carrageenin Fractionations," *Archives of Biochemistry and Biophysics*, vol. 54, (1954) 192-204.
20. Personal Viewing of National Geographic Special on "Cultivation of Seaweed" (1991).
21. T. Lee, "McDonald's Aims to be Lean, Mean, Burger Machine," *The Atlanta Journal*, March 13, (1991 ) A1 -A13.
22. K.B. Guiseley, N.F. Stanley, and P.A. Whitehouse, "Carrageenan," *Handbook of Water-Soluble Gums and Resins*, ed. R.L. Davidson, McGraw-Hill, (1980) 5.1-5.29.
23. G.W. Phelps and M.G. McLaren, "Particle Size Distribution and Slip Properties, ~ Ceramic Processing Before Firing, ed. G.Y. Onoda Jr. and L.L. Hench, John Wiley and Sons, (1978) 211-225.
24. D.A. Rees, "Mechanisms of Gelation in Polysaccharide Systems," *Gelation and Gelling Agents: Proceedings of a symposium held in London, (October 20, 1971) 7-12.*
25. D.B. Smith and W.H. Cook, "Fractionation of Carrageenin," *Archives of Biochemistry and Biophysics*, vol. 45, (1953) 232-233.
26. FMC Corporation Staff, "Water Gelling Properties of Carrageenan," G-39 (1988) 1-16.
27. D.A. Rees, *Polysaccharide Shapes*, Chapman and Hall, (1977) 147 - 149 .

28. FMC Corporation, "Gelcarin( ~ GP 911," Technical Information Sheet, (1989) 1.
29. H. Grasdalen and O. Smidsrod, "Cs NMR in the Sol-Gel States of Aqueous Carrageenan. Selective Site Binding of Cesium and Potassium Ions in k-Carrageenan Gels," *Macromolecules*, 14, (1981) 229-231 .
30. O. Smidsrod, I-L. Andresen, H. Grasdalen, B. Larsen and T. Painter, "Evidence for a Salt-Promoted 'Freeze-Out' of Linkage Conformations in Carrageenans as a prerequisite for gel formation," *Carbohydrate Research*, vol. 80, (1980) C11-C16.
31. Mear Corporation, "Powdered Agar Type S-100," Technical Information Sheet, (1989) 1.
32. T.J. Hwang, "A Model For Viscosity Of Organic Based Oxide Dispersions," a thesis presented to Ga. Tech, (June 1989) 63-65.

### 3.0 MECHANICAL BEHAVIOR OF HOLLOW SPHERES AND FOAMS

#### 3.1 UNIAXIAL COMPRESSIVE BEHAVIOR OF BRITTLE HOLLOW SPHERES

Mechanical behavior of hollow spheres was evaluated using finite element analysis. Failure mode and strength of spheres were determined from stress analysis. A parametric study of strength as a function of wall thickness to sphere diameter ratios indicated that strength is a function of relative density squared. Strength of aluminum oxide hollow spheres made by the coaxial nozzle powder process agreed reasonably with the finite element parametric model.

This research was done primarily to investigate the compressive strengths of individual hollow spheres. Sphere strength was defined for this research as the critical force exerted on a sphere at failure per maximum cross-sectional area of the sphere to represent a load bearing capacity of the sphere. Finite element analyses were used to calculate the sphere strengths for various sphere geometries. Stress distributions and the mode of failure of a sphere under compression were investigated. Parametric analyses were carried out to obtain the sphere strength as a function of sphere properties. Compressive strengths for hollow alumina spheres were measured experimentally and the finite element analyses results were compared with the empirical results.

##### 3.1.1 PREVIOUS MODELS

Compressive contact loading problems on a brittle solid sphere have well-established theoretical solutions<sup>1</sup>. However, contact loading on a hollow sphere does not have a widely accepted solution. Two of the few proposed models are reviewed.

**Bratt, Cunnion, and Spivack Model** - Bratt et al.<sup>2</sup> investigated the mechanical properties of thin-wall glass spheres. They proposed that under an uniaxial compressive force, a hollow sphere experiences a compressive stress on the axis and a tensile stress on the sphere surface at the equator. When the tensile stress exceeds the tensile strength of the wall material, fracture occurs and a circumferential crack forms around the equator splitting the sphere into two hemispheres. The tensile stress  $\sigma$ , on the surface was calculated as,

$$\sigma = \frac{3F(D/3)}{2(\pi D)t^2} = \frac{F}{2\pi t^2} \quad (3.1.1)$$

where  $F$  is the uniaxial compressive force.  $D$  is the diameter, and  $t$  is the wall thickness of the sphere. Sphere strength,  $\sigma_c$ , was defined as the stress on the sphere at failure. The sphere strength, according to the model, is equal to the tensile strength of the wall material,  $\sigma_w$ , and therefore is a constant for spheres made of the same material regardless of diameter. They argued that the critical force,  $F_c$ , at which a sphere fails was only related to the wall thickness,  $t$ , of the sphere and is independent of the size of the sphere as in equation (3.1.3).

The hollow glass spheres were tested by compressing a sphere between a flat tipped, conical rod and a stationary platen, which is a contact loading case. The experimental results for the uniaxial compression of the spheres were plotted as  $F_c$  versus  $t$ , which showed the critical force is a square function of the wall thickness.

**Swanson and Cutler Model** - Swanson et al<sup>3</sup>. investigated the stress and strength of hollow ceramic spheres as possible proppants, which are small particles mixed with fluid in hydraulic fracturing treatments of petroleum wells to stimulate production. They modeled the arrangement of spheres with uniform diameters in a hydraulic fracture cavity as a cubic close packed structure, each sphere contacting twelve neighbors in six pairs of diametral contact loadings. The overall loading on proppants is caused by the closure pressure,  $P$ , which is defined as the lithostatic confining pressure minus the pore pressure. Assuming that each of the twelve surrounding spheres exert the same contact force  $F$  on a sphere,  $F$  is given by

$$F = bP\pi r^2 \quad (3.1.2)$$

where  $b$  is a constant that depends on the packing geometry and  $r$  is the radius of the sphere. For the close packing with the packing factor of 0.74,  $b$  is  $4/(12 \times 0.74^{2/3}) = 0.41$ . Other packing geometries produce higher values of  $b$ .

The stress at the inner surface  $\sigma$ , could become critical for the failure of the sphere, and was calculated to be

$$\sigma = 1.243 \left( \frac{P}{1-2\xi+\xi^2} \right) \ln \left\{ \frac{33.61}{(1-\xi)} \left[ \frac{2+\xi^3}{1-\xi^3} + 0.667 \right] \right\} \quad (3.1.3)$$

where  $\xi$  is  $(r_i/r_o)$ , the ratio of the sphere inner and outer radii, and  $P$  is the closure pressure. The stress,  $\sigma$ , has a linear relationship with the closure stress and when the closure stress exceeds a critical stress  $P_c$ ,  $\sigma$  exceeds the bend strength of the wall material,  $\sigma_w$ , leading to the failure of the sphere. The fracture strength of the sphere can be defined as the critical closure stress,  $P_c$ , which causes the diametral failure loading,  $F_c$ , on the sphere. The sphere inside to outside ratio,  $\xi$ , can be substituted

by  $(1-t/r)$ , and Equation (3.3.3) suggests that the fracture strength of a hollow sphere under diametral concentrated loading is a function of the aspect ratio, and is not governed by a single factor of the wall thickness or the diameter of a sphere alone.

**Sphere Strength** - Sphere strength was defined for this research based on total cross-sectional area. When a sphere fails under a fracture load  $F_c$ , the sphere strength,  $\sigma_s$ , can be defined as the fracture load per maximum cross-sectional area of the sphere regardless of the deformation mode to represent the load bearing capacity of the sphere:

$$\sigma_s = \frac{F_c}{\pi r^2} \quad (3.1.4)$$

### 3.1.2 FINITE ELEMENT PROCEDURES AND LOAD CONDITIONS

Finite element model analyses were carried out to investigate the compressive behavior of hollow ceramic spheres and bonded-sphere foams. The MSC/NASTRAN V66A program was used on a Cyber 990 and a Vax 6440 main frame computers for the finite element model calculations. Linear elastic static analyses were performed because the primary concern of this research was in hollow brittle spheres.

Compressive behavior of a hollow sphere under uniaxial **concentrated** loading was calculated first for various aspect ratios (wall thickness to sphere radius ratios). Membrane forces, bending moments, deformations, transverse shear forces, and stresses on the spheres were analyzed. From the stress analysis, the critical loads required for the failure of the spheres were calculated. Secondly, compressive strength of hollow spheres under diametral **contact** loading by platens were simulated for comparison with the experimental results.

Finite element analyses were performed for a range of ideal alumina spheres with varying dimensions. The relative density of the sphere,  $(\rho_s/\rho_o)$ , can be expressed as a function of the aspect ratio,  $(t/r)$ ,

$$\frac{\rho_s}{\rho_o} = \frac{3\left(\frac{3}{r}\right) + \frac{1}{4}\left(\frac{t}{r}\right)^3}{1 + \frac{3}{2}\left(\frac{t}{r}\right) + \frac{e}{4}\left(\frac{t}{r}\right)^2 + \frac{1}{8}\left(\frac{t}{r}\right)^3} \quad (3.1.5)$$

where  $\rho_s$  is the sphere density and  $\rho_o$  is the wall material density. The radius of a sphere,  $r$ , used in this study is the distance from the center of a sphere to the midplane of the shell.

In these linear elastic analyses, only one set of load and sphere dimensions for an aspect ratio is necessary for the investigation. A uniaxial compressive force on the spheres of 2.45 N was simulated to evaluate the force and stress distributions on the spheres under the same load and to calculate sphere strengths. The material properties of ideal alumina,  $\text{Al}_2\text{O}_3$ , with Young's modulus, poisson's ratio,  $\nu$ , tensile strength, and compressive strength of 380 GPa, 0.26, 300 MPa, and 3450 MPa, respectively, were used in the finite element analyses.

Parametric studies were carried out to investigate the relationship between the sphere strength,  $\sigma_s$ , and the geometrical parameters of a hollow sphere. Fracture of a hollow sphere was determined from the stress analysis using the Griffith criterion. When a set of principal stress coordinates,  $(\sigma_1, \sigma_2)$ , at a point on the sphere is outside the criterion boundary, failure starts from that location. Accordingly, tensile stresses are far more critical for failure of the sphere than compressive stresses. When both principal stresses are tensile, the fracture criterion shows that failure will take place when the major principal stress exceeds the tensile fracture strength.

**Concentrated Loading** - The stress analyses and the fracture criterion dictates that under uniaxial concentrated loading, hollow brittle spheres should fail at the loading point inside the shell due to tensile stress. The sphere strengths were calculated from the critical stresses at the closest location to the loading point where stresses were calculated. The sphere strength was found to be a linear function of the relative density squared,  $(\rho_s/\rho_o)^2$ , as shown in Figure 3.1.1. The linear relationship in the figure is valid for spheres with relative densities up to about 40%. This encompasses the entire density range of actual spheres produced to date. The correlation coefficient squared,  $R^2$ , of the relationship is 0.99976. Rewriting the linear regression equation in the figure to include the strength of the wall material, the sphere strength is given by:

$$\sigma_s = 0.0275\sigma_o \left( \frac{\rho_s}{\rho_o} \right)^2 \quad (3.1.6)$$

The linear relationship between the sphere strength and the relative density squared holds true independent of the coefficients. Strength models developed in this research are valid for all ceramic materials with poisson's ratio of 0.26, although the finite element analyses were performed for ideal alumina spheres. This is because of the definition of the sphere strength as mentioned above and linear elasticity.

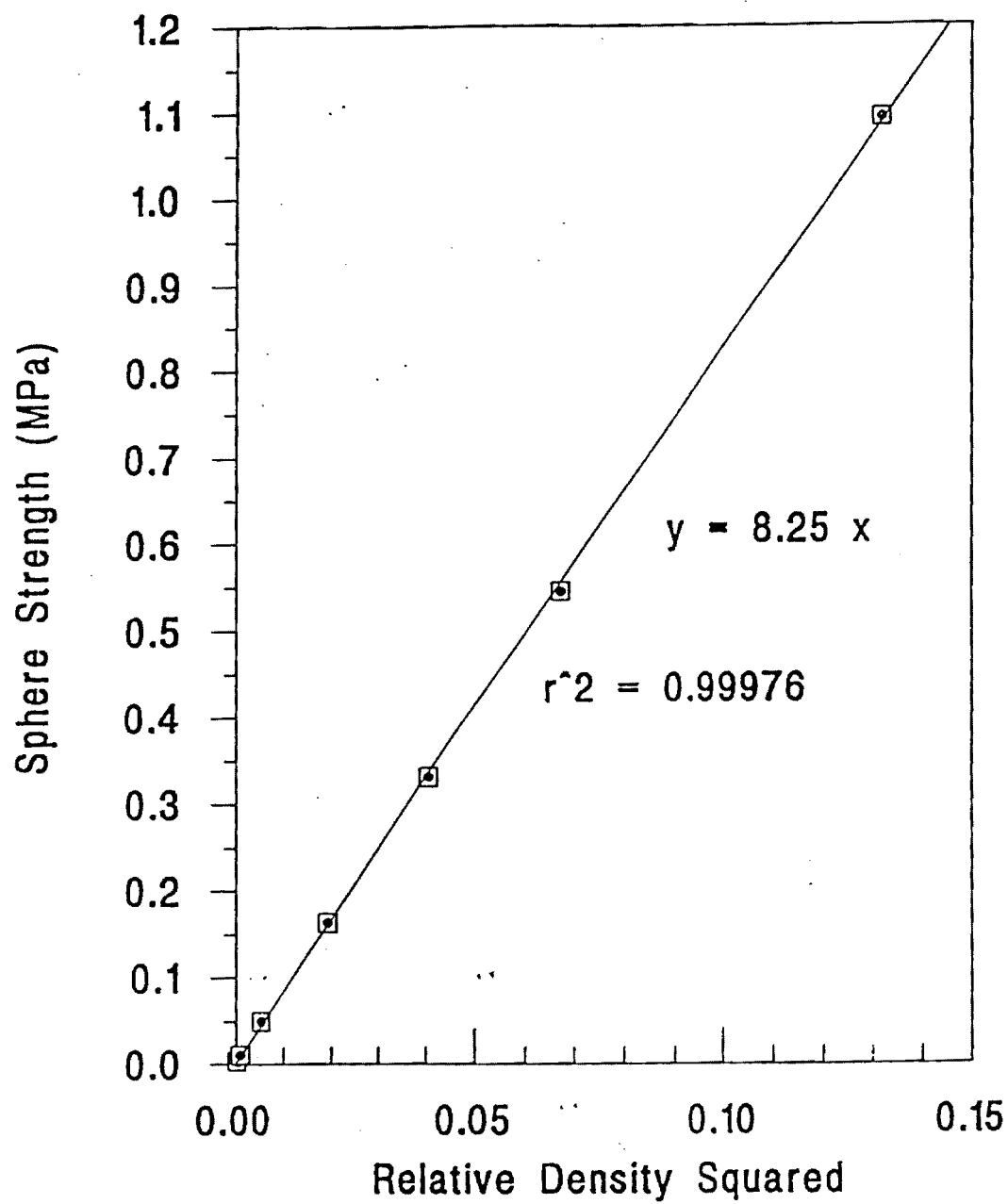


Figure 3.1.1

Sphere Strength  $\sigma_s$ , vs. Relative Density Squared,  $(\rho_s/\rho_o)^2$ , Under Uniaxial Concentrated Loading.

**Contact Loading** - In actual applications, the spheres will likely experience distributed or contact loading instead of concentrated loading. When a hollow brittle sphere is diametrically compressed between a pair of rigid platens, the sphere contacts the platens at the loading points initially. As soon as a load is applied to the sphere, however, it will start to deform by flattening at the contact area as illustrated in Figure 3.1.2. The critical region for failure was thought to be around the perimeter of the surface of contact. A failure criterion for contact loading situation was postulated to predict the sphere strength based on the uniaxial concentrated loading results and the above assumption. It was found that the location of minimum bending moment in the direction tangential to the latitude,  $M_y$ , is where the deformation of a hollow sphere wall starts to be significant under a uniaxial concentrated loading. The region where  $M_y$  is minimum under a concentrated loading was assumed to be the critical region in the contact loading situation. Thus, the principal stresses on the elements that lie at that region became important for the failure analysis.

When the normal- $x$  stress,  $\sigma_x$ , which is also a major principal stress, on the inner surface of an element in the critical region exceeds the tensile strength of the wall material, failure occurs at the inner surface of that element. The hollow sphere will break parallel to the loading axis into two hemispheres. From this failure model, sphere strengths of hollow brittle spheres under uniaxial compression between rigid platens were calculated for various aspect ratios. Parametric studies showed that the sphere strength under the contact loading is also a linear function of the relative density squared as shown in Figure 3.1.3. From the linear relationship the sphere strength is given by:

$$\sigma_s = 0.774\sigma_o \left( \frac{\rho_s}{\sigma_o} \right)^2 \quad (3.1.7)$$

The coefficient in Equation (3.1.7) is an order of magnitude larger than the one in Equation (3.1.6) which predicts that the sphere strength under a uniaxial contact loading between a pair of rigid platens will be much higher than under uniaxial concentrated loading.

To confirm the validity of the failure model for the contact loading, finite element analyses were performed for three aspect ratios, 0.015, 0.05, and 0.075. Instead of applying loads, displacements of grid points were forced to simulate a deformed contact area. Since this was a varying boundary condition problem, numerous simulations were iterated to find a situation when the sphere would fail. The coefficient in Equation (3.1.7) obtained from these analyses was in the range of 0.4 to 0.8 because simulating and determining the exact degree of deformation at failure



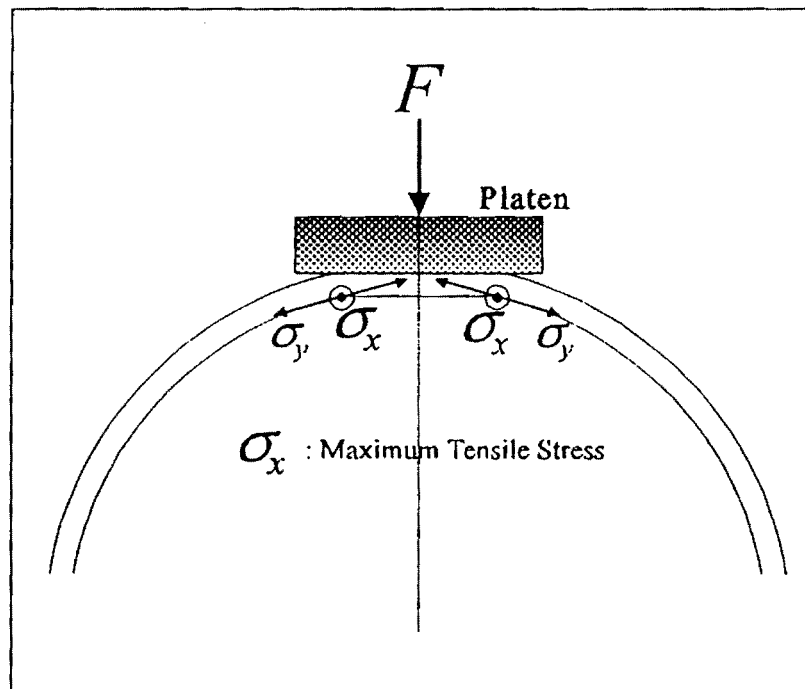


Figure 3.1.2      Deformation Mode of a Hollow Sphere under Contact Loading.

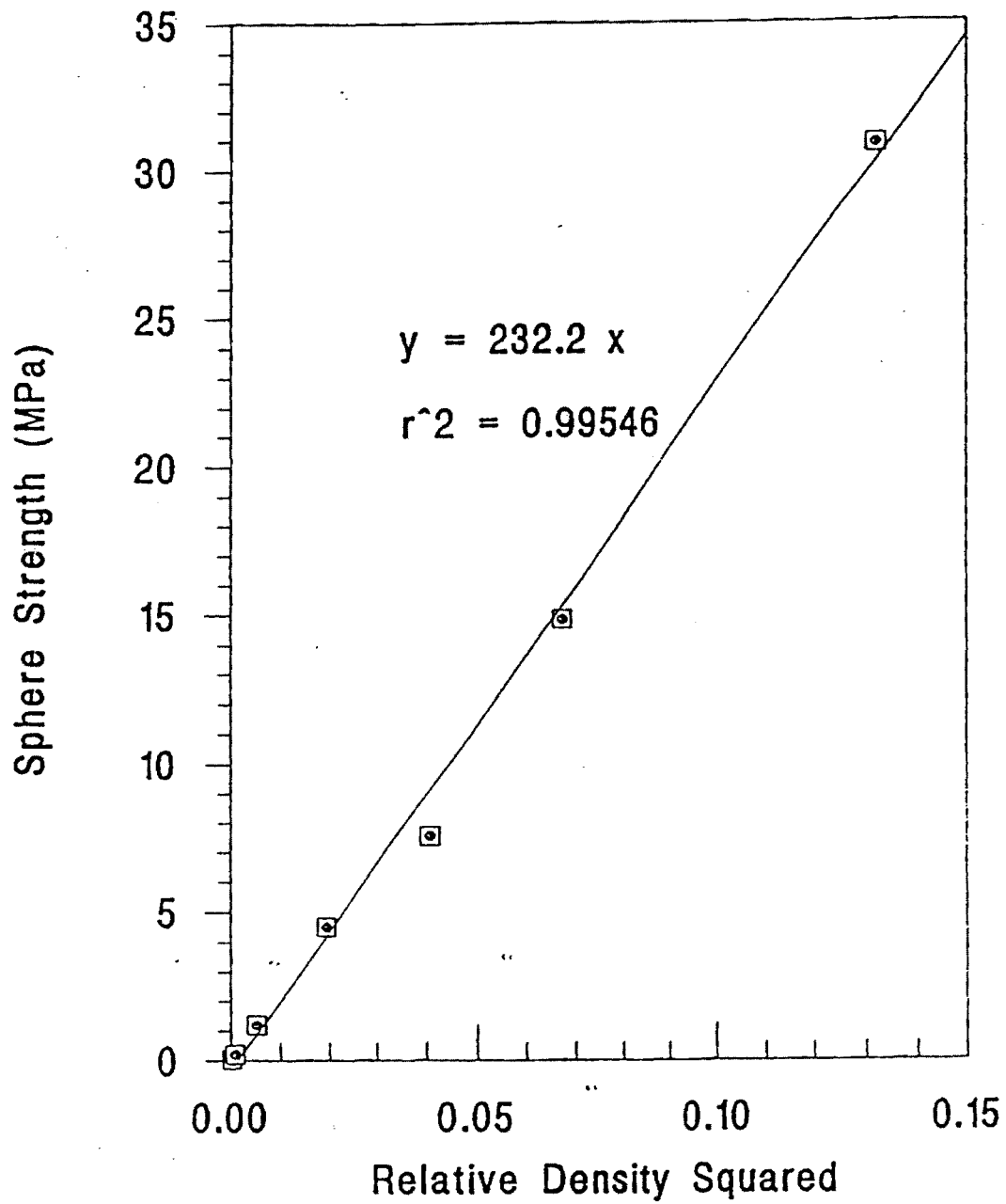


Figure 3.1.3

Sphere Strength  $\sigma_s$ , vs. Relative Density Squared,  $(\rho_s/\rho_o)^2$ , Under Contact Loading by Rigid Platens.

were difficult. However, this simulation of contact loading confirmed that the coefficient in Equation (3.1.7) is of a reasonable order.

### 3.1.3 EXPERIMENTAL RESULTS AND DISCUSSIONS

Hollow alumina spheres were produced by the coaxial nozzle technology using Alcoa XA-3000 alumina powder. The process can be controlled to produce monosized hollow spheres with predetermined size and wall thickness for the application. These hollow alumina spheres had densified walls after being sintered, typically at 1600°C for 3 hours.

The hollow alumina spheres were loaded on an Instron testing machine using a 50 kg load cell. A sphere was tested between a pair of polished, hardened steel platens using a crosshead speed of 0.1 inches per minute. Twenty-five to thirty spheres were tested for each batch of spheres. Fracture load,  $F_c$ , was recorded for each spheres. Sphere strength,  $\sigma_s$ , for each spheres was calculated from the fracture load and the diameter of the sphere.

The hollow spheres under uniaxial loading failed in several modes. Many spheres failed leaving two hemispheres as predicted by the finite element model. For small spheres, vertical or horizontal failure was not easily observed because failure was instantaneous and the objects were small. Large spheres with thick walls broke vertically into two hemispheres. Thus, the small spheres are also believed to have failed vertical because the finite element model predicts this failure mode for all spheres.

Some spheres failed leaving small holes at contact areas. The size of a hole varied from a very small hole to a large hole for various spheres. This can be explained by the fact that  $\sigma_s$  is close to  $\sigma_x$  inside a sphere near the loading axis, although  $\sigma_x$  is the critical stress for ideal hollow spheres. Considering the imperfect geometry of the spheres, it can be assumed that for some spheres,  $\sigma_y$  becomes the critical stress thus leaving a hole around the loading axis.

Other spheres failed leaving randomly shaped fragments of spheres. This can be also contributed to the imperfect sphere geometries. Once the fracture was initiated at the critically stressed region, the crack may propagate along the weakest path, *e.g.*, the thin part of the sphere, etc.

The hollow alumina sphere strength versus relative density squared is plotted in Figure 3.1.4. The experimental results show a strong linear relationship with the relative density squared as predicted by the finite element model analysis. The coefficient obtained from the linear regression of the experimental data is 0.252 whereas the

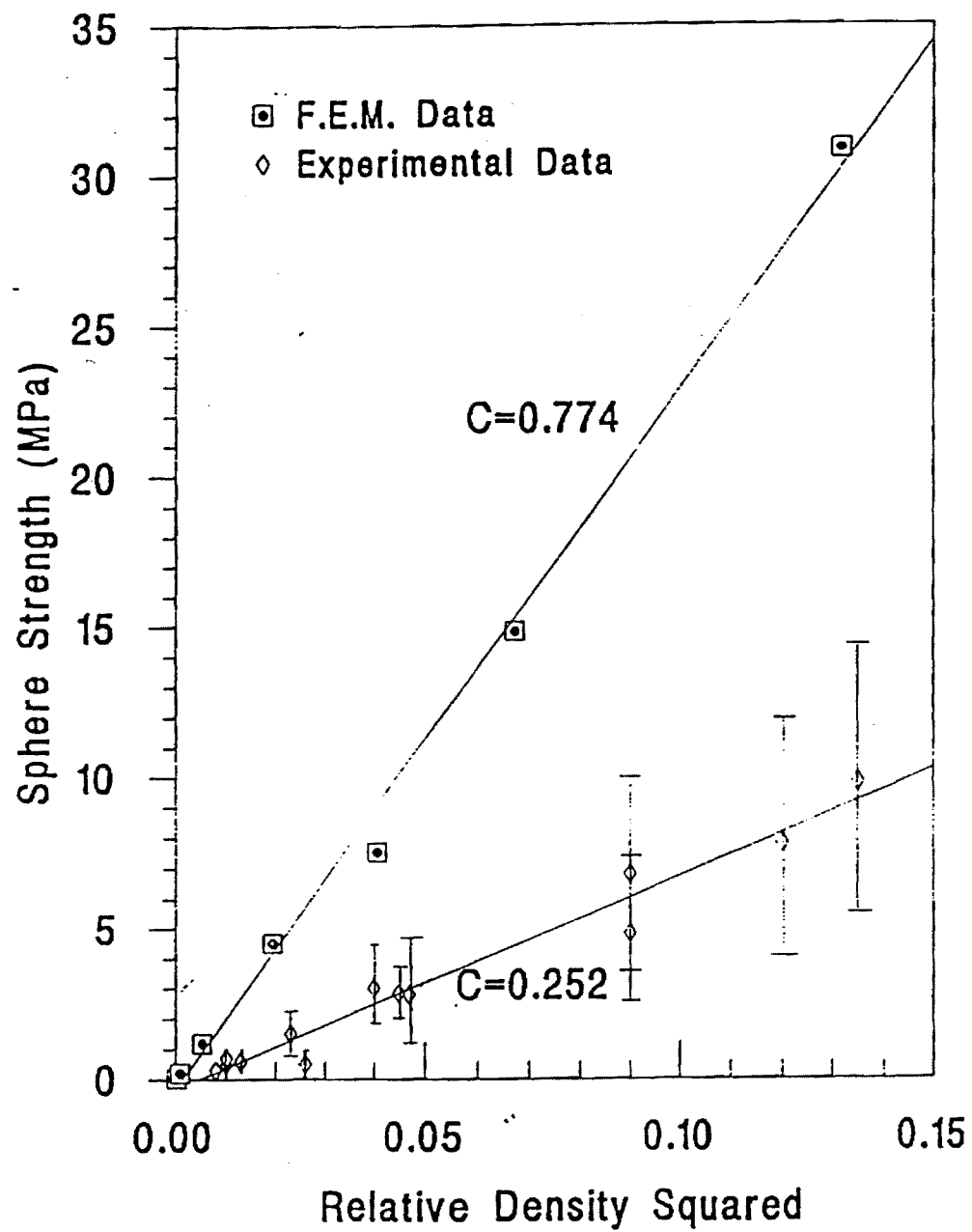


Figure 3.1.4 Sphere Strength vs. Relative Density Squared for Alumina Spheres.

coefficient in Equation (3.1.7) calculated from the finite element analysis is 0.774. The finite element model predicts about three times higher sphere strength than the actual sphere strength. However, the real spheres have imperfections such as non-uniform wall thickness, imperfect sphere geometry, flaws, small tials, etc. Considering these facts, the finite element model provides a respectable strength model for the hollow spheres. More important than the coefficient, the linear relationship between the sphere strength and the relative density squared predicted by the finite element model was confirmed by the experimental results.

**Model Comparisons** - Finite element methods were used to model the mechanical behavior of hollow ceramic spheres because satisfactory theoretical solutions could not be found. However, a comparison of the finite element model can be made to the existing model by Swanson and Cutler for the uniaxial concentrated loading condition. The concept of the closure stress in Equation (3.1.2) can be extended to describe the strength of a sphere under uniaxial compression. When sphere is loaded by only one set of diametral loading, the constant,  $b$ , in the equation can be replace by unity, and the closure pressure,  $P$ , can be replaced by  $\sigma$ , which represents the macroscopic overall stress state of the sphere:

$$\sigma = \frac{F}{\pi r^2} \quad (3.1.8)$$

Substituting the sphere strength for the closure stress in Equation (3.1.3), the sphere strength of a hollow sphere under a diametral concentrated loading is

$$\sigma_s = 0.805 \sigma_o \frac{(1-\xi)^2}{\ln \left\{ \frac{33.61}{(1-\xi)} \left[ \frac{(2+\xi^3)}{(1-\xi^3)} + 0.667 \right] \right\}} \quad (3.1.9)$$

Equation (3.1.9) predicts unreasonably low sphere strengths values, especially for thin-wall spheres, because it was derived on a thick plate foundation and for concentrated loading. While Equation (3.1.9) cannot be directly compared with Equation (3.1.6), rearranging Equation (3.1.9) by substituting  $(1-t/r)$  for  $\xi$  and then making the further substitution of  $t/r = (\rho_s/\rho_o)/3$  for small aspect rations places the equation in a form similar to that of Equation (3.1.6), and results in Equation (3.1.10)

$$\sigma_s = (0.006 \text{ } 0.01) \sigma_o \left( \frac{\rho_s}{\rho_o} \right)^2 \quad (3.1.10)$$

for the relative density range from 0.03 to 0.4 Equation (3.1.10) has the same form as Equation (3.1.6) except for the magnitude of the constant. The constant in Equation (3.1.6) depends on the size of the meshes around the loading point. Even if the meshes were refined until good convergence was observed as explained previously, precise stresses could not be expected near the loading point because the meshes could not be reduced infinitely. If the meshes are refined too small, a greater calculation error can result. Also, Equation (3.1.9) was divided by approximation and by substituting actual values for the aspect ratio. However, Equation (3.1.6) and Equation (3.1.10) agree well qualitatively, and the constants are of a same order of magnitude.

### 3.1.4 CONCLUSIONS

The mechanical behavior of hollow spheres with various aspect ratios under uniaxial concentrated loading was investigated using the finite element methods. The distributions of membrane forces, bending moments, and transverse shear forces on the hollow spheres were studied and the failure of the spheres was determined from the stress analysis using Griffith criterion for the failure of a brittle material for plane stress. Parametric studies were carried out and sphere strength under uniaxial concentrated loading was predicted to be a linear function of relative sphere density squared.

A failure model of a hollow sphere under a contact loading by platens was proposed to predict the sphere strength based on failure analysis of the sphere under uniaxial concentrated loading. The sphere strength under contact loading was also predicted to have a linear relationship with the relative sphere density squared.

1. *S.P. Timoshenko, J.N. Goodier, Theory of Elasticity, 3rd ed. (McGraw-Hill, 1970).*
2. *P.W. Bratt, J.P. Cunnion, and B.D. Spivack, "Mechanical Testing of Glass Hollow Microspheres," Advances in Materials Characterization, edited by D.R. Rossington, R.A. Condrate, R.L. Snyder (Plenum Press, New York, 1983)*
3. *S.R. Swanson, R.A. Cutler, "Fracture Analysis of Ceramic Proppants," J. Ener. Res. Tech., Vol.105, 128-133 (1983)*

### 3.2 COMPRESSIVE STRENGTH OF HOLLOW SPHERE FOAMS

As in any engineering design, mechanical properties of bonded sphere foams could be a limiting factor in their applications. Especially for use as a light structural material, the strengths of the spheres and the spheres foams need to be maximized. The factors governing the strengths must be understood and strength models need to be developed to achieve maximum strengths of the materials for given application conditions. There has been a few publications proposing strength models of ideal hollow elastic spheres and there are no models dealing directly with hollow sphere foams. The mechanical properties of cellular materials have been summarized by Ashby and are described below.

This research was performed primarily to investigate the compressive strengths of sphere foams. A model of basic unit structure in a spheres foam was proposed, and finite element analyses were performed to calculate the strength of the foam. A bonding technique was developed to form bonded spheres foams and the compressive strengths of the foams were measured. The finite element analyses results were compared with the empirical results and agreement reasonable.

#### 3.2.1 COMPRESSIVE STRENGTH OF CELLULAR SOLIDS

Ashby has summarized the mechanical properties of general cellular solids based on an open-cell and a closed-cell models as geometric foundations of cellular solids. An open-cell foam was modeled as a cubic array of members of length  $l$  and square section of side  $t$  which were arranged that adjoining cells meet at mid-points. In the open-cell model, the relative density of the cell,  $\rho_f/\rho_o$ , is given by

$$\frac{\rho_f}{\rho_o} \propto \left(\frac{t}{l}\right)^2 \quad (3.2.1)$$

where  $\rho_f$  is the density of the foam, and  $\rho_o$  is the density of the wall material. The second moment of the section of a member from the geometry is given by

$$I = \frac{t^4}{12} \quad (3.2.2)$$

A closed-cell foam was modeled as a cubic array of square plates of side  $l$  and thickness  $t$ . Adjoining cells were staggered similar to the open-cell model. The relative density of the closed-cell foam is given by

$$\frac{\rho_f}{\rho_o} \propto \frac{t}{l} \quad (3.2.3)$$

and the second moment of the section of a plate is given by

$$I = \frac{lt^3}{12} \quad (3.2.4)$$

Most artificial foams behave like open-cell foams because most of the solid material is concentrated into the cell edges due to the surface tension during the manufacturing process even if they have closed-cell faces.

For the analyses of the mechanical properties of the foams, a two-dimensional model of hexagonal cells, which is shown in Figure 3.2.1, was used. When a foam is under a compressive loading as shown in the figure, the cell walls which experience force components normal to them bend. A brittle foam shows a linear elastic deformation until it fails. Brittle foams fail by brittle crushing in compression and brittle fracture in tension. The brittle foam modeled in the figure will fail due to the bending fracture near the hinges. A force  $F$  exerts a moment which is proportional to  $Fl$  to the wall of length  $l$ . The stress on the foam,  $\sigma$ , is proportional to  $F/l^2$ . The bending moment,  $M_c$ , exerted by the force  $F_c$  acting on an open-cell at failure is given by

$$M_c = \frac{1}{6} \sigma_c t^3 \quad (3.2.5)$$

where  $\sigma_c$  is the modulus of rupture of the cell-wall material. Thus the brittle crushing strength of the foam,  $\sigma_f$ , is given by

$$\sigma_f \propto \frac{F_c}{l^2} \propto \frac{M_c}{l^3} \propto \sigma_c \left( \frac{t}{l} \right)^3 \quad (3.2.6)$$

and by substituting Equation (3.2.1) into Equation (3.2.6),  $\sigma_f$  for an open-cell foam is given by

$$\sigma_f = C_1 \sigma_c \left( \frac{\rho_f}{\rho_o} \right)^{\frac{3}{2}} \quad (3.2.7)$$

where  $C_1$  is a constant which is approximately 0.65 as given by Ashby. Equation (3.2.7) indicates that the compressive strength of a brittle open-cell foam is governed by the modulus of rupture of the cell-wall material, which is close to the tensile strength for a brittle solid, and has a linear relationship with  $(\rho_f/\rho_o)^{3/2}$ .



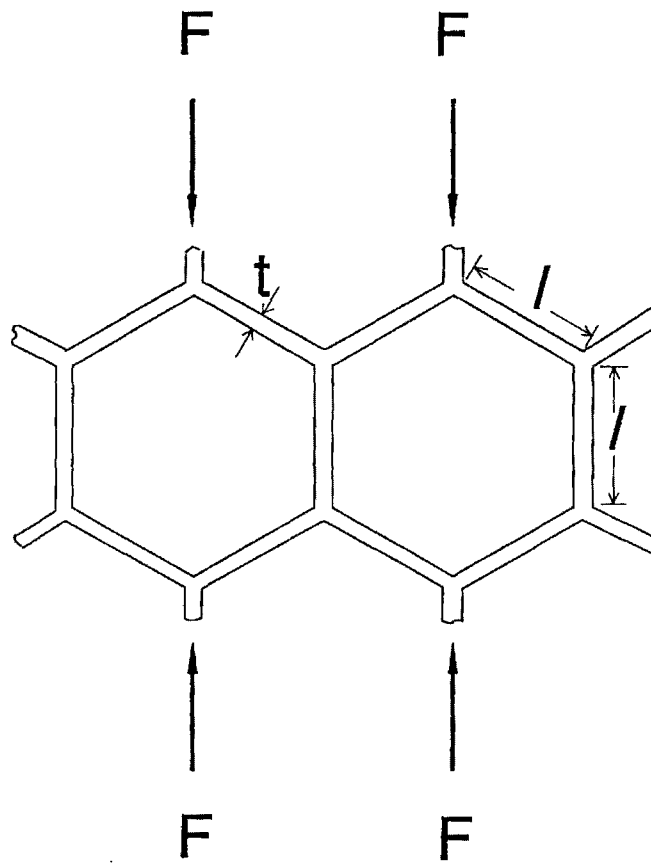


Figure 3.2.1 Two-Dimensional Model of Hexagonal Cells.

Compressive strength of a true closed-cell brittle foam with no thickening of the cell edges was calculated similarly using Equations (3.2.3) and (3.2.4) instead of Equations (3.2.1) and (3.2.2) as

$$\sigma_f = C_2 \sigma_c \left( \frac{\rho_f}{\rho_o} \right)^2 \quad (3.2.8)$$

where  $C_2$  is a dimensionless constant which needs to be determined experimentally. The compressive strength of a closed-cell brittle foam is a square function of the relative density of the foam.

It was suggested that even though the relationships were developed based on the three-dimensional structural models of the members and the plates, and the two-dimensional deformation model as shown in Figure 3.2.1, the relationships could be applied to general isotropic foams.

### 3.2.2 FINITE ELEMENT MODEL OF FOAM COMPRESSIVE STRENGTH

A closed-cell ceramic foam can be fabricated by bonding hollow ceramic spheres together. Most of the bonding material fills in the spaces around the contact points between spheres during the bonding process due to capillary forces, forming neck areas as shown in Figure 3.2.2. After drying and firing, the spheres in the bonded sphere foam transfer loads through the solid neck areas. Thus a sphere in the bonded sphere foam experiences distributed loadings at the neck areas instead of concentrated loadings or contact loadings. Compressive behavior of a hollow sphere under uniaxial distributed loading was investigated for comparison with the concentrated loading case. The solid angle  $\phi$  in Figure 3.2.2 was defined as the contact angle and used to describe the area of loading on a sphere. Finite element analyses were performed for the contact angles  $\phi = 10^\circ$ ,  $20^\circ$ , and  $30^\circ$  to study the effect of the size of the bonding area. Finally loading on a sphere in a bonded-sphere foam was modeled as three pairs of diametral distributed loading and finite element analyses were carried out also for various aspect ratios and contact angles.

**Sphere Strength under Uniaxial Distributed Load** - Failure of a hollow sphere under uniaxial distributed loading was investigated using the Griffith criterion<sup>15</sup> for the plane stress. Failure mode and location on a hollow sphere were determined from the stress analysis results. Table 3.2.1 shows the failure location in terms of  $\theta$  for spheres of different wall thicknesses and contact angle of  $10^\circ$ ,  $20^\circ$ , and  $30^\circ$ . Fracture would occur at  $12.5^\circ$  away from the loading axis on the outer surface of the sphere with 1 mm radius and 5  $\mu\text{m}$  wall thickness under a uniaxial distributed load with the contact

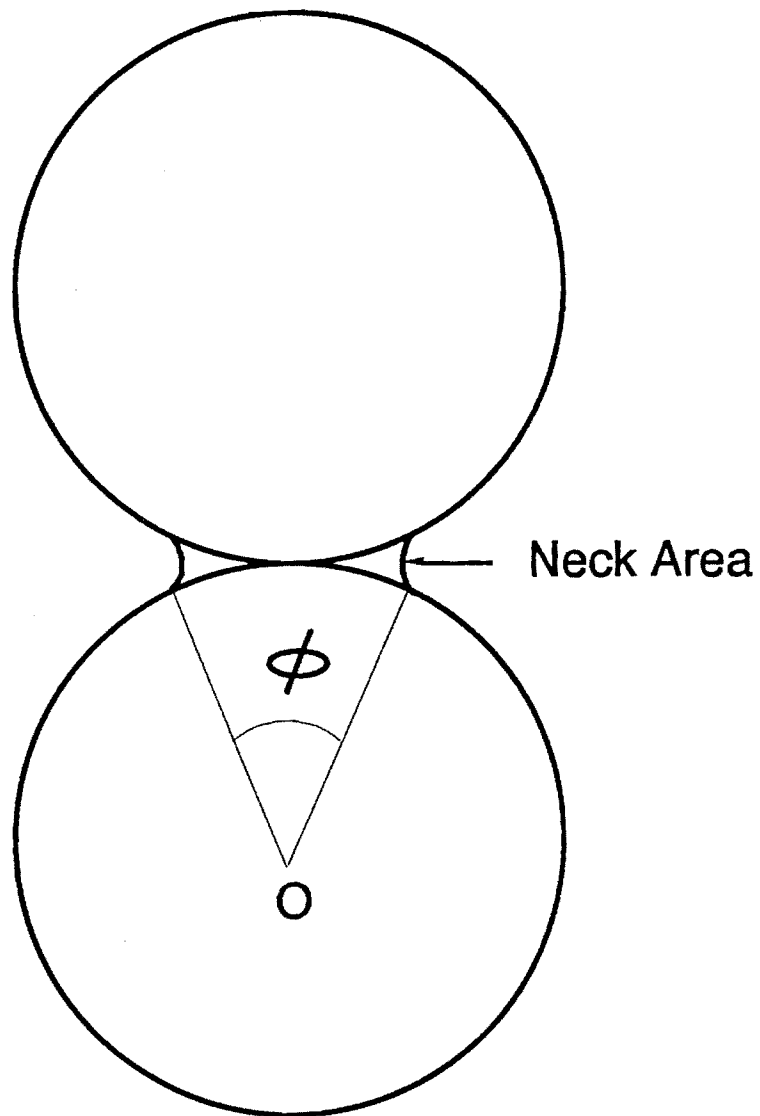


Figure 3.2.2 Neck Area Between Spheres and Contact Angle of a Distributed Load Produced by Point Contact Bonding.

Table 3.2.1 Failure Locations on Hollow Spheres under Uniaxial Distributed Loading.

t ( $\mu\text{m}$ )	$\phi = 10^\circ$		$\phi = 20^\circ$		$\phi = 30^\circ$	
	$\theta (^\circ)$	Surface	$\theta (^\circ)$	Surface	$\theta (^\circ)$	Surface
5	12.5	Outside	17.5	Outside	22.5	Outside
15	2.5	Inside	17.5	Outside	22.5	Outside
25	2.5	Inside	2.5	Inside	27.5	Outside
35	2.5	Inside	2.5	Inside	27.5	Outside
50	2.5	Inside	2.5	Inside	32.5	Outside
75	2.5	Inside	2.5	Inside	2.5	Inside
100	2.5	Inside	2.5	Inside	2.5	Inside

angle of  $10^\circ$  due to a tensile normal stress  $\sigma_x$ . A hollow alumina sphere with the same aspect ratio,  $t/r$ , of 0.005 or the same relative density of 0.01489 would fail in the same way. A hollow alumina sphere with the aspect ratio of 0.075 would fail in the immediate vicinity of the loading axis on the inner surface of the sphere when the contact angle is  $30^\circ$  also due to a tensile normal stress  $\sigma_x$ . The failure locations represented by  $\theta$  of  $2.5^\circ$  in Table 3.2.1 may actually be on the loading axis. In all cases the spheres would fail because of tensile normal stresses in the element- $x$  direction, which are major principal stresses.

Table 3.2.1 suggests that a sphere with a small aspect ratio may fail some distance away from the loading axis outside the loading area on the outer surface of the sphere. As the aspect ratio increases for the same contact angle, the failure location will move farther away from the loading axis on the outer surface which is the pattern for  $\phi = 30^\circ$  shown in the table. Spheres with larger aspect ratios would fail inside the loading area on the inner surface of the sphere. For a given aspect ratio, the failure location will move farther away from the loading axis as the contact angle increases. The above failure modes and the locations were determined using the Griffith criterion for the finite element stress analysis results. A load was applied to an area on a sphere as an uniform uniaxial distributed load parallel to the loading axis in the finite element model. In the actual loading situation, however, the load is applied on a sphere by solid material that bonds spheres together at neck areas as shown in Figure 3.2.2.

An assumption was made to determine failure modes, failure locations, and sphere strengths for the real case using the stress data obtained from the finite element model. It was assumed that the stress distribution on a sphere would be valid for the real loading situation and failure could be then determined using the Griffith criterion for the stress data except at the loading area. Failure of a sphere was assumed not to take place in the loading area because the area is reinforced by the solid bonding material and the failure criterion for plane stress may not be applicable to the neck area. When failure occurred inside a loading area from the previous failure analysis, it was excluded and another failure location was determined outside the loading area. Sphere strength was calculated from the critical stress at the failure location.

Table 3.2.2 shows the failure locations on hollow spheres determined by forcing failure outside the loading area. For  $\phi = 10^\circ$ , the spheres with wall thicknesses equal to or greater than  $15 \mu\text{m}$  in the table would fail right outside the loading area on the inner surface. For  $\phi = 20^\circ$ , the sphere with  $25 \mu\text{m}$  wall thickness would fail at  $\theta = 22.5^\circ$  on the inner surface, further away from the loading axis than the spheres with  $5 \mu\text{m}$  and  $15 \mu\text{m}$  wall thickness, which fail at  $\theta = 17.5^\circ$ . As the wall thickness increases to  $35 \mu\text{m}$ , the failure location moves further away from the loading axis to  $\theta = 27.5^\circ$ . Further increases in wall thickness brings the failure location to just outside

Table 3.2.2 Failure Locations on Hollow Alumina Spheres under Uniaxial Distributed Loading when Failure is Determined Outside the Loading Area.

$t \text{ (}\mu\text{m)}$	$\phi = 10^\circ$		$\phi = 20^\circ$		$\phi = 30^\circ$	
	$\theta (^\circ)$	Surface	$\theta (^\circ)$	Surface	$\theta (^\circ)$	Surface
5	12.5	Outside	17.5	Outside	22.5	Outside
15	7.5	Inside	17.5	Outside	22.5	Outside
25	7.5	Inside	22.5	Inside	27.5	Outside
35	7.5	Inside	27.5	Inside	27.5	Outside
50	7.5	Inside	12.5	Inside	32.5	Outside
75	7.5	Inside	12.5	Inside	17.5	Inside
100	7.5	Inside	12.5	Inside	17.5	Inside

the loading area at  $\theta = 12.5^\circ$ . When the contact angle is  $30^\circ$ , the spheres with wall thicknesses of  $75 \mu\text{m}$  and  $100 \mu\text{m}$  would fail just outside of the loading area on the inner surface instead of near the loading axis as shown in Table 3.2.1. The failure mode in all cases would be a tensile failure due to the normal tensile stress  $\sigma_x$  at the failure location.

Sphere strength under uniaxial distributed loading was calculated from the critical stress determined from the failure analysis. Parametric analysis was performed to characterize the sphere strength as a function of parameters such as sphere radius, wall thickness, or sphere density. As in the previous cases of the sphere strength under uniaxial concentrated loading and stiffness of sphere, the sphere strength under uniaxial distributed loading turned out not to be a function of either sphere radius or wall thickness. The parametric study revealed that the sphere strength could be reduced to linear relationships with the relative density squared, which is shown in Figure 3.2.3. The relationships between the sphere strength under uniaxial distributed loading and the relative density squared for each contact angle in the figure consist of two linear portions. For  $\phi = 10^\circ$ , the first linear portion is the line defined by the first two data points from the Y-axis, which represent two spheres with aspect ratios of 0.005 and 0.015. The second linear portion is defined by the data points with aspect ratios of 0.015 and higher. The first linear portion for  $\phi = 20^\circ$  is defined by the first four data points from the Y-axis and the second linear portion is defined by the fourth and successive data points from the axis. When the contact angle is  $30^\circ$ , the first linear portion of the relationship consists of the first six data points from the Y-axis and the second linear portion could be defined by the sixth and the seventh data points. Interestingly these linear portions have a pattern. The first linear portions represent spheres that fail away from the loading areas. The second linear portions represent the spheres which fail just outside the loading areas.

The sphere strength under uniaxial distributed loading can be expressed as a linear function of the relative density squared given by

$$\sigma_s = C_1 \sigma_o \left( \frac{\rho_s}{\rho_o} \right)^2 \quad (3.2.9)$$

for the initial linear portion and

$$\sigma_s = C_o + C_2 \sigma_o \left( \frac{\rho_s}{\rho_o} \right)^2 \quad (3.2.10)$$

for the second linear portion. The constants in Equation 3.2.9 and Equation 3.2.10

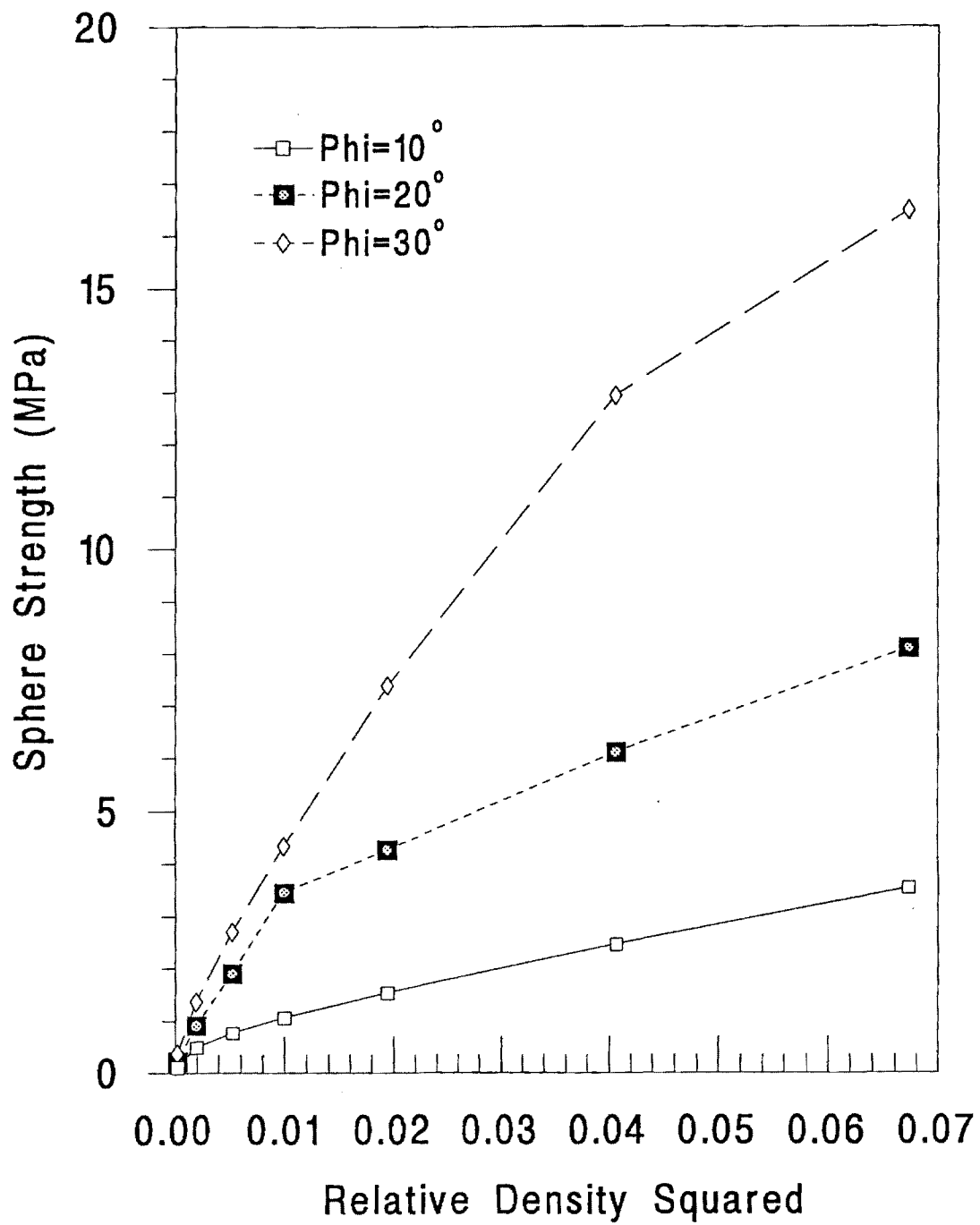


Figure 3.2.3

Sphere Strength,  $\sigma_s$ , vs. Relative Density Squared,  $(\rho_s/\rho_o)^2$ , under Uniaxial Distributed Loading.



were obtained from linear regression of the data in Figure 3.2.3. The constant  $C_1$  in Equation 3.3.9 was calculated by forcing the linear regression line to pass zero.  $C_1$ ,  $C_0$ , and  $C_2$  for  $\phi = 10^\circ$  were calculated as 0.843, 0.545, and 0.152, and the correlation coefficients squared were 0.9687 and 0.9929 for the first and the second linear portions respectively. When the contact angle is  $20^\circ$ , the constants were calculated to be 1.18, 2.69, and 0.271, and the correlation coefficients squared to be 0.9862 and 0.9982 in the same order. For  $\phi = 30^\circ$  the constants are 1.12, 7.53, and 0.443, and  $R^2$  for the first portion is 0.9663.

**Bonded Sphere Foam Model with Six-Directional Distributed Loading** -When a closed-cell ceramic foam is fabricated by bonding hollow ceramic spheres together, the spheres in the foam experience compressive loadings from many directions. Spheres inside the bonded sphere foam fabricated to date tend to be randomly packed. In such a random pack, a sphere contacts about six to eight spheres. The basic unit of the structure was proposed to be a sphere surrounded by six spheres as illustrated in Figure 3.2.4. The unit structure is an octahedron where the center sphere is diametrically bonded to three pairs of spheres at right angles. The foam structure then may be described as consisting of randomly oriented basic unit structures.

It was assumed that a bonded sphere foam would start to fail when the sphere in a basic unit structure fails. The load transfer to the center sphere by the surrounding spheres was assumed to be in the axial directions. Thus the center sphere would experience three pairs of diametral compressive loadings of equal magnitude when the bonded sphere foam is under a compressive loading. A finite element model of the center sphere in the unit structure developed. Loading areas which are represented by the contact angle,  $\phi$ , were again varied for  $\phi = 10^\circ$ ,  $20^\circ$ , and  $30^\circ$ . Uniformly distributed loads were applied to the loading areas parallel to the loading axes. Distributions of membrane forces, bending moments, transverse shear forces, and stresses were investigated. Despite the non-axisymmetry of the loading situation around a loading axis, the distributions of those parameters exhibited similar patterns as in the uniaxial distributed loading case with more or less axisymmetry around a loading area, especially for small contact angle, up to some distance away from the loading axis. The axisymmetry began to be disturbed past this distance because of effects from adjacent loading areas.

**Sphere Strength under Six-Directional Loading** - Sphere strength was calculated from the finite element stress data in the same way as in the uniaxial distributed loading case. The sphere strength versus the relative density squared is plotted in Figure 3.2.5. The linear relationships between the sphere strength and the relative density squared for different contact angles are similar to those in the uniaxial distributed loading case. The linear relationships for  $\phi = 10^\circ$  and  $30^\circ$  can be described by one line for each for practical purposes. For  $\phi = 10^\circ$ , the linear relationship can be given by

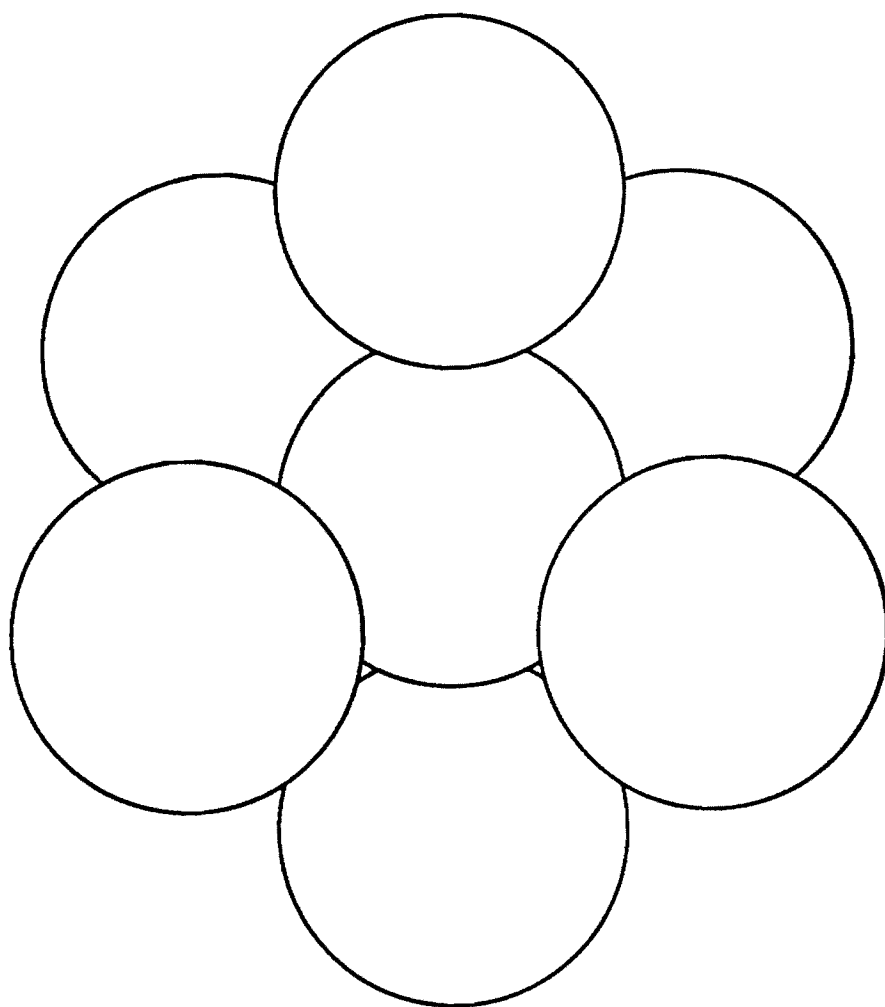


Figure 3.2.4 Basic Unit Structure of Random-Packed Bonded Sphere Foam.

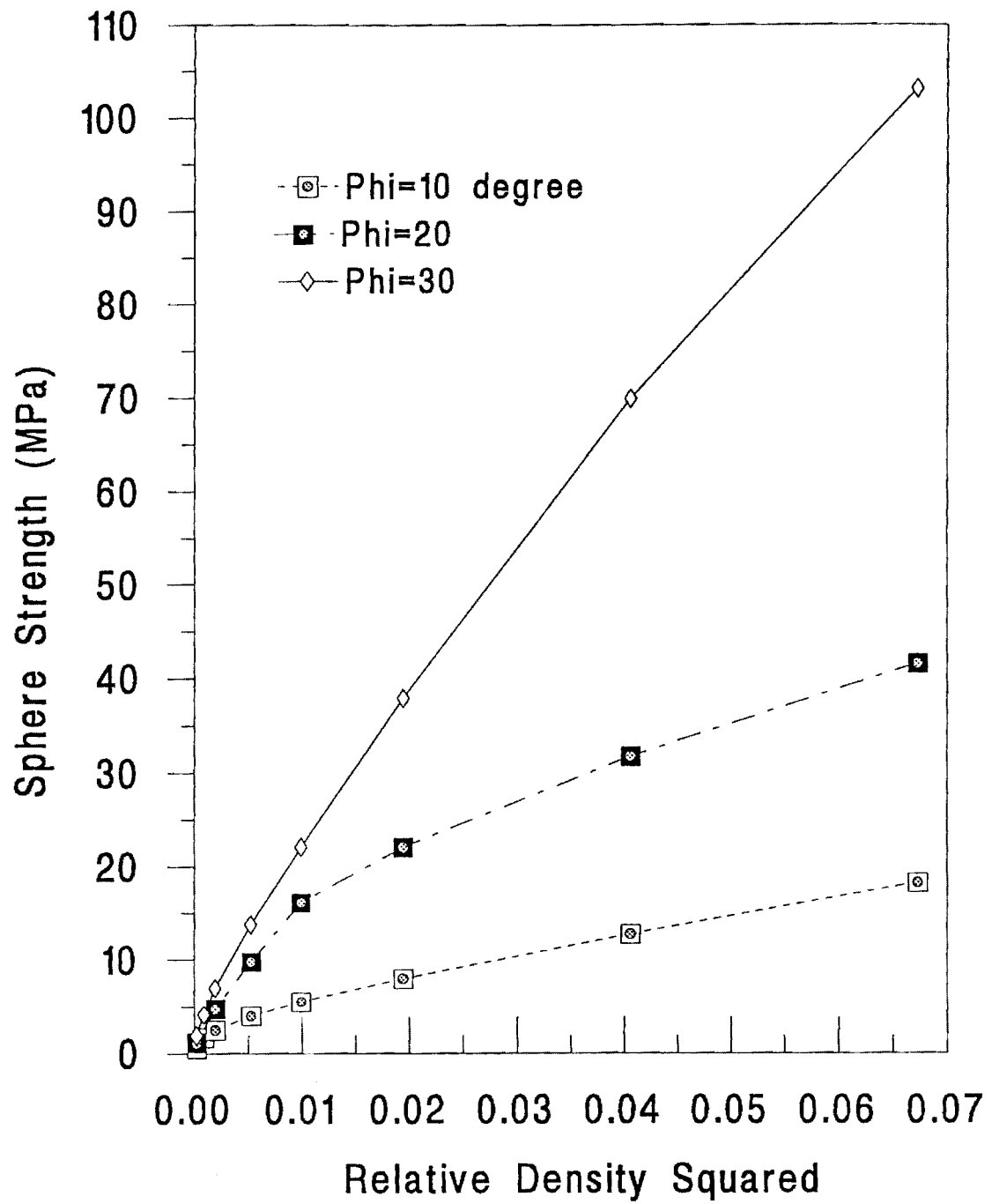


Figure 3.2.5

Sphere Strength  $\sigma_s$ , vs. Relative Density Squared,  $(\rho_s/\rho_o)^2$ , under Six-Directional Distributed Loading.

Equation 3.2.10 with  $C_0 = 2.84$ ,  $C_2 = 0.786$ , and  $R^2 = 0.9925$ . For  $\phi = 30^\circ$ , the linear relationship can be expressed by Equation 3.2.9 with  $C_1 = 5.40$  and  $R^2 = 0.9805$ . The first linear portion for  $\phi = 20^\circ$  has  $C_1$  of 5.67 and  $R^2$  of 0.9676 and the second linear portion has  $C_0 = 12.9$ ,  $C_2 = 1.46$ , and  $R^2 = 0.9909$ .

### 3.2.3 EXPERIMENTAL VERIFICATION OF FINITE ELEMENT MODEL

**Bonded Sphere Foam Fabrication** - Hollow alumina spheres were bonded mixing with a small quantity of slurry, which consisted of alumina, organic binder, and water. Precise control of the viscosity of the slurry as well as the batch composition of the ingredients was necessary to achieve strong bonds at points of contact and to maintain a low foam density. When the viscosity of the slip was too low, the bonding angle was usually small and the bonds between spheres did not have adequate strength resulting in the failure through the bonds. When the viscosity was too high the bonding material coated the spheres relatively evenly rather than concentrating at the neck areas thus increasing the density of the foam greatly and also resulting in low strength of the bonds. The spheres coated with slip were cast into a mold applying vibration and pressure to achieve better packing of the spheres. The casting was dried at room temperature and removed from the mold. The green foam was then fired at  $1600^\circ\text{C}$  for 4 hours to sinter the bonding material. Mullite spheres were also bonded into mullite foams using mullite slip to investigate the compressive strengths of mullite foams, Figure 3.2.6 shows a bonded alumina sphere foam after firing. The spheres at the surface of the foam show some degree of hexagonal packing because of mold wall forces. However, the spheres inside the foam are packed randomly as shown in Figure 3.2.7. Figure 3.2.7 shows a point contact bonded mullite sphere foam made of mullite spheres with 3.5 mm average diameter. Note that the fillets produce a distributed load with contact angle of  $\sim 20^\circ$ .

**Compression Testing of Bonded Sphere Foams** - For compressive testing of the bonded sphere foams, epoxy end caps were cast on the loading faces to transfer the load uniformly. Some foams were tested without epoxy caps but load was distributed using polyurethane pads and steel caps. The polyurethane pad was placed between the loading face of the foam and the steel cap. Bonded sphere foams were tested under compressive loading on an Instron testing machine. Swivel heads were used to transfer the load uniformly to the loading faces of the foam. The foam strength was calculated as the load at fracture per cross-sectional area of the foam.

**Bonded Sphere Foam Compressive Strength** - The bonded sphere foams with epoxy end caps failed horizontally across the foams in most cases. As the load increased some spheres began to pop out from the surface of the foam without apparent

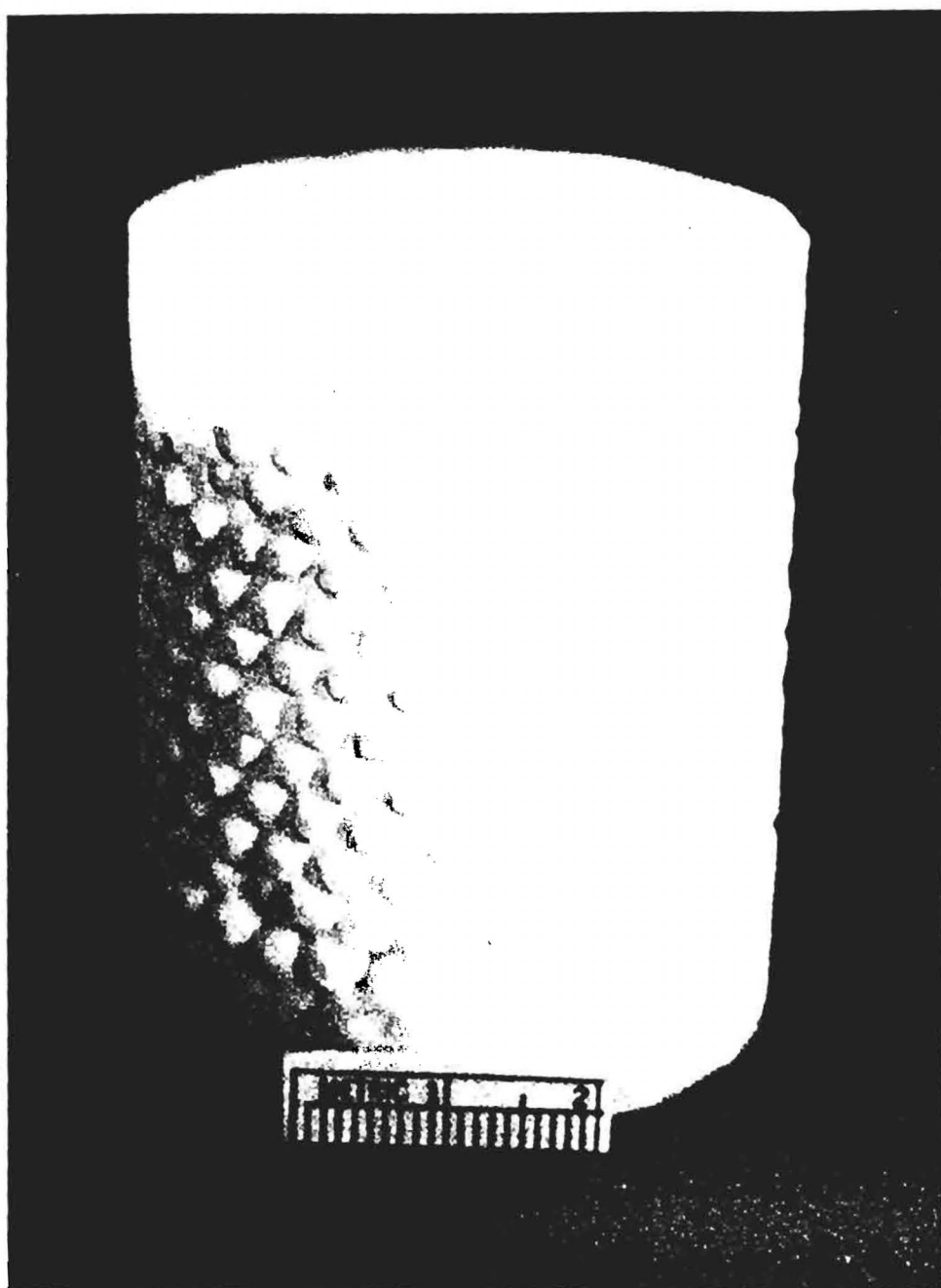


Figure 3.2.6      A Bonded Alumina Sphere Foam to be Tested under Compressive Load.

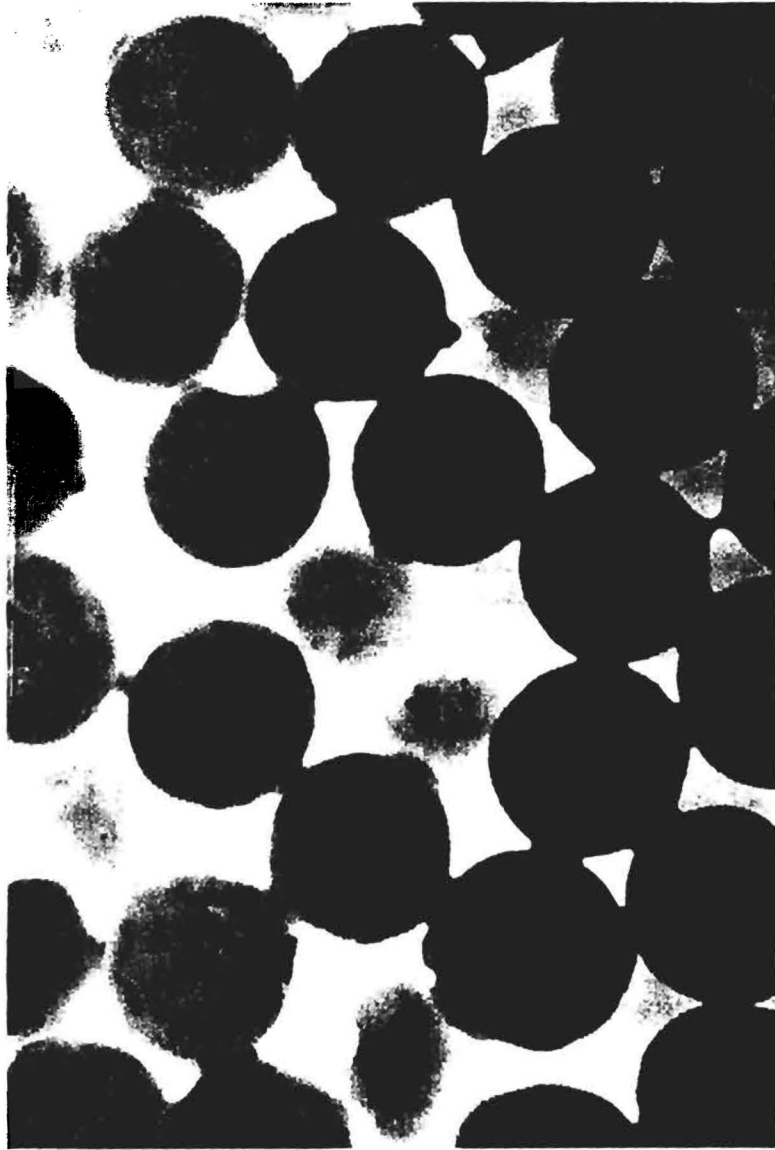


Figure 3.2.7 Cross Section of Bonded Mullite Sphere Foam Showing Random Packing and Point Contact Bonding.

catastrophic. The failures were almost explosive as in the typical crushing of a solid brittle material. Most of the foams tested with the polyurethane pads and the steel caps failed vertically indicating non-uniform loading on the foams.

The compressive strengths of the foams versus the foam densities are plotted in Figure 3.2.8. The experimental results are also compared with commercial ceramic foam (insulating fire brick) strength data. At comparable densities the bonded sphere foams have compressive strengths five to eight times higher than the insulating fire brick foams. The bonded-sphere foams with the epoxy end caps show higher strength than the same foams tested with the polyurethane pads and the steel caps because of the uniform load transfer.

The foam strengths data in Figure 3.2.8 were plotted again in Figure 3.2.9 based on the corresponding sphere density to evaluate the effect of the contact angle on the strength of foam. The alumina foams with densities of  $43 \text{ lb./ft}^3$  and  $54 \text{ lb./ft}^3$  shown in Figure 3.2.8 were made of same alumina spheres with a relative density squared of 0.02. Assuming packing factors are same for both foams, it is obvious from the two alumina samples with epoxy end caps in Figure 3.2.9 that the amount of bonding material affects the foam strength. There can be two possible reasons for this. If the bonds between the spheres do not have adequate strength, the foam fails at the bonds before the spheres fail thus not fully utilizing the sphere strength. If bonds have proper strength, the amount of bonding material will control the contact angle and will be a governing factor of foam strength as predicted by the finite element analysis. The difference in increased sphere wall thickness due to the coating of the spheres with bonding material was assumed to be negligible regardless of the amount of the bonding material, because most bonding material migrates to the neck area with the use of a proper bonding technique. Fracture surface of the samples showed that both foams failed through the sphere walls, not at the bonds. Accordingly the difference in the foam strength exhibited by these two samples can be adequately explained by contact angle. Since the sphere strength for various loading conditions has a linear relationship with relative density squared as determined previously, increasing the strength a factor of two requires that the relative sphere density squared should also increase by two, if bond angles (contact angles) are the same. In this case, the relative density squared of the two foams, however, increased only 63 %, while the foam strength increased approximately 100 %. Again, increased bond angle appears to have a larger effect than density increases as predicted by the model.

Mullite spheres and alumina spheres used in this research have similar wall material strength. Thus they can be compared with each other in Figure 3.2.9. The contact angles for the foams were not precisely determined. Calculation of the contact angle from the sphere density, the sphere size, and the foam density based on the basic unit structure model of the random packed monolith is proposed as future research.

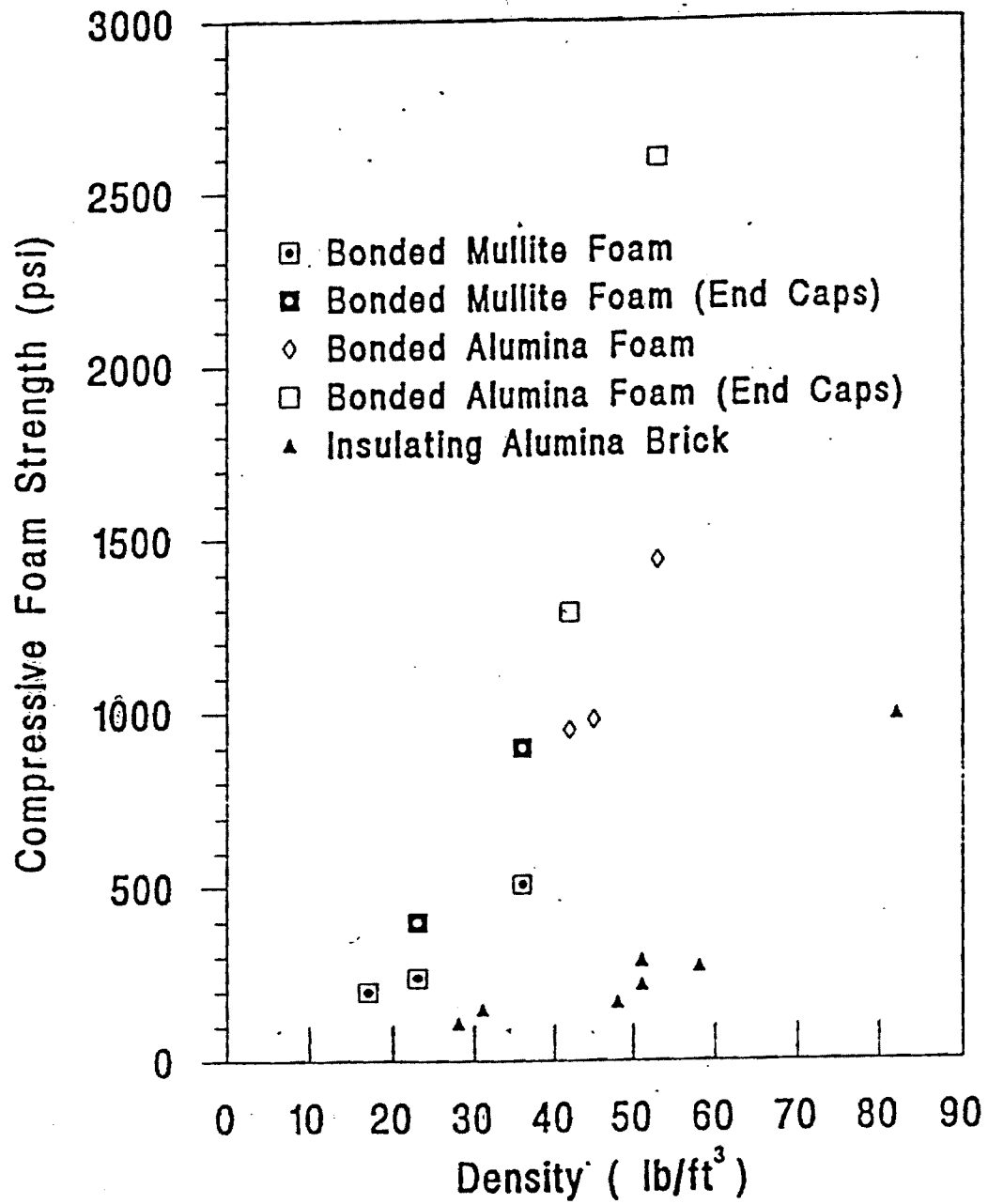


Figure 3.2.8

Bonded Sphere Foam Compressive Strength (psi) vs. Foam Density (lb/ft³).



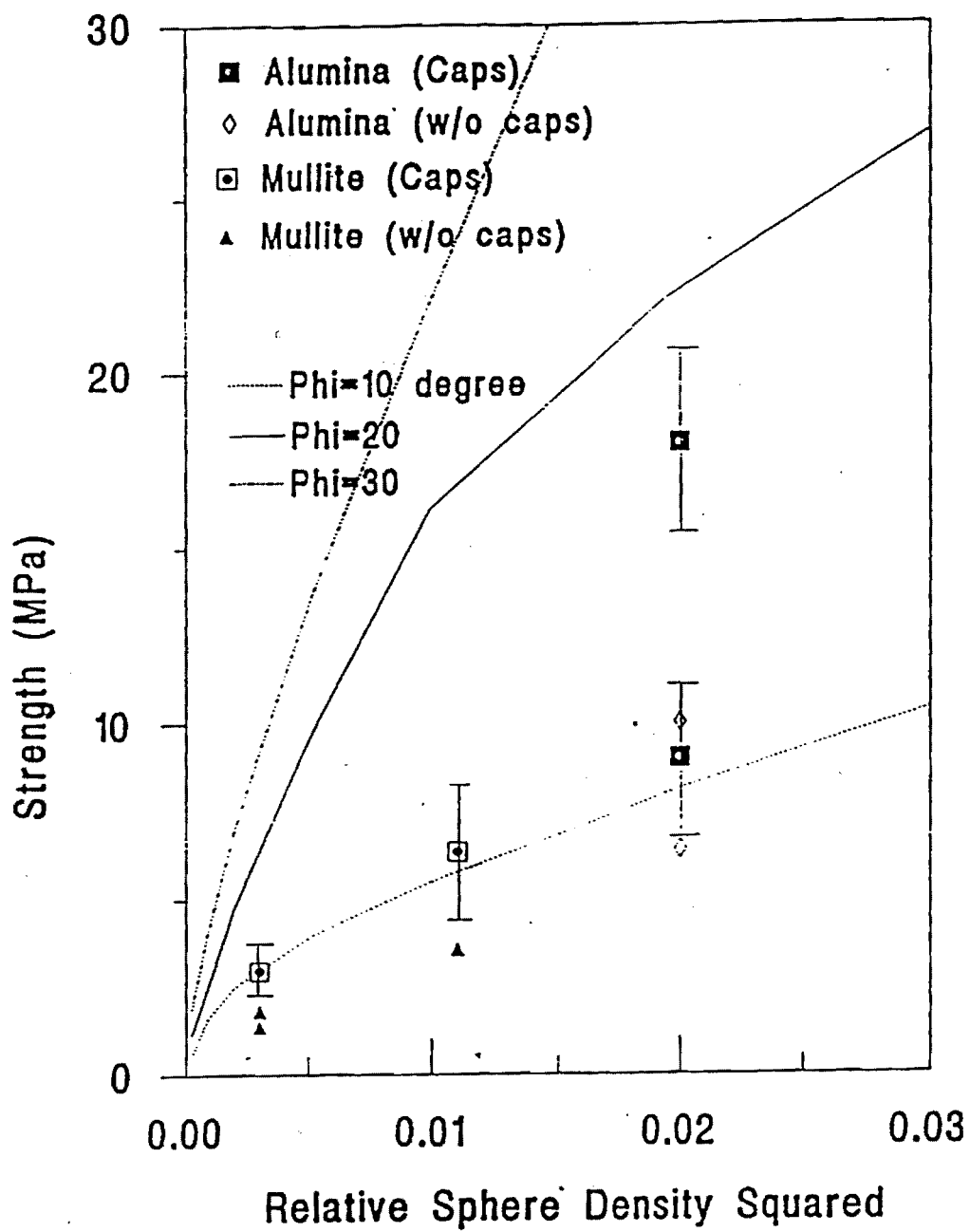


Figure 3.2.9 Foam Strength vs. Relative Sphere Density Squared.

decrease in the load at the constant crosshead speed and failure was sudden and catastrophic. The failures were almost explosive as in the typical crushing of a solid brittle material. Most of the foams tested with the polyurethane pads and the steel caps failed vertically indicating non-uniform loading on the foams.

The compressive strengths of the foams versus the foam densities are plotted in Figure 3.2.8. The experimental results are also compared with commercial ceramic foam (insulating fire brick) strength data. At comparable densities the bonded sphere foams have compressive strengths five to eight times higher than the insulating fire brick foams. The bonded-sphere foams with the epoxy end caps show higher strength than the same foams tested with the polyurethane pads and the steel caps because of the uniform load transfer.

The foam strengths data in Figure 3.2.8 were plotted again in Figure 3.2.9 based on the corresponding sphere density to evaluate the effect of the contact angle on the strength of foam. The alumina foams with densities of  $43 \text{ lb./ft}^3$  and  $54 \text{ lb./ft}^3$  shown in Figure 3.2.8 were made of same alumina spheres with a relative density squared of 0.02. Assuming packing factors are same for both foams, it is obvious from the two alumina samples with epoxy end caps in Figure 3.2.9 that the amount of bonding material affects the foam strength. There can be two possible reasons for this. If the bonds between the spheres do not have adequate strength, the foam fails at the bonds before the spheres fail thus not fully utilizing the sphere strength. If bonds have proper strength, the amount of bonding material will control the contact angle and will be a governing factor of foam strength as predicted by the finite element analysis. The difference in increased sphere wall thickness due to the coating of the spheres with bonding material was assumed to be negligible regardless of the amount of the bonding material, because most bonding material migrates to the neck area with the use of a proper bonding technique. Fracture surface of the samples showed that both foams failed through the sphere walls, not at the bonds. Accordingly the difference in the foam strength exhibited by these two samples can be adequately explained by contact angle. Since the sphere strength for various loading conditions has a linear relationship with relative density squared as determined previously, increasing the strength a factor of two requires that the relative sphere density squared should also increase by two, if bond angles (contact angles) are the same. In this case, the relative density squared of the two foams, however, increased only 63 %, while the foam strength increased approximately 100 %. Again, increased bond angle appears to have a larger effect than density increases as predicted by the model.

Mullite spheres and alumina spheres used in this research have similar wall material strength. Thus they can be compared with each other in Figure 3.2.9. The contact angles for the foams were not precisely determined. Calculation of the contact angle from the sphere density, the sphere size, and the foam density based on the basic unit

structure model of the random packed monolith is proposed as future research. However, assuming the increase in density from sphere density to foam density translates to the bond angle, the mullite foams tested with epoxy end caps, which relative sphere density squared are 0.0028 and 0.0113 in Figure 3.2.9 have similar bond angles. Also, the alumina foam with epoxy end cap, which relative sphere density squared and strength are 0.02 and 9 MPa, has a similar bond angle. These three foams lie within experimental error on the finite element analysis prediction for  $\phi = 10^\circ$ . It has already been shown that experimental sphere strength under contact loading provided one third the strength predicted by finite element model due to defects and the same is probably true here. The three data points should probably multiplied by three which would place them between the lines for  $\theta = 20^\circ$  and  $30^\circ$ . The bonds in the bonded-sphere foams had contact angles in that range. Thus the finite element prediction agrees reasonably with the only available data for comparisons.

### 3.3 ISOSTATIC COMPRESSIVE STRENGTH

Potential uses for hollow ceramic spheres include bonding together to form monoliths for high-temperature insulation or light structural materials in syntactic foams. They might also be introduced into various matrix materials to form light weight composites. Stresses on individual spheres would then be more uniformly distributed, rather than resulting from a simple uniaxial load. In such situations the isostatic compressive strength would serve as a better approximation of the mechanical properties of the sphere.

There are several methods described in the literature for determining the isostatic strength of small hollow spheres, specifically glass spheres. One method, the ASTM Standard Method of Test D3102<sup>5</sup>, is an isostatic compression test. However, it requires a special, costly set-up and reportedly<sup>6</sup> is seldom used. Another technique was described by Milewsky and Marsters<sup>7</sup>. In their technique, a pressure differential is created between the inside and the outside of the sphere and thus the sphere fails in tension. The problem with this method are that it also requires a special, costly set-up, it is only useful for relatively large spheres, and only one sphere at a time can be tested. The preferred method, described by Ciftcioglu and Akinc<sup>6</sup>, used a scanning mercury porosimeter.

The mercury porosimeter method allows a relatively large number of spheres to be tested at one time. The primary disadvantage is that individual sphere strengths cannot be determined. In this method, spheres are placed in the sample cell of the mercury porosimeter and the cell is filled with mercury. The pressure is gradually increased and as the spheres break, the void within each is filled with mercury and the change in volume is recorded. From the pressure-volume data, the distribution of the isostatic compression strengths is generated. Since values for individual spheres are not available, numbers such as the strength at twenty percent (20%) volume reduction or strength at fifty percent (50%) volume reduction are reported.

#### 3.3.1 BACKGROUND

When a thin wall spherical shell is placed in isostatic compression it may fail by one of two different modes, compressive wall failure or thin shell buckling. If a spherical shell is subjected to uniform external pressure in which it maintains its shape then the magnitude of the compressive stress is:

$$\sigma = \frac{Pr}{2t} \quad (3.3.1)$$

For  $r/t$  values less than 20, it is predicted<sup>3</sup> that the spheres should fail by crushing. Substituting from Equation (3.3.2),

$$\left( \frac{\rho_s}{\rho_o} \right) = \frac{3t}{r} \quad (3.3.2)$$

and rearranging gives the predicted critical crushing pressure:

$$P_c = \frac{2}{3} \sigma_{ultc} \frac{\rho_s}{\rho_o} \quad (3.3.3)$$

where  $\sigma_{ultc}$  is the ultimate compressive strength of the wall material. For the case of  $r/t > 20$ , as the pressure increases, the spherical form of equilibrium may become unstable and buckling then occurs<sup>8</sup>. Timoshenko and Gere<sup>8</sup> derived the equation for the classical critical stress in a sphere which fails by thin shell buckling. It is given by

$$\sigma_{cl} = \frac{Et}{r [3(1 - \nu^2)]^{1/2}} \quad (3.3.4)$$

where  $\nu$  is Poisson's ratio for the wall material. Rearranging gives the predicted critical pressure when failure occurs by thin shell buckling:

$$P_{cl} = \frac{2E}{9 [3(1 - \nu^2)]^{1/2}} \left( \frac{\rho_s}{\rho_o} \right)^2 \quad (3.3.5)$$

As was the case for uniaxial loading, these solutions depend on wall thickness uniformity. Ciftcioglu and Akinc<sup>6</sup> found the theoretical critical buckling pressure to be approximately twenty (20) times higher than the experimentally determined pressure for low-strength spheres and approximately four (4) times higher for high-strength spheres. The authors concluded that the degree of deviation from theoretical strength is a measure of perfection of the spheres. Because of the geometry of the spheres used in this investigation, they would probably fail at the thinnest spot yielding lower than expected values. Timoshenko and Gere<sup>8</sup> point out that "in the vicinity of the spherical shape of equilibrium of a compressed shell there exist forms of equilibrium slightly deviated from the spherical shape which require pressures much smaller [than predicted by Equation (3.3.5)]." Therefore a small disturbance during loading might result in failure at a much lower pressure than expected. This might partially explain the results obtained by Ciftcioglu and Akinc as the failure of one sphere within the sample cell might disturb the spheres around it and cause them to fail as well. This also helps to explain the wide scatter of the experimental results.

### 3.3.2 ISOSTATIC TESTING

Testing the isostatic strength of select groups of spheres was performed using mercury porosimetry by two independent laboratories. Batches 11186, 02057, and 03247 were tested by Micromeritics Corporation in Norcross, Georgia. Batches 05077 30/30, 05287 31/10, 05287 60/40, and 08267 70/40 were tested by PQ Corporation in Lafayette Hill, Pennsylvania.

The data received from the isostatic testing was in two different forms. The data from Micromeritics Corporation was tabulated as pressure and cumulative volume intruded. The data from PQ Corporation was in the form of graphs of percent volume loss versus log pressure. All data was retabulated and is plotted as percent volume loss versus log pressure in Figures 3.3.1 and 3.3.2. Table 3.3.1 tabulates pressures at 20, 50, and 80 percent volume loss ( $P_{20}$ ,  $P_{50}$ ,  $P_{80}$ ) as well as relative density for each batch tested.

Both labs reported problems associated with the penetrometer. The penetrometer is the part of the porosimeter which holds the sample and is made of glass. For an unknown reason it frequently broke during testing of the spheres. Some of the data was rendered unusable because of this. Other data could still be used when this happened but had to be adjusted to account for the volume intruded as a result of the breakage. The remainder of the data was quite satisfactory.

### 3.3.3 THEORETICAL STRENGTH

Under isostatic compression the spheres were expected to fail either by compressive wall failure or thin shell buckling depending on the radius to wall thickness ( $r/t$ ) ratio. If  $r/t$  is less than 20 [ $\rho_s/\rho_o > 0.150$ ] then crushing is predicted and Equation (3.3.3) applies. For the case of  $r/t$  greater than 20 [ $\rho_s/\rho_o < 0.150$ ] thin shell buckling is predicted and Equation (3.3.5) applies. However experimental results usually indicated that the buckling pressure is considerably smaller than the analytically predicted critical pressure<sup>8</sup>. Because thin spherical shells are imperfection sensitive<sup>9</sup>, a factor is used to relate the predicted to experimental results along with Equation 11:

$$P_{cv} = \Lambda P_{cl} \quad (3.3.6)$$

where  $\Lambda$  is a factor known as the "knockdown factor." This factor is dependent on parameters such as the radius to thickness ratio and for the spheres used in this investigation a reasonable value to use is  $0.6^{8,9,10}$ . The values which were used for the relevant material properties were:

$$\sigma_{ultc} = 3447 \text{ Mpa} = 5 \times 10^5 \text{ psi}$$

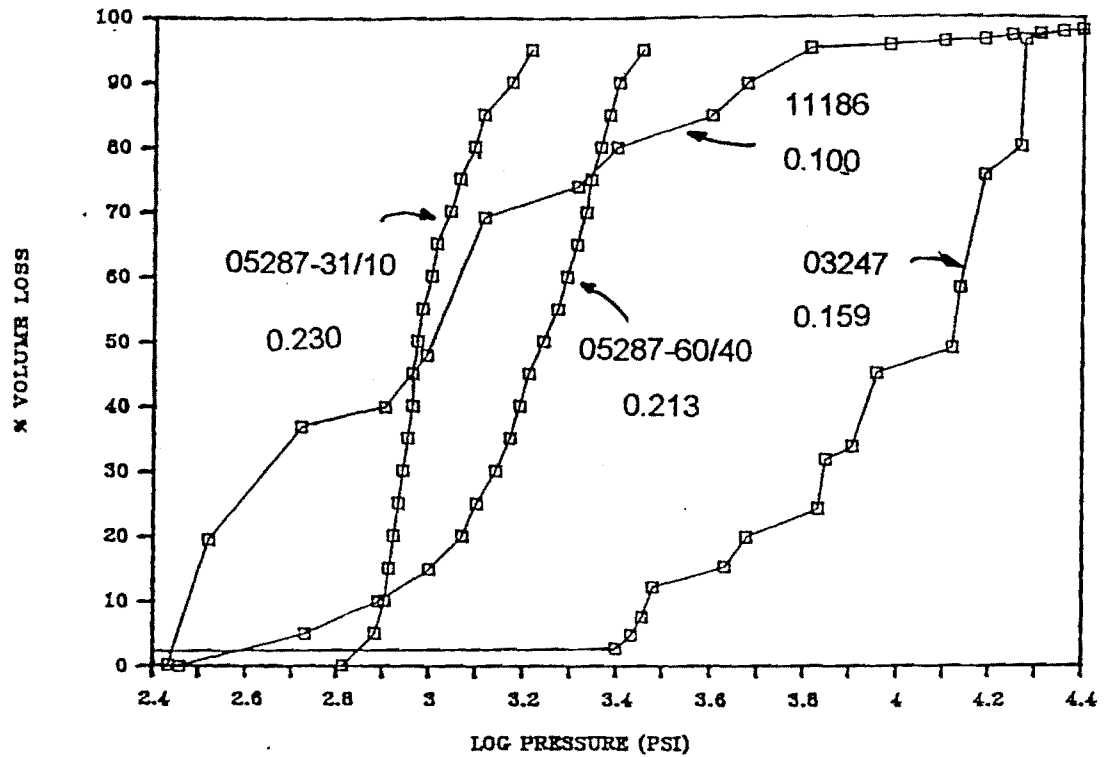


Figure 3.3.1 Isostatic Compressive Strength Distributions for Alumina Hollow Spheres from Hg Porosimetry

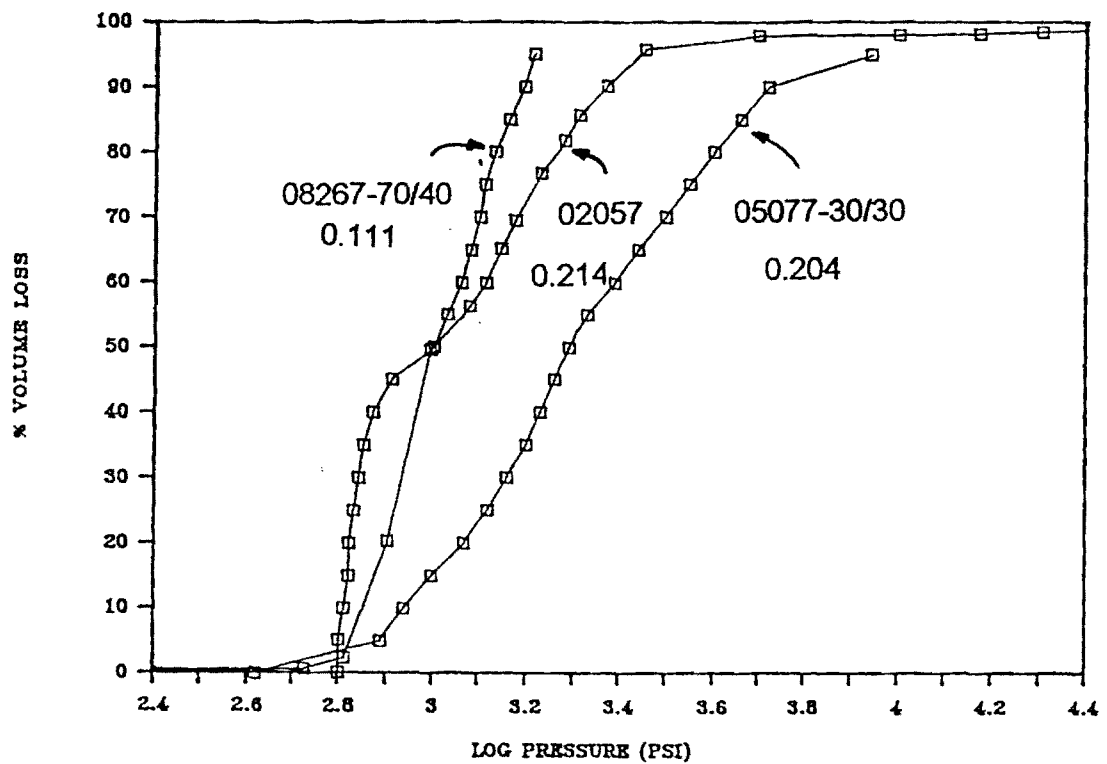


Figure 3.3.2 Isostatic Compressive Strength Distributions for Alumina Hollow Spheres from Hg Porosimetry

Table 3.3.1      Isostatic Strength (psi) of Alumina Hollow Spheres at 20, 50, and 80 Percent Volume Loss and Relative Density

Batch	P <sub>20</sub>	P <sub>50</sub>	P <sub>80</sub>	$\rho_s / \rho_o$
11186	395	1009	2485	0.100
08267 70/40	661	1000	1349	0.111
02057	799	1004	1904	0.214
05287 31/10	832	933	1230	0.230
05287 60/40	1175	1738	2291	0.213
05077 30/30	1175	1950	3981	0.204
03247	4775	13145	18402	0.159



$$E = 380 \times 10^9 \text{ Pa} = 55.1 \times 10^6 \text{ psi}$$

$$\nu = 0.26$$

The results of the theoretical calculations of  $P_{\text{fail}}$  are summarized in Table 3.3.2. Clearly, the predicted failure pressures, even with the knockdown factor, are still much higher than the experimental results even when compared to the  $P_{80}$  values. Figure 3.3.3 further illustrates this point where isostatic pressure is plotted versus relative density. The area shown represents a range for  $\sigma_{\text{ultc}}$  from 280,000 to 540,000 psi and for  $E$  from 50 to 55  $\times 10^6$  psi with the knockdown factor not included. These values are typical for fine grained polycrystalline alumina, such as produced here. This range represents a maximum range where the spheres might be expected to fall. The probable cause of the difference between theoretical and experimental results, as in the uniaxial case, is the variable wall thickness. In addition, nonsphericity can cause an appreciable reduction in the predicted critical pressures. Across all batches of spheres it was found that the average aspect ratio is approximately 1.02.

Obviously, the main improvements to isostatic compressive strengths would be produced by decreases in wall thickness variation. This is more dramatically illustrated when isostatic failure is compared to relative density. No correlation is present and, in fact, the strongest spheres had a density significantly less than four other much weaker groups of spheres. The theoretical limits for compressive strength are an order of magnitude greater than observed and improvements in sphere perfection could provide significant increases with no increase in density.

Table 3.3.2. Predicted Isostatic Failure Loads.

Batch	$\rho_s$ ----- $\rho_o$	Predicted Failure Mode	$P_{\text{fail}}$ ----- Mpa	$P_{\text{fail}}$ ----- psi
11186	0.100	Buckling	303	43,927
02057	0.214	Crushing	492	71,333
03247	0.159	Crushing	365	53,000
05077-30/30	0.204	Crushing	469	68,000
05287-31/10	0.230	Crushing	529	76,667
05287-60/40	0.213	Crushing	490	71,000
08267-70/40	0.111	Buckling	373	54,122

# ISOSTATIC FAILURE OF ALUMINA SPHERES

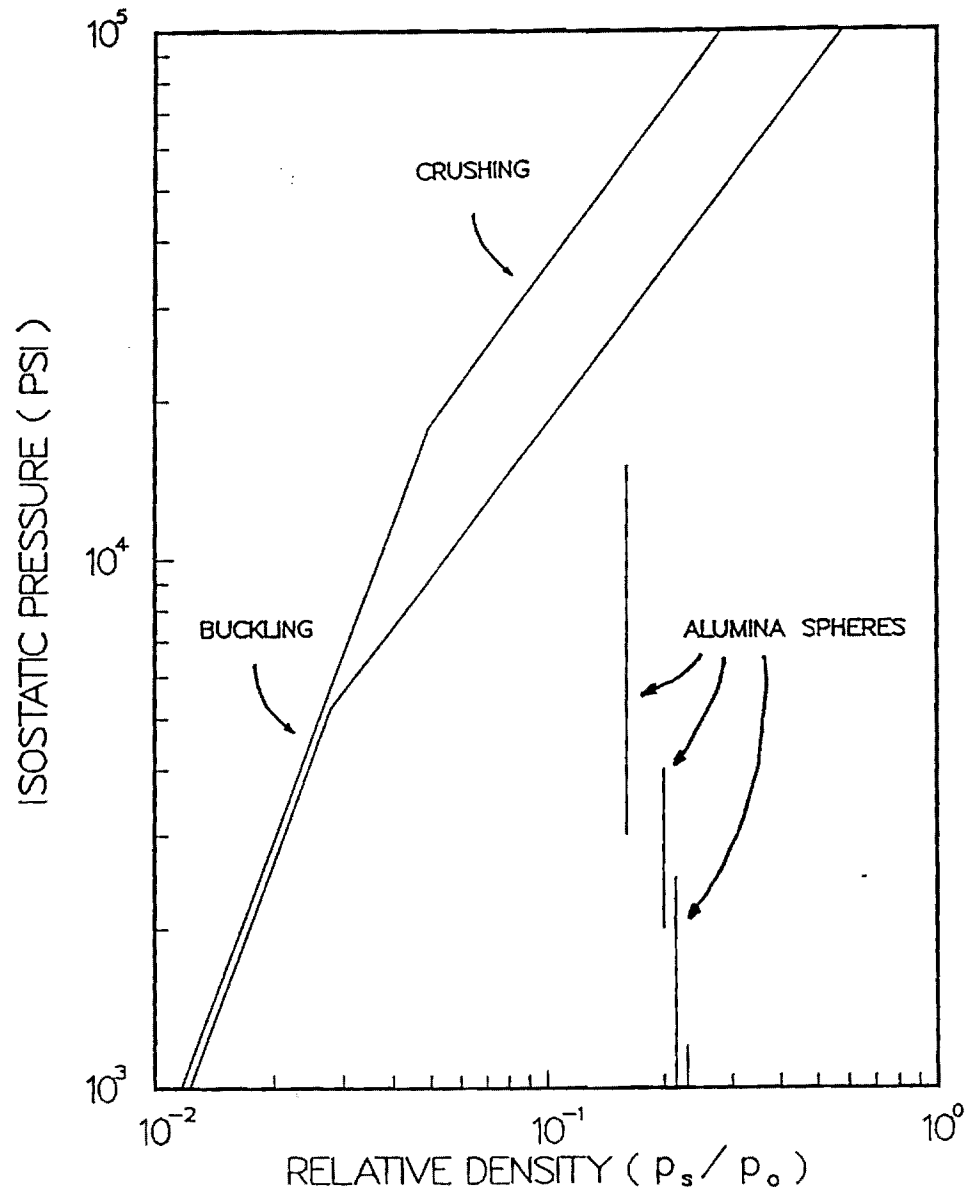


Figure 3.3.3

Isostatic Failure of Alumina Hollow Spheres as a Function of Density for Buckling and Crushing Compared to Experimental Values

#### 4.0 THERMAL CONDUCTIVITY OF HOLLOW SPHERES

Thin-walled, hollow ceramic spheres from conventional powder slurries which have been developed in this program are being targeted for use as high temperature, refractory insulation. Previous research has demonstrated that radiation transfer is the most significant contribution to the high temperature thermal conductivity of hollow spheres. A primary concern for this insulation is reducing the thermal conductivity, especially the contribution due to radiation transfer which is prominent at high temperatures. Available literature suggests that the degree of radiation transfer through a ceramic or glass is highly dependent on the microstructure of the material, and that materials with high infrared reflectance values show lower thermal conductivities. Infrared reflectance may be increased by adding second phase particles of a different refractive index to the microstructures of materials. This section explores the relationship between the microstructure, thermal conductivity, and infrared reflectance of thin-walled, hollow glass spheres containing second phase zirconia particles. The effects of zirconia content and particle size were studied.

Additions of zirconia particles significantly lowered the high-temperature thermal conductivity of glass spheres. The most effective composition lowered the thermal conductivity by slightly more than a factor of two. This reduction in thermal conductivity was a strong function of zirconia volume fraction. There existed a limit to the volume fraction of zirconia which was useful in lowering the thermal conductivity; exceeding this limit did little to reduce the thermal conductivity and may have even caused it to increase. This saturation limit occurred at approximately ten volume percent. The effect of particle size was less pronounced and inconclusive.

Infrared reflectance measurements were produced from glass pellets fabricated to duplicate the microstructure of the spheres. Zirconia scattering particles were found to significantly increase the infrared reflectance of these glass pellets. Like thermal conductivity, infrared reflectance was found to be a strong function of zirconia content, and also displayed saturation at approximately ten volume percent zirconia. The effect of particle size was again inconclusive.

Graphs of thermal conductivity vs. infrared reflectance demonstrated a nearly linear inverse relationship. In the future, infrared reflectance measurements may allow the accurate, rapid prediction of the thermal conductivity of hollow spheres while avoiding the time intensive process of fabricating spheres and measuring conductivity.

#### 4.1 RADIATION TRANSFER IN CERAMICS

This work advances the hypothesis that infrared radiation transfer is a significant contribution to the total thermal conductivity of hollow spheres at elevated temperatures. To try and lessen this component, an understanding of a ceramic material's ability to transfer radiation is essential.

Dielectric materials emit radiation at all temperatures above absolute zero. The intensity and wavelength distribution of the emitted radiation change with temperature. With increasing temperature, the maximum in the wavelength distribution decreases, while the intensity of the radiation increases dramatically. The maximum in the radiation distribution,  $\lambda_m$ , is approximated by Wien's law:

$$\lambda_m T = 2897.8 \mu m \cdot K \quad (2.6)$$

where T is the absolute temperature.

A material's complex coefficient of refraction,  $n^*$ , dictates much of its optical behavior, and is related to n, the index of refraction, and k, the index of absorption:<sup>7</sup>

$$n^* = n - ik \quad (2.7)$$

Both n and k are functions of wavelength and temperature. For most dielectric materials, the index of refraction, n, varies little with wavelength in the range with which this study is concerned.<sup>7</sup> The index of refraction may increase or decrease slightly with temperature. The index of refraction is related to density, with more dense materials tending to possess higher values. For dielectric materials, the index of absorption is more a function of wavelength than temperature. In the visible and near infrared regions, absorption is relatively low. Higher absorption at wavelengths smaller than that of the visible spectrum is due to electronic transitions in atoms, while resonant lattice vibrations cause absorption in the far infrared region.

The indices of refraction and absorption will dictate how radiation behaves when passing through a dielectric material. When electromagnetic radiation impinges on a dielectric layer, such as a hollow sphere wall, the radiation may be transmitted or inhibited due to three factors. Surface reflection may take place at air/ceramic interfaces, while absorption or scattering may take place within the bulk of the solid.

Surface reflection is the result of a difference in complex coefficient of refraction between the gas and solid, and may have both a specular and diffuse component. A specularly reflected ray is reflected from the surface at an angle equal to the incident angle. Diffusely reflected rays leave the surface at all angles and diffuse reflectance increases with surface roughness. For radiation normal to a smooth surface having a low index of absorption, the surface reflectivity R is approximated by:

$$R = \left( \frac{n-1}{n+1} \right)^2 \quad (2.8)$$

where R is the fraction of radiation reflected at a surface.

Within the solid, radiation may be inhibited by absorption and/or scattering. The sum of the effect of absorption and scattering is called extinction. This relationship is given as:<sup>8</sup>

$$C_{ext} = C_{abs} + C_{sca} \approx C_{sca} \quad (2.9)$$

where  $C_{ext}$ ,  $C_{abs}$ , and  $C_{sca}$  are the extinction, absorption, and scattering cross sections, respectively. Cross sections are functions of wavelength. If absorption is low at the wavelength of interest, then any extinction is due mainly to scattering as suggested in Equation 2.9.

Accounting for surface reflection, absorption, and scattering, the fractional in-line transmission,  $\tau$ , through a material is expressed as:<sup>8</sup>

$$\tau = (1-R)^2 \exp(-C_{ext} \times t) \approx (1-R)^2 \exp(-C_{sca} \times t) \quad (2.10)$$

where t is the thickness of the material. The in-line transmission is the fraction of radiation beam energy that traverses the medium without being scattered, reflected, or absorbed. Increasing the scattering cross section results in a decreased in-line transmission.

**Scattering Theory** - An understanding of scattering, and how its effect can be increased to maximize infrared reflectance and, hopefully, reduce radiant thermal conductivity, is necessary to this effort. Scattering simply refers to the redirection of electromagnetic radiation. A beam of radiation striking a scattering medium will be redirected, or scattered, in all directions. Thus, a scattering ceramic will diffusely reflect and transmit radiation. In a ceramic, scattering may be caused by a second phase with an index of refraction different from the primary phase. For example, pores, having an index of refraction of approximately 1, in a matrix of alumina, with an index of 1.76, will scatter radiation. Deliberately adding a second phase to a ceramic to increase reflectance is termed "opacification".

Assuming spherical particles, the scattering cross section is equal to:

$$C_{sca} = \frac{3V_p K}{4r} \quad (2.11)$$

where  $V_p$  is the volume fraction of scattering phase,  $K$  is the scattering factor, and  $r$  is the radius of scattering particles.<sup>8</sup> The scattering factor,  $K$ , is related to the radius of scattering particles,  $r$ , the wavelength of radiation,  $\lambda$ , and the relative refractive index,  $m$ . The relative refractive index is equal to the refractive index of the scattering phase divided by that of the surrounding matrix, and may be less than or greater than one, but always positive. More positive values give higher scattering factors, and hence stronger scattering. Figure 4.1.1 shows the relationship between these factors. The horizontal axis of this graph is the phase function,  $P$ , given as:<sup>4</sup>

$$P = \frac{4\pi r(m-1)}{\lambda} \quad (2.12)$$

The scattering factor, and hence scattering cross section, is very dependent on particle size. Figure 4.1.2 shows the scattering cross section as a function of particle size for a system of 1.0 V/O titania particles in glass, at a wavelength of 0.589  $\mu\text{m}$ .<sup>7</sup> Only a very narrow range of particles produces a maximum scattering cross section. Since all of the curves in Figure 2.9 show maximums at a phase function of 4.1, Equation 2.12 can be rewritten as:

$$d_{\max} = \frac{4.1\lambda}{2\pi(m-1)} \quad (2.13)$$

where  $d_{\max}$  is the particle diameter producing a maximum in the scattering factor. This equation assumes spherical particles of a uniform size, and is a good estimate of the size of particles required to produce a maximum in the scattering cross section for a given volume fraction (the estimate is not exact, since the size of particles giving a maximum in the ratio  $K/r$  may be slightly smaller than those giving a maximum in  $K$  alone). For most systems, the diameter of particles producing a maximum in the scattering cross section is on the order of the wavelength of radiation.

In practice, producing a scattering system of monosized particles is difficult. Most particles, unless specially produced, will have a particle size distribution. For the scattering of thermal radiation, however, a distribution of particle diameters is desired, because there is a distribution of wavelengths to be scattered.

**Dependent Scattering** - A limit exists to the amount of scattering phase that is beneficial. Above a certain volume fraction, the electromagnetic fields surrounding

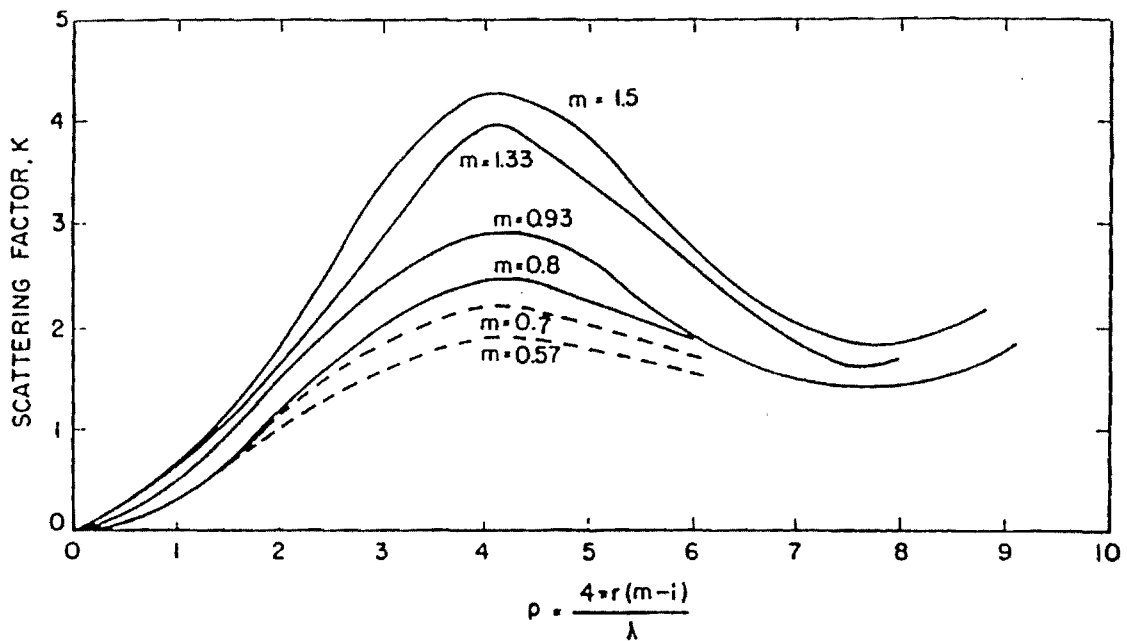


Figure 4.1.1

Scattering Factor,  $K$ , as a Function of Wavelength, Radius of Scattering Center, and Relative Refractive Index.

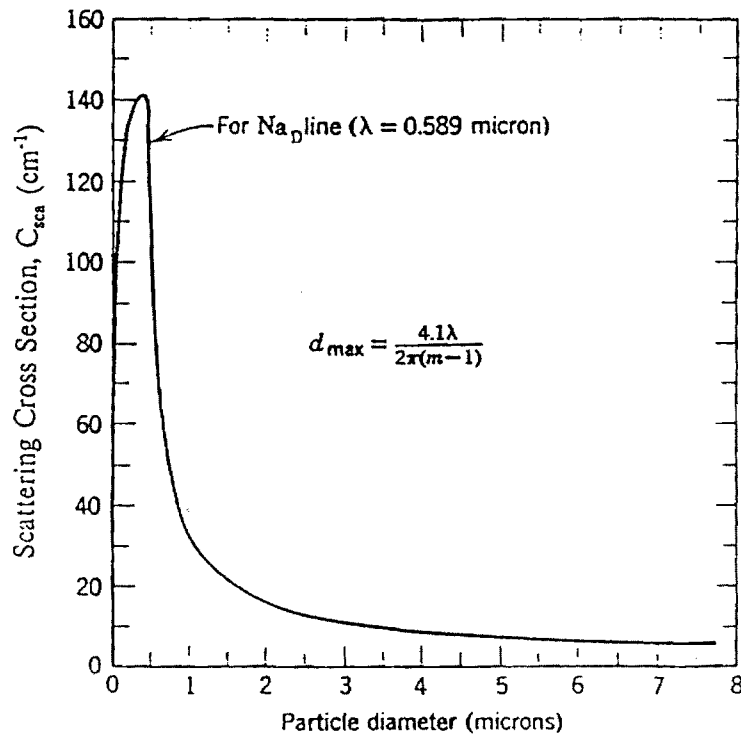


Figure 4.1.2

Effect of Particle Size on the Scattering Cross Section of a Fixed Volume of Particles (1.0 vol%) for a Relative Refractive Index of 1.8 ( $\text{TiO}_2$  in Glass).

individual scattering particles will begin to interfere because of their proximity, and the overall scattering factor will decrease. This interference is known as dependent, or multiple, scattering. The interparticle distance,  $c$ , at which individual particles cease to scatter independently is given by:<sup>11</sup>

$$\frac{c}{\lambda} = 0.3 \quad (2.16)$$

For a given wavelength, finer particles will encroach upon this limit at a lower volume fraction than coarse particles due to their greater number of particles per unit volume. This behavior is demonstrated in Figure 4.1.3<sup>11</sup>, where  $X$  is a measure of particle size called the size parameter, equal to:

$$X = \frac{2\pi r}{\lambda} \quad (2.17)$$

The area to the left of the curve represents particles far enough apart to scatter independently. Those particles close enough together to fall to the right of the curve will scatter dependently, and their scattering factors will be lower than if they had been sufficiently spaced apart. Equation 2.13 assumes independent scattering, a condition that limits its applicability to systems containing small amounts of scattering phases.

**Thermal Conductivity of Non-Opacified Hollow Spheres** - The thermal conductivity curves for two samples of thin-walled, hollow ceramic spheres made of alumina are compared in Figure 4.1.4.<sup>15</sup> Both sets of spheres were created in a like manner, the only difference being their bulk density. The general shape of these curves is typical of all hollow spheres, and the dramatic increase of thermal conductivity with temperature sharply contrasts with the behavior of solid (dense) polycrystalline aluminas. To understand this difference in thermal conductivity behavior, several factors must be recognized.

Hollow spheres, unlike bulk solids, possess a large volume of air both inside the spheres and in the interstices between spheres. Gas conductivity, therefore, contributes to the thermal conductivity of hollow spheres. However, the magnitude of the thermal conductivity due to air is in the range of 0.05 to 0.09 W/mK and is relatively low compared to the overall conductivity for hollow spheres. Although gas conductivity increases with temperature, the effect is minor and fails to explain the dramatic increase of thermal conductivity with temperature characteristic of hollow spheres.



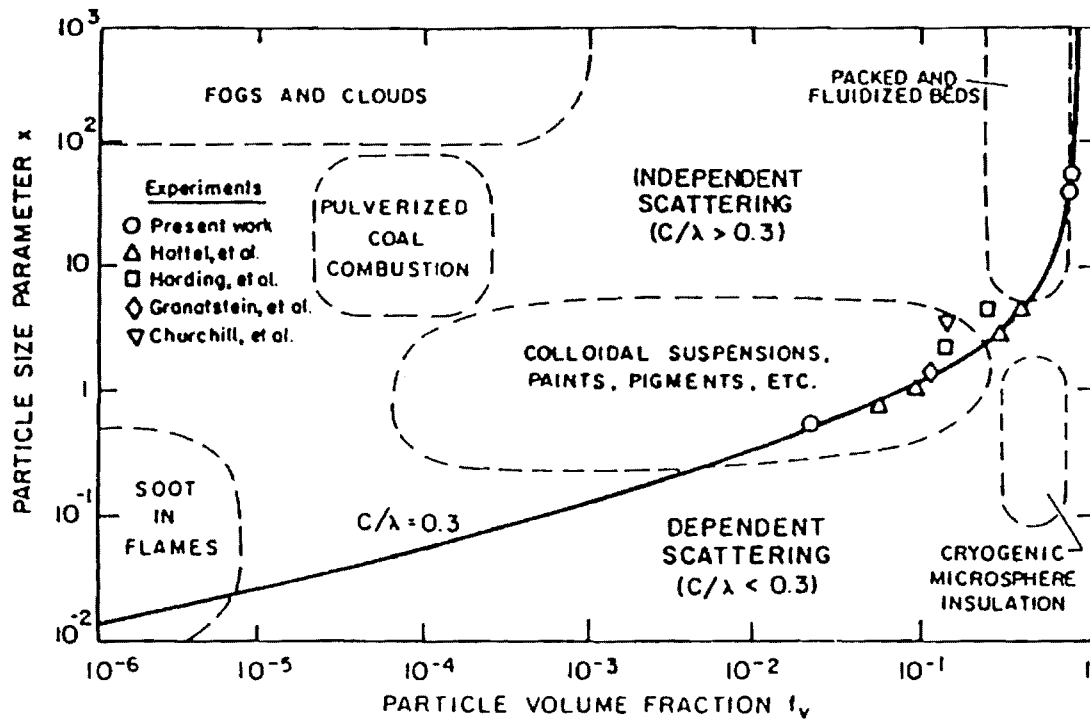


Figure 4.1.3 Independent and Dependent Scattering Regimes:  $x$  vs.  $F_v$

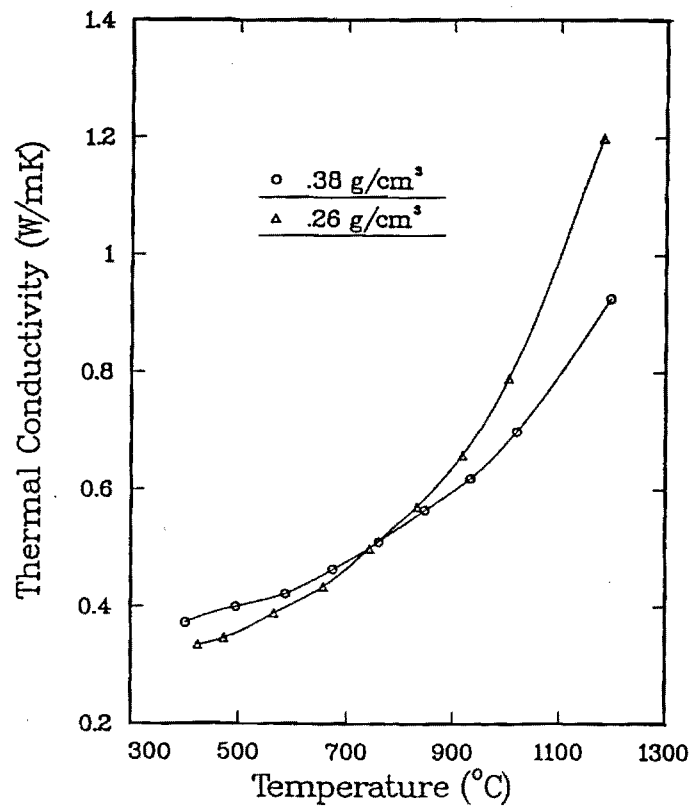


Figure 4.1.4 Thermal Conductivity of Alumina Hollow Spheres

The contribution of solid state conductivity to the total conductivity will be less for hollow spheres than for solid ceramics, since hollow spheres are less dense. The bulk densities of the alumina spheres in Figure 4.1.4 are 0.26 g/cc and 0.38 g/cc, while the density of solid alumina is 3.98 g/cc. As the amount of solid decreases, the solid state conductivity will decrease. The fact that the spheres are in contact with each other in a very limited fashion, at small, loose points of contact, also serves to limit the solid state conductivity. At high temperatures, the solid state conductivity of both crystals and glasses is relatively independent of temperature. Thus, like gas conductivity, solid state conductivity cannot explain the large increase of hollow sphere thermal conductivity with temperature.

The radiation conductivity for hollow spheres is much higher than for solid ceramics because of the lower amount of material present to scatter radiation. This radiation conductivity will increase dramatically with temperature, as predicted by the Rosseland approximation for radiant conductivity,  $k_r$ , which states the ability of a dielectric material to transmit radiation energy: <sup>4</sup>

$$k_r = \frac{16}{3} \sigma n^2 T^3 l_r \quad (2.5)$$

where  $\sigma$  is the Stefan-Boltzmann constant,  $n$  is the refractive index,  $T$  is the absolute (Kelvin) temperature, and  $l_r$  is the photon mean free path. This approximation applies when the mean free path is smaller than the sample thickness. Based on this temperature dependence, and armed with the knowledge that neither gas nor solid state conductivity explains the sharp increase of thermal conductivity with temperature of Figure 4.1.4, a reasonable assumption is that radiation transfer dominates the thermal conductivity of hollow spheres at high temperatures. Radiation conductivity explains the dramatic increase of thermal conductivity with temperature of hollow spheres.

Examining the thermal conductivity behavior of ceramic fibers lends credence to this interpretation. An analogy can be made between hollow spheres and ceramic fibers with respect to the fact that both have a continuous gas phase, a low solid volume to total volume ratio, and few and loose solid contacts. Air conductivity increases slightly with temperature, but is unaffected by changes in bulk density. Solid state conductivity through fibers increases slightly with bulk density, but seems unchanged by temperature fluctuations. The most significant change, with respect to both temperature and bulk density, is in the radiation component. The thermal conductivity due to radiation increases significantly with temperature, as predicted by the Rossland approximation. As the bulk density increases, this component decreases due to a larger quantity per unit volume of scattering material. Radiation transfer explains the majority of the increase of thermal conductivity with temperature of ceramic fibers and hollow spheres.

**Thermal Conductivity of Graphite Opacified Hollow Spheres** - Previous hollow sphere thermal conductivity research has suffered because the systems investigated have lacked an "ideal" scattering microstructure, i.e. one with discrete, separated scattering particles surrounded by a homogeneous matrix. Alumina and mullite hollow spheres, the emphasis of previous studies, are known to possess up to 30V/O of continuous porosity.<sup>16</sup> While this porosity certainly affects radiation transfer in some way, classical scattering theory is based on discrete particles and is useless for predicting this behavior.

Furlong<sup>15</sup> added particles of a second phase to alumina and mullite hollow spheres to scatter thermal radiation and decrease thermal conductivity. These second phases included chromia, silicon carbide, and zirconia. Also, graphite was added to some compositions as a "burn-out" material that would hopefully create, after firing, pores of a size suitable for scattering. Addition of graphite as a fugitive pore opacifier did significantly reduce conductivity at high temperatures. However, the graphite was flake like and produced flat pores 2-5 microns in diameter and 0.2-0.5 microns thick. These geometries do not fit the classical spherical geometries of scattering phases modeled in theory. As a result systematic changes with pore size and pore volume were not obtained.

Many of the comparisons made between the thermal conductivity of spheres with and without a second phase were inconclusive because bulk densities were not comparable. Additionally, analysis of the microstructure was limited to the viewing of fracture surfaces, and information regarding the size and separation distance of second phases, and the spatial relationship of these phases to the continuous porosity, could not be provided due to the difficulty of obtaining a flat polished surface from a microstructure of such high porosity.

#### **4.2 ZIRCONIA OPACIFICATION OF HOLLOW GLASS SPHERE WALLS**

A system was desired that would allow a closer comparison to classical scattering theory, one that would have minimal porosity. A glassy system for the sphere walls, one in which the raw materials are a clay and a feldspar, was chosen for two reasons. First, such a system undergoes liquid phase sintering and results in a microstructure with only a few large, separated pores. Thus the effect of porosity on radiation scattering can be assumed negligible. Secondly, this glass composition vitrifies at temperatures below which many second phase materials will begin to coarsen. During sintering, in a system of dispersed second phase particles, smaller particles may dissolve while larger particles may grow in size. This process is driven by the reduction of interfacial free energy, and is termed Ostwald ripening.<sup>7</sup> Thus, particles may coarsen and become too large to effectively scatter radiation. Such coarsening would also make unreliable any interpretation of results based on the measured particle size distributions of the zirconia powders, since these distributions

would change. Whether or not such coarsening was a problem in previous hollow sphere thermal conductivity research is unknown. Zirconia was chosen as the second phase to provide infrared scattering. This material has an index of refraction significantly higher than glass, and was readily available in the size ranges desired. Additionally, zirconia particles were expected to be stable at the sintering temperature of the glass system, a temperature of 1200°C.

To demonstrate the relationship between diffuse infrared reflectance and thermal conductivity, a model system based on zirconia particles dispersed in a glass matrix was developed. To initiate the system, the approximate zirconia size required for optimal infrared scattering was calculated. This calculation is presented first in this section. Then, specifications of the raw materials used to fabricate this system are followed by physical properties of the fabricated spheres. Next, the instruments and procedures used for measuring thermal conductivity and infrared reflectance are described. Finally, microstructural and phase analysis techniques are specified.

**Scattering Calculations** - Selection of zirconia powders for infrared opacification was based on a calculation of the approximate particle size required to produce maximum scattering in a glass matrix. The particle size calculation required specification of an exact radiation wavelength. This was based on a maximum thermal conductivity measurement temperature of approximately 1000°C for the glass spheres. Above this temperature, the spheres stick together and their removal from the thermal conductivity apparatus becomes difficult. Thus, a reasonable approach was to reduce radiation conductivity where it was most significant, and since radiation conductivity increases with temperature, the upper limit of 1000°C was chosen as the temperature where a maximum in thermal radiation scattering was to be produced.

Wavelength maximums were calculated for both a vacuum and glass as a function of temperature using Wein's Law, Equation 2.6. These calculations recognize that the wavelength of radiation entering the glass will be divided by a number equal to the index of refraction of the glass. The index of refraction of the glass was assumed to be 1.54.<sup>16</sup> At 1000°C, the maximum in the wavelength distribution of thermal radiation in the glass occurs at a wavelength of 1.48  $\mu\text{m}$ . Assuming that the index of refraction for zirconia is 2.17<sup>18</sup>, then the relative refractive index,  $m$ , is 1.41. From Equation 2.13, the zirconia particle size producing the largest scattering factor for these parameters has a diameter of 2.36  $\mu\text{m}$ .

There is some uncertainty in the values of refractive index. The indices for glass and zirconia are for visible wavelengths at room temperature. These values will certainly change somewhat at higher temperatures and longer wavelengths. Additionally, the value for zirconia is based on the monoclinic, or room temperature, form, and is the average of the index of refraction in the three crystalline directions. One of the zirconia powders was yttria stabilized, and likely possessed a different crystalline form (and somewhat different index of refraction) than the monoclinic phase. However, given the uncertainty of Equation 2.13 in accurately predicting the particle size

suitable for maximum reflectance, little purpose was seen in pursuing highly accurate refractive index values.

**Raw Materials and Sphere Fabrication** - Three different zirconia powders were used to gauge the effect of particle size on thermal conductivity and reflectance. These powders will be referred to as DK1, DK3CL, and RDF 371, and their particle size distributions are compared in Figure 4.2.1. DK3CL is the coarsest distribution, and RDF 371 is the finest. These powders were chosen because the particle size calculated in Section 3.1,  $2.36\mu\text{m}$ , lies within their distributions. Particle size analysis was performed with a Microtrac II Model 7997-20 SPA.

Feldspar (nepheline syenite) and clay (Georgia kaolin) were combined to provide the glass matrix in all sphere compositions, in a weight ratio of three to one. Varying amounts of the three zirconia powders were added to this standard feldspar/clay composition. Because thermal conductivity measurements were taken concurrently with sphere fabrication, the creation of spheres with increasing zirconia contents was halted when little additional effect was expected. This upper limit occurred at 20V/O zirconia.

All compositions were ball milled for approximately eighteen hours prior to hollow sphere fabrication. An attempt was made to fabricate all spheres with the same bulk density, to avoid the density effect on thermal conductivity. All compositions were fired to  $1200^{\circ}\text{C}$  for three hours in large alumina saggars. Spheres were packed in - 100 mesh tabular alumina to prevent sphere to sphere sticking. After cooling, the spheres were separated from the tabular alumina by screening.

The bulk densities and diameters of the spheres are recorded in Table 4.2.1. Bulk densities were based on three measurements with a one liter graduated cylinder. Spheres were poured into the cylinder without tapping, and their weight was divided by the volume. The diameter values were the average of six micrometer measurements. The bulk density and sphere diameter measurements are considered accurate to within  $.02\text{ g/cm}^3$  and  $.15\text{mm}$ , respectively ( $\pm$  two standard deviations).

**Thermal Conductivity Measurements** - Thermal conductivities were measured with a Unitherm Radial Thermal Conductivity Apparatus, Model 4141, manufactured by Anter Laboratories, Inc., of Pittsburgh, Pennsylvania. This device consists of a hollow ceramic cylinder (10cm inner diameter  $\times$  40cm length) surrounding a central axis heater. Three pairs of thermocouples lie in the gap between heater and cylinder at  $120^{\circ}$  intervals, and measure the temperature difference over a 3.0cm gap spanning the radius of the cylinder. Loose packed beds of spheres were introduced into the cylindrical cavity, without tapping, and thermal conductivities were calculated from heater power and the resulting temperature gradients. The theory of operation governing this apparatus has been discussed extensively elsewhere.<sup>15,17</sup>

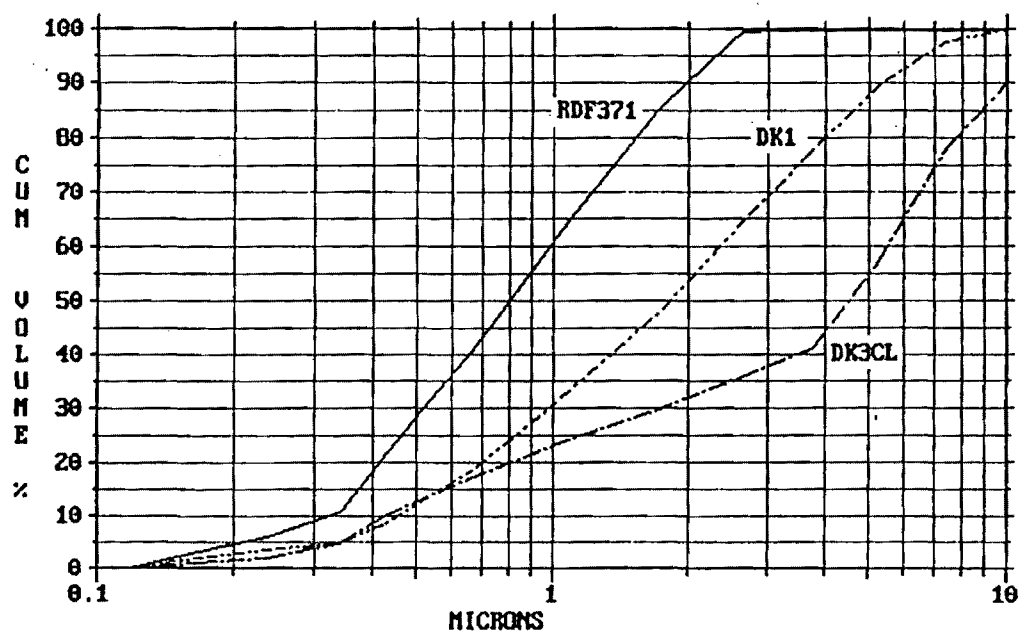


Figure 4.2.1 Combined Particle Size Distributions of RDF 371, DK1, and DK3CL Zirconia Powders.

Table 4.2.1      Diameters and Bulk Densities of Hollow Spheres.

Volume Percent Zirconia (%)	Bulk Density (g/cm <sup>3</sup> )	Diameter (mm)
<b>No Zirconia</b>		
0.00	.46	2.4
<b>RDF 371</b>		
2.50	.47	3.0
5.00	.45	2.9
10.00	.44	2.4
15.00	.42	3.3
<b>DK1</b>		
2.50	.47	2.7
5.00	.50	3.3
7.50	.49	2.9
10.00	.51	2.8
15.00	.56	2.6
20.00	.54	2.5
<b>DK3CL</b>		
2.50	.46	3.0
5.00	.46	2.8
10.0	.51	2.7
15.0	.44	3.3
20.0	.45	3.3

The Unitherm apparatus at Georgia Tech yields data that is somewhat higher than values measured at other locales for the same materials. Figure 4.2.2 compares the manufacturer's specifications and thermal conductivity values measured with the Anter 4141 apparatus for K-23 and K-30 firebrick produced by Thermal Ceramics of Augusta, Georgia. The Anter 4141 readings were higher for both materials. Thermal conductivities measurements of the same sample of hollow alumina spheres from Georgia Tech and the University of Kentucky also indicate that the Anter 4141 values are higher, Figure 4.2.3. Additional materials are being compared to establish a calibration curve. Roughly, conductivities in the range of 0.2 W/mK appear to be approximately 20% high as measured by the Anter 4141 and actual values in the 1.0 to 1.2 W/mK range will measure 80% to 100% too high.

For the purpose of this work, reproducibility was more important than accuracy. Furlong<sup>15</sup> twice measured the thermal conductivity of alumina hollow spheres with the Unitherm apparatus, emptying and reloading the machine between runs. He found the readings to agree within  $\pm 0.01$  W/mK. Ford<sup>17</sup> followed the same procedure for a solid ceramic monolith, and the values agreed within  $\pm 0.015$  W/mK. The Georgia Tech Unitherm 4141 apparatus appears to provide thermal conductivity measurements that are high but reproducible. Therefore, specific thermal conductivity readings should be ignored in favor of relative values and trends.

**Infrared Reflectance Measurements** - Infrared reflectance measurements were made with a Perkin-Elmer diffuse reflectance (PEDR) accessory, housed in a Perkin-Elmer Series 1600 FTIR spectrometer. A diagram of the PEDR accessory is shown in Figure 3.5.<sup>19</sup> The infrared beam enters the PEDR from the left and is reflected by five flat mirrors. The ellipsoidal reflector serves both to focus the beam onto the sample, and to collect the reflected radiation. The reflector collects radiation over a solid angle of  $\pi$  steradians.

Because of the small sample thickness, reflectance of hollow spheres could not be measured in the PEDR accessory. The sphere walls are thin enough to allow beam penetration and subsequent interaction with the sample holder. Additionally, since spheres have a curved surface, the direction of specular reflectance would change with sphere orientation and produce erroneous results. To avoid these problems, it was necessary to fabricate solid conical samples having the same microstructures as the hollow spheres. To this end, molds in the shape of the sample holder were manufactured. Slurries containing a 3 to 1 feldspar to clay weight ratio and varying zirconia content were wet milled to adequately mix the powders, and poured onto a flat piece of glass to facilitate rapid drying. The mixed powders were combined with a small amount of water to produce thick pastes, and pressed into the molds and allowed to dry. A thick paste was desired because zirconia is more dense than the feldspar or clay, and settling may have occurred if the original fluid slurry had been used. Five samples were fabricated of each composition.



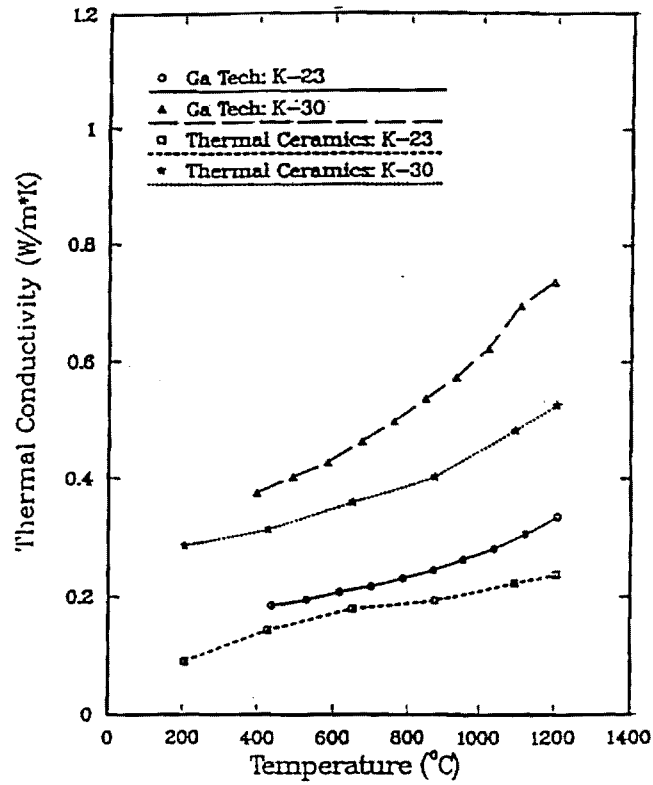


Figure 4.2.2

Comparison Between Georgia Tech Thermal Conductivity Measurements and Manufacturer's Specifications for K-23 and K-30 Firebrick.

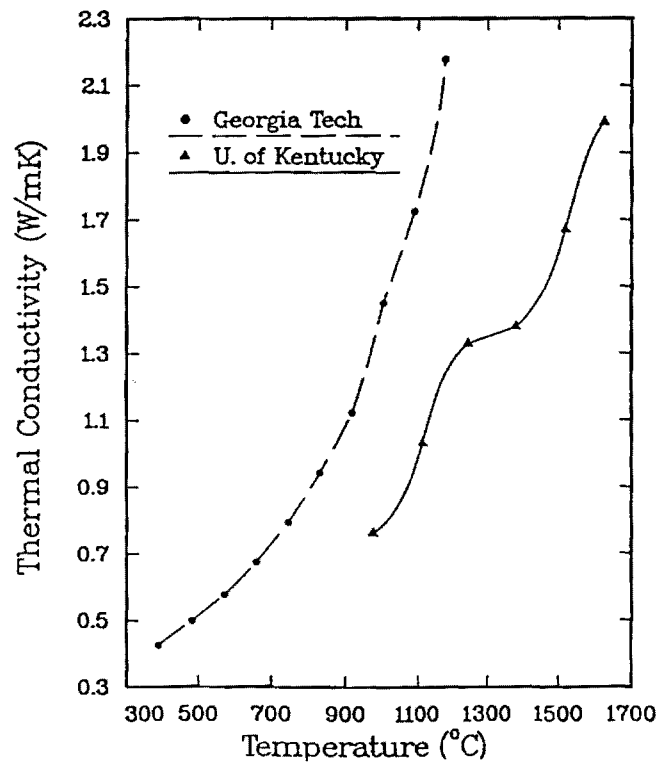


Figure 4.2.3

Thermal Conductivity of Alumina Hollow Spheres Measured at Georgia Tech and the University of Kentucky.

The solid spectrometer samples, like the spheres, were fired to 1200°C for 3 hours. The upper surfaces of the fired samples, those which would face the infrared beam, were uneven and rough. To prevent errors due to the surface texture variability, all upper surfaces were ground and polished with 180, 320, 600, and 1200 grit silicon carbide paper. The spectrometer samples had an upper surface diameter and thickness of approximately 9.3 and 2.7 mm, respectively, and filled a majority of the volume of the sample holder. One infrared scan was performed on each sample, producing five scans for each composition. The scans performed were ratio scans, meaning that they were taken relative to a standard. The standard was chosen as the glass/zirconia composition showing the highest infrared reflectance, so that all other compositions would be less than 100%. The sample containing 21.74V/O DK1 had the highest reflectance and was used as the standard. Infrared reflectance is shown for the three zirconias in Figure 4.2.4

**Thermal Conductivity Results** - All three zirconia powders significantly reduced the high temperature thermal conductivity of glass spheres, Figures 4.2.5-4.2.8. Conductivities at 1000C plotted as a function of zirconia content show the dramatic effect at high temperatures, Figures 4.2.9-4.2.10. Small amounts of zirconia reduced thermal conductivity dramatically, but additions in excess of approximately ten volume percent caused little change. In fact, RDF 371 glass spheres showed an increase in thermal conductivity as the zirconia content was raised from ten to fifteen volume percent.

#### 4.3 THERMAL CONDUCTIVITY AND INFRARED REFLECTANCE

The reflectance graphs, if turned upside down, are similar in shape to the graphs of thermal conductivity and  $\alpha$  coefficient vs. volume percent zirconia. This resemblance is especially true for the DK1 and DK3CL curves, and implies that a relationship may exist. Figures 4.3.1 AND 4.3.2 show the thermal conductivity at 1000°C versus reflectance for the DK1, DK3CL, and RDF 371 glass/zirconia systems. Since many of the spectrometer samples did not possess a zirconia fraction that corresponded exactly to that of the spheres, the raw data could not be compared directly. The data points shown, therefore, are from the best fit curves at various zirconia contents. The best fit straight lines, obtained using linear regression, are plotted together in Figure 4.3.2. All three compositions show a reasonably linear relationship. The best fit lines for the DK1 and DK3CL compositions are closely positioned to each other. The RDF 371 data yields a best fit line positioned lower on the graph.

The most interesting feature of the thermal conductivity vs. zirconia percent graphs is the upturn of the RDF 371 curve as the zirconia content is raised from 10V/O to 15V/O. Assuming that the thermal conductivity is related to reflectance, this upturn could be due to dependent scattering. This curve appears opposite in behavior to the curves in Figure 2.13, in which reflectance actually decreases above a certain volume

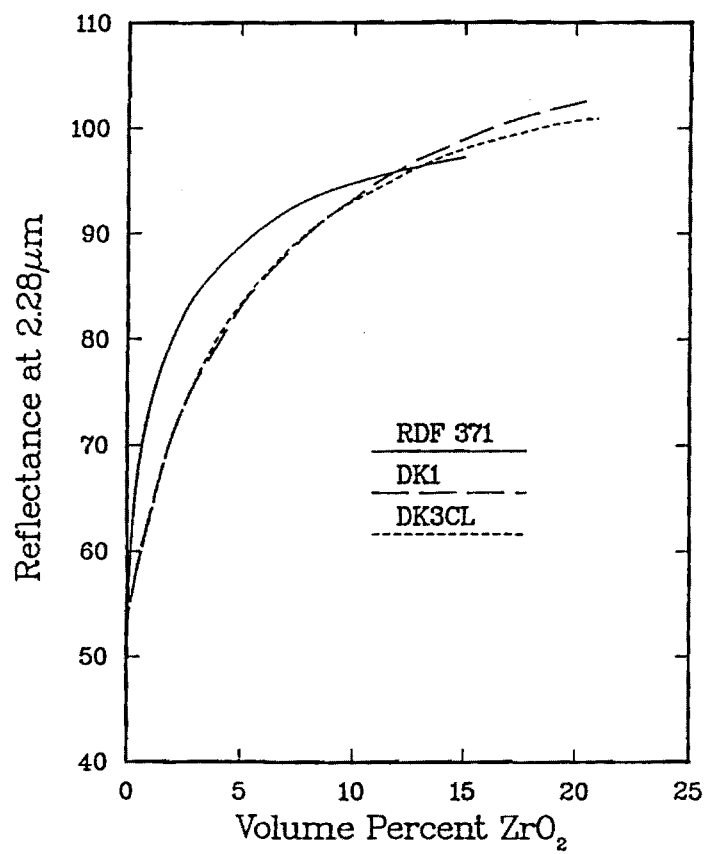


Figure 4.2.4

Combined Reflectance of DK1, DK3CL, and RDF371 Opacified Glass Spectrometer Samples Vs. Zirconia Volume Percent.

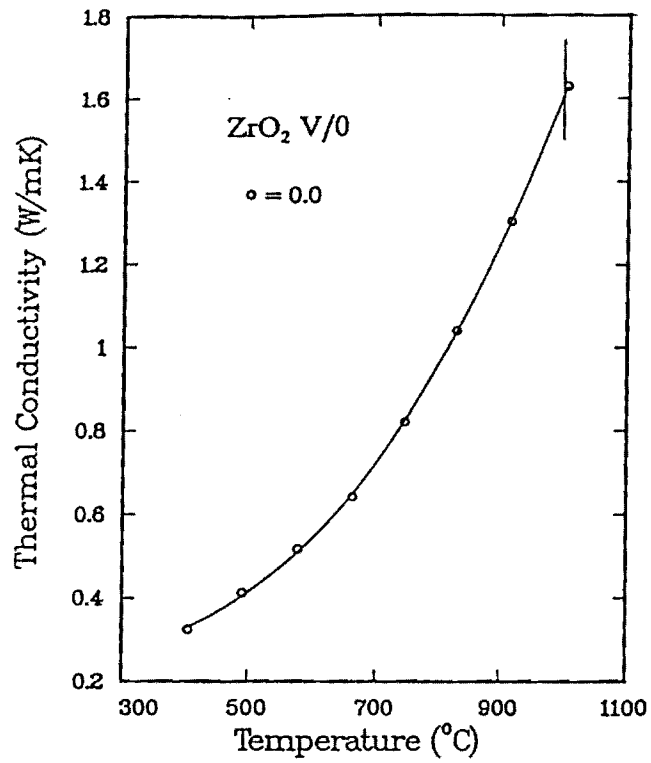


Figure 4.2.5 Thermal Conductivity of Unopacified Glass Spheres Vs. Temperature.

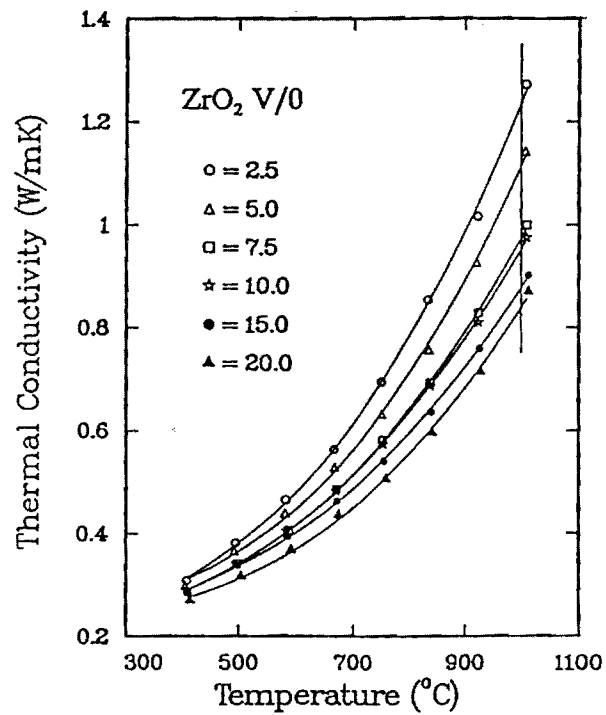


Figure 4.2.6 Thermal Conductivity of DK1 Opacified Glass Spheres Vs. Temperature.

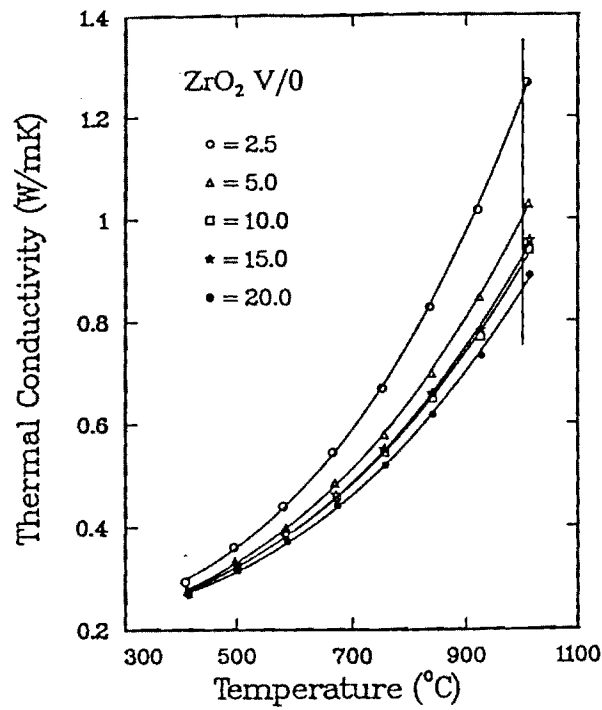


Figure 4.2.7 Thermal Conductivity of DK3CL Opacified Glass Spheres Vs. Temperature.

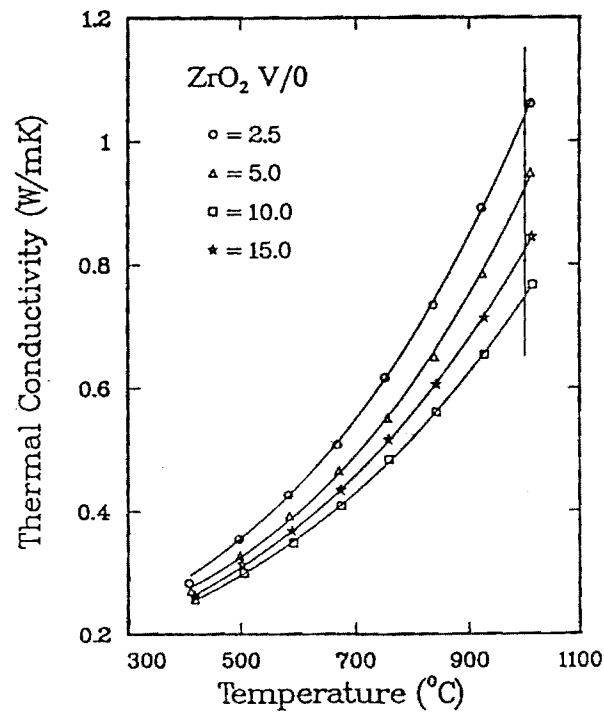


Figure 4.2.8 Thermal Conductivity of RDF 371 Opacified Glass Spheres Vs. Temperature.

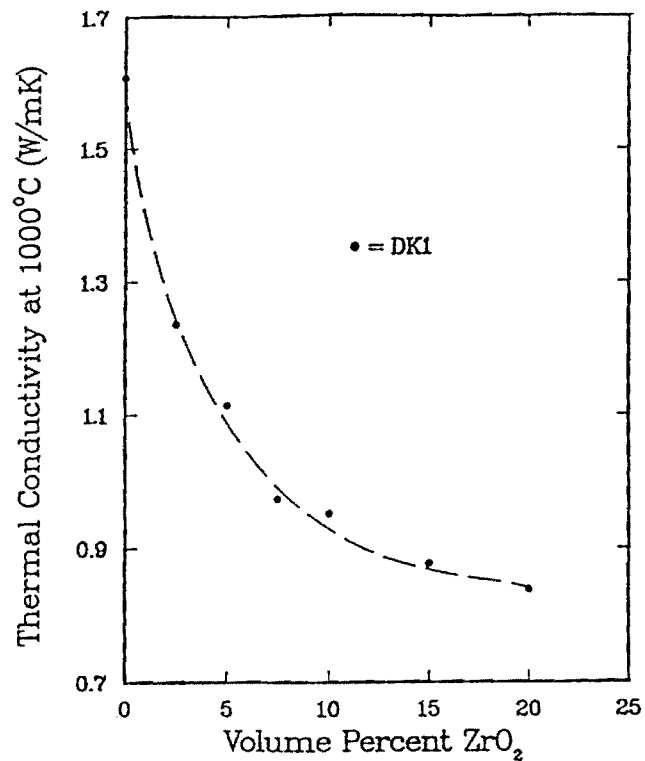


Figure 4.2.9 Thermal Conductivity of DK1 Opacified Glass Spheres Vs. Zirconia Volume Percent, at 1000°C.

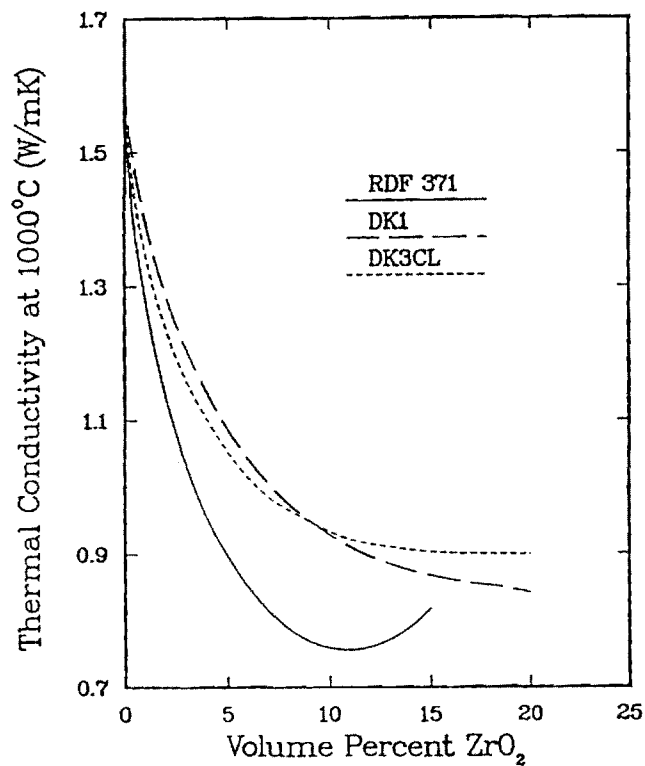


Figure 4.2.10 Combined Thermal Conductivity of DK1, DK3CL, and RDF 371 Opacified Glass Spheres VS. Zirconia Volume Percent, at 1000°C.

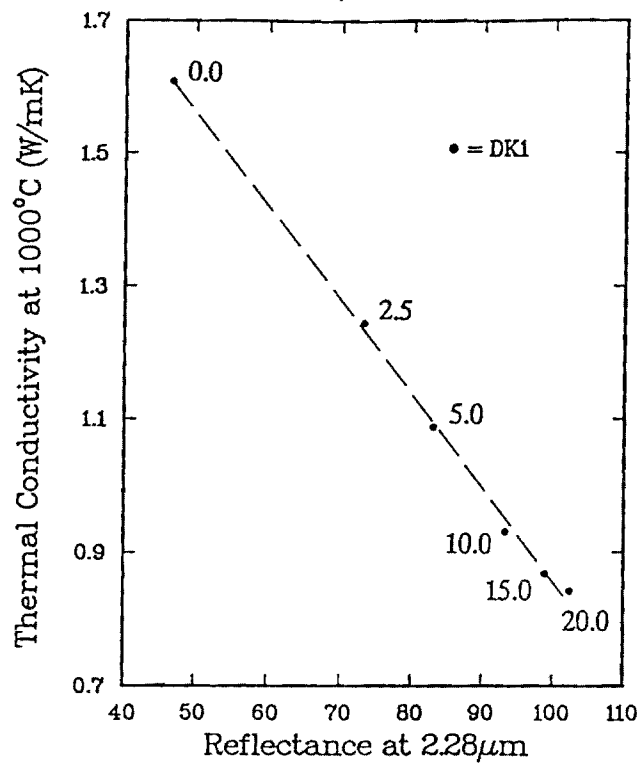


Figure 4.3.1

Thermal Conductivity at 1000°C Vs. Reflectance for DK1 Opacified Glass.

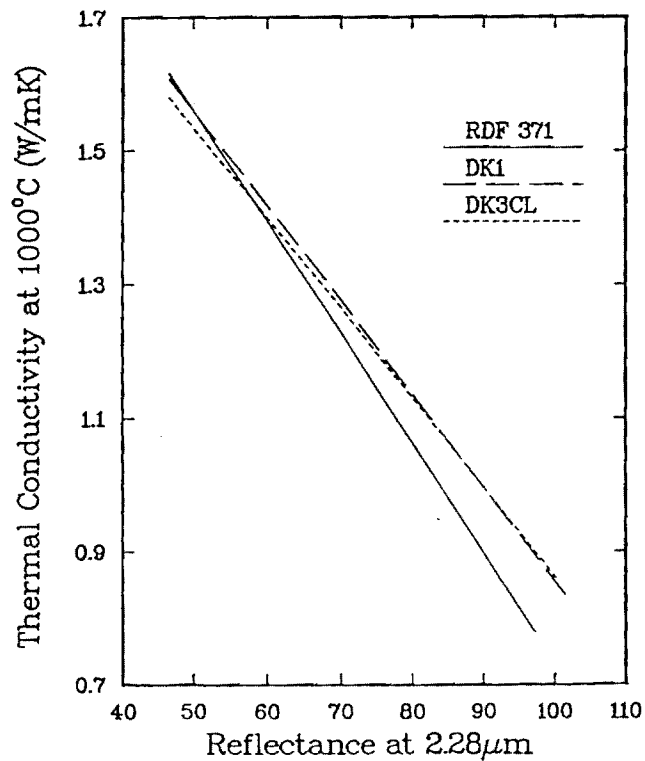


Figure 4.3.2

Thermal Conductivity at 1000°C Vs. Reflectance for DK1, DK3CL, and RDF 371 Opacified Glass.

content. However, the reflectance curve for RDF 371 does not show a downturn at similar volume fractions of zirconia, raising doubts about this interpretation.

The effect of zirconia particle size on thermal conductivity was difficult to assess. The DK1 and DK3CL curves are nearly identical, and demonstrate no observable particle size effect. The finer RDF 371 distribution did show lower thermal conductivities. However, unlike reflectance, where a particle size effect seemed evident because the results matched so closely to theory and to a similar previous study, the variation in thermal conductivity is not as easily explained by a particle size difference. At low volume percentages, the RDF 371 curve does drop more quickly with zirconia content than either DK1 or DK3CL, similar to the large change associated with the RDF 371 reflectance curve. However, unlike the reflectance curve, the RDF 371 thermal conductivity curve does not cross back over the DK1 and DK3CL curves. The effect of particle size on thermal conductivity is inconclusive.

**Model** - There appears to be a linear relationship between the thermal conductivity, measured at 1000°C, and the reflectance at 2.28μm (also between the c coefficient and reflectance). Based on this observed behavior, the following model is proposed. If there is no absorption, then the energy,  $I_o$ , of a beam passing through a scattering solid is given by:

$$I_o = R_H + \tau_H \quad (5.1)$$

$R_H$  is the hemispherical reflectance, composed of surface reflection and radiation scattered greater than 90°.  $\tau_H$  is the hemispherical reflectance, composed of unscattered in-line transmission and radiation scattered less than 90°. This equation is rewritten as:

$$\tau_H = I_o - R_H \quad (5.2)$$

At this point, the amount of radiation passing through the solid,  $\tau_H$ , is assumed to be proportional to the heat transfer per unit time,  $H$ , from Equation 2.1 (and, therefore, the thermal conductivity  $k$ ):

$$\tau_H \propto H \propto k \quad (5.3)$$

Substituting  $k$  for  $\tau_H$ :



$$k \propto I_o - R_H \quad (5.4)$$

and introducing the constants A and B:

$$k = A - BR_H \quad (5.5)$$

This equation is suitable for this data if one more assumption is made. The reflectance acquired with the PEDR accessory is assumed to be proportional to the hemispherical reflectance,  $R_H$ , even though it is taken over a smaller angular range:

$$k = A - BR_{PEDR} \quad (5.6)$$

Equation 5.6 is in the form of a straight line, and fits the graphs of thermal conductivity vs. reflectance well. The thermal conductivity term in Equation 5.6 may be replaced with the coefficient c. This equation assumes that the reflectance is read at a wavelength corresponding to the thermal conductivity temperature, as expressed by Equation 2.6.

The linear regression data fitting Equation 5.6, is plotted as the straight lines in Figure 4.3.2. All compositions agree well with the linear model. Based on its lack of similarity between hollow sphere and spectrometer sample microstructures, one may have expected the DK3CL system to show a significant deviation from this linear model, but this is not the case. The linear regression lines for DK1 and DK3CL are nearly identical in slope and position, while that of RDF 371 is lower on the graphs of both 1000°C thermal conductivity and c coefficient vs. reflectance. This variance in position may be explained by absorption, an effect that was assumed negligible. Some absorption will exist due to the presence of zirconia, and its magnitude will be a function the zirconia's exact chemical identity. DK1 and DK3CL are manufactured by the same company, and are unstabilized. RDF 371 is stabilized with yttria. Yttria may alter the overall absorption of the system, and change the exact relationship of thermal conductivity to reflectance.

The addition of zirconia significantly affects both the infrared reflectance and thermal conductivity of hollow glass spheres. Additions of zirconia increase the reflectance and decrease the thermal conductivity of glassy spheres by more than a factor of two. At low zirconia loading, the reflectance increases in a nearly linear fashion with zirconia content, as predicted by scattering theory. Reflectance levels off at higher zirconia volumes because of dependent scattering. Plots of thermal conductivity vs.

reflectance show a linear relationship, for which there is a theoretically reasonable, if somewhat simplified, model available.

The zirconia size affects infrared reflectance, but to a small degree. A significant difference in thermal conductivity present between one size distribution and two others may or may not be due to a particle size effect. In retrospect, although three different sized distributions were tested, they all shared the same range of particles. Based on these conclusions, the following recommendations are made:

1. In order to see any effects of particle size on reflectance and thermal conductivity, the zirconia size distributions should be narrower and more widely separated from each other.
2. The PEDR accessory should be used to examine the reflectance of compositions, such as mullite and alumina, that are more viable high temperature insulators. The size, volume percent, and distribution of pores in these two materials may significantly affect infrared reflectance, and much can be done to alter these parameters.

## REFERENCES

1. Halliday, D., and Resnick, R., Fundamentals of Physics, John Wiley & Sons, New York, p. 390, 1986.
2. Horie, E., Ceramic Fiber Insulation Theory and Practice, The Energy Conservation Center, Tokyo, Japan, Eibun Press Ltd., pp. 26-31, 1986.
3. Wawryk, R., and Rafalowicz, J., "Heat Transfer in Microsphere Insulation," Journal of Thermal Analysis, vol. 34, pp. 249-250, 1988.
4. Lee, D. W., and Kingery, W.D., "Radiation Energy Transfer and Thermal Conductivity of Ceramic Oxides," Journal of the American Ceramic Society, vol. 43, pp. 594-607, 1960.
5. Reed, R. J., North American Combustion Handbook, Volume I, 3rd Edition, North American Mfg. Co., Cleveland, Ohio, pp. 234-236, 1986.
6. McElroy, D. L., and Fulkerson, W., Techniques of Materials Preparation and Handling - Temperature Measurement and Control, John Wiley @ Sons, New York, p. 208, 1968.
7. Kingery, W. D., Bowen, H. K., and Uhlmann, D. R., Introduction to Ceramics, 2nd Edition, John Wiley & Sons, New York, 1976.
8. Peelen, J. G. J., and Metselaar, R., "Light Scattering by Pores in Polycrystalline

- Materials: Transmission Properties of Alumina," Journal of Applied Physics, vol. 45, no. 1, pp. 216-220, 1974.
9. Schmidt, R. N., Trevenfels, P. M., and Meehan, E. J., "Application of Mie Scatter Theory to the Reflectance of Paint-Type Coatings," Proceedings of the Symposium on Thermophysical Properties, 4th Edition, pp. 256-259, 1968.
  10. Hottel, H. C., Sarofim, A. F., Dalzell, W.H., and Vasalos, I. A., "Optical Properties of Coatings. Effect of Pigment Concentration," AIAA Journal, vol. 9, no. 10, pp. 1895-1898, October 1971.
  11. Brewster, M. Q., and Tien, C. L., "Radiative Transfer in Packed Fluidized Beds: Dependent Versus Independent Scattering," Journal of Heat Transfer, vol. 104, pp. 573-579, 1982.
  12. Peelen, J. G. J., "Light Transmission of Sintered Alumina," Philips Tech. Rev., vol. 36, no. 2, pp. 47-52, 1976.
  13. Makino, T., Kunitomo, T., Sakai, I., and Kinoshita, H., "Thermal Radiation Properties of Ceramic Materials," Heat Transfer - Jpn. Res. (USA), vol. 13, no. 4, pp. 33-50, October 1984.
  14. Torobin, L. B., U.S. Patent 4,671,909, 1987.
  15. Furlong, S. D., "Reduction of Radiative Thermal Conductivity in Thin-Wall Hollow Ceramic Spheres Using Scattering Phases," M.S. Thesis, Georgia Institute of Technology, Atlanta, GA, 1990.
  16. Cochran, J. K., Personal Conversation, Georgia Institute of Technology, February 1992.
  17. Ford, T. R., "Thermal Conductivity of Bonded Hollow Sphere Monoliths," M.S. Thesis, Georgia Institute of Technology, Atlanta, GA, 1991.
  18. Lide, D. R., CRC Handbook of Chemistry and Physics, 71st Edition, CRC Press, p. 4-118, 1990.
  19. "Perkin-Elmer Diffuse Reflectance Accessory Instructions," the Perkin Elmer Corporation, 1990.
  20. Shapiro, J. S., "An Experimental Investigation of the Thermal Conductivity of Thin-Wall Hollow Ceramic Spheres," M.S. Thesis, Georgia Institute of Technology, Atlanta, GA, 1988.

## 5.0 TECHNOLOGY TRANSFER

### 5.1 ADVISORY MEETING AND INDUSTRIAL VISITS

A major task of this program was to provide transfer of hollow sphere technology covering fabrication, properties of spheres and foams, and potential applications. To facilitate this process, Dr. Carl Vander Linden, Littleton, CO, agreed to serve as a "Technology Transfer Coordinator" and as a result of his efforts, an extensive number of visits and subsequent interactions resulted, many of which are continuing to this date. Technology transfer was initiated by organizing a planning committee meeting in Atlanta, GA. In the fall of 1989, personnel from industry, universities, and government met to review the hollow-sphere technology with the goal of commercializing this technology. In general, this group identified potential application areas and thought it appropriate to inform industry about the spheres at trade shows and through individual visits, rather than by trying to attract a large audience through a formal technology transfer conference. It was thought that by meeting with individual companies, the exchanges would be much more open and applications would be discussed more freely compared to an open conference where competitors at the same table would not want to exchange their application ideas.

The dissemination of sphere technology and property information to the industrial community was initiated in January 1990. Dr. Carl Vander Linden arranged most of the visits and Drs. Cochran and Vander Linden made 45 presentations to the 39 organizations listed below. These visits covered the time period 1991 and 1992. Multiple visits were made to Alcoa, Carborundum, and Thermal Ceramics. Extensive trip reports have been prepared by Dr. Vander Linden and an example of one to Rohr Industries is provided below for information. A typical visit would consist of a background presentation by Dr. Vander Linden for 10-15 minutes followed by a technical presentation by Dr. Cochran of 1-1.5 hours which included examples of many sphere compositions and point contact bonded foams.

As a result of these visits, many new applications have been uncovered where a unique property of the spheres provides a refractory product not previously available. Three examples follow: (a) the interest in the basic magnesia or spinal sphere is continually expressed and spheres of these compositions have been prepared at Georgia Tech, (b) during a visit to a major oil company, the need for a refractory to withstand the very corrosive atmospheres (containing fluorine and chlorine gases) present in hazardous waste incinerators used in most petrochemical plants was identified, and samples have been provided for testing by the interested company, and © the industry sponsored, Gas Research Institute, stated the need for a flat burner plate to spread heat uniformly over wide areas for drying. The capability to produce low expansion refractory ceramic spheres along with the uniform channels between

the monosized spheres suggested bonded-sphere plates may provide a superior product for this application, and samples have been fabricated for testing. These samples were provided to a GRI sponsored company and they performed well as radiant gas burner plates. This is an extreme thermal shock condition and suggests that bonded aerosphere monoliths have excellent thermal shock resistance.

Technology transfer trips continued into a second year under the direction of Dr. Carl Vander Linden and these visits created many subsequent interactions particularly with Rohr Industries and Hi Temp Corporation. In addition, a trade show booth at the American Ceramic Society Exposition in Cincinnati in May, 1991 and May, 1992 sponsored by Ceramic Fillers Inc. demonstrated Aerosphere™ (trade name for hollow spheres manufactured by the coaxial nozzle process) technology and generated considerable industrial interest.

As a result of these technology transfer contacts and the success that mullite radiant burner tiles have demonstrated under severe thermal shock conditions, the Gas Research Institute has funded two projects (one for one year and one for two years) to develop high emissivity radiant burner tiles based on the mullite point contact bonded hollow sphere foams as diffuser base flame arrestors. Another aerosphere monolithic insulation application is induction furnace insulation at the Y-12 plant where two design iterations have resulted in fabrication of a mullite tube 70 inches tall, 27 inches in diameter and a wall thickness of 1.5 inches, Figure 5.1.1. This tube was fabricated in four nesting parts with each section being 18 inches tall. Tolerances of 0.4 % were met in these near net shapes. In addition, insulation plates at Hi Temp Corporation and alumina aerosphere boards at Lawrence Livermore Laboratory have been supplied. The continued, growing interest in this technology by American industry is the best measure available for the success of the overall program. It should be noted that as a result of this program, 300,000 pounds of spheres are being manufactured annually for incorporation into syntactic foams where the polymer matrix is also foamed. These foams are being used as energy absorbing components for passenger protection in 6-8 different automobiles.

## **5.2 TECHNOLOGY TRANSFER TRIP REPORT**

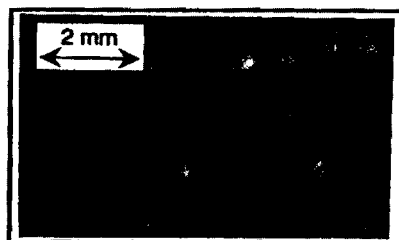
### **Hollow Sphere Technology Transfer with Rohr Industries in Chula Vista, CA (Prepared by Dr. Carl Vander Linden)**

Joe Cochran and I met with the following people from Rohr Industries at their Chula Vista headquarters on April 8, 1991. Their address is:

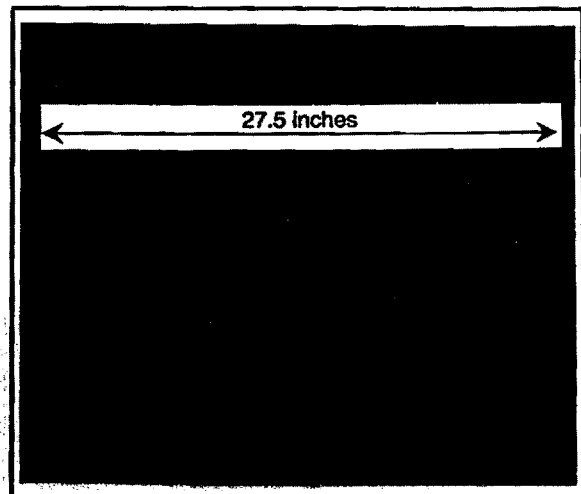
Rohr Industries, Inc.

## STRUCTURAL INSULATION from AEROSPHERE FOAMS

➤ Hollow Ceramic Spheres



➤ Furnace Insulation for Y-12 Plant



➤ Point Contact Bonded  
Hollow Sphere Foams

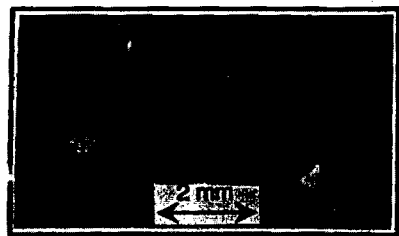


Figure 5.1.1 Point-Contact-Bonded, Hollow-Sphere, Mullite, Structural Insulation for Induction Furnace at Y-12 Plant.

Foot of H Street  
P.O. Box 878  
Chula Vista, CA 92012-0878

Dr. Brian Morris had arranged the meeting.

Dr. Brian Morris	Eng. Staff Specialist R & D Metals	619-691-3646
Frank Gojny	Deputy Project Mgr. R & D Metals	619-691-6465
Uwe Bockenhauer	Director of R & D	619-691-2516
Bruce Spivack	Eng.. Specialist Refractory Composites Carbon-carbon & Ceramics	619-691-3771
Paul Leholm	Sr. Research Eng.. Metals	619-691-3952
Rafael Castrejon	Research Eng.. Metals & Metallic Composites	619-691-2743
Herb Nagler	Eng.. Specialist	619-691-2354
Woody Wongwiwat	Eng.. Specialist	619-691-4227
Paul Lu	Eng.. Specialist	619-691-3925

Brian took us on a short tour before the meeting. We learned that Rohr is the largest user of titanium metal in the US. We saw the manufacture of titanium honeycomb panels. They supply both commercial and military aircraft, space vehicles, missiles, NASA shuttles, etc.

Joe gave his 35 mm slide presentation of both hollow ceramic spheres and hollow metal spheres, and shapes formed from these spheres. The reception was excellent with many questions and comments. The presentation and questions covered a two hour time period.

Brian expressed an interest in use of fibers in the sphere formation. There was a question about the effect of thickness on the strength of the shapes formed from the spheres. There was major interest in metal spheres. Joe said the density of the nickel

spheres (which had been made by forming nickel oxide spheres and reducing in hydrogen) was 0.9 g/cc and that it may be possible to achieve 0.5 g/cc.

The discussion then turned to titanium spheres which appeared to be a major interest. Frank Gojny was the most vocal spokesman. There was a discussion about possible methods of making them including use of a hydride as a starting material and possible use of titanium powder. They expressed concern about possible contamination if the hydride is a starting material. This led to a suggestion by Frank of a sponsored proprietary research project on making titanium spheres. Joe responded to Frank's question of "about how much" with a guess of \$50,000. Frank asked for a ball park estimate of the cost of making metal spheres exclusive of the material cost. Joe came up with an off the top of his head estimate of about \$500 per cubic foot. Joe and Frank discussed a joint project seeking funding from another agency. This also appeared to be of interest.

Someone talked about "spheres" they have made from titanium foil by rolling the foil to a tube and then stamping out the sphere. They cost about \$1,000 per cubic foot.

It was not clear what density sphere they needed. Their titanium honeycomb is 5 pcf at the low end and 12 pcf at the high end. Spheres may be better than honeycomb for sound attenuation on commercial aircraft. They asked about carbon spheres. They told us that Clarkson College of Technology is making spheres from colloids. They suggest that we talk with Lockheed about ferrite spheres. They mentioned that Al Taylor at NASA Langley handled shuttle materials problems.

### **5.3 TECHNOLOGY TRANSFER PRESENTATIONS**

1. Alcoa, Alcoa Center, PA
2. Allied Signal, Ceramic Components, Div., Torrance, CA
3. Amoco, Naperville, IL
4. Bethlehem Steel Corp, Bethlehem, PA
5. Babcock & Wilcox, Barberton, OH
6. Boeing Aerospace Corp. Seattle, WA
7. Carborundum Company, Keasbey, NJ
8. Chicago, Fire Brick, Chicago, IL
9. Coors Ceramics, Golden CO.
10. Dylon Ceramic Technologies, Berea, OH
11. Foseco, Inc. Cleveland, OH
12. Gas Research Institute, Chicago, IL
13. General Refractories Co., Warren, OH
14. Harbison-Walker, Refractory, Pittsburgh, PA
15. Hi Temp Insulation, Inc., Camarillo, CA



16. Institute of Gas Technology, Chicago, IL
17. Magneco/Metrel, Inc., Addison, IL
18. NASA Amer. Research Center, Moffett Field, CA
19. National Refractories, Livermore, CA
20. Naval Civil Engineering Laboratory, Port Hueneme, CA
21. Naval Research Laboratories, Washington, D.C.
22. North American, Refractories, Cleveland, OH
23. Pittsburgh Corning Corp, Plum, PA
24. Plibrico Co., Chicago, IL
25. Premier Refractories, King of Prussia, PA
26. Pryor-Giggey Company, Whittier, CA
27. Quigley Company, Easton, PA
28. Resco Products, Inc. Norristown, PA
29. Riverbank Acoustical Laboratory, Geneva, IL
30. Rohr Industries, Chula Vista, CA
31. Suppression Engineering, Walnut Creek, CA
32. The Refractories, Institute, Pittsburgh, PA
33. Thermal Ceramics, Augusta, GA
34. Timken Co, Canton, OH
35. UOP, Des Plaines, IL
36. USG Corp. Libertyville, IL
37. USX Corp, Monroeville, PA
38. W.R. Grace, Columbia, MD
39. Zedmak Refractories, Dover, OH

